The electrical and optical properties of Hg Te - In(_2) Te(_3) alloys

Sopan L. Dahake

THE ELECTRICAL AND OPTICAL PROPERTIES OF

$Hg\,Te - In_2Te_3$ ALLOYS

by

Sopan L. Dahake M.Sc.(Nagpur)

Thesis submitted for the degree of Doctor of Philosophy

Faculty of Science

University of Durham

England

1967

C O N T E N T S

A C K N O W L E D G M E N T S

INTRODUCTION

This thesis is concerned with the production of single crystals of particular compositions of the alloy system indium sesquitelluride (In_2Te_3) and mercury telluride 3(HgTe) and the investigation of their electrical, galvano-magnetic, thermo-magnetic and optical properties, with a view to obtaining some knowledge of the band structure of the system.

Though single crystals of the alloys had been produced earlier very little knowledge of the electrical properties of the alloys in the range 10 - 75 mol % In_2Te_3 was obtained. No definite information about the scattering mechanism in this alloy system was available. The values of the effective mass were therefore subject to the same uncertainty. The optical energy gap of single crystals of these alloys had not been measured before.

The alloy compositions investigated in this work are 0, 4, 7, 15, 34, 37.5, 40, 50 and 75 mol % In_2Te_3. In spite of the considerable amount of work carried out on HgTe it was thought necessary to study it as anomalous results had been reported in magnetoresistance, and magneto-Seebeck effects in HgTe and the 7 and 10 mol % alloys.

As the zero energy gap had been predicted for the 4 mol % alloy it was expected to show the smallest effective mass for the system. This composition was therefore studied in great detail. However the optical results indicated that the zero

energy gap should occur at the 7 mol % alloy. The 7 mol % alloy was therefore also investigated. The 15 and 34 mol % compositions were studied as they were the single phase alloys before and after the two phase region between 20 and 30 mol % In_2Te_3. As the band structure was expected to change at the 37.5 mol % composition and there were no earlier results available it was thought necessary to study the 37.5, 40 and 50 mol % alloys. The controversy regarding the ordering in the 50 % alloy was also to be settled. Moreover due to the uncertainties in the measurement of the Seebeck coefficient no values of the effective mass were reported. Very little electrical work was reported on single crystals of the 75 mol % alloy because of the difficulty in obtaining large single crystals.

Chapter 1 is a summary of relevant semiconductor physics required for this thesis. The first half of the chapter contains the band theory, the transport equation and coefficients, and the scattering mechanisms. In the second part is given, in brief, the theory of the absorption phenomena and the spectral response of photoconductivity.

Chapter 2 contains a review of the properties of HgTe, In_2Te_3 and the alloy system $Hg_3Te_3-In_2Te_3$. The work on HgTe and the alloys has been reported in detail, including the band structure.

The apparatus and the experimental techniques employed are described in detail in chapter 3. Reference is made to experimental results wherever necessary to preserve continuity and avoid repetition later.

The experimental results are presented in chapters 4 and 5. Chapter 4 deals with the electrical, galvano-magnetic and thermomagnetic phenomena. Each alloy composition is dealt with separately. Discussion of the results is given simultaneously and the conclusions are given at the end of the chapter.

The optical results are presented in chapter 5 together with X-ray data on lattice parameter. The optical data include the energy gap obtained from absorption measurements and the spectral response of photoconductivity. The conclusions are given at the end of the chapter.

C H A P T E R 1:

RELEVANT THEORY

Section 1: ## Interatomic Bonding

The properties of semiconductors depend, in
the first instance upon the forces binding the
atoms into a continuous solid body. Three types
of forces may be distinguished, covalent, ionic,
and Van der Waal's type (1).

1a ### Covalent Bond

Covalent forces bind the atoms into crystals
by the sharing of one or two pairs of electrons.
These produce covalent or valence bonds which
are orientated in definite crystallographic
directions. Valence bonds differ from metallic
or ionic bonds in that the pair of electrons
binding any two atoms does not participate at
the same time, in any other bonds in the crystal.

Such bonds, due to quantum exchange forces, are called saturated bonds. The elemental semiconductors Ge, Si and gray tin have covalent bonds. Valence crystals are difficult to cleave.

1b. Ionic Bond

In ionic bonds, an electron is transferred from the more electro-positive atom to the more electro-negative atom, creating positive and negative ions. The cohesive energy of these crystals is, to a large extent, determined by the coulomb interaction between oppositely charged ions. Ionic binding forces are not saturated. Ionic crystals may be cleaved easily.

1c. Van der Waal's Type Bond

The electrons in the outer shells of rare gas atoms form closed cells. Therefore the atoms have little or no tendency to give up electrons or share them with others. The atoms in liquid or solid state are therefore

held together by the so called dispersion
forces. The interaction between the moving
electrons and the nucleus of an atom gives rise
to fluctuating dipoles. The interaction bet-
ween these dipoles associated with neighbouring
atoms then gives rise to a relatively weak
binding.

1d. Mixed Bond

     All semiconducting compounds have bonds
which are a mixture of covalent type and ionic
type. The principal characteristics of the
type of bonding will then depend on whether
the covalent or ionic bonding predominates.
Valence bonding is predominant in crystals
having zinc blende structure, such as InSb,
HgTe. Substances in which the bonding is
predominantly ionic form crystals with one
of the cubic structures.

1e. Correlation of Bond and Band Picture

     The bond picture can be related to the
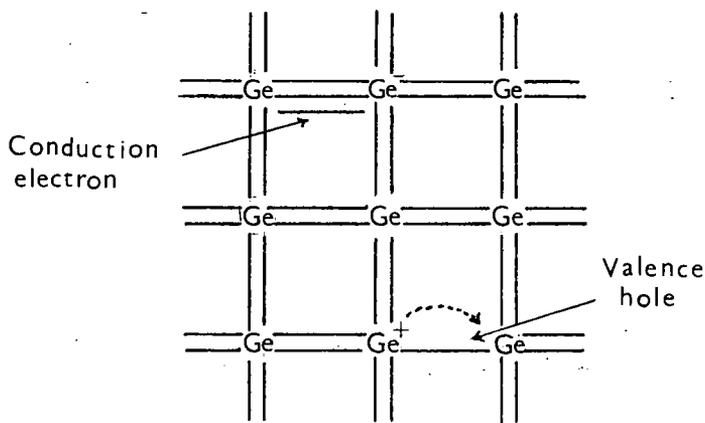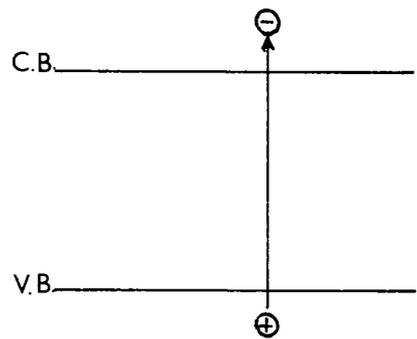
a) Bond picture   b.) Band picture

Fig. 1·1. Formation of electron-hole Pair
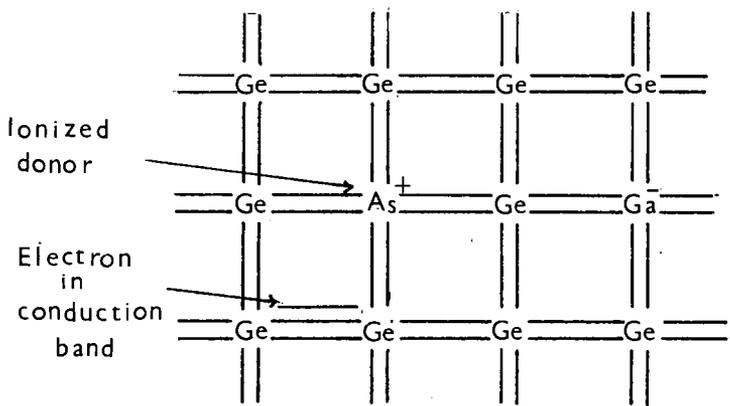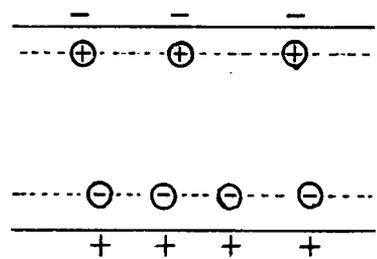
a) Bond picture   b) Band picture

Fig. 1·2. Effect of impurity
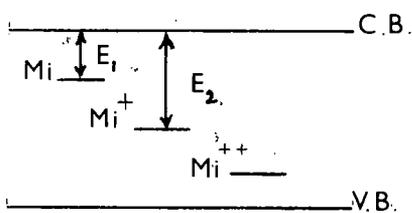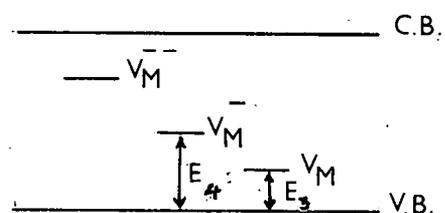
a) Interstitial atom of type –M   b) M – vacancy

Fig. 1·3. Creation of carriers in a compound MX due to departure from stoichiometry.

band picture. The valence band corresponds
to the valence electrons forming the bonds.
The minimum energy required to break a bond
i.e. to create an electron-hole pair is equal
to the separation between the valence and the
conduction bands. The process for this is
shown schematically in fig(1.1) , (2). For
elemental semiconductors the energy gap E_g
decreases with increasing atomic weight, e.g.
the values for Diamond, Si, and Ge are 5.6 ev
1.12 ev and 0.67 ev respectively.

Section 2:   Imperfections

2a. Elemental Semiconductors

      The addition of impurities to a semicon-
ductor produces allowed energy levels in the
forbidden gap between the valence and conduction
bands. In an elemental semiconductor like Ge,
substitutional atoms of group $\underline{V}$ act as donors,
and those of group III act as acceptors, fig(1.2)
These impurities require some energy to provide
electrons in the conduction band or holes in the

valence band, though it is much smaller than
that required to create an electron hole pair.
The impurity atoms, by being virtually all
ionized at room temperature, can completely
swamp the intrinsic behaviour of the pure
semiconductor.

2b. Stoichiometric and Nonstoichiometric
Compounds.

In a stoichiometric compound MX, in which
M is the electro-positive component and X is
the electronegative component, an interstitial
atom of type M would act as a donor (3)

$$M_i + E_1 \longrightarrow M_i^+ + (-)$$

$$M_i^+ + E_2 \longrightarrow M_i^{++} + (-)$$
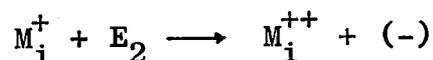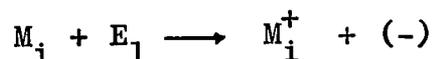
where E_1 and E_2 are the ionization energies,
and (-) represents an electron. The energy
E_1 is small as the dielectric constant of
the crystal is usually large.

A vacancy created by the removal of an
atom of the electropositive constituent would
act as an acceptor

$$V_M + E_3 \longrightarrow V_M^- + (+)$$

$$V^- + E_4 \longrightarrow V_M^{--} + (+)$$
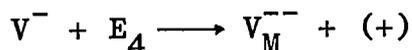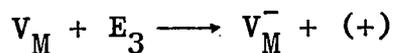
similar processes can be described for an atom of the electronegative constitent. The various processes are shown schematically in fig.(13).

In a non-stoichiometric compound, there is an excess of one constituent over the other. Thus the excess of atoms of X-type would produce equal number of vacancies V_M or interstitial X_i atoms depending upon the kind of disorder. The V_M vacancies or the interstitial X_i atoms will act as acceptors. A detailed discussion of imperfections in crystalline solids is given in references (2) and (3) .

Section 3:   Band Theory

3a.   Sommerfeld's Free Electron Model of a Solid.

To explain the physical properties of solids several models had been proposed. Sommerfeld used quantum statistics and the

Pauli exclusion principle. In Sommerfeld's model, the crystalline potential is assumed constant, and the electrons move independently in a field-free space, bounded by the surface of the solid. However, this model could not satisfactorily explain the scattering mechanism and also why some materials are metals and others are insulators or semiconductors.

3b. <u>Bloch Waves, Allowed and Forbidden Bands</u>.

Bloch (4) took account of the periodic crystal field acting on an electron in a solid. The potential experienced by an electron depends on: (i) the periodic array of atomic cores consisting of the nucleus and the inner electronic shells, and (ii) all the valence electrons. Assuming that the atoms remain fixed in position, the contribution of the cores to the potential will vary spatially with the periodicity of the lattice. Bloch assumed that the time-averaged effect of all the outer shell electrons would also be the same in each unit cell of the

crystal. The total crystal potential $V(\bar{r})$ will have the threefold periodicity of the lattice i.e.

$$V(\bar{r}) = V(\bar{r} + \bar{1}) \qquad (1.1)$$

where $\bar{r}$ is the position co-ordinate and $\bar{1}$ is any lattice vector.

Bloch showed that the solutions of the time dependent Schrodinger equation

$$\frac{\hbar^2}{2m_o} \nabla^2 \psi + \left[i\hbar \frac{\partial}{\partial t} - V(\bar{r},t) \right] \psi = 0 \quad (1.2)$$

when $V(\bar{r})$ is periodic and independent of time are then of the form

$$\psi_k(\bar{r},t) = U_k(\bar{r}) \exp i(\bar{k}.\bar{r} - \omega_r t) \qquad (1.3)$$

where $U_k(\bar{r})$ is a function having the periodicity of the lattice, i.e.

$$U_k(\bar{r}) = U_k(\bar{r} + \bar{1}) \qquad (1.4)$$

$\psi_k(\bar{r},t)$ is the wavefunction for the electron, $\bar{k}$ is the wavevector, and E is the energy of the

electron given by

$$i\hbar \, \frac{\delta \psi}{\delta t} = E\psi$$

When $\bar{k}$ is real the solutions given by
equation (1.3) are well behaved and acceptable,
and represent running plane waves modulated
with the periodicity of the lattice. Thus
the electron wavepacket is not attenuated
under the influence of a perfectly periodic
potential, i.e. there is no scattering and
the mean free path is infinite. The phase
velocity of the wave is ω/k and the group
velocity of the wave-packet is

$$= \frac{d\omega}{dk} \doteq \frac{1}{\hbar} \frac{dE}{dk} \qquad (1.5)$$

$\psi_k(\bar{r}, t)$ would grow without limits for an
imaginary value of $\bar{k}$, and thus would not represent
a physically admissible solution. In any given
direction of $\bar{k}$, therefore, there are energy
regions corresponding to imaginary $\bar{k}$ values,
which are forbidden, i.e. allowed bands alternate
with forbidden bands.
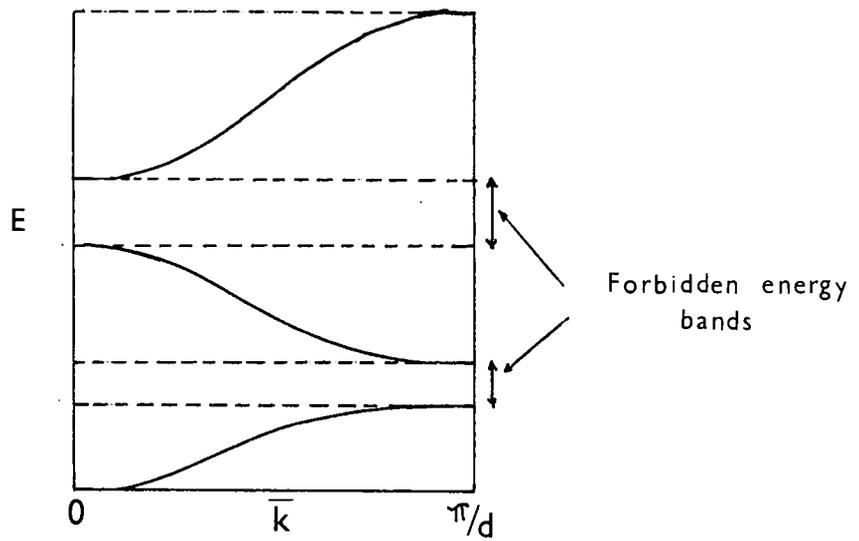
Fig. 1·4. Reduced representation of energy as a function of $\bar{k}$.
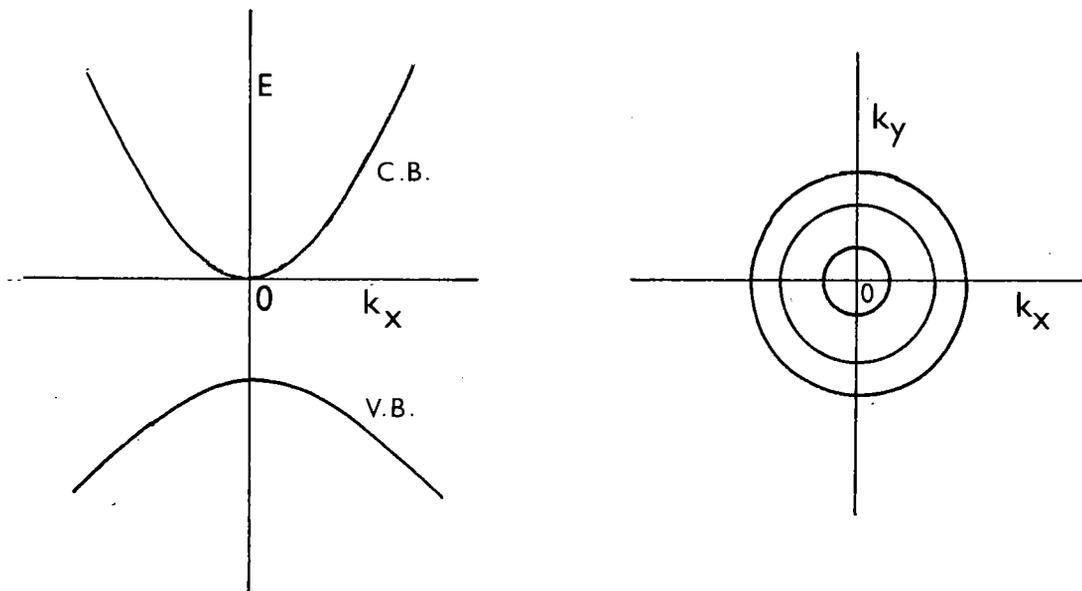
Fig. 1·5. Parabolic energy bands and spherical energy surfaces.

Consider a state ψ_k having a wavevector $\bar{k}$ such that (5)

$$\bar{k} = \bar{k}' + \bar{g}$$

where $\bar{g}$ is the reciprocal lattice vector. Now Bloch's theorem for electron waves is $\psi_k(\bar{r} + \bar{l}) = e^{i\bar{k}.\bar{l}} \psi_k(\bar{r})$, giving

$$\psi_k(\bar{r} + \bar{l}) = e^{i(\bar{g} + \bar{k}').\bar{l}} \psi_k(\bar{r})$$

$$= e^{i\bar{k}'.\bar{l}} \psi_k(\bar{r}) \tag{1.7}$$

Since $e^{i\bar{g}.\bar{l}} = 1$

Thus the state ψ_k satisfies Bloch's theorem as if it had the wavevector $\bar{k}'$, i.e. $\bar{k}$ is not uniquely defined. The arbitrariness of $\bar{k}$ makes it possible to bring all wavevectors into the first Brillouin zone by adding or subtracting reciprocal lattice vectors. ψ_k are thus multivalued functions of the $\bar{k}$-vectors lying inside the first Brillouin zone, and E_k separates into branches or bands as shown in fig(1.4).

3c. Brillouin Zones

The first Brillouin zone in three dimensions is the smallest volume enclosed by the planes (6)

$$2 \, \bar{k}.\bar{g}. \; - \bar{g}^2 \; = \; 0 \qquad\qquad (1.8)$$

and in one dimension lies between $k = \pm \pi/a$. Perturbation theory shows that the energy discontinuities lie on the boundary of the Brillouin zones, and their size is determined by the potential within the unit cell. Since the size and shape of the Brillouin zone is entirely determined by the crystal structure, the band structure i.e. the E – k relationship is completely determined by the crystal structure and the potential within the unit cell.

The number of states in the Brillouin zone is limited by the size of the crystal and is equal to the number of unit cells N in the crystal. As each state can be occupied by at most two electrons of opposite spin, each energy band can provide place for a maximum of 2N electrons. If there are 2N electrons in a

band it is completely filled and the electrons
cannot take part in conduction.   This leads
to the distinction between metals, semi-
conductors and insulators.

3d. Band Shapes for Semiconductors

The main problem of the band model is to
determine the $E - \bar{k}$ relationship, as many
electrical and optical properties of a pure
semiconductor can be explained in terms of the
band structure.   Fortunately only the bands
near the maximum or minimum value of $E(\bar{k})$ need
be known, as it is only these states that con-
tribute to the optical and electrical phenomena.

Since $E(\bar{k})$ is an even function of $\bar{k}$ (7)
it must contain only quadratic terms near $\bar{k} = 0$
i.e. $\frac{\delta E}{\delta k} = 0$ at $\bar{k} = 0$, if there is no degeneracy
at $\bar{k} = 0$.   Similarly it can be shown that at all
points on the surface of a Brillouin zone, the
normal derivative $\frac{\delta E}{\delta k_n}$ is zero.   So the $E-\bar{k}$
curves must be similar to that shown in fig.(1.4).
At $\bar{k} = 0$ there may be either a maximum or a
minimum.   Other maxima or minima may occur.   If

they are the lowest minimum or highest maximum
they will be of paramount importance.

3d. Simple Band Structure

The simplest band structure occurs when the
lowest unfilled band has a minimum at the zone
centre, and is non-degenerate. $E(\bar{k})$ may then be
expanded in powers of k_x, k_y, k_z

$$E(\bar{k}) = E_o + Ak_x^2 + Bk_y^2 + Ck_z^2 + \text{ higher powers} \tag{1.9}$$

A, B, C being positive constants. For an isotropic
crystal the Brillouin zone also has cubic symmetry,
hence $A = B = C$. For small values of $\bar{k}$ near the
minimum, taking zero of energy at the minimum

$$E(k) = \frac{h^2}{2m^*} (k_x^2 + k_y^2 + k_z^2)$$

$$= \frac{h^2 \bar{k}^2}{2m^*} \tag{1.10}$$

The band is parabolic and has spherical symmetry
i.e. the constant energy surfaces are spheres in
k-space. The scalar m^* has the dimensions of
mass and as eqn.(1.10) is similar to that for free

electrons but with the free electron mass replaced by m^*, m^* is called the effective mass.

A maximum at $\bar{k} = 0$ can similarly be described by

$$E = -E_g - \frac{\hbar^2}{2m_h^*} (\bar{k}^2) \qquad (1.11)$$

In this case the electrons behave like free particles with negative charge but with a negative effective mass, which can be interpreted in terms of holes. The form of the energy bands corresponding to the above conditions is shown in fig.(1.5). No semiconductor is known to have this band structure. The applicability of the simple parabolic band model is restricted to pure semiconductors at low temperatures.

(ii) Ellipsoidal Energy Surfaces

Maxima and minima may occur elsewhere e.g. on the surface of the Brillouin zone along any of the symmetry axes. Considerations of crystal symmetry then allow other extrema to be predicted. For a cubic crystal, if a minimum occurs along the x-axis i.e. the fourfold symmetry axis [100]
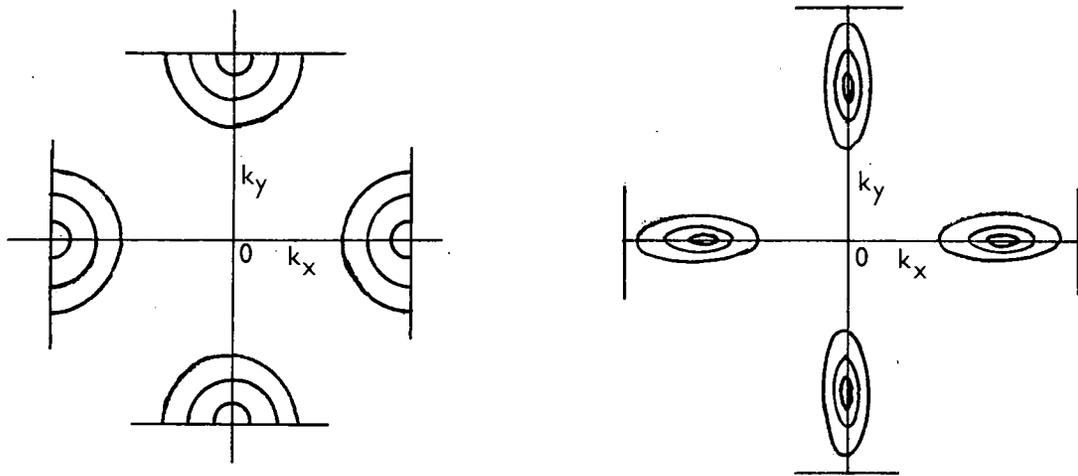
a) Spherical energy surfaces at $\bar{k} = \pi/d$ b) Ellipsoidal surfaces at $k < \pi/d$

Fig. 1·6. Constant energy surfaces as intersections with (k_x, k_y) plane

Heavy hole band

Light hole band

$k = 0$
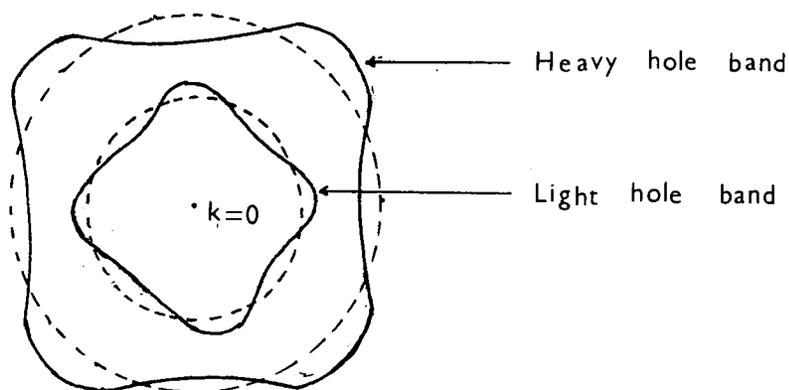
Fig. 1.7. Contours of constant energy surfaces for the two uppermost valence

bands of Si as viewed by a cross-section of the (110) plane in $\bar{k}$-space.

(a)   (b)   (c)
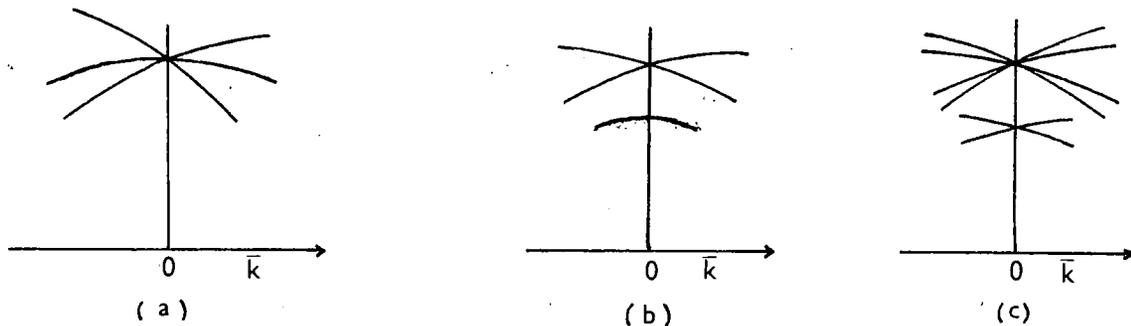
Fig. 1.8. Effect of spin-orbit interaction at $\bar{k} = 0$. a) 6 levels degenerate at

$\bar{k} = 0$. b) In lattice with inversion symmetry spin-orbit interaction leaves all

states doubly degenerate. c) without inversion symmetry degeneracy is completely

resolved.

on the surface of the Brillouin zone

$$E = \frac{\hbar^2}{2m} \left[(\frac{\pi}{a} - k_x)^2/m_1 + (k_y^2 + k_z^2)/m_2 \right] \quad (1.12)$$

In this case the effective mass is different in different directions and the energy surfaces are ellipsoidal in form with cylindrical symmetry about the x-axis. There will be other equivalent minima e.g. along the k_y and k_z axes. If the minimum does not occur on the surface of the Brillouin zone, there will be six equivalent minima instead of three. Similarly the [111] axis being a threefold symmetry axis the energy surfaces of the <111> bands are also ellipsoids of resolution. The [110] axes are twofold axes and therefore the energy surfaces of the <110> band are ellipsoids (8). Constant energy surfaces for various extrema are shown in fig(1.6).

(iii) Warped Energy Surfaces

When degeneracy arises i.e. when two energy bands touch at a point, the band structure is more complicated. When degeneracy arises at $\bar{k} = 0$ the constant energy surfaces are distorted

from the spherical shape, fig (1.7). The
relation between E and $\bar{k}$ remains essentially
quadratic. To this class belong valence bands
of many semiconductors, including Si and Ge
described by the well known formula (9)

$$E = \bar{k}^2 \left[A \pm \left\{ B^2 + C^2 (\alpha^2 \beta^2 + \beta^2 \gamma^2 + \alpha^2 \gamma^2) \right\}^{1/2} \right] \quad (1.13)$$

where $\alpha = \dfrac{k_x}{|k|}$, $\beta = \dfrac{k_y}{|k|}$ $\gamma = \dfrac{k_z}{|k|}$

(iv) Spin-Orbit Interaction

In heavy atoms there is a strong spin-orbit
interaction. In the free atom this has the
effect of removing the degeneracy between some
states of the same space wave-function but
opposite electron spin (10) e.g. a P state is
split into two states $P_{3/2}$ and $P_{1/2}$ corres-
ponding to the total angular momentum $j = 3/2$
and $j = 1/2$ respectively. Similarly the spin-
orbit interaction may thus resolve the deg-
eneracy between the bands at $\bar{k} = 0$. These
effects are important at the top of the valence

band in Semiconductors as shown in fig(1.8).

(v) Nonparabolicity

The second type of deviation from simple band structure occurs when the constant energy surfaces remain spherical or ellipsoidal but the relation between energy and wavevector ceases to be quadratic. Kane (11) has calculated the band structure for InSb for the region around the Γ point by taking into account the interaction of the conduction band with the threefold degenerate valence band. Considering only this interaction Kane derived the following expression for the conduction band energy $E(\bar{k})$

$$E(\bar{k})= 1/2 \left[\frac{\hbar^2 k^2}{m} + E_g + (E_g^2 + \frac{8k^2 P^2}{3})^{1/2} \right] \qquad (1.14)$$

where E_g is the energy gap and P is a universal constant having a value 8.5×10^{-8} ev-cm. This expression is valid if the spin-orbit splitting of the valence band is much greater than E_g and

$\bar{k}$. $\bar{P}$. This model is applicable to semiconductors with small effective masses such as InSb, HgSe, HgTe.

Equation (1.13) shows that though the conduction band is parabolic near its minimum, with increasing $\bar{k}$ the curvature decreases and the effective mass of the electrons, therefore, increases. The effective mass should thus increase with increasing carrier concentration. The susceptibility effective mass m_s is given by (12)

$$\frac{1}{m_s} = \frac{1}{\hbar^2 k} \left(\frac{dE_c}{dk}\right) \qquad (1.15)$$

From eqns (1.14) and (1,15) one gets

$$\frac{1}{m_s} = 1 + \frac{4}{3} \frac{P^2}{\hbar^2}$$

$$(E_g^2 + 8k^2 P^2/_3)^{1/2} \qquad (1.16)$$

In the case of sharp degeneracy, the free electron concentration n is equal to $\frac{k^3}{\pi}$ and

consequently

$$\frac{m_S}{1-m_S} = 32.5 \times 10^{-32} \frac{E_g^2}{P^4}$$

$$+ 8.27 \times 10^{-30} \frac{n^{2/3}}{P^2} \qquad (1.17)$$

Thus a plot of $(\frac{m_S}{1-m_S})^2$ vs $n^{2/3}$ will give a straight line with slope proportional to $\frac{1}{P^2}$ and intercept proportional to E_g^2/P^4 , if Kane's theory is applicable. This relationship is found to hold good for InSb and HgTe (13). Koldoziejczak et al (14) showed that a convenient measure of deviation from the simple parabolic law is

$$\gamma = 1 - \frac{m_S}{m_C} \qquad (1.18)$$

where m_C is the conductivity effective mass defined by

$$\frac{1}{m_C} = \frac{1}{3} \sum_i \frac{1}{m_{ii}} = \frac{1}{3\hbar^2} \left[\frac{d^2E}{dk^2} + 2\frac{1}{k} \frac{dE}{dk} \right] \qquad (1.19)$$

m_c determines an average acceleration of electrons of energy $E(\overline{k})$ under the influence of an applied field. For a parabolic band $\gamma = 0$. For Kane's band γ is '0' at the bottom of the band and tends to 1/3 high up in the band (15).

3e. The concept of Effective Mass

The acceleration of an electron in an external field is given by

$$a = \frac{dv}{dt} = \frac{1}{\hbar} \frac{d}{dt} \left(\frac{\delta E}{\delta k} \right) = \frac{1}{\hbar} \frac{\delta^2 E}{\delta k \delta k} \cdot \dot{\overline{k}} \qquad (1.20)$$

The force resulting from the external field is given by

$$F = \hbar \dot{k} = \left(\frac{\hbar^2}{\delta^2 E / \delta k \, \delta k} \right) a = m^* a \qquad (1.21)$$

The tensor quantity $m^* = \left[\frac{1}{\hbar^2} \left(\frac{\delta^2 E}{\delta k \, \delta k} \right) \right]^{-1}$ (1.22)

is thus the equivalent of a dynamical mass of an electron and is called the effective mass. Thus by considering the quasi-free electrons having mass m^* which are not affected by the strong

lattice forces, the totality of electrons can be treated as a free electron gas (16). This simplifies the concept and the laws of mechanics can be utilized.

By a suitable choice of axes the tensor may be diagonalized so that the non-diagonal terms vanish when only three principle effective masses are needed to specify the motion of the electron

$$\frac{1}{m_i^*} = \frac{1}{\hbar^2} \frac{\delta^2 E}{\delta k_i^2} \qquad i = x, y, z \qquad (1.23)$$

For example in a semiconductor with energy surface of the form

$$E(\bar{k}) = \frac{\hbar^2 k_1^2}{2 m_1} + \frac{\hbar^2 k_2^2}{2 m_2} + \frac{\hbar^2 k_3^2}{2 m_3} \qquad (1.24)$$

m_1, m_2, m_3 are the three effective masses. In the case of spherical energy surfaces, the three components of effective mass become equal so that

$$\frac{1}{m^*} = \frac{1}{\hbar^2} \frac{\delta^2 E}{\delta k^2} \qquad (1.25)$$

The density of states effective mass for ellipsoidal energy surfaces of the form (1.24) is given by (17)

$$m_d = (m_1 \ m_2 \ m_3)^{1/3} \qquad\qquad (1.26)$$

The effective mass can be determined by many methods e.g. Cyclotron resonance, thermo-electric effect, magnetoresistance effect, optical phenomena etc.

3f. The Concept of Hole

Eqn.(1.22) implies that at the top of an energy band m^* is negative as $\frac{d^2E}{dk^2}$ is negative. To deal with this case the concept of a hole in the energy band is introduced. If an entire band is full except for the state with wave-vector $\bar{k}$, one says that there is a hole with such vector. One can write this formally (18) as a determinantal wave function with elements made out of wavepackets of all states but Ψ_k. The velocity of the hole is the same as that of the missing state, the wavepacket will be carried

through space at the same rate as its neighbours
on either side. It is therefore convenient to
discuss the properties of a few holes in a
nearly full band rather than those of electrons
with negative mass.

It can be shown that the hole behaves like
a positively charged particle having a positive
mass. Consider an electric current associated
with a hole (18). There is no current in a
full band. The current of an electron in
state $\overline{k}$ is $-e\overline{V}_k$. Therefore the current of a
full band with one electron missing is

$$\overline{J}_h = 0 - (- e\overline{V}_k) = e\overline{V}_k \qquad (1.27)$$

A hole thus behaves like a positively charged
particle. The rate of change of current in
an electric field $\overline{E}$ is

$$\frac{dJ_h}{dt} = e\ddot{\overline{V}}_k = \frac{e}{\hbar} \frac{\delta^2 E}{\delta\overline{k}\,\delta\overline{k}} \left[- \frac{e\overline{E}}{\hbar} \right]$$

$$= e \left[- \frac{1}{\hbar^2} \frac{\delta^2 E}{\delta\overline{k}\,\delta\overline{k}} \right] (e\,\overline{E}) \qquad (1.28)$$

which is the acceleration equation for a particle of positive charge e and mass $m_h^* = -\left[\dfrac{1}{h^2} \dfrac{\delta^2 E}{\delta \overline{k} \, \delta \overline{k}}\right]^{-1}$ which is opposite in sign to the mass of an electron which is negative at the top of a band. Thus the hole behaves as a particle of positive charge and positive mass.

Section 4. Carrier Concentrations in Thermal Equilibrium

4a. Intrinsic Semiconduction

Consider an ideally pure semiconductor with an energy gap E_g having no impurities and take the zero of energy at the bottom of the conduction band. At $T = 0^O K$ the valence band is completely filled and the conduction band is empty. At any temperature T there are a few electrons in the conduction band and an equal number of holes in the valence band. If N(E) is the energy density of states in the band, N(E) dE is the number of levels lying between the energies E and E + dE. The number of electrons in the conduction band is therefore

$$n = 2 \int_0^\infty N(E) \ f \ (E) \ dE \qquad (1.29)$$

where $f(E) = \dfrac{1}{1 + \exp (E-E_F)/kT}$ \hfill (1.30)

is the probability that an electron occupies state of energy E. The factor 2 in equation (1.29) takes account of the spin degeneracy.

In the case of parabolic band structure with spherical energy surfaces the function N(E) is easily evaluated and is given by (19)

$$N(E) = \frac{2(2\,m_e^*)^{3/2}\,E^{1/2}}{4\,\pi^2\,\hbar^3} \hspace{1cm} (1.31)$$

Equation (1.29) then takes the form

$$n = \frac{(2m_e^*)^{3/2}}{2\pi^2\hbar^3} \int_0^\infty E^{1/2}\, f(E)\,dE$$

$$= \frac{(2m_e^*\,kT)^{3/2}}{2\pi^2\,\hbar^3} \int_0^\infty \frac{x^{1/2}}{1 + e^{x-\eta}}\,dx \hspace{1cm} (1.32)$$

$$= 2\,\frac{(2\pi\,m_e^*\,kT)^{3/2}}{(h^2)^{3/2}}\,F_{1/2}\,(\eta)$$

$$= N_c F_{1/2}\,(\eta) \hspace{2cm} (1.33)$$

where $x = E/kT$ and $\eta = E_F/kT$

Integrals of the type

$$F_n \ (\eta) \ = \ \frac{2}{\sqrt{\pi}} \ \int_0^\infty \frac{x^h \ dx}{1 \ + \ e} \ x-\eta \qquad (1.34)$$

are called the Fermi integrals (20).

If the number of electrons per unit volume is small the exclusion principle becomes unimportant at normal temperatures as far as $f(E)$ is concerned i.e. $f(E)$ approaches the classical Boltz-mann distribution. Thus when $E-E_F \gg kT$

$$f(E) \ = \ \exp \ (E_F \ - \ E) \ /_{kT}$$

$$\text{giving} \quad n \ = \ 2 \ (\frac{2\pi \ m_e^* \ kT}{h^2})^{3/2} \qquad \exp \ E_F /_{kT}$$

$$= \ N_c \ \exp(E_F kT) \qquad (1.35)$$

A similar calculation for the number of holes in the valence band, the top of which has energy -Eg gives

$$p \ = \ N_v \ \exp \ \left[\ -(E_F \ + \ E_g)/kT \right] \qquad (1.36)$$

where $\quad N_v = 2(\dfrac{2\pi\, m_h^*\, kT}{h^2})^{3/2}$

Since the number of electrons in the conduction band is equal to the number of holes in the valance band

$$n_i = p_i \quad \text{giving}$$

$$E_F = \dfrac{-E_g}{2} + \dfrac{3\, kT}{4}\, \ln\, (\dfrac{m_h^*}{m_e^*}) \qquad (1.37)$$

If $\; m_h^* = m_e^*$ the Fermi level lies exactly halfway between the bottom of the conduction band and the top of the valence band. If the effective masses are not equal the Fermi level will shift with increasing temperature in the direction of the band possessing the smaller effective mass. The distribution in the latter band might then become degenerate.

The product np is given by

$$np = N_c\, N_v\, \exp\, (-E_g/kT) \qquad (1.38)\ (a)$$
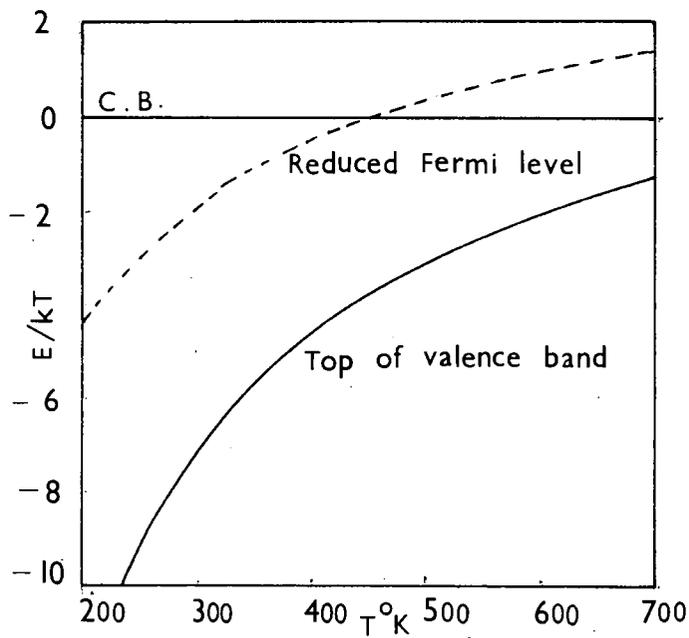
Fig. 1.9. Variation of energy gap and Fermi level with temperature for In Sb.
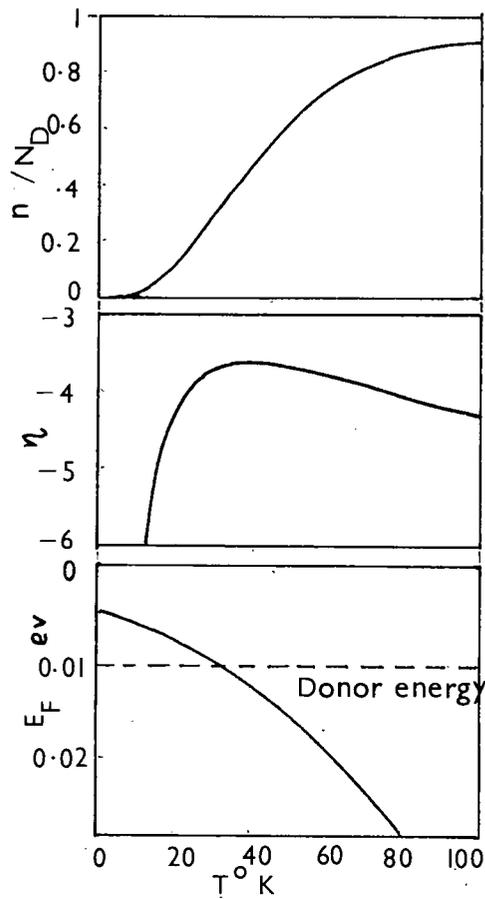
Fig. 1.10. Temperature dependence of n/N_D, η and E_F for uncompensated donor model.

or $n_i = 4.83 \times 10^{15} \, T^{3/2} \, (\dfrac{m_e^* \, m_h^*}{m_o^2})^{3/4}$

$\exp \, (-E_g/2kT)$ (1.38) (b)

The intrinsic carrier concentration n_i is thus primarily a function of the temperature and the energy gap E_g, and is independent of the Fermi energy. Equation (1.38)(a) is valid even when acceptor and donor impurities are present.

From equation (1.38)(b) one sees that $\ln \, (\dfrac{n_i}{T^{3/2}})$ vs $\dfrac{1}{T}$ should be linear with slope $E_g/2$. However the intrinsic energy gap is usually a function of temperature. Moreover m_e^* and m_h^* may also be temperature dependent. The above relationship deviates from linearity when the Fermi level approaches and enters the conduction band. Fig(1.9) shows the variation of E_g and E_F with temperature for intrinsic InSb(21).

4b. Extrinsic Semiconduction

(i) Uncompensated Impurities

For small impurity concentrations it is

appropriate to treat the impurity levels as
localized about the impurity centres. The
statistics must then be suitably modified
from that of a band state (22). Although
the electron in the localized level may have
either orientation of spin, once the state
is occupied it cannot accommodate a second
electron of opposite spin because of the elec-
trostatic interaction of the two. However,
each impurity atom will usually offer more
than one state for either the neutral or
ionized configuration. Therefore we have
to take into account the factor called "Impurity
level spin degeneracy". Thus the probability
that a discrete level at an energy E_D below
the conduction band will contain an electron
is

$$f(E_D) = \frac{1}{1 + (1/\beta) \exp \left[\dfrac{-E_D - E_F}{kT} \right]} \qquad (1.39)$$

where β is called the impurity level spin
degeneracy and is equal to 2 for monovalent
donors.

The number of electrons excited to the conduction band is again given by equation (1.33).

Since the sum of the electrons remaining in the donor levels and those excited to the conduction band must be equal to the donor concentration N_D

$$n = N_C \, F_{1/2} \, (\eta) = N_D \, - \, \frac{N_D}{1 + (1/\beta) \exp \, (\frac{E_D - E_F}{kT})}$$

$$= N_D \left[1 + \beta \exp \, (\frac{-E_D - E_F}{kT}) \right]^{-1} \quad (1.40)$$

The position of the Fermi level can thus be determined. Figure (1.10) shows the variation of n/N_D, η and E_F with temperature for a mono-valent donor model (24).

(ii) Partly Compensated Impurities

Since it is quite impossible to prepare a semiconductor containing only one type of impurity, the simultaneous presence of both donors and acceptors must be considered.

Let N_D denote the number of donors and N_A the number of acceptors, and let $N_D > N_A$.

Now the acceptors will all be occupied by electrons which have dropped down from the donor levels. There will be very few holes in the valence band. Some electrons from the donor levels will be excited into the conduction band. Thus the total number of ionized donors is equal to $(n + N_A)$ which is also equal to $(N_D - N_{Dn})$, where N_{Dn} is the number of neutral donors. Thus (25)

$$n + N_A = N_D \left[1 + \beta \exp \left(\frac{E_F + E_D}{kT} \right) \right]^{-1} \qquad (1.41)$$

Rewriting

$$\frac{\exp(E_F/kT)(n + N_A)}{(N_D - N_A - n)} = (1/\beta) \exp \left(\frac{E_D}{kT} \right)$$

If n is small so that there is no degeneracy

$$\exp \left(\frac{E_F}{kT} \right) = \frac{n}{N_C} \qquad \text{giving}$$

$$\frac{n(n + N_A)}{(N_D - N_A - n)} = \frac{N_C}{\beta} \exp (-E_D/kT) \qquad (1.42)$$

The solution of equation (1.42) for the number of conduction electrons can be examined in three different temperature ranges.

In the exhaustion range when $kT > E_D$ but $\ll E_g$, $n = N_D - N_A$ and the electron concentration is essentially independent of the temperature. This range of temperature extends from room temperature to liquid Nitrogen temperature for Ge and Si.

As the temperature is decreased, the electrons begin to freeze out into the donor levels and the second range of temperature starts. When $n < N_D - N_A$ and $n > N_A$ the electron concentration is given approximately by,(26)

$$n = (N_D - N_A)^{1/2} \ (N_c/\beta)^{1/2} \ \exp(-E_D/2kT) \qquad (1.43)$$

At very low temperatures where $n < N_D - N_A$ and $n < N_A$ the approximate solution gives

$$n = \frac{N_D - N_A}{N_A} \ (N_c/\beta) \ \exp(-E_D/kT) \qquad (1.44)$$
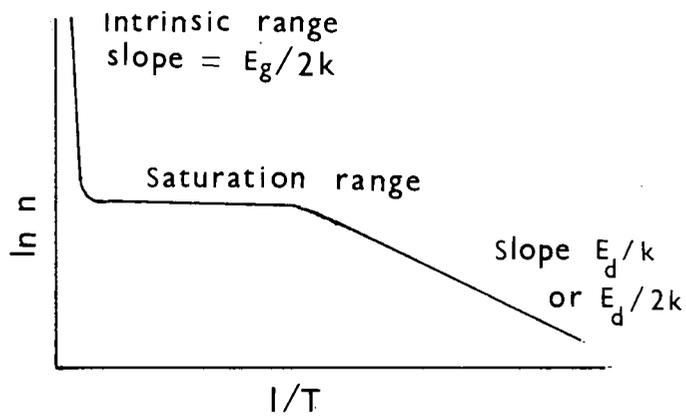
Fig 1·11. Variation of carrier concentration n with 1/T ; $N_D > N_A$.
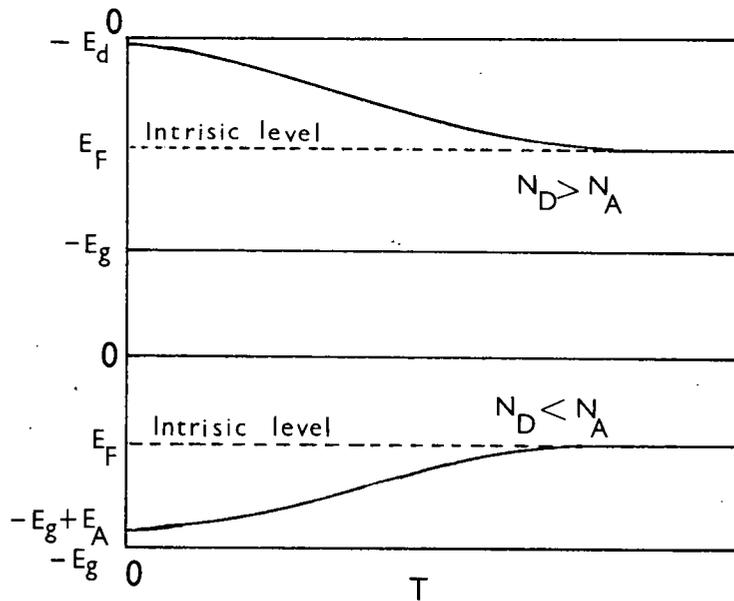
Fig. 1·12. Variation of Fermi level with temperature.

When the electron concentration is so high that degeneracy sets in the above equations must be modified. Figure (1.11) shows the variation of n with 1/T and Figure (1.12) shows the variation of the Fermi level with temperature (27)

(iii) Impurity Band Conduction

At very low temperatures when kT is less than the donor or acceptor ionization energies most of the electrons are in the donor levels. The Bohr radius of the electron is proportional to the dielectric constant and inversely proportional to the effective mass. As a result the electronic wavefunctions can overlap significantly at small impurity concentrations and form an impurity band. The results can then be interpreted in terms of conduction in an impurity band.

(iv) Hopping Conduction

When the impurity concentration is not too great, the electron may jump from one localized state to another in the impurity band. The mobility is extremely low and the effective mass is usually large.

Section 5. The Boltzmann Equation

5a. Formulation of the Equation

The carrier distribution function $f(\overline{r}, \overline{k}, t)$ gives the average number of particles which are in the state described by $(\overline{r}, \overline{k})$ at time t In order to calculate the transport coefficients it is necessary to know how the distribution function $f(\overline{r}, \overline{k}, t)$ varies under the action of external forces such as electric and magnetic fields and a temperature gradient. Secondly the internal forces e.g. scattering by lattice vibrations, other electrons and static imperfections will tend to restore the electron distribution to the true equilibrium value $f_0(\overline{r}, \overline{k})$. Therefore in the steady state

$$\left[\frac{\delta f}{\delta t} \right]_{\text{external}} = -\left[\frac{\delta f}{\delta t} \right]_{\text{internal}} \qquad (1.45)$$

Now $\left[\dfrac{\delta f}{\delta t} \right]_{\text{external}} = \left[\dfrac{\delta f}{\delta t} \right]_{\text{diffusion}}$

$$+ \left[\frac{\delta f}{\delta t} \right]_{\text{field}} \qquad (1.46)$$

To find $\left(\dfrac{\delta f}{\delta t}\right)$ diff. suppose that $\bar{V}_k$ is
the velocity of a carrier in state $(\bar{k})$. After
time t the carriers in this state move a distance
$t\bar{V}_k$. But according to Liouville's theorem on
the invariance of volume occupied in phase
space, the number of carriers in the neigh-
bourhood of $\bar{r}$ at time t is equal to the number
of them at $(\bar{r} - t\bar{V}_k)$ at time o, (28)
Thus

$$\left(\frac{\delta f}{\delta t}\right)_{\text{diff.}} = -\bar{V}_k \frac{\delta f}{\delta \bar{r}} = -\bar{V}_k \nabla_r f \qquad (1.47)$$

The force acting on carriers in electric
field $\bar{E}$ and magnetic field $\bar{\bar{H}}$ is the
force

$$F = e\left[\bar{E} + \frac{\bar{V}_k \times \bar{\bar{H}}}{c}\right] = \frac{dp}{dt} = \hbar\dot{k} \qquad (1.48)$$

This imparts a velocity

$$\bar{V}'_k = \frac{e}{\hbar}\left[\bar{E} + \frac{\bar{V}_k \times \bar{\bar{H}}}{c}\right] \qquad (1.49)$$

to the carrier in $\bar{k}$-space, so by analogy with
(1.47)

$$\left(\frac{\delta f}{\delta t}\right)_{field} = -\dot{k}\,\frac{\delta f}{\delta k}$$

$$= -\frac{e}{\hbar}\left[\overline{E} + \frac{\overline{V}_k \times \overline{H}}{C}\right]\frac{\delta f}{\delta k} \qquad (1.50)$$

It will be assumed that external forces do not greatly alter the equilibrium distribution function $f_o(\overline{r},\overline{k})$ i.e. $f - f_o \ll f_o$ where $f(\overline{r},\overline{k})$ is the perturbed distribution function. The internal collision term may be described in general by scattering processes which take a carrier from state $\overline{k}$ to state $\overline{k}'$. The problem is greatly simplified when the carrier scattering can be described by a relaxation time $\tau(\overline{k})$, in such a way that the approach to equilibrium arising from collisions is given by

$$\left(\frac{\delta f}{\delta t}\right)_{scattering} = -\frac{f - f_o}{\tau} \qquad (1.51)$$

The introduction of relaxation time is an approximation which is justified in two cases: (1) when the change of the carrier

energy on collision is small, and (2) when
scattering produces a random distribution of
velocities so that the probabilities of
transitions to states with velocities $\overline{V}$ and
$-\overline{V}$ are equal (29).

The Boltzmann equation in the relaxation
time approximation becomes

$$\overline{V}_k \cdot \nabla_r f \; + \; e \left[\overline{E} + \frac{\overline{V} \times \overline{H}}{C} \right] \nabla_k f$$

$$= - \frac{f - f_o}{\hat{\tau}}$$

5b. Method of Solution

The following assumptions will be made in
finding a simple solution of the transport
equation : (1) The conditions of non-degeneracy
exist so that $f_o(E) = \exp \dfrac{E_F - E}{kT}$ for $E_F \ll kT$.
(2) The surfaces of constant energy are spherical.
(3) The relaxation time is a power function of
energy, i.e. $\tau = \acute{u}E^S$ where s depends upon the
scattering mechanism. (4) $(f - f_o)$ is small
so that the products of $\overline{E}$, $\overline{H}$ and $\dfrac{df}{dE}$ may be

neglected.

Assume that the solution has the form
(30)

$$f = f_o - \overline{V}. \ \overline{C}(E) \ \frac{\delta f_o}{\delta E} \qquad (1.53)$$

Substituting this value in (1.52) one gets

$$-e \ \overline{E}. \ \overline{V} + kT \ \overline{V} \ \nabla_r \ \frac{E-E_F}{kT} + \frac{e}{m^*} \ \overline{V} \ .$$

$$(\overline{H} \times \overline{C}(E)) = \overline{V}. \ C(E) \ \frac{1}{\tau} \qquad (1.54)$$

From equation (1.54) one sees that if $\overline{H}$ and $\overline{C}(E)$ are parallel the transport properties are exactly the same as if $\overline{H}$ were zero provided that τ is unaffected by $\overline{H}$ i.e. $\overline{H}$ is small. Thus all longitudinal effects disappear in weak fields if the energy surfaces are spherical (31). For multiband case, however, one would not expect the longitudinal effects to be vanishingly small.

To obtain an expression for $\overline{C}(E)$ assume that all the electric fields and temperature

gradients are in the (x,y) plane, and that H is in the z-direction. Then the perturbing force will act only in the x,y plane and hence only x and y components of $\overline{C}$ need be considered.

Resolving (1.54) into x and y components gives

$$C_x + \frac{e\tau}{m^*} H_z C_y = -\tau \left\{ eE_x - kT \frac{d}{dx} \left(\frac{E_F}{kT}\right) - \frac{E}{kT} \frac{d}{dx} (kT) \right\}$$

$$-\frac{e\tau}{m^*} H_z C_x + C_y = -\tau \left\{ eE_y - kT \frac{d}{dy} \left(\frac{E_F}{kT}\right) - \frac{E}{kT} \frac{d}{dy} (kT) \right\}$$

solving for C_x and C_y yields

$$C_x = \frac{\beta - \alpha\gamma}{1 + \alpha^2} \quad , \quad C_y = \frac{\gamma + \alpha\beta}{1 + \alpha^2} \tag{1.55}$$

where

$$\beta = \tau \left\{ eE_x - kT \frac{d}{dx} \left(\frac{E_F}{kT}\right) - \frac{E}{kT} \frac{d}{dx} (kT) \right\}$$

$$\gamma = -\tau \left\{ eE_y - kT \frac{d}{dy} \left(\frac{E_F}{kT}\right) - \frac{E}{kT} \frac{d}{dy} (kT) \right\}$$

The electric current density J and the heat flow W are given by

$$J_i = -e \int \overline{V}_i \, dn = -e \int_0^\infty \overline{V}_i \, f(E) \, N(E) \, dE$$

$$= -e \int_0^\infty \overline{V}_i^2 \, \overline{C}_i \, \frac{\delta f_o}{\delta E} \, N(E) \, dE \qquad (1.56)$$

and

$$W_i = e \int E \, \overline{V}_i \, dn = e \int_0^\infty E \, \overline{V}_i \, f(E) \, N(E) \, dE$$

$$= e \int_0^\infty E V_i^2 \, \overline{C}_i \, \frac{df_o}{dE} \, N(E) \, dE \qquad \text{where } i = x, y \qquad (1.56)$$

The first term on the right hand side of equation (1.53) does not contribute to current, since no current flows in equilibrium.

After substituting for $\overline{C}_i(E)$ in (1.56) one finds that each current is expressed in terms of four variables, the electric field components and the thermal gradient components. More conveniently one can express the electric fields and the thermal currents in terms of the experimental variables, namely the electric currents and temperature gradients. Thus one can obtain the expressions for the various

transport coefficients for the weak field
case. For details see (32).

An electron in crossed electric and
magnetic fields describes a complex trajectory
in the plane at right angles to $\bar{H}$ and its
mean velocity will be zero only in the
direction at right angles to $\bar{E}$ and $\bar{H}$. If
R is the radius of curvature of its revolution
about $\bar{H}$ and l is the mean free path $l = \omega R \tau$
where $\omega = \dfrac{eH}{m_e^* c}$ the cyclotron resonance
frequency. The weak field case is defined
by the condition that $1/R = \beta \ll 1$ (33)
i.e. $\dfrac{eH\tau}{m^* c} = \dfrac{\mu H}{c} \ll 1$
Only the weak field case will be considered
unless stated otherwise.

5c. Expressions for Transport Coefficients

(i) Electrical Conductivity

The electrical conductivity σ is defined
by

$$\sigma = \frac{J_x}{E_x} \ , \qquad \nabla_r T = 0 \qquad (1.57)$$

One then obtains,(34)

$$\sigma = \frac{4 \ ne^2}{3 \ m^* \sqrt{\pi}} \quad \omega' \ (kT)^s \ \lceil(s + 5/2) \qquad (1.58)$$

giving

$$\mu_c = \frac{4 \ e}{3m^* \ \sqrt{\pi}} \quad \omega'(kT)^s \ \lceil(s+ 5/2) \qquad (1.59)$$

which for acoustic lattice scattering, i.e.

$s = -1/2$ becomes

$$\mu_{cl} = \frac{e \ \langle\tau\rangle}{m^*} \ = \ \frac{4}{3} \quad \frac{e \ l}{(2\pi m^* kT)^{1/2}} \qquad (1.60)$$

Since $l = \frac{A}{T}$ where A is a constant

$$\mu_{cl} = B \ T^{-3/2} \quad \text{where B is a constant.}$$

For mixed conduction

$$\sigma = \sigma_1 + \sigma_2$$

$$= ne\mu_e + pe\mu_h \qquad (1.61)$$

(ii) <u>The Hall Effect</u>

When a magnetic field is applied at right angles to the direction of current flow in a material, an electric field is produced in mutually perpendicular direction. This is the Hall field, and the effect is known as the Hall effect. The isothermal Hall constant R is defined by the ratio

$$R = \frac{E_y}{J_x H_z} \quad , \quad \nabla_r T \equiv 0 \text{ and } J_y = 0$$

giving, (35)

$$R = -\frac{3\sqrt{\pi}}{4} \cdot \frac{1}{ne} \cdot \frac{\Gamma(2s + 5/2)}{\left\{\Gamma(s + 5/2)\right\}^2} \qquad (1.62)$$

$$= -r \frac{1}{ne} \qquad (1.63)$$

where r is a constant depending upon the scattering mechanism.

For acoustic lattice scattering

$$R = -\frac{3\pi}{8} \frac{1}{ne} \qquad (1.64)$$

And for ionized impurity scattering, $s = 3/2$

$$R = -\frac{315.\,\pi}{512\,ne} \qquad (1.65)$$

Thus the number and type of carrier can be determined by measuring the Hall coefficient. In the case of degeneracy the Hall coefficient becomes

$$R = -\frac{1}{ne} \qquad (1.66)$$

For mixed conduction, the Hall coefficient is given by

$$R = \frac{R_1\,\sigma_1{}^2 + R_2\,\sigma_2{}^2}{(\sigma_1 + \sigma_2)^2}$$

$$= -\frac{r}{e}\,\frac{nb^2 - p}{(nb + p)^2} \qquad (1.67)$$

where $b = \dfrac{\mu_{ce}}{\mu_{ch}} = \dfrac{\mu_{He}}{\mu_{Hh}}$, the mobility ratio, provided that s is the same for electrons and holes; when $b \gg 1$

$$R = -\frac{r}{ne} \qquad (1.68)$$

equivalent to the extrinsic conduction case of
equation (1.63).

The intrinsic case is given when $n_i = p_i$
in equation(1.67), so

$$R = \frac{-r}{n_i e} \cdot \frac{b - 1}{b + 1} \qquad (1.69)$$

If the value of n_i from equation (1.38) is
substituted in equation (1.69), it is seen that

$$RT^{3/2} = D. \exp (E_g/kT) \qquad (1.70)$$

Where D is a constant, if b does not vary much.
However as mentioned in section 5a, m_e^*, m_h^* and
E_g may depend upon temperature. From the slope
of a graph of $\ln RT^{3/2}$ against $\frac{1}{T}$, an indication
of the value of the energy gap may be obtained.

From equation (1.67) one sees that for
mixed conduction the Hall coefficient becomes
zero when

$$nb^2 = p \qquad (1.71)$$

then

$$\sigma = \sigma_i = n_i \, e \, (\mu_1 + \mu_2) \qquad (1.72)$$

At a temperature at which the Hall coefficient exhibits a negative maximum

$$p = nb \qquad (1.73)$$

At this temperature,(36)

$$R_{max} = - \frac{r}{e} \, \frac{1}{4(p-n)} \, \frac{(b-1)^2}{b} \qquad (1.74)$$

and

$$n_i = (p-n) \, \frac{b^{1/2}}{(b-1)} \qquad (1.75)$$

Now $(p-n)$ is obtained by measuring the Hall coefficient in the exhaustion region, R_{exh}; b can be found from

$$\frac{R_{max}}{R_{exh}} = \frac{(b-1)^2}{4 \, b} \qquad (1.76)$$

In strong magnetic fields ($\beta^2 > 1$) the Hall coefficient is given by

$$R = \frac{\sigma_1^2 R_1 + \sigma_2^2 R_2 + \sigma_1^2 \sigma_2^2 R_1 R_2 (R_1 + R_2) H^2}{(\sigma_1 + \sigma_2)^2 + \sigma_1^2 \sigma_2^2 (R_1 + R_2)^2 H^2} \qquad (1.77)$$

Thus R will depend on H even if R_1, R_2, σ_1 and σ_2 are all independent of H. In the limiting case of $\beta \longrightarrow \infty$, $R_\infty = -\frac{1}{ne}$ $\qquad (1.78)$

Thus at a temperature such that

$$\sigma_1^2 R_1 + \sigma_2^2 R_2 = 0 \qquad (1.79)$$

the dependence of R on H will be maximum. This temperature comes out to be the temperature at which R = 0.

The Hall mobility $\mu_H = |R\sigma|$ is obtained from equations (1.62) and (1.58) viz

$$\mu_H = \frac{e}{m^*} \, \omega \, (kT)^s \, \frac{\Gamma(2s + 5/2)}{\Gamma(s + 5/2)} \qquad (1.80)$$

The ratio $\dfrac{\mu_H}{\mu_C}$ is a quantity of great importance in semiconductors and is given, from equations

(1.59) and (1.80) by

$$\frac{\mu_H}{\mu_C} = \frac{4}{3\sqrt{\pi}} \quad \frac{\lceil (2s + 5/2)}{(\lceil s + 5/2)^2} \tag{1.81}$$

giving

$$r = \frac{9\pi}{16} \quad \frac{\mu_H}{\mu_C} \tag{1.82}$$

(iii) The Magnetoresistance Effect

If the restriction $\beta = \frac{\mu H}{c} \ll 1$ is removed all the effects become dependent on the magnetic field strength. The most important of these is the magnetoresistance effect, i.e. the variation of resistance with magnetic field. Here two cases can be considered: (1) The low field case when β^2 and higher power powers can be neglected and (2) The high field case where $\beta \to \infty$. Let the conductivity in zero field given by equation (1.58) be denoted by σ_o, and the Hall mobility for weak fields by $\mu_H = R_o \sigma_o$. Then σ for non-degenerate case is given by [37]

$$\sigma = \sigma_0 \left\{ 1 - \mu_H^2 H^2 \left[\frac{\Gamma(s+5/2) \; \Gamma(3s+5/2)}{(\Gamma 2s + 5/2)^2} - 1 \right] \right\} \quad (1.83)$$

$$= \sigma_0 \left\{ -\mu_H^2 H^2 \zeta \right\} \quad (1.84)$$

giving

$$- \frac{\Delta\sigma}{\sigma_0} = \zeta \, \mu_H^2 H^2 \quad (1.85)$$

where

$$\zeta = \frac{\Gamma(s + 5/2) \; \Gamma(3s + 5/2)}{(\Gamma 2s + 5/2)^2} - 1 \quad (1.86)$$

is the magneto resistance coefficient. For non-degeneracy, ζ has the values 0.57, 0.275 and 0.08 for ionized, acoustic and optical mode scattering respectively. $\zeta = 0$ when τ is constant, which is effectively the case for a degenerate semiconductor for which , for all the averages, their value at the Fermi level may be taken. From equation (1.85) it is seen that $\dfrac{\Delta\sigma}{\sigma_0}$ is proportional to H^2.

In the limit $\beta \rightarrow \infty$, σ is given by, (38)

$$\sigma = \frac{9\pi}{16} \frac{\sigma_o}{\lceil(5/2 - s) \lceil(5/2 + s)} \qquad (1.87)$$

which shows that σ should tend to a limit at high fields. This result is not well substantiated by experiments. This could be both due to the inhomogeneities in the material and the quantum effects due to large magnetic fields.

For mixed conduction in the low-field case, $\beta^2 \ll 1$, (39)

$$\frac{\Delta\sigma}{\sigma_o} = -H^2 \mu_{Hh}^2 \left\{ \frac{npb(1+b)^2}{(nb+p)^2} + \frac{(nb^2 + p)}{(nb + p)} \right\} \qquad (1.88)$$

provided that s is the same for both electrons and holes. Both terms on the right hand side of equation (1.88) represent negative contributions to $\Delta\sigma$.

(iv) Thermo-electric Power.

The thermoelectric power, also known as Seebeck effect, is defined by

$$\alpha = \frac{E_x}{\delta T/\delta x} \qquad J_x = J_y = \frac{\delta T}{\delta y} = 0 \text{ giving}, (40)$$

$$\alpha_e = \frac{-k}{e} \left\{ (s + 5/2) - \frac{E_F}{kT} \right\} \tag{1.89}$$

For partial degeneracy α is given by

$$\alpha_e = \frac{-k}{e} \left\{ (5/2 + s) \frac{F_{(s + 3/2)}}{F_{(s+1/2)}} - \eta \right\} \tag{1.90}$$

where the intergrals $F_n(\eta)$ are given by equation (1.34). For acoustic lattice scattering α_e becomes

$$\alpha_e = -86.5 \left\{ \frac{2F_1}{F_o} - \eta \right\} \frac{\mu V}{{}^{\circ}C} \tag{1.91}$$

When the semiconductor is completely degenerate i.e. $\eta \gg 0$

$$\alpha_e = \frac{-k}{e} \frac{\pi^2}{\eta} \left(\frac{s}{3} + \frac{1}{2} \right) \tag{1.92}$$

Thus the values for the degenerate condition are greatly reduced compared to the non-degenerate condition.

The Fermi level can be calculated from the appropriate equation for α and using equations (1.63) and (1.33) for R and n respectively, an approximate value of the effective mass may be obtained.

For mixed conduction α is given by

$$\alpha = \frac{\alpha_1 \sigma_1 + \alpha_2 \sigma_2}{\sigma_1 + \sigma_2} \qquad (1.93)$$

on substituting the values of α_1, α_2 and σ_1, σ_2 for the non-degenerate case into equation (1.93) one obtains

$$\alpha = -\frac{k}{e} \left\{ \frac{nb(s + 5/2 - \frac{E_F}{kT}) - p(s + 5/2 + \frac{E_g + E_F}{kT})}{nb + p} \right\} \qquad (1.94)$$

From equation (1.94) it can be shown that, for p-type material, α will change sign when approximately $p = nb$, and this corresponds to the temperature at which the Hall coefficient is a

maximum.

Since the Seebeck coefficient for semi-conductors is usually much larger than that for metals little error is introduced by measuring α of a semiconductor against a metal, e.g. the leads of a copper-constantan thermocouple.

(v) <u>Magneto-seebeck or Longitudinal Nernst Ettinghausen Effect.</u>

When a magnetic field is applied at right angles to the temperature gradient, an electric field is produced parallel to the temperature gradient. This is called the longitudinal Nernst Ettinghausen Effect. The longitudinal Nernst Ettinghausen coefficient is given by (41)

$$Q^{l.l.} = \frac{E_x}{\delta T/\delta x} \qquad J_x = J_y = 0 \qquad \frac{\delta T}{\delta y} = 0$$

$$= \frac{E_x(H) - E_x(O)}{\delta T/\delta x} \qquad (1.95)$$

The magnetoseebeck effect is regarded as positive if the absolute value of the thermo-electric field $E_x(0)$ increases in a magnetic field i.e. if $|E_x(H)| - |E_x(0)| > 0$. For $(\frac{\mu H}{c})^2 \ll 1$ i.e. weak field case, (42)

$$Q^{1.1} = \frac{E_x}{\delta T/_{\delta x}} = -2s \; (b_s - \frac{a_s^2}{2}) \; \frac{k}{e}(\frac{\mu H}{c})^2 \qquad (1.96)$$

where $a_s = \dfrac{3\sqrt{\pi}}{4} \; \dfrac{\Gamma(5/2 + 2s)}{\{\Gamma(5/2 + s)\}^2}$

and $b_s = \dfrac{9\pi}{16} \; \dfrac{\Gamma(5/2 + 3s)}{\{\Gamma(5/2 + s)\}^2}$

Therefore in weak magnetic fields there is a quadratic dependence of $Q^{1.1}$ on $\mu H/c$. When $(\mu H/c)^2 \gg 1$

$$Q^{1.1} = -\frac{sk}{e} \qquad (1.97)$$

i.e. in strong fields $Q^{1.1}$ tends to saturation and can be used to determine the scattering parameter s. Fig(1.13) shows the dependence
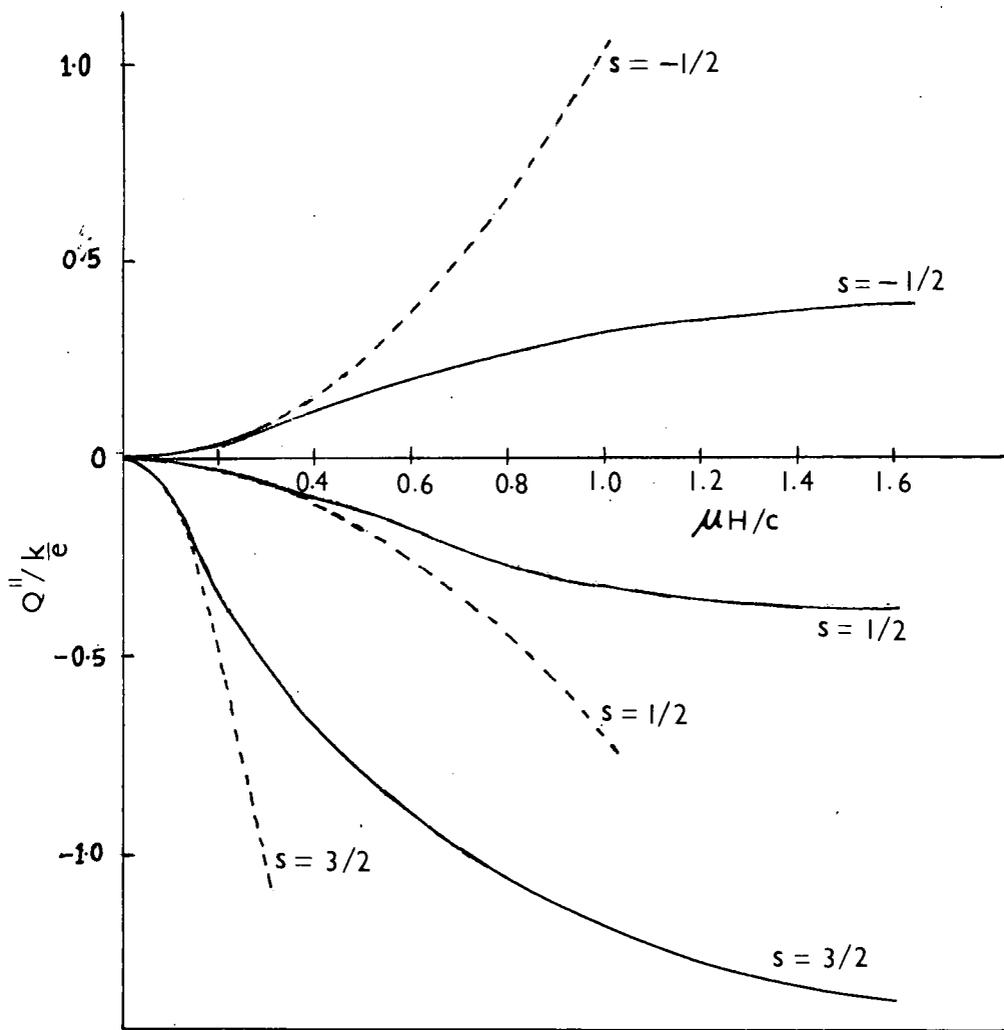
Fig. 1.13. Dependence of the magneto-Seebeck coefficient on $\mu H/c$, ------ weak-field case, ——— strong-field case.
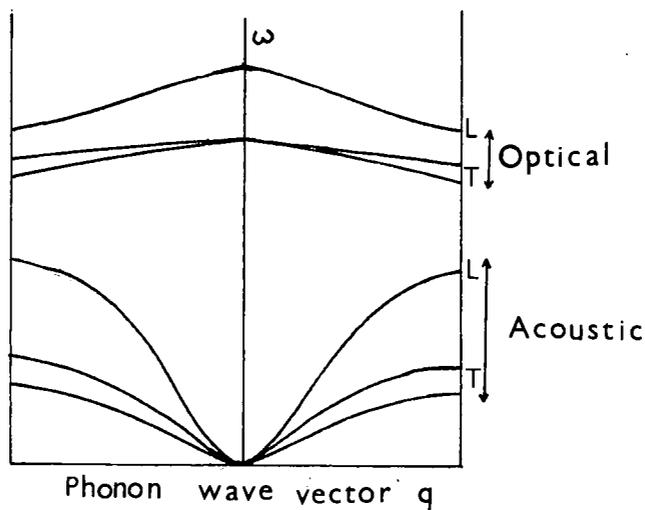
Fig. 1.14. Frequency spectrum for Phonons in a solid containing two atoms per unit cell. L = longitudinal, T = transverse.

of $Q^{1,1}$ on $\frac{\mu H}{c}$ for s = -1/2, + 1/2 and + 3/2 .
It is seen that for acoustic lattice scattering,
the sign of the magnetoseebeck effect is positive,
for all others negative. Actually for s = 0
the effect should disappear. Thus the sign of
the effect can be taken as a test for the
scattering mechanism. However, any departure
from the assumptions could affect the sign of
the effect.

Sosnowski et al (14) have derived formulae
for the thermoelectric and thermomagnetic
effects in the more general case of non-parabolic
but spherically symmetric bands, assuming
arbitrary degeneracy (15). In this case the
density of states, the effective mass, and
the relaxation time all depend on energy.
The formulae show that thermoelectric and
thermomagnetic effects are highly sensitive
to a deviation from a parabolic dispersion law,
and may even undergo a reversal of sign.

For mixed conduction the dependence of
$Q^{1,1}$ on $\frac{\mu H}{c}$ is the same as in single carrier
semiconductors i.e. in weak fields $Q^{1,1} \propto (\frac{\mu H}{c})^2$

while in strong fields $Q^{\shortparallel}$ tends to saturation
(43). The saturation limit for extrinsic
and intrinsic conduction is different. When
$n \neq p$ the limit is governed primarily by the
difference ($n \sim p$), but when $n = p$ this limit
is governed by the difference ($\mu_e \sim \mu_h$). There
will be a large variation in $Q^{\shortparallel}$ with magnetic
field at the temperature at which α changes
sign.

Section 6. Electron Scattering Mechanisms

Electrons are scattered by (i) vibrations
of the lattice, and (ii) imperfections in the
crystal.

6a. Phonons

For a crystal containing N atoms there
are 3N independent modes of vibration of the
lattice. These vibrations are called lattice
waves and are classified as longitudinal or
transverse, depending on whether the direction
of vibration is parallel or perpendicular to
the direction of propagation of the wave. There
are two transverse waves but only one longitudinal
one.

Each vibration is characterized by its
wavevector $\bar{q}$ and an index p which character-
izes the type of vibration, and its angular
frequency $\omega(p,\bar{q})$. Fig(1.14) shows a typical
lattice spectrum for a crystal with two atoms
per unit cell. The energy of each vibrational
mode is quantized, the quanta being known
as phonons. Phonons obey Bose-Einstein statistics.
This means that the average number of phonons
n in a state $(\bar{q},p)$ is given by,(44)

$$n(\bar{q},p) = \exp\left\{\frac{\Theta(\bar{q},p)}{T} - 1\right\}^{-1} \qquad (1.98)$$

where $\Theta(\bar{q},p)$ is the characteristic temperature
of the phonons.

6b. Acoustic Lattice Scattering

Acoustic scattering is important in semi-
conductors with predominantly covalent-type
binding. There are two types of acoustic
scattering. Deformation potential scattering
is the most important as it can occur in any
solid. The other type is the piezo-acoustic

scattering, which only occurs in crystals
that are piezo-electric. Since the HgTe
crystal lattice does not possess a centre of
symmetry, this type of scattering could make
an appreciable contribution. Acoustic scattering
can be assumed to be elastic as the change of
energy of the electron is small, the scattering
being limited to phonons of small wave-vector.
Therefore, a relaxation time exists. Bardeen
and Schockley (45) have used the deformation
potential method for calculating lattice
scattering in non-polar semiconductors. The
deformation potential is the change of energy
of the band edge per unit dilatation (46). The
relaxation time τ for scattering by longitudinal
acoustic modes for a semiconductor with spherical
constant energy surfaces is given by (47)

$$\tau = \frac{\rho U_1^2 h^4}{8\pi^3 (2m^*)^{3/2} E_1^2 kT} E^{-1/2} \qquad (1.99)$$

where ρ is the density, U_1 is the velocity of
the longitudinal compressional waves in the

crystal and E_1 is an energy defined by

$$\Delta E_C = E_1 \frac{\Delta V}{V_o}$$

ΔE_C is the change in the energy of bottom of the conduction band corresponding to the change ΔV of the original volume V_o.

It is seen that the free path of electrons $l = \tau v$ is independent of energy for acoustic lattice scattering. From equation (1.99)

$$\tau \propto E^{-1/2} T^{-1} m^{*-3/2} \qquad (1.100)$$

When the constant energy surfaces are not spherical the effective mass may be replaced by an appropriate averaged value.

The mobility in the range of temperature in which acoustic scattering predominates is obtained by substituting equation (1.99) into the relation $\mu = \dfrac{\sigma}{ne} = \dfrac{e}{m^*} \langle \tau \rangle$

where $\tau = \dfrac{4 \; m^{*1/2} \quad 1}{3(2\pi kT)^{1/2}}$, giving

$$\mu_1 = \frac{2^{3/2} \; \pi^{1/2} \; e\hbar^4 \; U_1^2 \; \wp}{3 \; m^{*5/2} \quad E_1^2 (kT)^{3/2}} \qquad (1.101)$$

Thus $\mu_1 \propto T^{-3/2} \; m^{*-5/2}$

A similar treatment could be given for holes.
The formula for μ_1 for holes is the same as
(1.101) except that m^* and E_1 are replaced
by corresponding quantities for holes and
the valence band.   We then get

$$\frac{\mu_{el}}{\mu_{hl}} = \left(\frac{m_h}{m_e} \right)^{5/2} \left(\frac{E_{1h}}{E_{1e}} \right)^2 \qquad (1.102)$$

If $E_{1h} = E_{1e}$

$$\frac{\mu_{el}}{\mu_{hl}} \simeq \left(\frac{m_h}{m_e} \right)^{5/2} \qquad (1.103)$$

For a degenerate semiconductor it is found that the electron mean free path is still independent of the energy due to the predominance of medium-energy electrons in the interactions with long-wavelength phonons. Therefore the relaxation time is again given by equation (1.99). However, as E is independent of temperature the mobility is proportional to T^{-1}.

The scattering by transverse shear modes has similar variation with temperature and energy to that for longitudinal modes. But the relative contribution for semiconductors with spherical energy surfaces should be smaller except at low temperatures where scattering of phonons on crystal boundaries becomes important (48).

Enz(49) pointed out that at high temperatures two phonon processes may occur, and the mobility should then be more strongly temperature dependent i.e. $\mu \propto T^{-2}$.

Intervalley scattering requires the

emission or absorption of phonons whose wave-
vectors are comparable to the principle wave-
vector of the reciprocal lattice (50). Since
the energy of such phonons is not negligible
compared to that of the electron being
scattered, the scattering cannot be assumed
to be elastic. However, since intervalley
scattering randomizes the velocity of the
charge carrier , a relaxation time approximation
can still be used.

6c. Optical Mode Scattering

When there are two or more atoms per
unit cell, optical modes, in which the two
atoms move in opposite directions, are
present. If the two atoms are similar,
as in elemental semiconductors like Ge, there
can be no polarization, but scattering is
still caused by the lattice distortion produced.
This nonpolar optical mode scattering has
been discussed in detail by Harrison (51).
He expects that at room temperature nonpolar
optical mode scattering would be of the same

order as acoustic mode scattering in most cases.

When the atoms are dissimilar and carry opposite charges as in a polar crystal, their displacement in opposite directions causes an electric polarization of the lattice, which scatters the electrons. Since this type of scattering should be important in HgTe it will be discussed in more detail.

The energy associated with the optical modes is greater than that associated with the acoustical modes and is $\sim k\Theta_D$ where $\Theta_D = \frac{h\omega_O}{k}$, ω_O being the maximum frequency of the longitudinal optical mode.

At high temperatures, when $T > \Theta_D$ or in degenerate semiconductors, the change in carrier energy on absorption or emission of a phonon is negligibly small. Therefore a relaxation time can be used. τ is proportional to $E^{1/2}$ for optical mode scattering. The mobility is given by

$$\mu_O = A\Theta_D \, T^{-1/2} \, m^{*-3/2} \qquad (1.104)$$

where A is a constant.

At low temperatures when $T < \Theta_D$ the electrons can only absorb phonons and their energy can change greatly, so that a relaxation time cannot be assumed. The expression for mobility then becomes

$$\mu_o = B \, m^{*-3/2} \, (\exp \frac{\Theta_D}{T} - 1) \qquad (1.105)$$

where B is another constant.

6d. <u>Ionized Impurity Scattering</u>

When an electron passes close to an impurity ion it is deflected due to the coulomb field of the ion. The scattering is highly anisotropic, small angles of scattering being strongly favoured. The coulomb field of the impurity centre is modified by neighbouring ionized impurities, and also by the presence of free electrons and holes. Conwell and Weisskoff (52) use a coulomb potential cut off abruptly at d, where 2d is the average distance between impurities $(2d = N_I^{-1/3})$. This is done to avoid an infinite scattering cross section.

Brooks and Herring (53) deduce an exponential fall in the potential by considering the screening effect of the free electrons.

The relaxation time can be calculated assuming that (1) the masses of the impurity ions are infinitely great compared with electron masses,(2) impurity ions are distributed at random and scatter independently of one another, and (3) Collisions are elastic i.e. the scattering produces a small perturbation of the electron motion (Born approximation). The Born approximation is valid if the potential energy of a particle in an external field is small compared with its kinetic energy. The Born approximation is always applicable to fast particles, and fails at very low temperatures.

The expression for relaxation time τ according to Brooks and Herring is

$$\tau_I = \frac{16\pi \ (2m^*)^{1/2} \ E^{3/2} \ \epsilon^2}{Z^2 \ e^4 \ N_I \ \log \ (\beta^2)} \qquad (1.106)$$

where ϵ is the permittivity, Z_e is the charge
on the impurity ion, N_I is the concentration
of ionized ions, n is the carrier density,
and
$$\beta = \frac{\hbar^2 \; e^2 \; n}{8m^* \; \epsilon \; kT \; E}$$

Assuming that $n = N_I$, and on averaging over
E, one gets

$$\mu_I = \frac{e}{m^* \langle \tau \rangle} = \frac{64 \; \pi^{1/2} \; \epsilon^2 \; (2kT)^{3/2}}{N_I \; Z^2 e^3 \; m^{*1/2}}$$

$$\left\{ \ln \frac{24 \; m^* \; k^2 T^2 \epsilon}{e^2 \hbar^2 \; N_I} \right\}^{-1} \tag{1.107}$$

The important property of ionized impurity
scattering is that the mobility is approximately
proportional to $T^{3/2}$ though the log term
cannot be neglected. Obviously μ_I is inversely
proportional to N_I. This scattering is impor-
tant at low temperatures and may make the
mobility pass through a maximum with temperature.

Mansfield (54) obtained an expression
for μ_I for arbitrary degeneracy. For complete
degeneracy he showed that the mobility is only

dependent on the number of impurities through
a logarithmic term and it is independent of
temperature.

6e. Neutral Impurity Scattering

At low temperatures when most of the
impurity atoms are not yet ionized, scattering
on neutral atoms may be important. Pearson
and Bardeen (55), and later Erginsoy (56),
showed that electron scattering on neutral
impurities is analogons to scattering of
slow electrons by hydrogen atoms. The orbit
of an electron bound to an impurity centre will
extend over a large number of lattice spacings
so that the effective scattering cross section
is large. Two processes are important, namely
(1) direct elastic scattering and (2) exchange
scattering, in which the incident electron
changes places with the electron of the impurity
centre.

The calculations show that the relaxation
time τ_N for neutral impurity scattering is
given by,(57)

$$\tau_N = \frac{m^*}{20 \, a_o \, \hbar \, N_n} \tag{1.108}$$

where N_n is the concentration of neutral impurity atoms and $a_o = \frac{\hbar^2 \, \epsilon}{e^2 \, m^*}$ is the orbital radius of a bound electron, ϵ is the permittivity. Thus τ is independent of temperature and carrier energy.

The mobility is independent of temperature and is given by

$$\mu_N = \frac{e^3 \, m^*}{20 \, \hbar^3 \, \epsilon \, N_n} \tag{1.109}$$

6f. <u>Scattering by Dislocations</u>

At low temperatures the scattering of electrons on dislocations (lattice defects) may be important and could be observed in very pure semiconductors. Dexter and Seitz (58) calculated the scattering by dislocation stress fields using the deformation potential theory. They found that the relaxation time and mobility are both proportional to temperature.

$$\mu_{dis} = DT \qquad\qquad (1.110)$$

where $D \propto \frac{1}{N_{dis}}$, N_{dis} being the number of edge dislocations per cm^2.

6g. Electron Hole Scattering

Electron hole scattering can be considered in the intrinsic range by applying the ionized impurity scattering formula and regarding the holes as the static charged centres. However, at low temperatures the holes are not static but are drifting in opposite directions to the electrons. The electrons are thus scattered into a frame of reference which is at rest with respect to the holes. This is analogous to the "phonon drag" effect.

6h. Electron-Electron Scattering

The scattering of electrons by electrons tends to redistribute the energy of the faster electrons amongst the slower ones and hence the total scattering will be increased. The scattering is essentially the same as impurity scattering except that the interacting particles

have comparable masses. Therefore a signif-
icant fraction of energy is exchanged. The
carrier-carrier scattering is proportional
to $E^{-3/2}$.

(i) Alloy Scattering

In an alloy of two semiconducting com-
pounds or elements the carriers can be scattered
by random fluctuations in the composition of
the material. As the energy of the band edge
is a function of composition, the fluctuations
in composition give rise to a deformation
potential similar to that produced by lattice
scattering. The relaxation time τ is there-
fore proportional to $E^{-1/2}$. As the amplitude
of the band edge fluctuation does not depend
upon temperature, there is no temperature term
in τ and therefore τ and μ are both proportional
to $T^{-1/2}$.

If there are two or more independent
mechanisms with relaxation times τ_1, τ_2,
τ_3 etc. the resultant τ is obtained by writing

$$\frac{1}{\tau} = \frac{1}{\tau_1} + \frac{1}{\tau_2} + \frac{1}{\tau_3} + \qquad (1.111)$$

Section 7.   Inhomogeneities

7a. Random Inhomogeneities

It will be assumed that the inhomogeneities
are statistically isotropic and involve only
the carrier concentration and not the mobilities.
The observed magnetoresistance in the presence
of random inhomogeneities is significantly
different from that given by equation (1.84),
and there is an intermixing of transverse
and longitudinal effects. Thus the longitudinal
magnetoresistance will be nonzero even for
spherical energy surfaces. The transverse
magnetoresistance in strong fields does not
saturate, but is asymptotically proportional
to H, (59).

7b. Gross Inhomogeneities

When gross inhomogeneities exist in the
sample, it is necessary to take into account
the distortion of the current lines. Only
the case of an exponential carrier density
variation along the direction of current flow
will be considered here, as this is the most
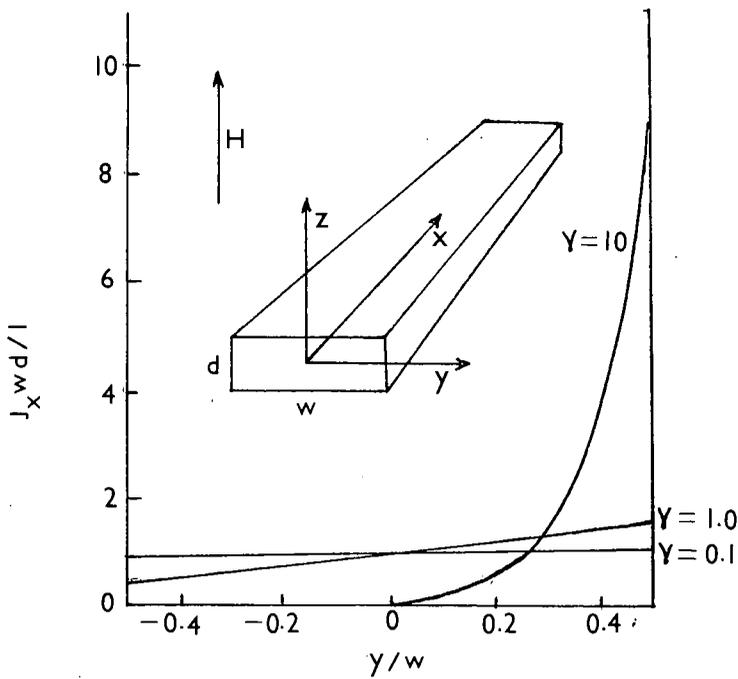
Fig. 1.15. Effect of trasverse magnetic field on longitudinal current density in the presence of a longitudinal gradient in carrier density.
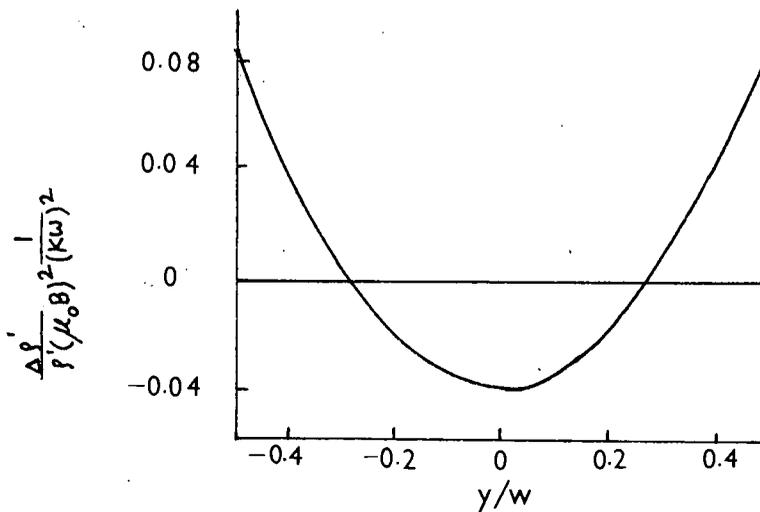
Fig. 1.16. Inhomogeneity contribution to the weak field transverse magneto-resistence as a function of the y-coordinate of the probe positions

important case. It can be shown that for a
long rectangular sample of width w and thick-
ness d, the current density far from the
boundaries of the sample is given by, (60)

$$J_x = \frac{I}{wd} \frac{\gamma/2}{\sinh \gamma/2} \exp(\frac{-\gamma y}{w}) ; \quad J_y = J_z = 0 \quad (1.112)$$

where I is the total current and $\gamma = Kw\beta$.
$K(x) = \frac{1}{n} (\frac{dn}{dx})$ is the fractional change in
carrier concentration per unit distance along
x, and $\beta = RH\sigma$ is the tangent of the Hall
angle assumed to be constant.

From equation (1.112) it is seen that
the effect of the magnetic field is to move
the current towards one side of the sample.
This distortion can be severe for large Hall
angles, even for small concentration gradients.
This effect is shown in fig(1.15) for various
values of γ. Thus for $\gamma \sim 10$ the current
effectively avoids half of the sample, and
can lead to negative values of transverse
magneto-resistance. Also the reversal of the

magnetic field will not give an identical
value of the magnetoresistance, except for
contacts located at the centre (y = 0).
After an average over both directions of H
the expression for the voltage across the
contacts becomes

$$\frac{(V_1 - V_2)_H}{(V_1 - V_2)_0} = \frac{\rho_H}{\rho_0} \frac{\gamma/2}{\sinh \gamma/2} \cosh\left(\frac{\gamma y}{w}\right) \quad (1.113)$$

The magnetic field dependence of the inhomo-
geneity factor thus depends on the location
of the contacts. At the centre of the specimen
(y = 0) the factor is $(\gamma/2)/\sinh \gamma/2$ so
that the apparent magnetoresistance is reduced,
and can readily become negative. For contacts
at the edges of the sample (y = $\pm$ w/2) the
inhomogeneity contribution at large γ will
vary as $|\gamma/2|$ i.e. linearly with H.

For $\gamma \ll 1$ and for weak magnetic fields
equation (1.113) becomes

$$\left\{\frac{\Delta\rho}{\rho_0 \, (\mu_H H)^2}\right\}_{eff} = \frac{\Delta\rho}{\rho_0(\mu_H H)^2} + 1/2(Kw)^2$$

The second term on the right hand side of
equation (1.114) is the inhomogeneity
contribution, and is plotted in fig(1.16).
It is seen that this is negative over a
large part of the sample width. If the
true magnetoresistance coefficient is small
e.g. due to spherical energy surfaces and
degeneracy, a negative transverse magneto-
resistance can occur even in the limit of
zero magnetic field.

Results similar to that of the magneto-
resistance can be expected for the magneto-
seebeck effect, though the actual variations
should be relatively smaller.

In the above treatment it was assumed
that $J_y = 0$. However, if $J_y \neq 0$ the Hall
coefficient involves an intermixing of Hall and
magnetoresistivity effects, and shows a large
dependence on magnetic field. The magneto-
resistance again depends upon the location of
the potential probes.

Part II   <u>Optical Properties</u>

section 1   <u>Optical Absorption</u>

     1a.   <u>Absorption Coefficient</u>

The theory of propagation of electro-
magnetic waves in conducting materials is
based on Maxwell's field equations which may
be written (61)

$$\text{Curl } \bar{E} = -\mu\mu_o \frac{\delta \bar{H}}{\delta t}$$

$$\tag{1.115}$$

$$\text{Curl } \bar{H} = \sigma \bar{E} + \epsilon\epsilon_o \frac{\delta \bar{E}}{\delta t}$$

$$\text{div } \bar{H} = 0$$

$$\text{div } \bar{E} = 0$$

where ϵ_o and μ_o are the dielectric constant
and permeability of free space and ϵ and μ
refer to the medium. Since there is no
permanant charge density in a conducting medium
div $\bar{E}$ is taken as zero. It can be shown that

$$\psi = A \exp \; i\omega(t - x/v) \tag{1.116}$$

is a solution for one of the components of

$\overline{E}$ or $\overline{H}$ provided

$$\frac{1}{v^2} = \mu_o \, \epsilon_o \, \mu\epsilon - i\sigma\mu_o\mu/\omega$$

Equation (1.116) represents a wave of frequency $\omega/2\pi$ propagating in the x direction with velocity $v = \frac{c}{N^*}$ where N^* is the complex refractive index of the medium. Hence

$$N^{*2} = c^2(\mu\epsilon - i\sigma\mu/\omega \, \epsilon_o)\mu_o \, \epsilon_o \qquad (1.117)$$

But for free space $N^* = 1$, $\epsilon = 1$, $\mu = 1$ and $\sigma = 0$, giving

$$c = 1/\sqrt{\epsilon_o\mu_o}$$

Thus

$$N^{*2} = \mu\epsilon - \frac{i\sigma\mu}{\omega \, \epsilon_o} = \mu(\epsilon - \frac{i\sigma}{\omega \, \epsilon_o}) = \epsilon^* \qquad (1.118)$$

where ϵ^* is the complex dielectric constant. The refractive index is complex when $\sigma \neq 0$, and may be written as

$$N^* = n' - ik' \qquad (1.119)$$

where

$$n'^2 - k'^2 = \mu\epsilon$$

$$2n'k' = \frac{\sigma\mu}{\omega\epsilon_0}$$

(1.120)

Equation (1.116) now becomes

$$\psi = A \exp(\frac{-i\omega k'x}{c}) \quad \exp\left\{i\omega(t - \frac{xn'}{c})\right\}$$ (1.121)

showing that the wave travels with a velocity $\frac{c}{n}$, and suffers an attentuation or absorption. The absorption coefficient K is defined by the condition that the energy in the wave falls by e : 1 in a distance 1/K. As the energy flow is given by the Poynting vector which is the product of the amplitudes of the electric and magnetic vectors, the attenuation is $\exp(-\frac{2i\omega k'x}{c})$ giving

$$K = 2\omega k'/c = \frac{4\pi k'}{\lambda}$$ (1.122)

k' is called the absorption index .

Measurements of transmission through samples of the material of different thicknesses may thus be used to determine K and k' directly. For highly

absorbing materials it is difficult to measure
transmission as very thin specimens are necessary.
Therefore reflection measurements using polarized
light are made, which give the values of both
n' and k'.

1b. Trasmission and Reflection Coefficients

The most important observable quantities
are the transmission coefficient T and the
reflectivity R. They are defined as the ratios
of the energy flows normal to the surface. At
normal incidence they are given by (62)

$$T = \frac{(1 - R)^2 \; e^{-Kx}}{1 - R^2 \; e^{-2Kx}} \qquad (1.123)$$

$$R = \frac{(n' - 1)^2 + k'^2}{(n' + 1)^2 + k'^2} \qquad (1.124)$$

For angles of incidence other than normal, the
reflection coefficient depends on the polarization,
and by making observations for different angles
of incidence both n' and k' may be determined
when k' is not too small.

In any practical transmission experiment on
semiconductors $\exp 2Kx \gg R^2$ so the transmission is

given by

$$T = (1 - R)^2 \exp(-Kx) \qquad (1.125)$$

The reflectivity R may be measured directly from a thick sample which is then ground down until it is thin enough for transmission measurements. Alternatively transmission measurements on two thin samples of the same material may be made to eliminate R. O r, if the refractive index is known at the appropriate wavelength, R may be calculated.

In the transparent region of the spectrum where $Kx \ll 1$, T becomes

$$T = \frac{1 - R}{1 + R} = \frac{2n'}{1 + n'^2} \qquad (1.126)$$

so the refractive index can be determined.

1c. Absorption Edge of Semiconductors

Light quanta are absorbed in a solid by two processes. Firstly, they can raise the energy of an electron in the band model by $h\nu$. This gives information about the parameters of the band model. Secondly, the photon can excite lattice vibrations. This interaction with lattice gives
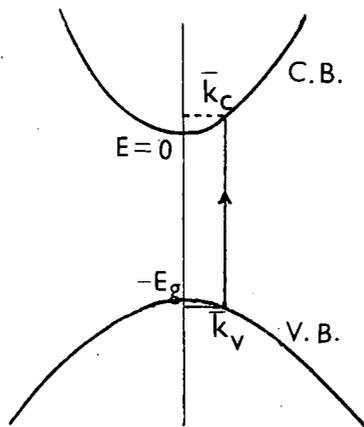
Fig. 1.17.   Direct   transitions.
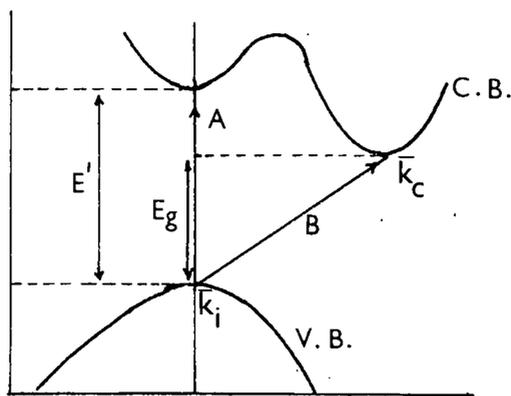
Fig. 1.18.   Indirect   transitions.
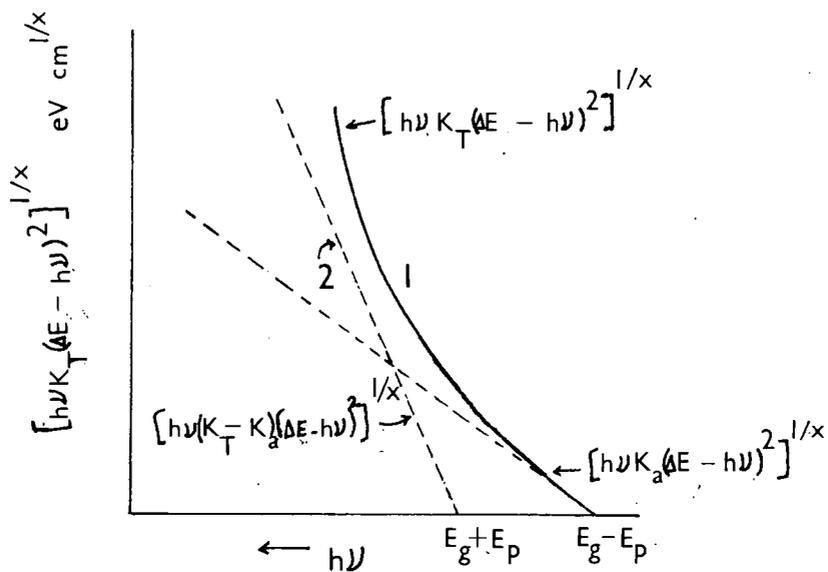
Fig. 1.19. Determination of E_g and E_p for indirect transitions.

information about bonding, ionicity, and char-
acteristic frequencies of the lattice vibrations.

Optical transitions occurring between
different bands lead to the appearance of absorption
edges in the absorption spectrum at the minimum
transition energy, or to the appearance of
absorption peaks if transitions are confined to
narrow energy regions.

1d., Direct Transitions

Consider a simple band structure, Fig(1.17).
In an absorption process crystal momentum must
be conserved.. Thus, if $\bar{k}_v$ and $\bar{k}_c$ are the wave
vectors of the electron in its initial and final
states, and $\frac{\nu}{c'}$ is the wave vector of the photon

$$h \bar{k}_v - h \bar{k}_c = \frac{h\nu}{c'} \qquad (1.127)$$

Since c' is large, the momentum of the photon is
negligible.   Therefore

$$\bar{k}_v = \bar{k}_c \qquad (1.128)$$

The wave vector of the electron is conserved
i.e. the transitions are vertical.

From equations (1.10) and (1.11) we have

$$E_c = \frac{h^2 \bar{k}^2}{2m^*} \qquad \text{for the conduction band,}$$

$$E_v = -E_g - \frac{h^2 \bar{k}^2}{2m_h^*} \qquad \text{for the valence band.}$$

Since energy must be conserved in the absorption process,

$$h\nu + \left\{ -E_g - \frac{h^2 \bar{k}^2}{2m_h^*} \right\} = \frac{h^2 \bar{k}^2}{2m_e^*} \tag{1.129}$$

giving

$$\bar{k}^2 = \left\{ \frac{h^2}{2} \left(\frac{1}{m_e^*} + \frac{1}{m_h^*} \right) \right\}^{-1} (h\nu - E_g)$$

$$= \left\{ \frac{h^2}{2m_r^*} \right\}^{-1} (h\nu - E_g) \tag{1.130}$$

Now suppose that photons lie in the energy range $h\nu$ to $h(\nu + d\nu)$, that photons of energy $h\nu$ are absorbed by the electrons at E_v, and those of energy $h(\nu + d\nu)$ are absorbed by electrons at $E_v + \frac{dE_v}{d\nu} d\nu$. Then

$$\frac{dE_v}{d\nu} d\nu = \frac{d}{d\nu} \left\{ -E_g - \frac{m_r^*}{m_h^*} (h\nu - E_g) \right\} d\nu$$

$$= - \frac{m_r^*}{m_h^*} h \, d\nu \tag{1.131}$$

Thus the number of electrons in the range $- \frac{m_r^*}{m_h^*} h \, d\nu$

is given by some constant A times $\bar{E}^{1/2}$ $\dfrac{m_r^*}{m_h^*}$ h$d\nu$

where $\bar{E}$ represents E_v measured downwards from the top of the valence band, i.e.

$$\bar{E} = (h\nu - E_g) \frac{m_r^*}{m_h^*}$$

Therefore the number of electrons in the range

$$- \frac{m_r^*}{m_h^*} \, h d\nu$$

$$= A\left(\frac{m_r^*}{m_h^*}\right)^{3/2} (h\nu - E_g)^{1/2} \, d\nu \qquad (1.132)$$

Suppose that the probability per unit time of electrons in state $\bar{k}$ in the valence band absorbing a photon of correct energy is $P(\bar{k}^2)$. Then the total probability per unit time of photons in the range ν to $\nu + d\nu$ being absorbed is

$$P(\nu)d\nu = \text{(no of electrons in the range)} d\nu \ P(\bar{k}^2)$$

$$= B(h\nu - E_g)^{1/2} \, d\nu \ P(\bar{k}^2) \qquad (1.133)$$

where B is a constant equal to $A\left(\dfrac{m_r^*}{m_h^*}\right)^{3/2} h$.

Thus, as the absorption coefficient K is proportional to $P(\nu)$

$$K = \text{const } (h\nu - E_g)^{1/2} \ P(\bar{k}^2) \qquad (1.134)$$

for $h\nu \geqslant E_g$.

If $h\nu < E_g$, $K = 0$

For $h\nu \simeq E_g$, K^2 is small, so expanding $P(\bar{k}^2)$
in powers of $\bar{k}^2$

$$P(\bar{k}^2) = a_o + a_1 \bar{k}^2 + a_2 \bar{k}^4 +$$

If $a_o \neq 0$

$$K = \text{constant } (h\nu - E_g)^{1/2} \qquad (1.135)$$

for allowed direct transitions. If one plots
K^2 against $h\nu$ one would get a straight line
with intercept E_g on the energy axis.
It often happens that $a_o \equiv 0$, then $P(\bar{k}^2 = 0) = 0$
Thus the transitions at $\bar{k} = 0$ are forbidden. This
results from a quantum mechanical selection rule
and is associated with the symmetry properties
of the electron states at $\bar{k} = 0$ in valence and
conduction bands. The symmetries are related to
lattice symmetry.

   If the symmetry is the same at $\bar{k} = 0$ in both
the bands $a_o \equiv 0$, leading to forbidden transitions.
If the symmetries are different $a_o \neq 0$, the
transitions are allowed.

For forbidden transitions we have to take the variation of P with $\bar{k}^2$ into account. Thus $P(\bar{k}_v^2) = \text{const} (\bar{k}_v^2)$ for forbidden transitions, giving

$$P(\bar{k}_v)^2 = \text{const} \left\{ \frac{h^2}{2m_r} \right\}^{-1} (h\nu - E_g)$$

$$K = \text{const} (h\nu - E_g)^{3/2} \qquad (1.136)$$

1e. Indirect Transitions

Indirect transitions take place when a phonon is absorbed or emitted during the absorption of a photon. If $\bar{q}$ is the wavevector of the phonon, the conservation of momentum leads to

$$\bar{k}_c - \bar{k}_i = \pm \bar{q} \qquad (1.137)$$

Thus, in figure (1.18) the transition B can take place only with the emission or absorption of a phonon, so that all non-vertical transitions are indirect. However transition A can be direct or indirect depending upon whether phonon participation takes place or not.

The minimum energy for which transition B is possible is given by

$$h\nu = E_g \overset{+}{\underset{-}{}} E_p \qquad\qquad (1.138)$$

The theory of indirect non-vertical transitions is given by Bardeen, Blatt and Hall (63), and Fan et al (64). For a single phonon process, the absorption coefficient K_a due to simultaneous absorption of a photon and a phonon is given by ,(65)

$$K_a = \frac{A(h\nu + E_p - E_g)^x}{h\nu (\Delta E - h\nu)^2 (e^{E_p/kT} - 1)} \qquad\qquad (1.139)$$

when $h\nu > E_g - E_p$; $K_a = 0$ when $h\nu < E_g - E_p$, A is a constant nearly independent of the photon energy $h\nu$, and ΔE is the energy gap of the virtual or intermediate state near $\overline{k} = 0$.

The corresponding expression for the emission of a phonon is given by

$$K_e = \frac{A e^{E_p/kT}(h\nu - E_p - E_g)^x}{h\nu (\Delta E - h\nu)^2 (e^{E_p/kT} - 1)} \qquad\qquad (1.140)$$

for $h\nu > E_g + E_p$. $K_e = 0$ if $h\nu < E_g + E_p$. The value of x is 2 for allowed transitions and 3 for forbidden. In the photon energy range $h\nu > E_g + E_p$ the total absorption coefficient K_T is given by

$$K_T = K_a + K_e \qquad\qquad (1.141)$$

If one plots the quantity $\{h\nu K_T(\Delta E-h\nu)^2\}^{1/x}$ against $h\nu$ one obtains a curve as shown in fig(1.19). The straight line obtained at lower photon energies corresponds to the phonon absorption term having a slope of $A/(e^{E_p/kT}-1)$ and photon energy intercept at $(E_g - E_p)$. Thus the contribution of K_a can be subtracted from K_T. Curve 2 shows such plot of $\{h\nu(K_T - K_a)(\Delta E - h\nu)^2\}^{1/x}$ corresponding to the phonon emission term having a slope of $\{Ae^{E_p/kT}/(e^{E_p/kT}-1)\}^{1/x}$ and photon energy intercept at $(E_g + E_p)$. Thus E_g and E_p can be determined from experimental results.

1f. <u>Shift of Absorption Edge with Impurity Concentration</u>

The shift of the absorption edge to higher energies with impurity concentration gives in-formation about the effective mass in the conduc-tion band. This effect will be important for semiconductors with small effective mass of charge carriers, since then the density of states is small and degeneracy appears at small doping levels. For spherical energy surfaces when the
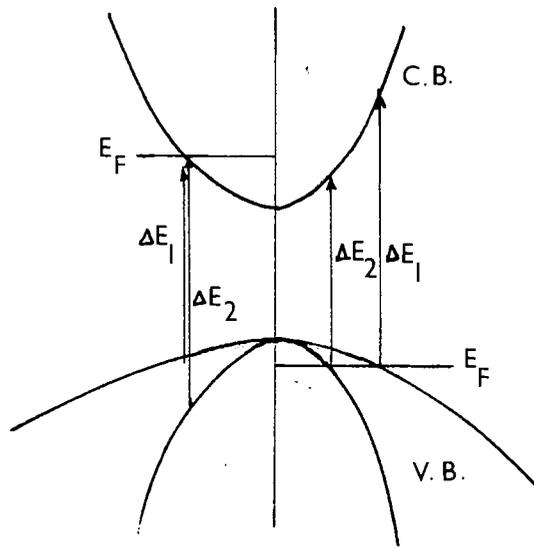
Fig 1.20. Semiconductor with isotropic parabolic bands. Left hand side — Fermi level in conduction band. Right hand side — Fermi level in valence band.
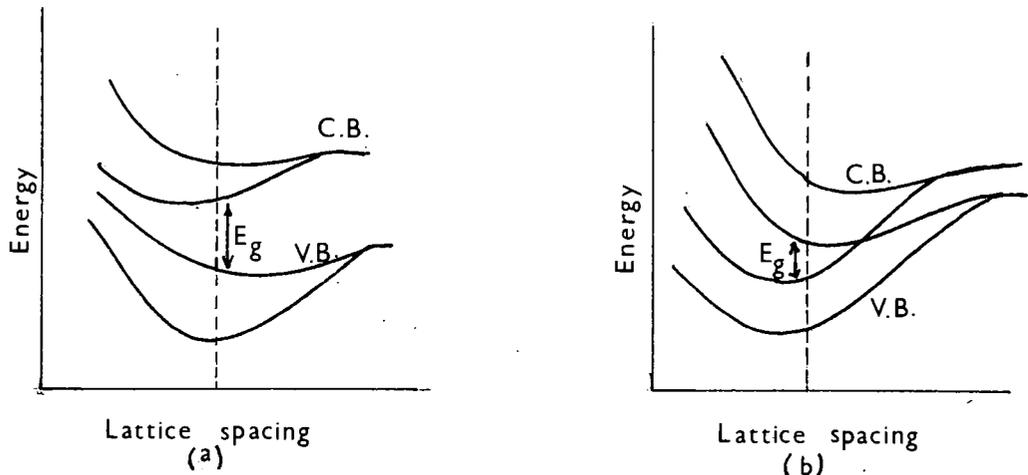
Fig 1.21. Effect of pressure on the energy gap. a) E_g decreases with increase of pressure. b) E_g increases with increase of pressure.
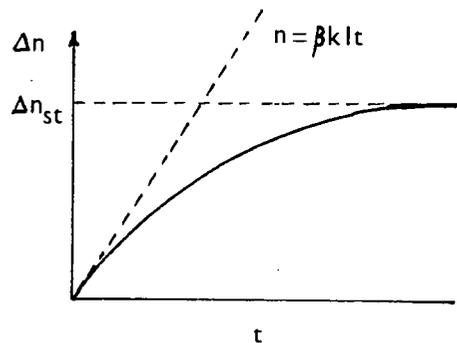
Fig. 1.22. Variation of carrier density with time during illumination.

conduction band has high curvature i.e. $m_e^* < m_h^*$
the number of conduction electrons required to
fill the band to height E is given by, (66)

$$\eta = \int_o^{\Delta E} d \; N(E) = \frac{8\pi}{3h^3} \left\{ 2m_e^* \; \Delta E \right\}^{3/2} \qquad (1.142).$$

Thus knowing the impurity concentration and measure-
ing the shift of the absorption edge ΔE gives
the value of m_e^*.

Information about the shape of the valence
band may be obtained from the band to band absorp-
tion of degenerate samples. In fig.(1.20) (left
half) direct transitions can take place only
above $\Delta E_1 > E_g$. Additional transitions from the
V_2 - band above ΔE_2 lead to an increased absorption.
The measurement of absorption coefficient makes it
possible to measure $\Delta E_1 - \Delta E_2$ and if the bands
are parabolic, the ratio of the effective masses
$\frac{m_{h_2}^*}{m_{h_1}^*}$. When the Fermi level lies in the valence
band (right half of fig.(1.20)), the absorption
starts at ΔE_2 and increases once more dis-
continuously at ΔE_1. If the V_2 band has a
large curvature, ΔE_2 is almost equal to E_g.
The absorption edge is then not shifted by
degeneracy.

1g. <u>Pressure and Temperature Dependence</u>

<u>of the Absorption Edge</u>

Pressure decreases the lattice constant and thus changes the band structure. The most important effect is the shift of the absorption edge with pressure. In figure (1.21) is shown the behaviour of the energy levels. It is clear from the figure that, in the first case (a) the energy gap will decrease on compression, whereas for (b) the gap will increase on compression. Therefore, the pressure dependence of the absorption edge, can be of either sign. For very small changes in lattice spacing, which occur in the accessible pressure range, the change in the energy gap with dilatation or pressure may be taken as linear. We may put $\frac{dE_g}{dV/V} = \frac{dE_g}{\chi dP}/P = 2(\pm C_e \pm C_h)$, where V and P are the volume of the specimum and pressure, χ is the compressibility and C_e and C_h are constants applying to C.B. and V.B. respectively.

Pressure may also change the distribution of electrons among the bands and the impurity states. The deformation of individual bands changes the density of states and thereby the

effective mass of the carriers.

There are two factors contributing to the temperature dependence of the absorption edge. The dilatation part is given by, (67)

$$\left\{\frac{dE_g}{dT}\right\}_d = -\left(\frac{\beta}{\chi}\right)\frac{dE_g}{dP} = 2\ (\overset{+}{-}C_e\overset{+}{-}C_h) \qquad (1.144)$$

where β is the coefficient of linear thermal expansion.

The second contribution arises from an electron lattice interaction term which is temperature dependent. The qualitative result is that the bands broaden on heating, so that this part of the energy shift $(\frac{dE_g}{dT})_b$ is always negative.

1h. <u>Transitions within the Valence and Conduction Bands</u>

Inter valence-band transitions e.g. $V_2 \rightarrow V_1$ were observed by many workers. The spin orbit splitting and the effective masses for these bands can be determined from experimental observations.

Similarly transitions between sub bands of the conduction band have been reported in many materials e.g. GaAs, GaP.

1i. Free Carrier Absorption

Absorption by free, conduction electrons is significant at long wavelengths. The Drude theory of absorption by free electrons leads to an absorption coefficient, (68),

$$K = \frac{4 \pi \sigma}{n} \left(1 + \frac{\nu^2}{\gamma^2}\right)^{-1} \qquad (1.145)$$

where σ is the low frequency conductivity, γ the damping factor given by $2\pi\gamma = \frac{e}{\mu_e m_e}$, and n is the index of refraction. The quadratic relation with frequency is expected to hold good for wavelenths upto a few hundred microns. All the parameters in equation (1.145) are measurable, so that a value of γ and hence m_e may be obtained. The quadratic relation should hold good only for photon energies $<$ kT because of the assumption of constant damping factor for all electrons.

Part II

Section 2. Photoconductivity

2a. Equilibrium and Non-equilibrium Carriers, Non-equilibrium Conductivity

Free electrons and holes liberated by

thermal ionization are in thermal equilibrium
with the lattice and are called equilibrium
carriers. In the generation of excess
carriers by other means e.g. optical excitation,
the energy is retained mainly by the electrons,
and the average thermal energy of the lattice
remains practically unaffected. Consequently
the equilibrium between the lattice and electrons
is disturbed. Therefore carriers formed in
someway other than by thermal ionization are
called "non-equilibrium" (69).

When the external excitation is removed,
the small number of excess electrons will re-
combine with the holes without practically affect-
ing the temperature of the lattice. Thus we may
assume that the application or removal of an
excitation changes the density of non-equilibrium
carriers without affecting the density of
equilibrium ones. The total density (n or p)
is simply the sum of the equilibrium (n_o, p_o)
and non-equilibrium (Δn, Δp) carrier densities.
Thus

$$n = n_o + \Delta n$$

$$p = p_o + \Delta p$$

(1.146)

The presence of non-equilibrium carriers alters

the conductivity of a semiconductor, and in a general case

$$\sigma = e \ (\mu_e n_o + \mu_h \ p_o + \mu_e \ \Delta n + \mu_h \ \Delta p) \qquad (1.147)$$

The excess conductivity is then

$$= e \ (\mu_e \ \Delta n + \mu_h \ \Delta p) \qquad (1.148)$$

Let $\Delta n'$ and $\Delta p'$ be the numbers of electrons and holes respectively generated per unit time per unit volume and I be the light intensity. Then the amount of light energy absorbed per unit time in unit area of a layer of thickness dx is

$$-dI = KIdx \qquad (1.149)$$

The optical energy absorbed per unit time per unit volume is

$$- \frac{dI}{dx} = KI \qquad (1.150)$$

Thus $\Delta n'$ and $\Delta p'$ should be proportional to KI. Thus

$$\Delta n' = \Delta p' = \beta KI \qquad (1.151)$$

where β represents the 'quantum yield' i.e.
the number of pairs formed by a single quantum.
The density of non-equilibrium carriers would thus
increase with time without limit according to the
law

$$\Delta n = \Delta p = \beta KIt \qquad (1.152)$$

However this does not happen because of the
converse process of recombination. After a certain
time from the commencement of illumination a
constant photoconductivity $\Delta\sigma_{st}$ is established
corresponding to the steady state values of the
carrier densities Δn_{st} and Δp_{st}. In the
steady state the rate of generation of carriers
is equal to the rate of recombination. Fig(1.22)
shows the variation of carrier density with time
during illumination.

Let τ be the average lifetime of the carriers
$(10^{-2} - 10^{-7}$ sec). The steady state carrier density
is then equal to the product of the rate of gener-
ation per unit volume and the average time of their
existence in the band before recombination, τ_e

$$\Delta n_{st} = \beta KI\tau_e$$

$$\qquad (1.153)$$

$$\Delta p_{st} = \beta KI\tau_h$$

and $\quad \Delta\sigma_{st} = \Delta\sigma_n + \Delta\sigma_p = e\beta KI(\mu_e\tau_e + \mu_h\tau_h) \qquad$ (1.154)

If one of the terms in the parentheses is **larger** than the other, we have "unipolar" non-equilibrium conductivity due to carriers of one sign only

$$\Delta\sigma_{st} = e\mu\tau\beta KI \qquad\qquad (1.155)$$

K and β govern the process of generation of carriers and μ and τ represent the processes of motion and recombination of non-equilibrium carriers.

2b. Spectral Response of Photoconductivity

The spectral response curves of photoconductivity usually show a fairly sharp maximum at a wavelength slightly longer than that corresponding to the absorption edge. The location of the maximum is dependent on the thickness of the crystal and the recombination parameters (70). At longer wavelengths the excitation decreases simply because the absorption coefficient K decreases. For wavelengths shorter than the maximum, the radiation is being strongly absorbed and produces excitation only near the surface. Thus the maximum occurs when a transition from surface excitation to volume excitation takes place, and

is most prominent when the volume lifetime is much larger than the surface lifetime, i.e. in photosensitive crystals. De Vore (70) has shown that there is a photoconductivity maximum if $S > D/\tau$, where S is the surface recombination velocity, D the diffusion constant, and τ the volume recombination lifetime. This is the case of applied field perpendicular to the direction of light, carrier motion being determined by diffusion.

The threshold of photoconductivity is often determined on the basis of "Moss Criterion" i.e. that wavelength for which the response has fallen to one-half of the maximum (71)(72). Whatever criterion is used, the energy gap derived from the spectral response is 10 to 20% lower than the value obtained from both electrical and absorption experiments (71), for many semiconductors.

C H A P T E R   2:

PREVIOUS STUDIES ON THE MATERIALS

Introduction

This chapter is divided into three sections. In the first section a brief survey of the literature on HgTe is made. Because of its small energy gap, high electron mobility and large mobility ratio, considerable interest has been generated in its properties. The earlier results were analysed assuming it to be a small gap semiconductor, but the recent results have been interpreted on the basis of a band structure of a semimetal type.

In the second section properties of the defect compound In_2Te_3 are described briefly. Much less work has been reported on In_2Te_3 because of the difficulty in obtaining single crystals.

A full discussion of the previous studies of the $Hg_3Te_3-In_2Te_3$ alloy system is given in the third section.

Section 1. The Mercury-Tellurium Binary Alloy System

1a. Phase Diagram of Hg-Te system

Hansen and Adenko (73) and Delves and Lewis (74) have given a clear picture of the principle features
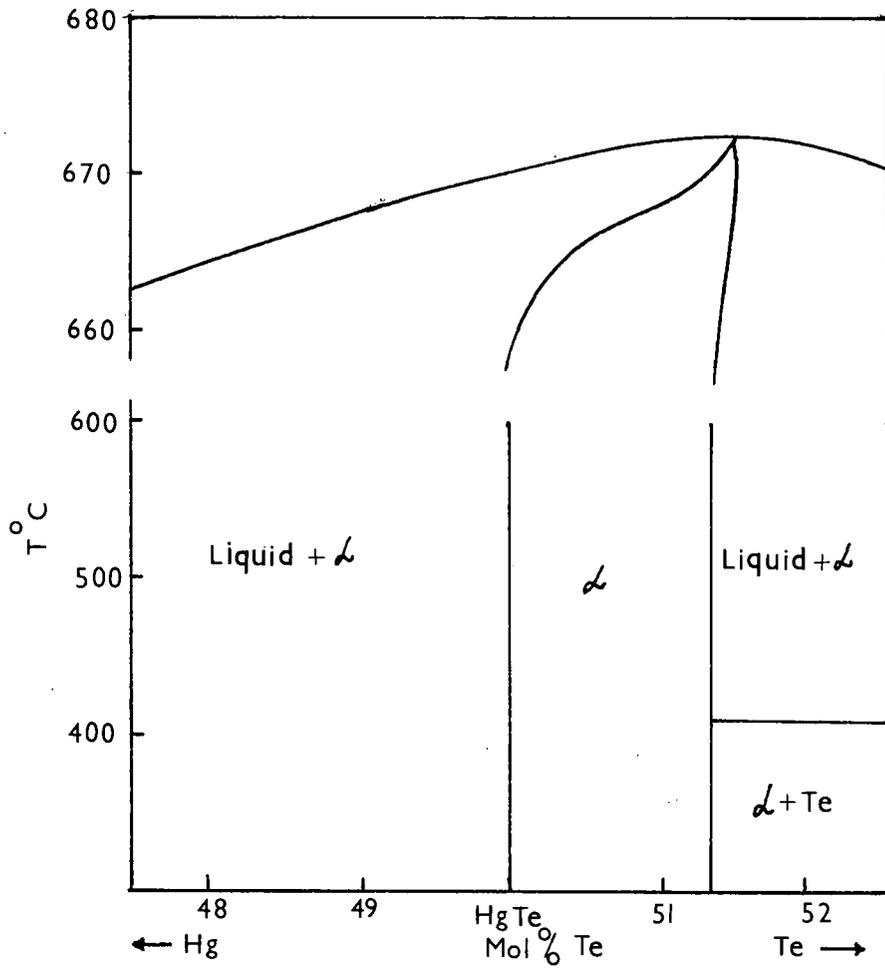
Fig. 2.1. Phase diagram in the region of HgTe , (Delves & Lewis).
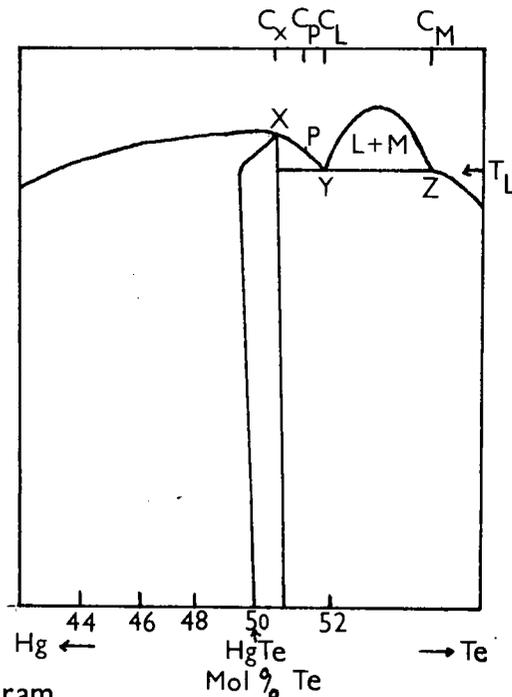
Fig. 2.2. Phase diagram for HgTe showing a region with two immiscible liquids , (Delves 1965).

of the T – x diagram of the Hg-Te system. Analysis of
the Te – rich part of the system reported in reference (75)
shows that the only compound is HgTe which is sharply
defined, and that there is an eutectic at 88 atomic
percent tellurium at a temperature of $409 \pm 2^{O}C$, the
melting point of Te being $435^{O}C$. Delves and Lewis (74)
have determined the main features of the phase diagram near
the composition HgTe by differential thermal analysis and
vapour phase equilibrium. Their results are shown in
fig(2.1). They have found the melting point of HgTe
to be $670 \pm 1^{O}C$ and not $600^{O}C$ as reported by Lawson et
al (76). A maximum in the liquidus occurs on the Te
rich side between 2.5 and 4 atomic percent. They have
found a solid solubility of Hg in HgTe of considerably
less than 2 atomic % but a considerable solubility of Te
in HgTe of upto 2.5 atomic %. This solubility corresponds
to a composition of 51.25 atomic % Te.

Brebrick and Strauss (77) have found that the solid
solubility of Te in HgTe is considerably less than 2.5
atomic % reported by Delves and Lewis. They obtain an
upper limit of 0.5 atomic % Te upto $578^{O}C$. From the
analysis of the electrical measurements on HgTe Brebrick
and Strauss conclude that the homogeneity range would be
only about 0.01 atomic % wide. They agree with Delves and
Lewis as far as the solid solubility of Hg is concerned.

Delves (78) has shown that in a binary system where the solid is in equilibrium with two immiscible liquids at a monotectic, crystal growth can take place without any diffusive segregation and constitutional supercooling does not occur. A two liquid region has been found in the Hg-Te system and the phase diagram near the stoichiometric composition HgTe is shown in fig(2.2). To explain inhomogeneity Delves has suggested that the segregation coefficients depend on crystal orientation.

1b. Preparation of HgTe

The natural form of HgTe, Coloradoite occurs only in small impure deposits. In the earlier studies on HgTe by the Russian workers (reference 79 - 82) sintered or pressed samples of HgTe were used. Carlson (83) has prepared samples from polycrystalline ingots formed from stoichiometric quantities of elements fused by the two furnace technique. He has found that copper acts as an acceptor and zinc as a donor. Room temperature electron mobilities of nearly 10,000 cm^2/vsec have been obtained.

Black et al (84) were the first workers to prepare large single crystal ingots of HgTe by the Bridgman technique, which is described in detail in Chapter 3. By zone refining some carefully prepared material Lawson et al (76) were able to produce both p and n-type HgTe. Harman et al (85), Quillet et al(86), and Rodot and Triboulet(87)

carried out long-time heat treatments at low temperatures, in controlled mercury vapour pressure in an attempt to increase the purity of HgTe. At fixed ingot temperatures, n-type samples were obtained for the higher pressures and p-type samples for the lower pressures. For intermediate pressures purest samples which remained intrinsic at 77^OK or even at 20^OK were obtained. This technique of annealing has been used by most of the later workers.

Dziuba (88) has managed to produce high purity HgTe, by a method of multiple distillation in vacuum coupled with annealing in Hg-vapour. Krucheanu et al (89) have grown HgTe from the gas phase. Two methods were used: (1) a dynamical one consisting of the transport of compound vapours in a hydrogen or argon stream from the sublimation point to the crystallization point, with a temperature gradient between the two points; (2) a static one consisting of the sublimation of compound vapours and their crystallization within an evacuated and sealed quartz ampoule with a 100° C/cm temperature gradient. The HgTe crystals obtained contained Te in excess of the stoichiometric composition and belonged to the cubic system with zincblende-type lattice.

Rarenko et al (90) have grown HgTe single crystals by various methods in order to determine the most effective technique of growing crystals and controlling the stoichiometry. Zone melting of HgTe was carried out by regulating

the Hg-vapour pressure over the melt and controlled annealing in Hg-vapour was performed in order to obtain low charge carrier concentrations and high purity. The Czochralski method was also found highly effective for growing HgTe single crystals.

Crucceanu et al (91) have grown HgTe single crystals from solutions and found that the specimen showed a high degree of perfection of the sphalerite structure.

Moronchuck et al (92) have investigated the effects of temperature, vapour deposition, and base layer parameters on the structure of single crystal layers of HgTe. With an excess of Hg-vapour they obtained highly oriented single crystal n-type layers with a high carrier mobility. At low Hg-pressures and slow evaporation rates polycrystalline p-type HgTe layers with low carrier mobility and very fine crystalline grains were obtained.

Kobus et al (93) prepared thin (0.1,0.3μ) polycrystalline films of HgTe by vacuum deposition of solid HgTe on a mica substrate for use as Hall generators. The films were heat treated in an atmosphere of Hg-vapour and argon to correct for the non-stoichiometry of Hg that arose due to the partial decomposition of HgTe.

1c. Electrical Properties of HgTe

The highest value of electron mobility at room temperature in polycrystalline HgTe was 10,000 cm^2/vsec, and

the mobility ratio was estimated at between 40 and 100 (83).

Lawson et al (76) obtained electron mobilities between 19000 cm^2/vsec at 300^OK and 23400 cm^2/vsec at 77^OK in single crystal samples and deduced an energy gap of 0.01 ev for the material. Analysis of measurements on p-type samples gave a mobility ratio of 70 and an intrinsic carrier density of 6.4 x 10^{17}/cm^3 at 174^OK.

M. and H. Rodot (94) measured the magnetoseebeck effect, which was negative at low temperatures but changed sign at room temperature. This indicated that the scattering at room temperature was by acoustic phonons.

Strauss et al (95), from the measurements of R_H and σ, estimated the intrinsic carrier concentration for HgTe to be 2 x 10^{16} cm^{-3} at 4.2^OK. Since this was found to be too high to be consistent with an energy gap between the valence and conduction bands, they concluded that HgTe is a semimetal.

High electron mobilities were recorded by Rodot and Triboulet (87) and Quillet et al (86) on material which had been annealed in controlled mercury vapour pressures at low temperatures. The intrinsic carrier concentration at 77^OK was 6 x 10^{16} cm^{-3}. In contrast to unannealed samples the Hall constant in annealed samples was found to be magnetic field independent. It was suggested that unannealed samples contained microprecipitates of Hg

which were redissolved by annealing. Electron microscopic
observations confirmed this hypothesis.

Rodot (96) deduced a mobility ratio of 65 at 77^OK.
He found that the variation of Hall coefficient with
magnetic field depended on the temperature at which the
sample had been annealed. For low temperature anneals
no variation was found for magnetic field strengths of
upto 5000 gauss. For the temperature range 250 - 350^OC,
the Hall coefficient depended strongly on the magnetic
field, but for a sample annealed at 400^OC, no variation
was found. Above 400^OC the variations in the Hall co-
efficient again appeared very strongly. Rodot suggested
that these variations were due to inhomogeneities through-
out the material. Above 220^OC HgTe commences to decompose
with the appearance of microprecipitates of Te causing
inhomogeneities. But for T > 350^OC the Te can begin to
occupy vacant Hg sites, causing anti-structure defects.
Around 400^OC there is an equilibrium between the micro-
precipitates of Te dissolving in the antistructure defects
and hence a field independent Hall coefficient. Above
400^OC the antistructure defects cause the variation of the
Hall coefficient. Quillet et al (86) also suggested
that the Te precipitates could be the cause of the Hall
coefficient variations. Giriat (97) also found Hall
coefficient variations below room temperature in specimens

annealed between 250 and 300°C.

For a given vapour pressure, Giriat found an optimum time of anneal which produced the highest mobility, 77000 cm^2/vsec having been recorded at 77°K. Giriat explained it by considering the anneal to take place in two stages. In the first reaction the microprecipitates of Te are dissolved, and in the second reaction Hg-vapour enters the material, ultimately making it stoichiometric, at which point the mobility is maximum. If the anneal is continued beyond this point excess Hg will enter the material and non-stoichiometry will again result with a consequent reduction in the value of the mobility. The conductivity σ decreases due to an increase in scattering associated with the excess Hg. Assuming acoustic mode lattice scattering at room temperature Giriat obtained a value of $m_e^* = 0.035 \, m_o$ for the effective mass and found that m_e^* was constant in the temperature range 215-400°K.

Sharavskiy (98) et al prepared HgTe samples by fusing the main components with addition of super-stoichio-metric Hg and annealed them in nitrogen atmosphere. They found that σ, R_H and μ_H changed sharply after annealing at 200°C probably due to the diffusion of Hg in the HgTe lattice. The source of Hg was thought to be the micro-inclusions due to the excess of Hg.

Giriat et al (99) obtained high mobilities and an

intrinsic carrier concentration of 4×10^{16} cm^{-3} at 77°K. The samples were intrinsic above 20°K. Assuming a simple parabolic conduction band they deduced the value of E_g = 0.

Dziuba (100) investigated the effect of doping with group III atoms on the electrical properties of HgTe. The doping was carried out by melting together appropriate quantities of HgTe and impurities in silica tubes in vacuo. In, Ga and Tl acted as donors, Doping with Al gave inhomogeneous structure.

Dziuba and Zakrzewski (101) measured, R_H,μ_H and α of high purity HgTe samples annealed in Hg-vapour at 260°C, in the region of intrinsic conductivity. Assuming a parabolic band model they deduced that the value of the reduced Fermi level in the temperature range 20 - 400°K remained constant. Measurements of α in a large temperature range gave a constant value of α, showing that the quantity A in $\alpha = -\frac{k}{e}(A - E_F/kT)$ remained constant throughout the temperature range. For constant α, optical scattering at high temperatures and electron-hole scattering at low temperatures gave the same value of the reduced Fermi level. The effective mass at room temperature assuming optical mode scattering was found to be m* = 0.02 m$_o$. The mobility data could also be satisfactorily interpreted by assuming scattering by optical phonons at high temperatures and electron-hole scattering at low temperatures.

105

From the slope of the $\ln R_H T^{3/2}$ vs $1/T$ plot the value
of the energy gap extrapolated to $T = 0$ was found to
lie between $\pm$ 0.0003 eV. The analysis of the temper-
ature dependence of R_H in the low temperature range
gave $\frac{dEg}{dT} \simeq - 10^{-4}$ ev/deg which was in good agreement
with the temperature dependence of E_g for another material
with zincblende structure.

The values of intrinsic carrier concentration in the
temperature range 77 to 400°K agree with the values
reported by Giriat (97).

Tovstyuk et al (102) measured the galvanomagnetic
and thermomagnetic properties of single crystals of HgTe.
From the variation of R_H with H at several different
temperatures, and the value of the Nerst effect, they
concluded that these properties were best explained by
assuming the presence of an extra heavy hole mass, i.e.
a three carrier situation. However no quantitative
results were quoted.

Ivanov-Omskii et al (103) have carried out measure-
ments on single crystal samples of HgTe prepared by zone
melting followed by annealing in Hg-vapour. Mobility
as high as 200,000 cm^2/vsec was obtained at low temperatures.
They measured R_H, σ, μ_H and $\frac{\Delta\rho}{\rho_0}$ of p and n-type samples
over the temperature range 2 to 300°K. R_H depended
considerably on H for n-type samples, which they thought

could be due to the complexity of the band structure of
HgTe or inhomogeneity. No saturation in $\frac{\Delta\rho}{\rho_0}$ was observed
upto 10 KO_e at any temperature. The slope of $\frac{\Delta\rho}{\rho_0}$ vs H
was found to be changing continuously.

Hlasnik (104) found that the measured variations in
galvanomagnetic parameters could be caused by mobility
and concentration gradient of current carriers perpendicular
to the surface of the sample. These gradients can arise
by diffusion during and after thermal treatment. In some
cases autodiffusion of Hg becomes so strong that after
a certain time, small Hg drops appear on the surface.
Hlasnik pointed out that the variations in R_H, σ and
μ_H observed by Ivanov-Omskii (103) could be satisfactorily
explained by the concentration gradients.

Chubova et al (105) measured the Hall coefficient
and the transverse magnetoresistance at 293, 90, 77
and 20.4^{O}K on n and p-type samples of HgTe. The purest
samples were n-type with a carrier density of $\sim 5 \times 10^{17}$
cm^{-3} and $\mu_e = 2 \times 10^4$ $cm^2/vsec$ at room temperature. At
20.4^{O}K, n = 4×10^{16}, and μ_e showed a maximum between
77°K and 300°K. Ionized impurity scattering dominated
at low temperatures. The field dependence of the magneto-
resistance at 20.4^{O}K and its anisotropy could not be
explained on the basis of a simple two band model.

Kolosov et al (106) investigated the magnetoseebeck
effect in p-type HgTe with various carrier concentrations

in magnetic fields from 0 to 20 KG at different temperatures (180 to 340°K). They found that at low temperatures (188°K) the thermal e.m.f. decreased with magnetic field increase. It was also observed that a sign change occurred under these conditions (in 2 out of three samples), in comparatively weak fields, in which electron compensation by low mobility holes is not likely. Kolosov et al interpreted this assuming the existence of light holes which do not take part in intrinsic conductance, the gap between the conduction band being greater than the thermal energy corresponding to T_{ave} = 188°K (~ 0.016 ev). Thus for each sample there should be a temperature T_o, at which the thermal e.m.f. does not depend on the magnetic field.

Lewis (107) and Lewis and Wright (108) have measured the galvanomagnetic and the thermomagnetic effects in single crystal samples of HgTe. The highest mobility recorded was 30,000 cm^2/vsec at 77°K, though the material was not intrinsic at low temperatues and α changed sign near 80°K. The samples were intrinsic at 300°K with a carrier density near 3.10^{17}. Above room temperature the mobility followed the law $\mu \propto T^x$, with x between -1.5 and -2. The magnetoseebeck effect at room temperature was positive indicating that the scattering parameter s was negative. s varied between

-0.1 and -0.2 showing that there was a mixed type of
scattering apparently with a contribution from acoustic-
mode lattice vibrations. The effective mass had a mean
value of 0.04 m_o assuming acoustic-mode scattering and
$0.02m_o$ assuming optical-mode scattering.

The magneto-seebeck effects at low temperatures
were complicated by two carrier effects because there
were more holes than electrons below 200^oK. With in-
creasing magnetic field the positive value of the
seebeck coefficient increased. This indicated that
with increasing magnetic field the negative electron
contribution to α was greatly reduced because of the
high electron mobility and the hole contribution
remained and saturated at fields approaching 20 KO_e.

Recently Wagini and Reiss (109) have measured the
transport properties of p-type HgTe samples at
temperatures between 100° and 300^oK. They analysed
their results assuming Kane's band model. The
problem was reduced to a two band model with $E_2 = 0$,
Fig(23) the heavy hole band and the conduction band
meeting at $\bar{k} = 0$. The light hole band is 0.15 ev
below the heavy hole band and since its density is
small (small effective mass) only a small number of
states are thermally occupied so that this band could be
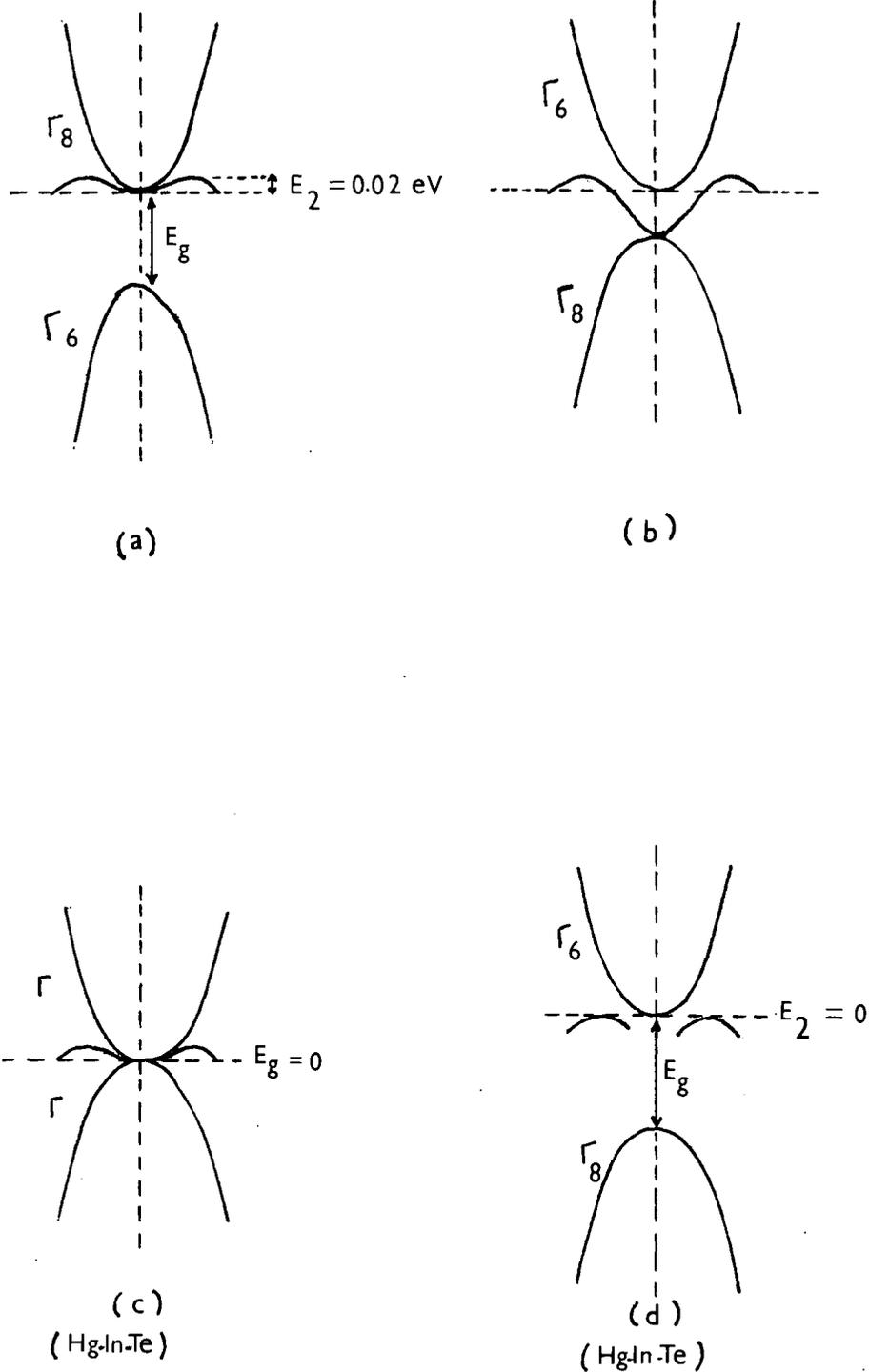
Fig. 2.3. Band structure of HgTe: a) Groves and Paul model, b) conventional semimetallic, c) bands at cross-over $E_g = 0$, d) $E_2 = 0$.

neglected as far as transport phenomena were concerned.
The experimental results agree with theoretical calculations
for polar optical-mode scattering above 260^OK. Below
260^OK there is a strong contribution from ionized
impurity scattering. The maximum value of the hole
mobility was calculated and was ~ 500 cm^2/vsec at
room temperature.

1d. **Band Structure of HgTe**

From a detailed analysis of the electrical data on
HgTe and HgTe-CdTe alloys Strauss et al (95) concluded
that HgTe was a semimetal. As solid solutions made by
replacing Hg by Cd, Sn, In or Mn become semiconductors,
a systematic study of these compounds can give valuable
information about the band-structure of HgTe. Groves
and Paul (110) proposed a new type of band-structure for
gray tin and Harman et al (111) extended their model
to HgTe (fig 2.3a) and its alloys with CdTe. Wright
(112) applied it to Hg_3Te_3-In_2Te_3 alloys. The
essential point of this model is the location of the Γ_8
level above the Γ_6 level, contrary to the configuration
observed in all other semiconductors with diamond and
zinc-blende structures. Γ_8 corresponds with

the bottom of the conduction band Ec. The band corresponding with Γ_6 is a mirror image of Γ_8. The top of the valence band (heavy hole band) E_v is higher than E_c with an overlap $E_2 = 0.02$ ev. $E_g = 0.14$ ev (111). The maxima in the valence band do not occur at $\bar{k} = 0$ due to terms linear in $\bar{k}$ in Kane's formula for the heavy-hole band (113). The shape of the new conduction band is given by Kane's formula for light holes (114)

$$E_c = \frac{\hbar^2 k^2}{2m_{k=0}} + \frac{1}{2}\left[\left(E_g^2 + \frac{2\hbar^2}{m_e^*}|E_g|\right)^{1/2} - |E_g|\right]$$

It is known that in all diamond and zincblende compounds examined so far, the level Γ_6 shifts upwards with pressure faster than Γ_8. Thus $\frac{d}{dP}\left[\Gamma_6 - \Gamma_8\right]$ is positive and of the order of 10^{-5} ev/atm. Therefore for the above model $\frac{d\,Eg}{dP} < 0$. Piotrzkowski et al (114) measured the variation of α and R_H with pressure and found that $\frac{d\,Eg}{dP} < 0$ which indicates that Groves and Paul model describes the band structure of HgTe satisfactorily.

One consequence of fig(2.3a) is that part of the valence band near $\bar{k} = 0$ has a negative effective mass and will be an electron like state. This has been predicted theoretically by Cardona (115). Galvanomagnetic measurements on (HgMn)Te by Delves (116) suggest extra electron-like carriers which are believed to be these negative mass

holes. The presence of light holes required by both figures (2.3a) and (2.3b) has been suggested by Kolosov (106) in the interpretation of the magneto-Seebeck data.

By considering the above band structure and using Kane's theory Olimpu et al (117) have calculated the overlapping of the bands in HgTe to be about 0.04 ev.

Recently Yamamoto and Fukuroi (118) have proposed a new band model for HgTe from the studies of the Shubnikov-de-Haas effect at 1.1^OK in a magnetic field up to 18 KG. They infer that there should be two conduction bands with different effective masses and that the Fermi surfaces of the two kinds of electrons are nearly spherical. This proposal may also explain the non-observance of the de·Haas-van-Alphen effect by a torque method.

le. Optical Properties of HgTe

Optical absorption in HgTe has been measured by Lawson et al (76), Quillet (119) and Blue et al (120). Lawson et al found that samples of HgTe were opaque to radiation out to 38 microns, about 0.033 ev, the limit of their apparatus. Quillet observed transmission through annealed p-type samples in the range 3 to 15 μ and deduced a value of 0.01 ev for the direct energy gap. Blue measured optical absorption in thin samples of HgTe at different temperatures (323, 296, 208 and 90^OK). The

absorption was quite intense and did not decrease below
1400 cm^{-1} at room temberature. The increase at low photon
energies was attributed to free-carrier absorption which
masked the shape of the actual absorption edge. With
increasing temperature the absorption shifted to higher
photon energies. Thus HgTe was found to be the only zinc
blende semiconductor exhibiting a positive shift of
absorption edge with temperature (2 x 10^{-4} ev/oK for ab-
sorption coefficients of 2-5 x 10^3 cm^{-1}) However,
Dziuba and Zakrzewski, (section 1c.) obtained
$\frac{dEg}{dT} = -10^{-4}$ev/^{o}K, in contradiction to Blue et al.
Blue et al assuming HgTe to be a small gap semiconductor
and direct absorption mechanism deduced an energy gap
of Eg = 0.03 $\pm$ 0.02 ev. They pointed out that the
effect of the temperature dependence of E_g on the electrical
properties of HgTe could be substantial.

The reflectivity of HgTe has been measured by
Cardona and Greenaway (121), Scouler and Wright (122)
Varie and Decamps (123), and Blue (120). Cardona and
Greenaway measured the reflectivity in the fundamental
absorption region of HgTe over the energy range 1 to
25 ev at 300°K and 1 - 6.5 ev at 77°K. Blue measured
it at 30, 50 and 100°C and found that the increasing
carrier concentration as the temperature increased caused
a decrease in the reflectivity at long wavelengths.

Cardona and Greenaway and Scouler and Wright identified
the corners and maxima in the reflectivity with interband
transitions at the symmetry points Γ , L and X. The
doublets due to the effects of spin-orbit interaction,
were resolved when the samples were cooled to He
temperature. The shape of the reflectivity curves is
similar to that for the III-V compounds. At about 12 ev
the reflection spectrum of HgTe and other II-VI compounds
showed a structure which has been assigned to transitions
from d-electron levels in the metal to the conduction band.
The effective mass in HgTe estimated by Blue, was
$m_e^* = 0.020$ for a carrier concentration of 4.8×10^{17} cm^{-3}
and increased with increasing carrier concentration.
Varie and De Camps obtained $m_e^* = (0.017 \pm 0.02)m_o$ and
$E_g = -0.15$ ev.

Siniadower et al (124) carried out measurements of
magneto-reflection in the region of the plasma minimum,
and estimated the effective mass from the splitting of
the plasma minimum. They deduced a value of $m_e^* =$
$(0.044 \pm 0.003)m_o$, for the carrier concentration n =
$(1.35 \pm 0.07) \times 10^{18}/cm^3$. The dielectric constant was
evaluated to be $\epsilon = 14.2$

Photoelectric emission has been investigated by
Sorokin (125) and by Ivanov-Omskii et al (126). The
spectral curve was found to possess a smooth threshold at
4.0 ev which was followed by a steep rise to 4.8 ev and

had a maximum at 6.0 ev.

Wojas (127) investigated the external photoelectric effect in HgTe. Using monochromatic light of wavelengths 2537 and 2480 Å for excitation he determined the current-voltage characteristics. The mean values of the thermo-electric and photoelectric work function were found to be (4.12 $\pm$ 0.005) ev and (4.13 $\pm$ 0.005) ev respectively.

Photoconductivity has been studied by Braithwaite (128), Ivanov-Omskii et al (126) and Kruse et al (129). The longwavelength threshold for photoconductivity in a thin film of HgTe at 77^OK was found to be 3.1μ, about 0.4 ev. It would seem that the photoeffects were due to electron transitions between the lower valence band and the lowest unfilled levels in the conduction band, with a minimum energy change of 0.4ev.

1f. Thermal and other properties of HgTe

Carlson (83) measured the thermal conductivity of polycrystalline samples of HgTe and obtained a value of K = 27 mW/cm^{O}C at room temperature. The thermal conductivity of single crystals of HgTe has been measured by Ioffe et al (130), Rodot et al (131), Spencer (132), and Keleman et al (133). They all agree on the value of the phonon contribution to the thermal conductivity, but only Carlson reports that the thermal conductivity varies as T^{-1}. Kelemen **et** al found the Debye temperature of HgTe to be 114.3^{O}K.

Absorption measurements of 139 GC/S microwaves have been reported by Stradling et al (134) for very high purity HgTe. An electron effective mass of $(0.03 \pm 0.005)m_o$ was deduced from measurements with thicker samples.

Mavroides and Kolesar (135) determined the room temperature elastic constants of HgTe using the ultrasonic pulse technique. A fundamental lattice absorption frequency $\omega_o = 1.87 \times 10^{13}$ ^{c}/sec was calculated. They obtained the Debye characteristic temperature at absolute zero $\Theta_D = 105^o$K.

1g.   Summary of the Properties of

HgTe.

Property	Value or Nature	Source and comments
Lattice	Zincblende	High pressure modification to cinnabar type (89)
Space group classifica-tion.	$\overline{4}3m$	High pressure modification to class 32 (89)
Lattice con-stant.	6.461 $\overset{o}{A}$ (average)	(76),(74),low value of 6.429 reported by (73)

Summary of the Properties of HgTe (contd.)

Property	Value or Nature	Source and comments
Dielectric Constant	14.2	(124)
Density	8.12 gm/cc	(101)
Debye temperature	114.3°K	(133)
	105°K at 0°K	(135) From elastic constants
Energy gap	$E_1 = E_g = -0.14$ ev	(11)
	$E_g = -0.15$ ev	(123) From reflectivity
	$E_g = 0.03$	(120) from optical absorption.
	$E_g = 0.01$	(119) from optical absorption.
	$E_2 = 0.02 \pm 0.01$	(111)
	$E_2 = 0.04$ ev	(117) Theoretical.

Temperature	Electron Mobility cm^2/vsec	Carrier con./cm^3	Mobility Ratio	Reference and Remark
300°K	10,000		40-100	(83) polycrystalline material.
300°K	25,000	6×10^{16}		(101) Annealed in Hg.

Temperature	Electron Mobility cm^2/vsec	Carrier con./cm^3	Mobility Ratio	Reference and Remark
300°K	22,500	3×10^{17}		(107) Annealed in Hg
300°K	19,000	3×10^{17}	~40	(109) Annealed in Hg
200°K	20,000	1.7×10^{17}	> 20	(109) Annealed in Hg
77°K	23,000		70	(83) Polycrystalline material.
77°K	31,000		65	(96) Annealed in Hg
77°K	77,000	4×10^{16}	> 500	(97) Annealed in Hg
20°K	140,000			(101) Annealed in Hg
20°K or lower	200,000			(103)
4.2°K	60,000	7×10^{15}		(101)

Effective mass ratios and scattering mechanisms for electrons.

Carrier conc/cm^3 at 300°K	300°K	150°K	100°K	Reference and Remark
	0.035 Acoustic			(97)
	0.02 Optical			(101) from electrical properties
	0.017			(123) from reflectivity

Carrier conc/cm^3 at 300°K	300°K	150°K	100°K	Reference and Remark
1.35 ± 0.07 x 10^{18}	0.044			(124) from magnetoreflection
	0.031	0.027	0.007	(94)
2.9×10^{17}	0.035 Acoustic			(107)
6.4×10^{16}	0.023			(111) from reflectivity and magnetoreflection
4.3×10^{17}	0.038			

Thermal Conductivity mw/cm$^{\circ}$K

Quantity	300°K	77°K	Reference and comment
K_{total}	27	270	varies as $1/T$ (83)
K_{total}	24		(132)
K_{phonon}	21		(131)
K_{phonon}	19		(132)
K_{phonon}	19		(130)
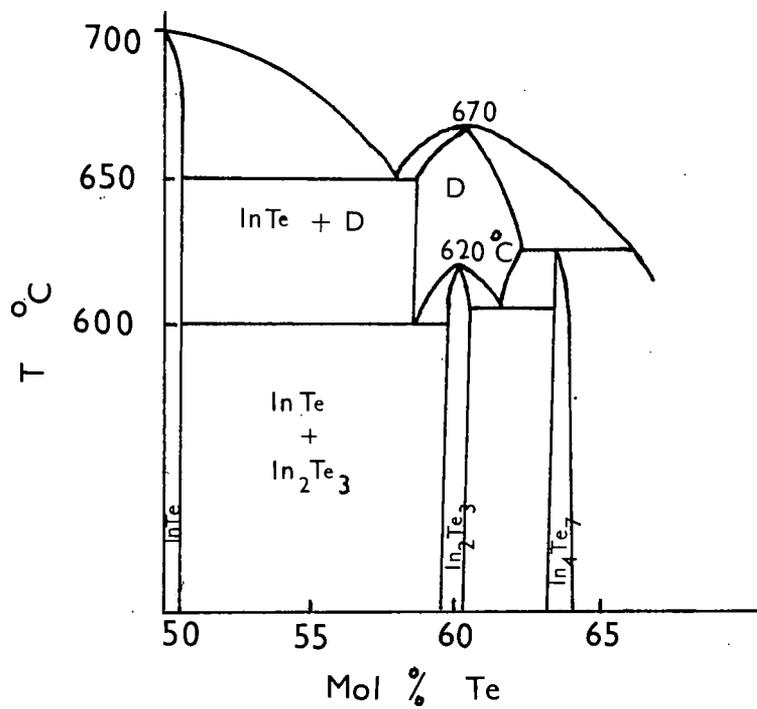
Fig. 2.4. Phase diagram in the region of In_2Te_3
(Holmes et al, 1962.)

Section 2. The Indium-Tellurium Binary Alloy System

2a. Phase Diagram

A detailed study of the phase diagram of In-Te system has not been carried out, but a clear outline of it is given by Hansen and Adenko (136). Holmes et al (137) investigated the compositions in the region of In_2Te_3 and modified the phase diagram to include the poly-morphism of In_2Te_3 and the peritectic compound In_4Te_7 as shown in fig(2.4). There is an eutectic at 90 at. percent Te at a temperature of 427^OC. The compound In_2Te_3 has two forms, a disordered phase β existing above 600^OC and a low temperature ordered phase α. Zaslavskii and Sergeeva (138) studied the phase composition of polycrystalline specimens obtained under various conditions of synthesis and heat treatment, heating and cooling curves were also taken and X-ray structure analysis was carried out.

2b. Preparation of In_2Te_3

Ingots of In_2Te_3 have been prepared from stoichiometric amounts of the elements, by directional freezing, Woolley and Pamplin (139); by zone refining in a background temperature of 600^oC, Holmes et al (137); and by very slow cooling from the melt, Zaslavskii and Sergeeva (138), Zhuse et al (140). In all cases good single crystals were not obtained and the crystal grains were only a few m.m. in size, though Zaslavskii and Sergeeva managed to extract thin flakes of up to 16 m.m.^{2} in area for optical and photoelectric work. Sclar et al (141) have prepared the metallic high pressure form of In_2Te_3, which has the NaCl structure, under high pressure at 150^oC.

By using infra-red microscopy Holmes et al (137) have observed three types of inhomogeneities in their material. The opague regions corresponding to grain boundaries have been shown by X-ray diffraction to consist exclusively of InTe. The other two defects, small random blobs and opaque needles might also be due to InTe as Te is more likely to be lost by evaporation than In from In_2Te_3. The opaque needles dissolve above 600^oC and it is thought that there is a wide range of solid solution in the high temperature phase.

Atroshchenko et al (142) have also shown the existance of a considerable region of homogeneity in the In-Te system near the composition. In_2Te_3, from metallographic, thermo-

graphic and X-ray phase-analyses. Palatnik et al (143) have studied the deviation from stoichiometry in In_2Te_3 and suggest that the deviation in a compound with stoichiometric vacancies, like In_2Te_3, is caused by the introduction of super-stoichiometric atoms in the nonionized state.

2c. Structure of In_2Te_3

In In_2Te_3 crystals each atom forms four tetrahedrally directed bonds (though 1/3 of the sites in the In sublattice are vacant - hence defect structure). Woolley et al (139) and Zaslavskii and Sergeeva (138) found the high temperature phase to be of the zincblende type with a random distribution of vacancies on the tetrahedral sites of the In sublattice. Zaslavskii and Sergeeva proposed a lattice parameter of a_o = 6.166 Å which agrees reasonably with a_o = 6.146 Å proposed by Hahn and Klinger (144). Woolley et al and Gasson et al (145) suggested that the low temperature phase could be of the fluorite type. Zaslavskii and Sergeeva found it to have a face centred cubic structure with a unit cell of a_o=18.5 Å and a space group classification F $\overline{4}$3m. The unit cell would contain 72 In atoms and 108 Te atoms. Inuzuka and Sugaike (146) had expressed some doubt as to the validity of the space group classification and had proposed an ordered unit cell of rather larger dimensions than a_o = 18.5 Å.

2d. Electrical Properties of In_2Te_3

Because of the difficulty in obtaining large single crystals most of the electrical properties have been measured on polycrystalline specimens. It is difficult to measure bulk properties below 300^OK because of low mobility and low carrier density in the intrinsic material.

Woolley and Pamplin (147) together with early workers, observed a discontinuity in the R_H and σ vs T curves near 470^OK in both ordered and disordered specimens. However this effect was not seen by Zhuze et al (140) who explained it as being due to the formation of a thin well conducting layer on the sample surface because of oxidation or loss of Te. The layer effectivly shunted the sample. Zhuze et al observed that, when the conducting surface layers were removed, the activation energy was constant up to the melting point 667^OC, being 1.12 ± 0.05 ev which agrees well with the value of the optical energy gap. Woolley and Pamplin reported room temperature values of 14 and 50 cm^2/vsec for the mobility of the disordered and ordered phases respectively. Zhuze et al observed a mobility of 5-.75cm^2/vsec at room temperature in the disordered material. However, contrary to the findings of Woolley and Pamplin, Zhuze et al found that the ordering of In_2Te_3 reduced the carrier mobility. They explained this as due to the reduction of the electron mean free path because of the halving of the

mean distance between vacancies which scatter electrons, and due to the segregation of vacancies.

The electron mobility in the intrinsic range was found to be nearly independent of temperature in both investigations, which suggests that the scattering is predominantly caused by the electrically neutral cation vacancies. These vacancies also cause the mobility to be smaller than that found in the neighbouring isoelectronic binary compounds like CdTe, with fewer imperfections. Zhuze et al found that Bi acted as donor and I as acceptor in In_2Te_3. However other impurities Mg, Cd, Cu, Hg, Sb, Sn, Zn, Si and Ge did not produce impurity conduction. In a n-type sample the mobility rises exponentially with temperature as $\exp(-\frac{\Delta E}{kT})$. The activation energy of electrons amounts to about 0.2 ev. From the variation of the See-beck coefficient with temperature Zhuze et al obtained a mobility ratio of about 4. They also quote the electron effective mass of 0.7 m_o and a hole effective mass of $\sim$ 1.2 m_o.

Ioffe (148) has pointed out that the conduction processes in In_2Te_3 should be theoretically explained in terms of hopping processes because of the very low mobilities observed.

Chizhevskaya and Glazov (149) have studied the variation of conductivity and viscosity with temperature and alloy composition. The conductivity increases

exponentially up to the melting point as observed by Zhuze et al, giving an activation energy of about lev. Immediately above the melting point the conductivity increases sharply but begins to level off at about $60^{\circ}C$ above the melting point. This they interpreted as due to the change in the structure which is retained above the melting point.

Sergeeva and Shelykh (150) have investigated the effect of pressure on the conductivity of In_2Te_3. They report that there is no effect observed on the n-type samples, but a threefold increase in conductivity occurs for p-type samples. In the intrinsic case the conductivity pressure curve shows a minimum at about 3000 kg/cm^2 after which there is a continuous rise in conductivity upto the maximum pressure exployed, 7000 kg/cm^2.

2e. Optical Properties of In_2Te_3

Large differences exist in the values of the energy gap obtained by different workers from absorption and photoconductivity measurements. Petrusevitch and Sergeeva (151) explained these as arising from the strong scattering of radiation by the samples in the fundamental absorption region. When this strong scattering was allowed for, a sharp absorption edge was obtained. The cause of the scattering was unknown. The scattering was found to be several times stronger in the disordered phase than in the ordered phase. The absorption measurements have been

interpreted using the formula for indirect transitions
and the values of the energy gap obtained were 1.026 ev
for the ordered and 1.02 ev for the disordered material.
The half maxima points in the photoconductivity curves
gave values of 0. 94 and 0.92 ev for the ordered and
disordered material respectively. A difference of this
type between absorption edge and photoconductivity threshold
is observed in other materials. The authors interprete
these low values as due to the strong scattering observed.

Woolley et al (152) have obtained values of 1.16 ev
and 1.10 ev for the energy gap of the ordered and dis-
ordered material respectively. The energy gap has been
defined as that energy at which the absorption coefficient
changes by 300 cm^{-1} from the background value.

Spencer (132) measured optical absorption in thin
polycrystalline samples of In_2Te_3 and obtained a value of
1.14 ev for the energy gap of the ordered compound.

2f. Thermal properties of In_2Te_3

Zaslavskii et al (153) have measured the thermal
conductivity of cast and compressed In_2Te_3 after sub-
jection to various heat treatments. They found that the
abnormally low value of 6.8 mw/cm^oC was characteristic
of the disordered phase and that the value was independent
of temperature in that region. The value steadily increased
with increasing ordering in the structure and finally gave

a room temperature value of 11.2 mw/cm^{o}C. Zhuze et al
(140) also observed that ordering of In_2Te_3 raised the
lattice thermal conductivity, the mean free path of the
phonons being increased due to the halving of the mean
distance between vacancies.

Zaslavskii et al also observed that course
crystalline specimens showed higher heat conductivity
than fine crystalline specimens. This could be explained
by assuming that the extra heat was conducted by electro-
magnetic radiation, similar to processes which Smirnow
and his associates (154) had discovered in Te and Ge.
Petrusevitch et al (155) later verified this hypothesis
by experimental work on In_2Te_3.

Gasson et al (145) had obtained the values of 3.5 mw/
cm^{o}C and 8 mw/cm^{o}C for the disordered and ordered material
respectively

2g. Summary of the Properties of In_2Te_3

Property	β-disordered	α-ordered	Source and Comment
Lattice	zincblende, with random vacancies on the In sub-lattice	Face centred cubic, with ordered super-lattice formed from the vacancies	(140), (138)

Property	β-disordered	α-ordered	Source and Comment
Space Group	$\overline{4}3m$	F $\overline{4}3m$	(136)
Lattice Const-ant.	6.160 Å	18.5 Å	(136)
	6.146 Å	18.4 Å	(144),(146)
No. of atoms per unit cell.	2	72 In and 108 Te.	(138).
No. of cation vacancies/cm^3.	5.5×10^{21}, random.	5.5×10^{21}, ordered into superlattice.	(140)
Density at 20°C gm/c.c.	5.73	5.79	(140)
Energy gap at 300°K.	1.02 ev	1.026 ev	(151) from optical absorption.
	0.92 ev	0.94 ev	(151) from photo-conductivity.
	1.10 ev	1.16 ev	(152) from optical absorption
		1.14 ev	(132) from optical absorption.
Electron mob-ility	14	50	(147)
cm^2/vsec	15	decreases on ordering	(140)

Property	β-disordered	α-ordered	Source and Comment
Mobility ratio	4 approx	4 approx	(140)
Effective mass at 300°K		$m_e^* = 0.7 \, m_o$ $m_h^* = 1.12 m_o$	(140) scattering by neutral vacancies
Intrinsic carrier concentration at 334°K		7.68×10^{11}	(140)
417°K		4.1×10^{13}	(140)
556°K		1.6×10^{15}	(140)
Thermal Conductivity	6.8mw/cm°C 3.5mw/cm°C	11.2mw/cm°C 8mw/cm°C	(153) (145)

Section 3. The Hg_3Te_3-In_2Te_3 Pseudo-binary Alloy System

3a. Phase diagram, composition and lattice parameters.

Hahn et al (156) first investigated a very limited range of the Hg_3Te_3-In_2Te_3 system. They reported the occurence of chalcopyrite-type ($CuFeS_2$) ordering in the 75 mol % composition, $HgIn_2Te_4$. The C/S ratio being 2 a pseudo-cubic lattice parameter, corresponding to that for the zinc blende structure could be determined.

Woolley and Ray (157) studied this alloy system mainly on the In_2Te_3 rich side. They measured the lattice parameters
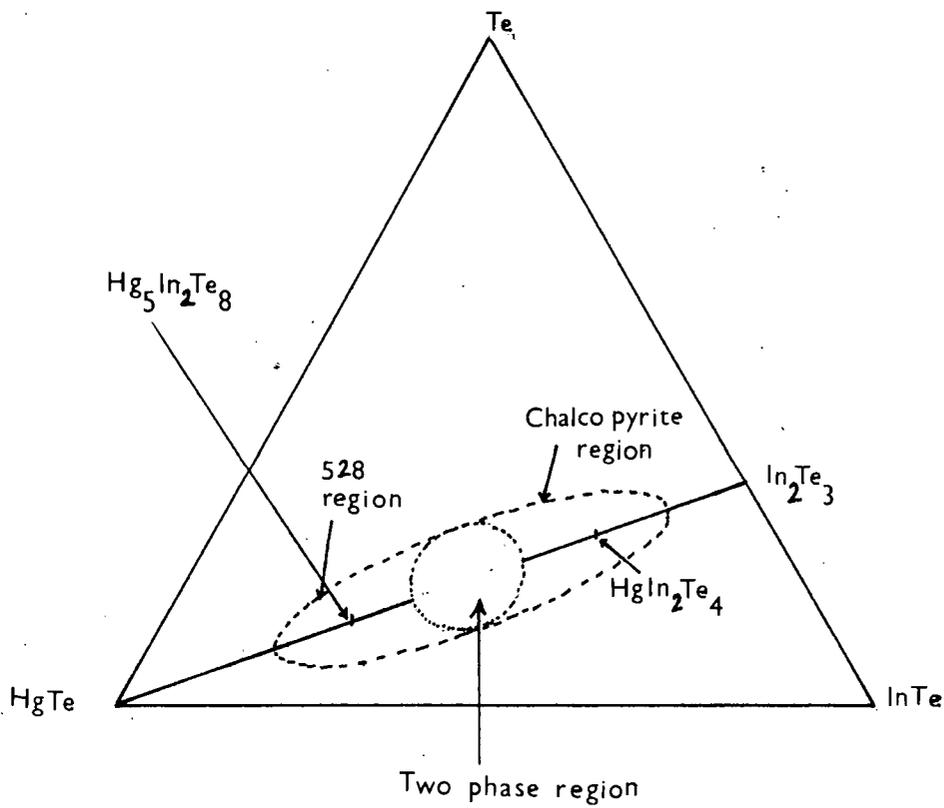
Fig. 2.5 . Ternary diagram for Hg-In-Te system.
(Spencer , Pamplin & Wright , 1962)

and the limits of solid solution of various alloy composi-
tions. Two ordered regions centred on the 40 and 75
mol % In_2Te_3 were observed and the 50 mol % composition
was also found to be ordered. A two phase region between
48 and 60 mol % In_2Te_3 was found. Woolley and Ray
suggested that the structure of the ordered 37.5 mol % alloy
might be orthorhombic.

Pamplin (158) in his thesis, began investigations
into the compound $Hg_5In_2Te_8$, at 37.5 mol % In_2Te_3, mainly
on its structure which was known to be highly ordered, and
measured its lattice parameter. Spencer, Pamplin and
Wright (159) measured the lattice parameters of a number
of compositions from HgTe to $Hg_5In_2Te_8$. The ternary
diagram for Hg, In and Te from their paper is reproduced
in fig(2.5). They found the lower limit of the ordered
region centered on the 37.5 mol % compound to be around
25 mol % In_2Te_3, below which the alloys were disordered and
had the zinc blende structure.

From X-ray analysis and optical examination of ann-
ealed samples for phases and homogeneity, Spencer (132)
proposed a phase diagram for the system Hg_3Te_3-In_2Te_3,
drawing heavily on the Cd_3Te_3-In_2Te_3 phase diagram proposed
by Mason and Cook (160). Spencer found that the melting
points of spot compositions in the region of 40 and 50
mol % In_2Te_3 appeared to be a few tens of degrees higher

than the common value 670°C for HgTe and In$_2$Te$_3$. From
this he inferred the existence of the compound Hg$_3$In$_2$Te$_6$
(50 mol %) which was not peritectic. The defect zinc blende
α -phase extended from 0 to 20 mol % In$_2$Te$_3$, the ordered
β-phase from 36 to 42 and the γ-phase was limited to a
narrow region around 50 mol % In$_2$Te$_3$. The δ phase extended
from 62 to 80 mol % In$_2$Te$_3$ and the region around In$_2$Te$_3$
was complex. Spencer could not obtain the disordered
37.5 mol % phase by quenching from above or below the
melting point, and concluded that the ordered state con-
tinued right up to the solidus. He found that the lattice
parameter varied linearly with composition from HgTe to the
50 mol % composition.

Ray and Spencer (161) determined the liquidus in
the Hg$_3$Te$_3$-In$_2$Te$_3$ system using thermal analysis techniques.
By combining the DTA results with X-ray analysis and
microscopic examination, they determined the phase diagram.
The liquidus was found to follow the form suggested by
Spencer (132) with a maximum of 711°C occurring at 50 mol %
In$_2$Te$_3$. The α-phase was found to continue as far as the
50 mol % composition. They suggested that the ordered
phase existing in the region of 37.5 mol % In$_2$Te$_3$ might
extend only to a maximum temperature of about 445°C at the
composition and to lower temperatures at neighbouring
compositions. This could not however be verified without

FIG. 2.6 PHASE DIAGRAM OF $Hg_3Te_3 - In_2Te_3$ SYSTEM. (RAY & SPENCER,1967)
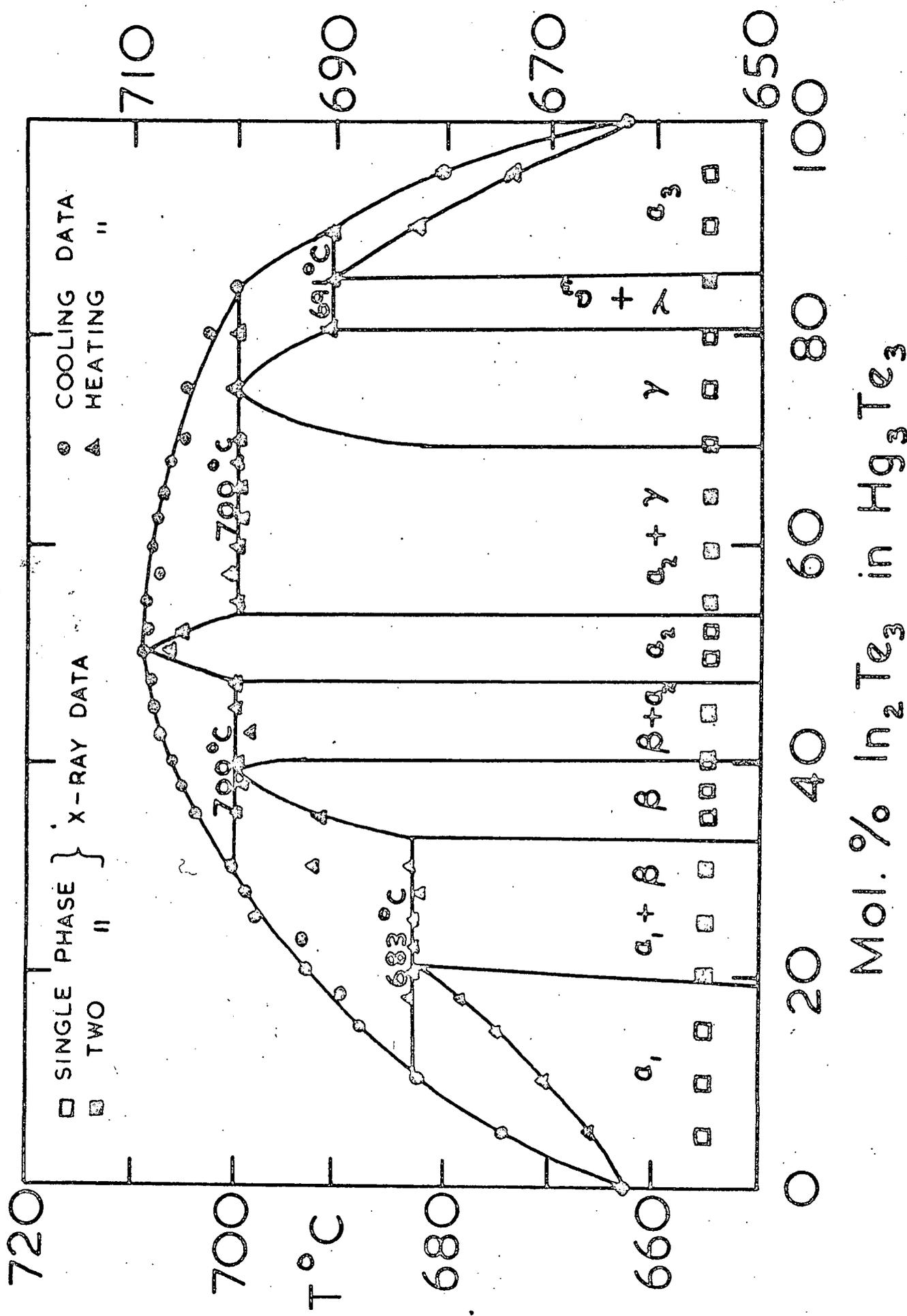
work with a high temperature X-ray camera. The phase diagram near In_2Te_3 was found to be complex. The 50 mol % composition was found to be disordered confirming Spencer's results.

Ray and Spencer (162) have since done some more work on the system and the modified phase diagram is shown in fig(2.6). The phases α_1 and α_2 are defect zinc blende, γ is chalcopyrite and α_3 is disordered In_2Te_3. They have not yet been able to ascertain the phase change in the β-phase, but if it exists their DTA results indicate that it should be in the region of $420^{\circ}C$.

Lewis (106) measured the lattice parameter of the compositions from HgTe to 50 mol % In_2Te_3 and found that the lattice parameter varied linearly with composition. He could not detect a second phase either in the 30 or the 40 mol % composition by metallographic examination, though the X-ray lines were broad and blurred. Contrary to the findings of Ray and Spencer the 50 % composition was found to be ordered.

3b. <u>Preparation of Hg_3Te_3-In_2Te_3 Alloys.</u>

The various compositions can be prepared by melting together the stoichiometric amounts of pure elements or the two compounds HgTe and In_2Te_3. Single crystals of the composition $HgIn_2Te_4$ were prepared by Busch et al (163). Lewis (107) found that good quality single crystal ingots

of all compositions in the range 0 to 50 mol % In_2Te_3 excluding the two phase ones, could be made by the Bridgman method. Ray and Spencer (161) found that the specimens in the system $Hg_3Te_3-In_2Te_3$ required annealing times of the order of several weeks to reach equilibrium, followed by slow cooling to room temperature. Unannealed and rapidly cooled samples frequently showed separation of liquid mercury from the bulk of the material.

3c. Electrical Properties of $Hg_3Te_3-In_2Te_3$ Alloys

Busch et al (163) measured the electrical properties of 75 mol % In_2Te_3 between 300 and 800°K using both polycrystalline material and single crystals. They obtained a mobility ratio of 1.4 from the Seebeck coefficient, and from the intrinsic Hall effect the electron mobility of 200 cm^2/vsec at 625°K falling to110 cm^2/vsec at 77°K.

Spencer, Pamplin and Wright (159) began some studies on the effects of ordering on the properties of the system and the electrical properties of a number of compositions from HgTe to $Hg_5In_2Te_8$ were measured with a view to thermo-electric applications. From the measurements made on polycrystalline annealed samples, values of conductivity, Hall coefficient and Seebeck coefficient were obtained for this region. The highest electron mobility observed at room temperature was 17000cm^2/vsec in the 4 mol % alloy.

The variation of μ_H between 290 and 410°K followed very closely the $T^{-3/2}$ law.

Spencer (132) in his thesis made detailed studies of the electrical properties of the alloys from HgTe to $Hg_3In_2Te_6$. However, all the samples investigated were polycrystalline. The electron mobility which was around 14,000 $cm^2/vsec$ for HgTe at room temperature, dropped sharply and was only 2000 $cm^2/vsec$ at 15mol % In_2Te_3. The reduction of the electronic mobility with increasing concentration of In_2Te_3 was attributed to the increase in the energy gap and the concentration of vacancies. Mobility ratios varying between 60 and 20 were obtained. Ordering was found to increase the mobility above the general trend. The values of the scattering parameter calculated from the slope of log μ_H vs log T plots indicated that the scattering at room temperature was predominantly by acoustic mode lattice vibrations. The values of the effective mass obtained for the 10, 22.5 and 37.5 mol % alloys were $0.01m_o$, $0.06m_o$ and $0.07m_o$ respectively.

Lewis (107) continued the work on the $Hg_3Te_3-In_2Te_3$ system for his doctoral thesis, some of which has been reported by Lewis and Wright (108). Single crystal samples of size 12 mm x 4 mm x 2 mm oriented in different crystallographic directions were prepared. Measurements of electrical conductivity Hall effect and Seebeck coefficient

were carried out in the temperature range 77 - 455°K.
The 7, 10 and 37.5 mol % compositions gave samples all of
which were n-type from 77°K to 455°K with carrier dens-
ities at 300°K between 0.6 x 10^{17} and 11 x 10^{17}/cm^3. As
will be seen later the 37.5 mol % samples investigated by
Lewis were actually the 7 mol % samples. The highest
observed values of μ_H were near 25,000 at 200°K for 7
mol % samples.

It was noted that there was contributions from
lattice as well as impurity scattering at room temperature
in almost all the samples. The scattering at 450°K,
however, could be assumed to be solely due to the lattice,
and that at 100°K due to ionized impurity. The summary
of the values of the effective mass obtained is given
at the end of this chapter. The electron effective mass
is similar for the 7 and 10 mol % alloys to that for HgTe
i.e. near 0.04m$_o$ at 450°K assuming acoustic lattice
scattering and near 0.02m$_o$ assuming optical mode scattering.
The effective mass was found to increase with increasing
carrier concentration as well as with increasing temper-
ature indicating a non-parabolic conduction band.

The 30 and 40 mol % samples were also n-type above
77°K. The electron mobility for the 30 mol % sample was
1300 cm^2/vsec at 77°K falling to 600 at 455°K. Assuming
acoustic scattering the values of m_e^* were 0.028 m$_o$ at 300°K

and 0.043 m_o at 455^oK. The maximum mobility in the 40 mol % alloy was 200 cm^2/vsec.

The 50 mol % samples had high resistivity and some showed positive Hall coefficients at low temperatures. In a typical specimen σ was 6 x 10 $^{-4}$ ohm^{-1} cm^{-1} at 100^oK, rising to 1.7 x 10^{-3} at 278^oK. A steep rise of two orders of magnitude was observed at 278^oK, reaching 2 x 10^{-1} ohm^{-1} cm^{-1} at 455^oK. A marked increase in the Seebeck coefficient at 278^oK was also observed. The estimated values of the effective mass were 0.0003 m_o and 0.5 m_o at 250^oK and 400^oK respectively. The maximum value of the electron mobility recorded was 250 cm^2/vsec at 300^oK, and the mobility ratio was 13.

Magnetoresistance and magnetoseebeck effects were measured in the 7, 10 and 37.5 mol % alloys but anomalous results were obtained with one or the other in each sample.

3d. Optical Properties of Hg_3Te_3-In_2Te_3 Alloys

Woolley and Ray (157) investigated the optical energy gap of the alloys from 75 mol % In_2Te_3 to In_2Te_3. Spencer, Pamplin and Wright (159) and Spencer (132) reported the results for the compositions in the range HgTe to $Hg_3In_2Te_6$. The variation of the optical energy gap, obtained from the measurements of the absorption edge, with composition exhibited two plateau, one centred at 25 mol %, the other at 45 mol %. A sharp increase in energy

occurred between these two plateau at around 35 mol %
In_2Te_3. The plateau between 20 and 30 mol % at 0.35 ev
corresponds to the two-phase region in the system. A
linear variation was obtained in the low In_2Te_3 content
alloys up to about 20 mol % In_2Te_3. The increase in the
values at 37.5 and 40 mol % alloys was thought to be
due to the effect of ordering. Spencer noticed the
presence of indirect transitions in the 37.5 mol % compound
at about 0.58 ev.

3e.   Thermal Properties of $Hg_3Te_3-In_2Te_3$ Alloys

Spencer (132) measured the thermal conductivity of
the alloys from 0 to 50 mol % In_2Te_3. The thermal
conductivity was found to drop sharply with the In_2Te_3
content and by 10 mol % of In_2Te_3 had fallen to the low value
of In_2Te_3. Spencer suggested that this could mean that
the electronic component of the thermal conductivity was
negligible for compositions beyond 10 mol % In_2Te_3. The
thermal conductivity remained almost constant for the
rest of the system despite the increasing concentration
of vacancies. Ordering did not have noticeable effect on
the value of the thermal conductivity.

3f.   Band Structure of $Hg_3Te_3-In_2Te_3$ Alloys

From the effective mass data Spencer (132) suggested
that the band structure of the alloys may change such
that at about 15 mol % In_2Te_3 the non-parabolic conduction
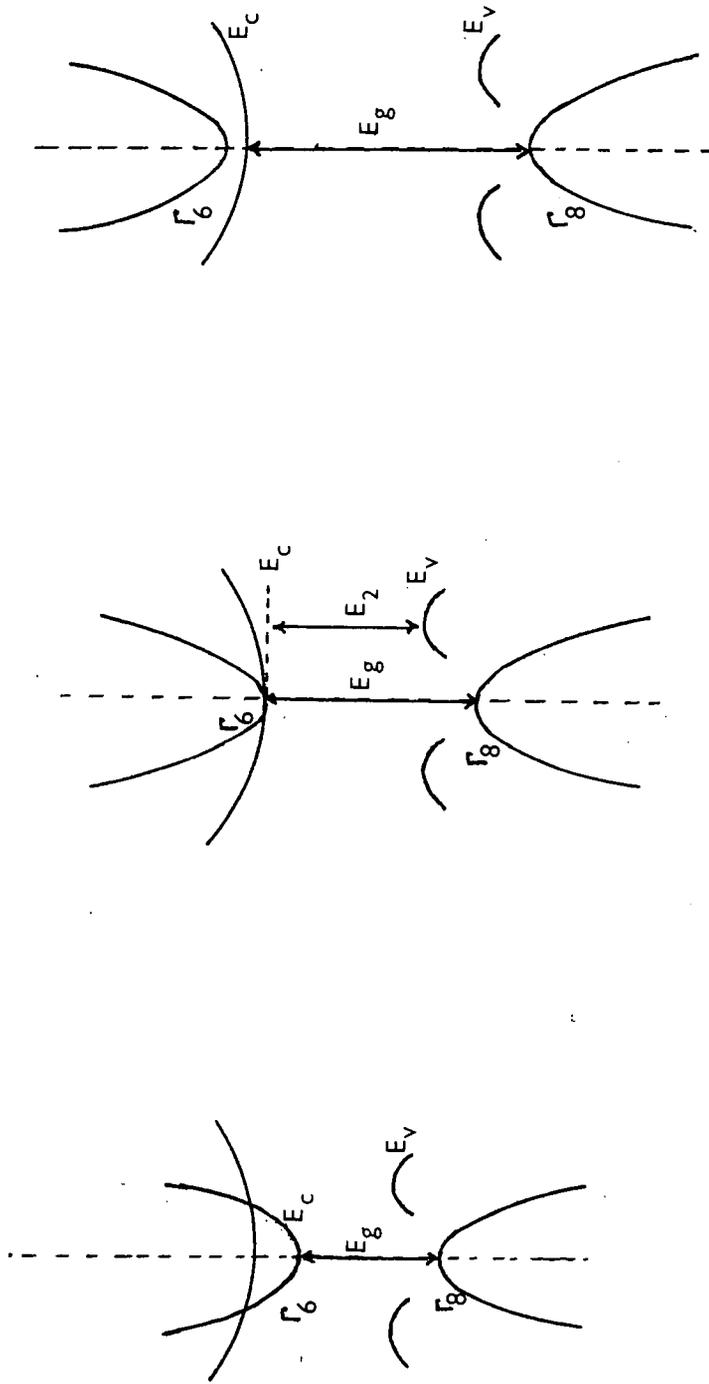
Fig. 2.7. Band structure of $Hg_3Te_3-In_2Te_3$ alloys near the composition $Hg_5In_2Te_8$

a) little less than 37.5 % , b) 37.5 % , c) little more than 37.5 % In_2Te_3.

(Wright, 1965)

band associated with the low effective mass of the alloys near HgTe is replaced by a broader band of low mobility. The overlap in energy responsible for the semimetallic characteristics of HgTe may also be removed at about 15 mol % In_2Te_3.

Wright (112), after Harman et al, extended the Groves and Paul model for gray tin to the $Hg_3Te_3 - In_2Te_3$ system. From the optical results of Woolley and Ray (157) and Spencer (132) he concluded that there was a linear variation of the direct energy gap from HgTe to at least 37.5 mol % In_2Te_3. From the break in the plot of E_g against a_o near the 37.5 mol % composition he suggested that a high effective mass conduction band moves below Γ_6 on passing the 37.5 mol % composition. The postulated band structure with little less than 37.5 mol %, 37.5 mol % and a little more than 37.5 mol % In_2Te_3 is shown in fig(2.7) a, b, c, respectively.

The value of E_g obtained for In_2Te_3 by extrapolation from 37.5 mol % to 100 mol % In_2Te_3 was 2.0 ev which agrees reasonably with the reflectivity peak observed by Greenaway and Cardona. The value of E_g for HgTe again obtained by extrapolation from 37.5 mol % In_2Te_3 was $E_g = -0.11$ ev. A zero value of E_g corresponding to the lattice parameter $a_o = 5.446$ Å was therefore predicted, which corresponded with the 4 mol % alloy.

From the sharp increase in conductivity, Seebeck coefficient, and the effective mass above 280^OK in the 50 mol % alloy Lewis (107) concluded that a heavy mass band is activated above 280^OK, and therefore that the heavy mass band moves below Γ_6 at the 50 mol % composition instead of the 37.5 mol % composition as suggested by Wright (112).

3g. Summary of the Properties of Hg_3Te_3-In_2Te_3 Alloys

Alloy and Structure	Lattice Parameter Å	Energy Gap E_g/eV	Temperature °K	Carrier conc/cm³	Mobility cm²/vsec	Assumed Scattering Mechanism	m^*/m_o	Reference
7% In_2Te_3 disordered zincblende			300	2.0×10^{17}	8500		0.018	(107)
			300	2.95×10^{17}	22500		0.018	
			77	7.75×10^{16}	4600		0.025	
			77	1.75×10^{17}	8000		0.021	
10% In_2Te_3 disordered zincblende	6.428	0.14	300		4150	Acoustic Mode	0.1	(132)
			300	2.5×10^{17}	12000		0.019	(108)
			450			Acoustic	0.034	(108)
			450			Optical	0.016	(108)
			100			Ionized Impurity	0.01	(108)
22.5% In_2Te_3	6.385	0.35	300		800	Acoustic	0.06	(132)
30% In_2Te_3			300	3.7×10^{17}	1000			(108)
			450			Acoustic	0.043	(108)
			450			Optical	0.02	(108)

3g. Summary of the Properties of Hg_3Te_3-In_2Te_3 Alloys (Continued)

Alloy and Structure	Lattice Parameter Å	Energy Gap E_g/eV	Temperature °K	Carrier conc/cm^3	Mobility cm^2/vsec	Assumed Scattering mechanism.	$\dfrac{m^*}{m_o}$	Reference
37.5 % In_2Te_3	6.338	0.73	300		600	Optical	0.07	(132)
40% In_2Te_3			300	5.0×10^{17}	190		0.045	(107)
			77		50			
50% In_2Te_3	6.29	0.74	300		54 (hole)		0.4 (hole)	(132)
			300	1.02×10^{14}	165		0.00046	(107)
			400				0.28	(107)
			450				0.34	(107)
			250	3.4×10^{14}			0.0003	(107)
			77		13			(107)
75% In_2Te_3		0.97	300		200			(132)
			300					(163)
			300		140 (hole)			(163)
	6.19							(157)

C H A P T E R   3:

APPARATUS AND EXPERIMENTAL

TECHNIQUE

Introduction

This chapter is divided into two parts. In the first part an account is given of the synthesis, preparation and examination of the materials, and the techniques used in preparing single crystal samples for electrical and optical work. A brief reference is made to experimental results where ever necessary. The experimental procedure to determine the various transport coefficients and the optical energy gap is described in the second half.

Part I

Section 1. Preparation of Materials

la. Furnace Technique

Three furnaces were used in preparing and annealing the materials. Impervious mullite tubes, on which 18 or 20 swg Kanthal A wire was wound to the required number of turns per inch, were used in all the furnaces.

The tellurium purifying furnace was made with a gradual temperature gradient down its tube, to separate out impurities
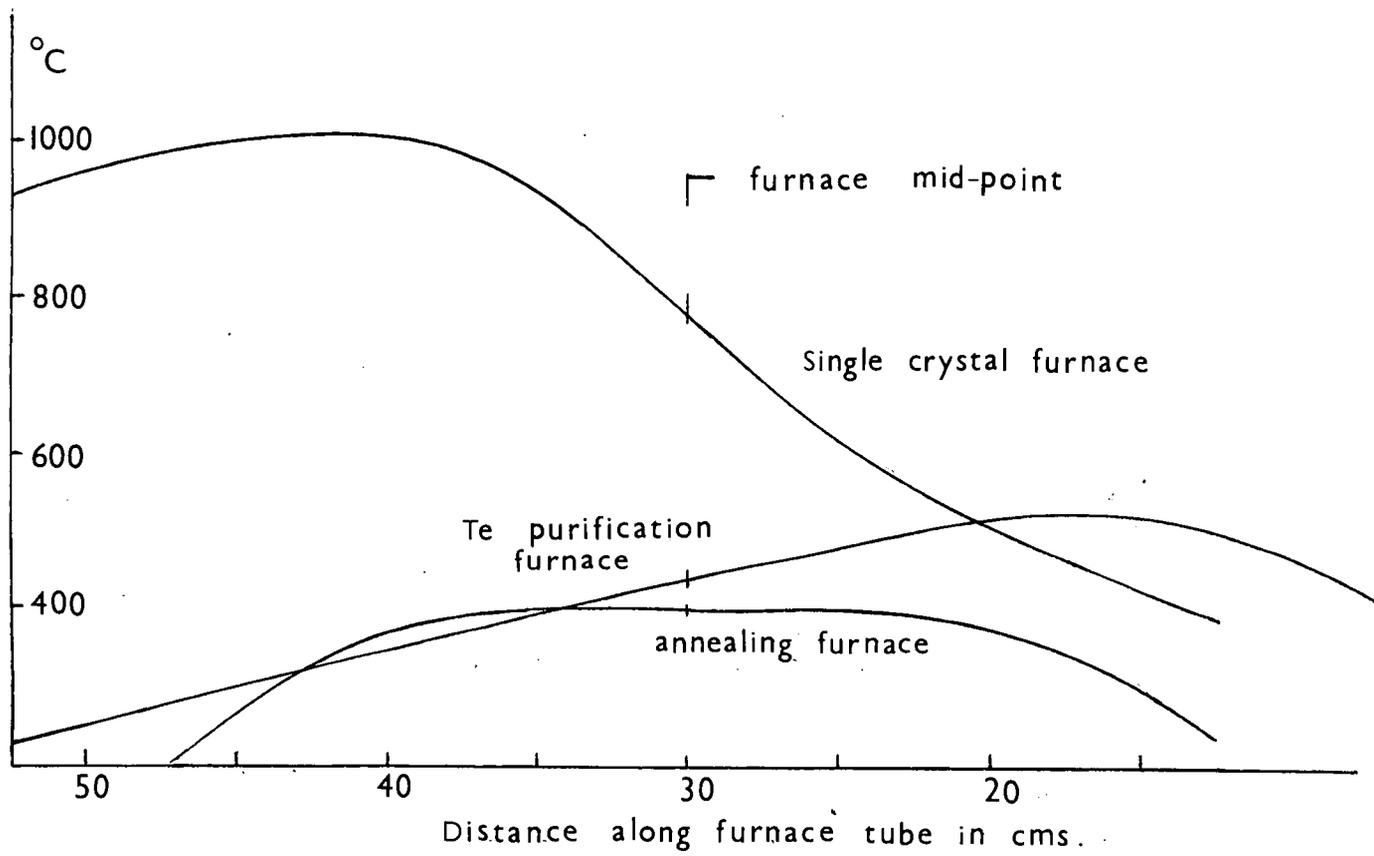
Fig. 3.1. Furnace temperature profiles.

(mainly oxides) in the tellurium. The windings decreased progressively from 10 t.p.i. at one end to 4 t.p.i. at the other.

The furnace to grow single crystals was wound uniformly at 5 t.p.i. on a 26 mm bore, 1 metre long tube and was centre tapped so that different voltages could be applied to the upper and lower halves, enabling a sharp temperature gradient to be set up along the tube.

For the annealing furnace a 35 mm tube of 1 metre length was used. It was wound at 10 t.p.i. at the ends, decreasing progressively to 4 t.p.i. over the central 20 cms of the tube.

Typical temperature profiles of these furnaces are shown in fig.(3.1). The resistance of these furnaces was about 80 ohms, so that about half a kilowatt power was required to reach a temperature of $800^{\circ}C$.

The outer casings of the furnaces were made from sindanyo asbestos sheet and the insulation was dexarimite blocks with granular vermiculite to pack the remaining spaces.

The temperature inside each furnace was controlled by an anticipatory Transistrol instrument, using a 0/13 % Pt-Rh thermocouple. This thermocouple, in its silica sheath, was placed on the outside of the furnace tube, and its exposed head was placed as close to the windings as possible. Thus a temperature control within $\pm$ $1^{\circ}C$ was achieved.

1b. Purification of Materials

All the materials were obtained in high purity elemental form from L. Light and Co. Mercury, 99.9999% pure was bought in 500 gm ampoules, and it was not necessary to purify it further. Indium bought had 99.999% purity but could not be purified further. Immediately on purchase it was etched in an HCl etch to remove the surface tarnish, and was then stored in small quantities under vacuum, in glass phials.

Tellurium obtained was of 99.999% purity and had a dull grey coating of oxide on it. It was further purified by melting in a silica tube sealed under vacuum. The ampoule was left in the temperature gradient for at least 12 hours, at a temperature well above its melting point (460°C). The furnace was then slowly cooled, using a motor to lower the temperature. The central part of the ingot thus obtained was used. Later zone refined tellurium obtained from Canadian Copper Refiners Ltd. was used without further purification.

1c. Preparation of the Charge

As none of the elements used reacted with quartz, single crystals were prepared in transparent silica ampoules. Furthermore, this material is easily worked, can be obtained in a very pure form, and can withstand the necessary temperature and pressure.

To start with, a silica tube, 10 mm internal diameter and 30 cm long, was closed at one end to a fine point, to facilitate nucleation of a single crystallite, using an oxygen-coal gas flame. The tube was then thoroughly cleaned by boiling concentrated nitric acid in it for about 5 minutes. It was washed thoroughly in distilled deionized water and dried under vacuum using the torch. Care was taken to ensure that no rubber particles from the vacuum system entered the tube when releasing the vacuum, and a small drop of mercury was rolled around the tube to ensure that all impurities had been removed. Impurities showed themselves if the mercury wetted the surface or as smears on the surface of the mercury, in which case the tube was cleaned again. If an unclean tube is used a single crystal is rarely formed as nucleation takes place on the sides, and the ingot sticks to the tube.

Stoichiometric amounts of the elements required for each composition of the alloy were weighed to an accuracy of 0.1 milligram and carefully introduced into the silica tube. Care was taken to avoid Te dust as it sticks to the weighing glass and introduces large errors. The mercury was introduced into the tube first, then the tellurium. The mercury was then carefully moved around the tube so that it floated away any small particles of Te from the mouth of the tube. Lastly, indium was introduced.

A neck was then formed on the tube above the materials, which were protected from oxidation and evaporation by wet tissue wrapped around the tube. The ampoule was then evacuated for at least 5 hours, at a pressure of about 1 micron of mercury, using an oil diffusion pump coupled to a rotary backing pump. During this time the mercury was carefully boiled to remove any occluded air, again using a wet tissue wrapped below the neck. Finally, the neck of the ampoule was closed, care being taken to leave as thick a wall as possible.

1d. Growth of Single Crystals

The ampoule was placed inside the vertical furnace tube on a metal rod, so that good thermal contact was made with it, fig(3.2). This ensured that the isotherms within the furnace, including the charge, would remain flat. If the solid liquid interface became concave, the resultant sideways cooling would cause spurious nucleation giving a polycrystalline ingot, fig(3.3) (164). The lower end of the ampoule was held at the centre of the furnace tube where the temperature gradient was steep.

The temperature of the ampoule was raised slowly and uniformly with the help of a cam from $200^{O}C$ to $700^{O}C$ in about 12 hours. A rapid increase in temperature causes explosions due to the high vapour pressure of mercury at these temperatures (50 atm at $700^{O}C$). The maximum melting

point of the alloy system being about 710°C the temperature
of the charge was held at 750°C for a further 6 hours to
allow the reaction to be completed. The vapour pressure
of mercury over the melt was kept constant during crystalliz-
ation by controlling the temperature of the upper half of
the furnace. Crystallization was effected by withdrawing
the metal rod together with the ampoule, at the rate of
3 mm/hr from the furnace, by a lead-screw mechanism worked
by a small motor. This gave a cooling rate of about 5°C/
hour. After the ampoule had been lowered by about 15 cm,
the furnace was cooled to room temperature using the same
cam mechanism in reverse. Single crystal ingots of alloys
about 10-15 cm long were usually obtained by this method.
Single crystals of tellurium could also be grown with the
same technique.

Mr. Alper in this laboratory has grown single crystals
of HgTe about 2.5 cm in diameter, by keeping the ampoule
fixed and lowering the temperature of the furnace at the
rate of 3°C/hour. The temperature gradient in the furnace
was 40°C/cm. The number of etch pits in these crystals
was found to be of the order of $10^{7}/cm^{2}$.

Section 2. <u>Cutting, Grinding, Polishing, Etching and</u>
<u>Microscopic Examinations of Samples</u>

2a. <u>Cutting Nonoriented Samples</u>

Ampoules were opened by cutting off each end, then

the ingot could usually be pushed out. Cutting was carried out with a 4" diameter diamond wheel at 6000 r.p.m., cooled in a jet of soluble oil. Non-oriented samples for electrical work were cut by mounting the ingot on a steel block with glue (Durofix), the block being gripped in the rotatable chuck of the cut-off machine. Two planes at right angles were then cut in. For optical measurements samples 2-3 mm thick were cut. It was found that samples cut with a carborundum wheel, 0.015 cm thick, did not have much damage if the cutting was done slowly.

2b. Cutting Oriented Samples

For cutting oriented samples, the ingot was mounted on a small precision goniometer head and **was aligned** in a known direction by X-ray back reflection technique. The datum planes for this direction were the faces of the mounting track of the X-ray generator. A similar track was mounted on the cut-off machine, with one of the datum faces parallel to the plane of the wheel, and the other perpendicular to it. Thus by aligning the [100] plane of the crystal parallel to a datum face it was possible to cut along this plane and at right angles to it.

2c. Preparation of Samples by Grinding.

Having obtained two faces at right angles the sample was then mounted in accurately machined steel jigs which allowed the other faces of the rectangular parallelopiped

to be ground out. Later the two original faces were also
ground to remove the damage caused during cutting. The
grinding was done using a paste of 800 grade silicon
carbide powder on a flat glass plate. The surface of the
sample was reasonably rough, which prevented surface con-
duction and decreased surface recombination rates. The
sample size for electrical measurements was determined in
terms of the recommended dimensions i.e. a length to width
ratio greater than 3 or 4 (165). The usual size was
12 x 3 x 2 mm.

For photoconductivity measurements samples of size
12 x 2 x 0.2 mm were prepared with the same surface roughness
as mentioned above. The sample thickness could not be
reduced further as the sample invariably shattered, though
it would be desirable to get as high a resistance as possible.

For optical absorption measurements thin   samples of
thicknesses varying between 10 - 75μ were made by grinding
and polishing. To start with, discs about 2 - 3 mm thick
were ground on both sides using a paste of 800 grade silicon
carbide powder on glass. When the thickness of the disc
was reduced to about 0.5 mm, one side of the disc was
polished figure 8 -wise using 800 grade powder on selvyt
polishing cloth. This removed all the scratches on the
surface of the disc. At this point crystal grains became
apparent, each different orientation showing obliquely in
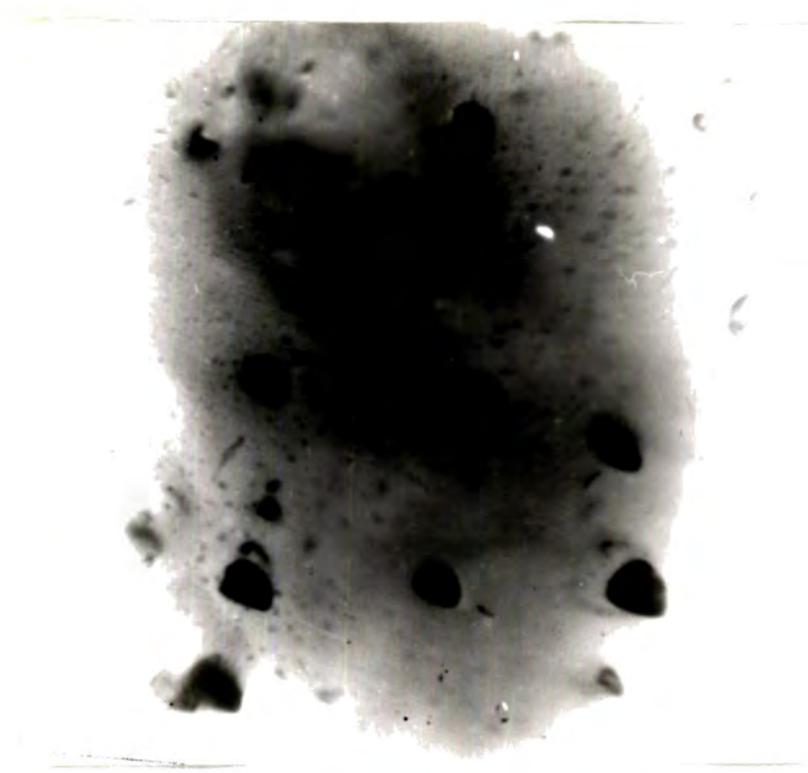
Fig. 3.5 b   Etch pits on Te crystal.
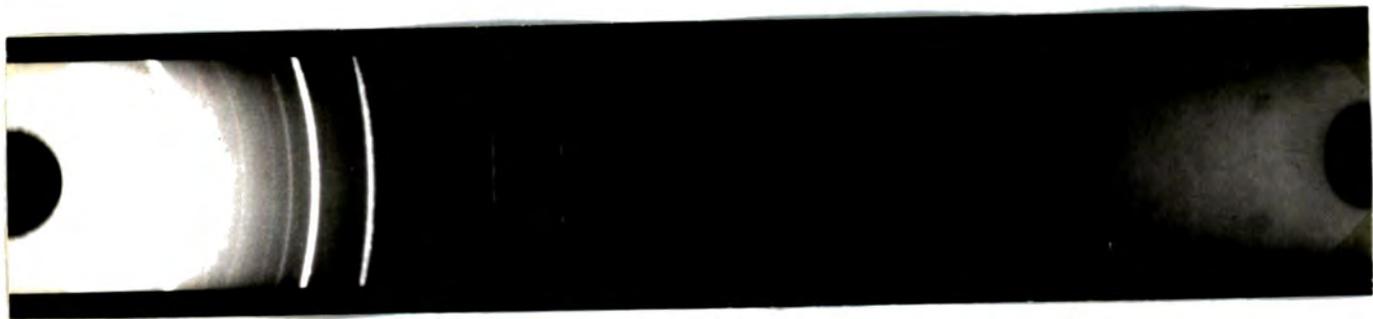
20 %

37.5 %

Fig. 3.6   Powder photographs of 20 and 37.5 % In_2Te_3.

reflected light. The same face was then polished to get a mirror finish by using $1/4\mu$ polishing alumina powder on selvyt polishing cloth. To get a thin parallel-faced sample out of the disc, a special polishing jig shown in fig(3.4) was used. The sample was mounted on the detachable steel disc with a glue (Durofix) for grinding the other side. Durofix was found preferable to thermosetting glues as it could be easily removed without heating or damaging the sample which was very brittle. The sample was then ground slowly with 800 grade powder on the polishing cloth. Grinding with 800 grade on glass at this stage invariably shattered the sample. When the sample was ground to a desired thickness it was polished with $1/4\mu$ polishing alumina. Samples for investigating the current-voltage characteristics were prepared in the same manner. The thickness of the samples was measured using a microscope and a stage micrometer. The accuracy in the measurement was $\pm 2\mu$.

2d. <u>Microscopic Examination</u>

Surfaces of samples polished to mirror finish were examined, under a microscope using polarized light, for two-phase regions and defects. However, two-phase regions as reported by Spencer (166), were not found in any composition studied, not even in the 20 and 30 mol % compositions which showed two phases in X-ray powder photographs.
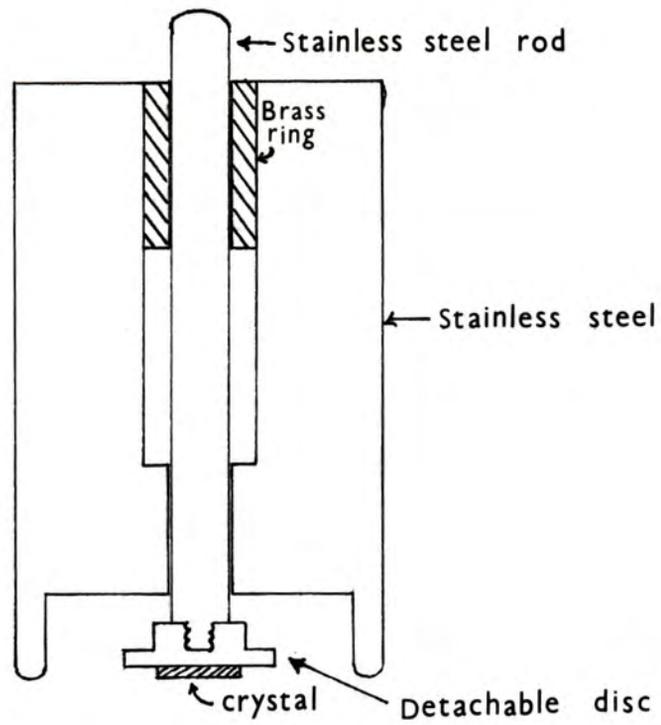
Fig. 3.4. Crystal Polishing jig.

Fig. 3.5a. Etch pits on the (111) face of HgTe.

Silica ampoule

Thermocouple to
Ether temperature
controller

Thermocouple

Supporting rod

Motor & lowering
mechanism
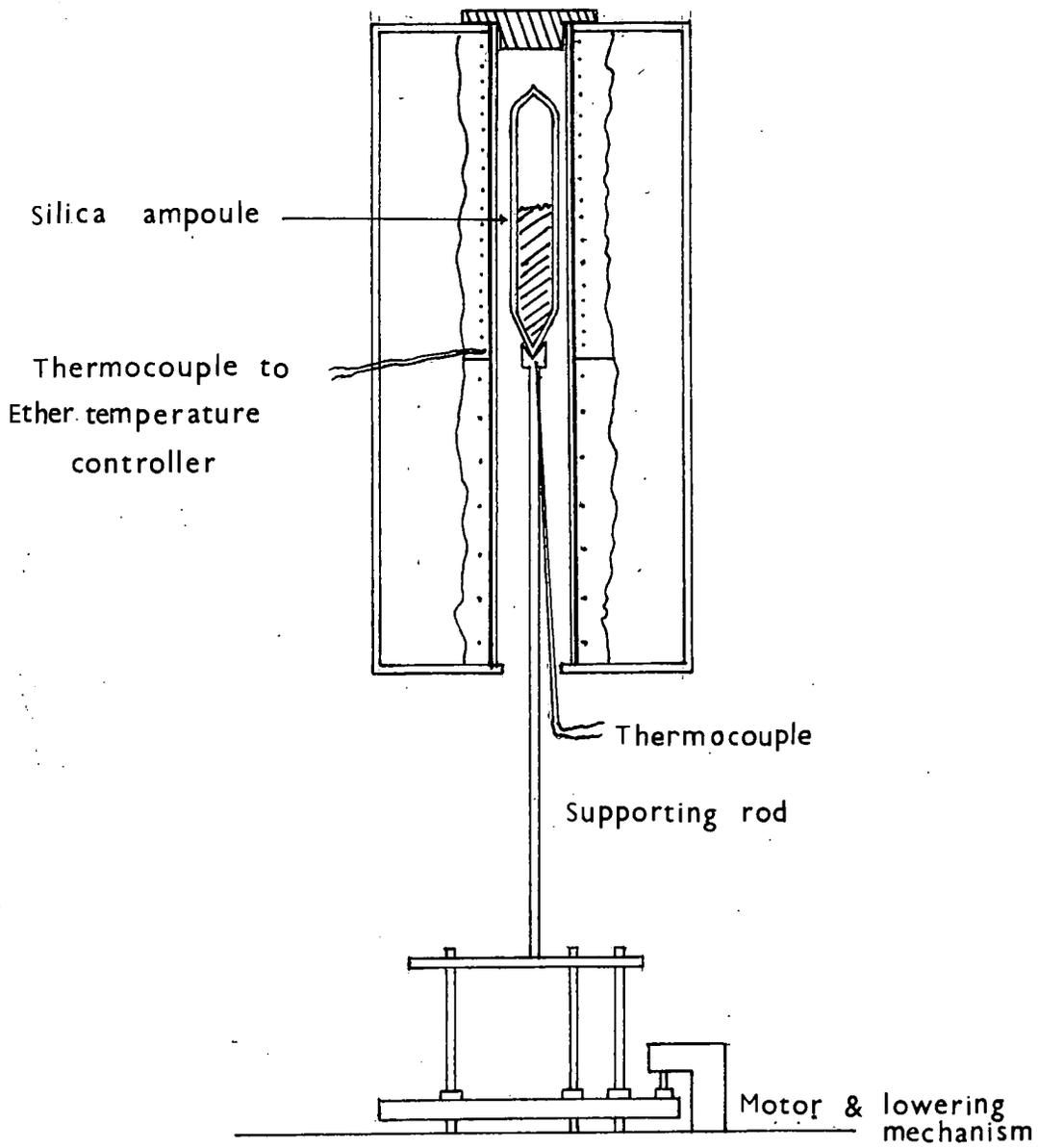
Fig. 3.2. Single crystal growing furnace.
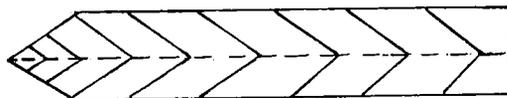
Fig. 3.3. Polycrystalline ingot, effect of sideways cooling.

2e. Etching Technique

It was found that HgTe and its alloys with In_2Te_3 could be chemically polished using aqua regia ($HNO_3:HCl-1:1$) However, it was difficult to obtain surfaces with metallic lustre due to the deposition of black tellurium layers on the etched surfaces. A little addition of bromine to the solution produced shining surfaces with etch pits. A satisfactory composition of the etching solution was as follows

HNO_3 - 10ml

HCl - 10ml

H_2O - 5 ml

Bromine - 10 mg

After the polished specimens were immersed in the solution for 1 - 2 minutes at room temperature, they were rinsed with deionized water and carefully dried on filter paper. Well defined etch pit patterns like those shown in fig(3.5) were observed on the etched surface by a microscope of low magnification.(x 100-x450). The etch pit count in HgTe was $\sim 10^6/cm^2$ and in Tellurium crystals $\sim 10^5/cm^2$.

Section 3. X-Ray Techniques

3a. Powder Photographs

Powder photographs of top, bottom and central portions of each ingot were taken to see whether the composition varied along the length. However, no detectable variation

in lattice parameters along the length of any ingot was found, showing that it was homogeneous to within $\pm$ 1%.

Powder photographs were taken using Philips type No. PW 1024 powder camera using CuKα radiation through a Ni filter. Exposures of up to 50 hours were necessary for some compositions to discern the high angle lines even with a very fast fine grain film, Ilford Industrial G. Small samples from representative ingots were powdered in an agate mortar and pestle, and then mounted on glass fibres with collodion. Neither the glass nor the collodian gave rise to any lines, only background darkening especially at low angles. If the samples were finely powdered the low angle lines were sharp but the high angle lines were not well resolved. This was due to the distortion of the crystalline structure by excessive grinding. This diff-iculty was overcome by achieving a compromise between uniform low angle lines and well resolved high angle lines.

The sharpness of the lines is influenced mainly by the homogeneity of the composition, i.e. whether it is single phase or not. The 30 mol % composition showed diffuse high angle lines and all low angle lines were broadened, indicating the presence of a second phase. The 20 mol % showed two distinct lattice parameters. Order-ing lines could also be detected in both these alloys, though they were weak compared to those in 34, 37.5, and
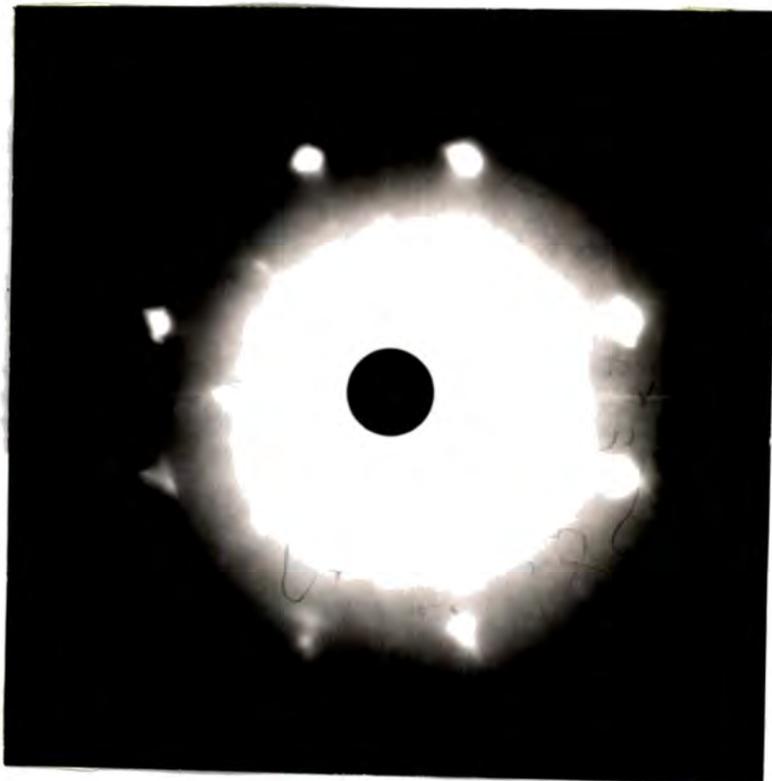
Fig. 3.7   Laue   photograph   of   strained   single   crystal   in [100] direction .
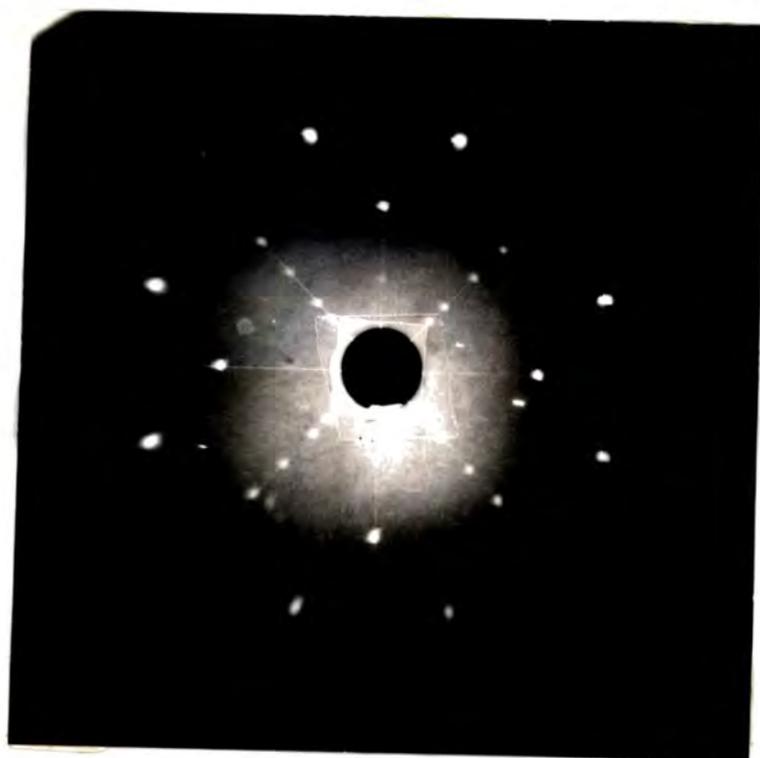
Fig. 3.8   Laue   photograph   of   unstrained   single   crystal   in [100] direction

40 mol % compositions. Ordering did not appear to make the lines diffuse, contrary to the suggestion by Lewis (167). The powder photographs of 37.5 and 20 mol % compositions are shown in fig(3.6). The 50 mol % composition was not found to be ordered, and confirms Spencer's results (168). The sample in which ordering was reported by Lewis (169) was prepared from 1 part Hg_3, 0.94 part In_2, and 2 part Te_3.

3b. Laue Photographs

Laue back-reflection X-ray photographs gave information on the inhomogeneity of the ingots and any strain present at the surface. Strain caused blurring of the pattern on the photograph as shown in fig(3.7). After the damage had been removed by grinding and polishing, the well defined pattern shown in fig(3.8) was obtained. The photographs of oriented samples showed a fourfold symmetry around the [100] axis and a threefold symmetry about the [111] axis as expected.

3c. Determination of Lattice Parameter

The asymetric method of mounting the film in the powder camera was used. This method has the advantage that no calibration of the camera is needed, since by measuring both high and low angle lines, the positions corresponding to $\Theta = 0$ and $\Theta = 90^O$, Θ being the angle of reflection, can be found. After careful processing, the

25 x 355 mm film was fixed on a Hilger and Watts varnier film measurer so that the position of the lines could be measured to an accuracy of 0.05 mm.

The cubic lattice parameters were calculated according to the standard method (170). As many high angle doublet lines (due to $CuK\alpha_1$ = 1.54050 Å and $CuK\alpha_2$ = 1.54434 Å) as could be resolved were measured, and the value of the lattice parameter calculated for each. These results were plotted against the function $\frac{1}{2}(\frac{\cos^2 \Theta}{\sin \Theta} + \frac{\cos^2 \Theta}{\Theta})$ (171) to correct for absorption and devergence of the X-ray beam and the value of the extrapolation to $\Theta = 90°$ was taken as the correct lattice parameter, a_o. The accuracy depended mainly on the sharpness of resolution of the high angle doublets. For well defined doublets the error in a_o was about 0.002 Å.

For the cubic system, the lattice parameter is calculated from the reflection angle Θ using the Bragg equation

$$2 \, a_o \sin \Theta = \sqrt{N} \, \lambda \tag{3.1}$$

where λ is the wavelength of the radiation and N is defined from the Miller indices h, k, l of the reflecting plane by the relation

$$N = h^2 + k^2 + l^2 \tag{3.2}$$

crystal

glass plate
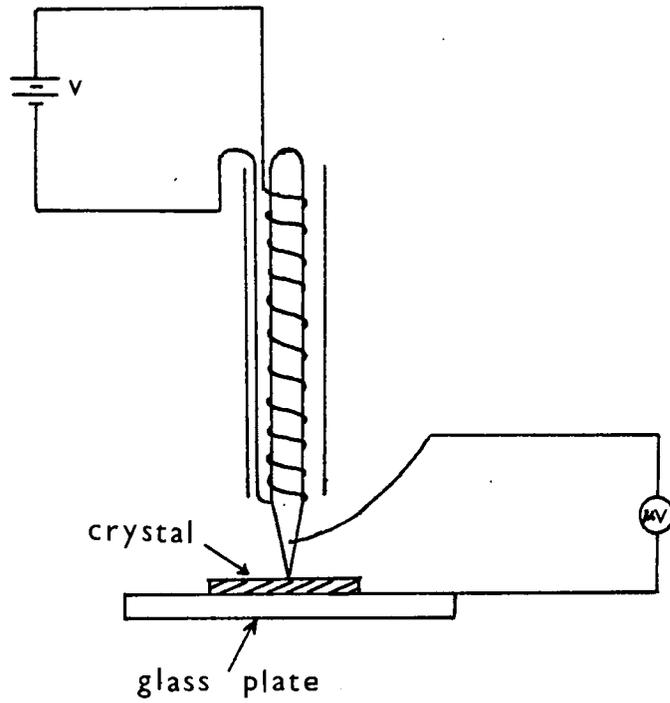
Fig. 3.9 Circuit for thermoelectric probe.

Values of N for the zinc-blende structure are restricted to values of (h, k, l) which are either all even or all odd. There are also forbidden numbers which cannot be expressed as a sum of 3 squares, namely N = 7, 15, 23, 28 ---. Thus the photographs of the compositions had a characteristic pattern, due to the superposition of two sets of lines one being the diamond pattern indexed N = 3, 8, 11, 16, 19, 24, 32 --- , and the other being the face centred cubic pattern N = 4, 12, 20, 36 ---. A few of these latter lines are only faintly seen for zincblende materials. They were visible in HgTe and 4, 7 and 15 mol % alloys, and became indistinct in higher compositions.

Section 4.

4a. <u>Thermoelectric Probe</u>

Qualitative estimate of the homogeneity of a sample could also be obtained by using a thermoelectric probe. The probe used was essentially an electrically heated copper rod with a small blunt point 0.3 mm in diameter at one end that protruded from beyond the insulating sheath that surrounded it. A diagram of the circuit used is shown in fig(3.9). The probe was placed at different points on the upper face of the sample and the variation in the thermoelectric voltage was noted. This indicated the homogeneity of the sample.
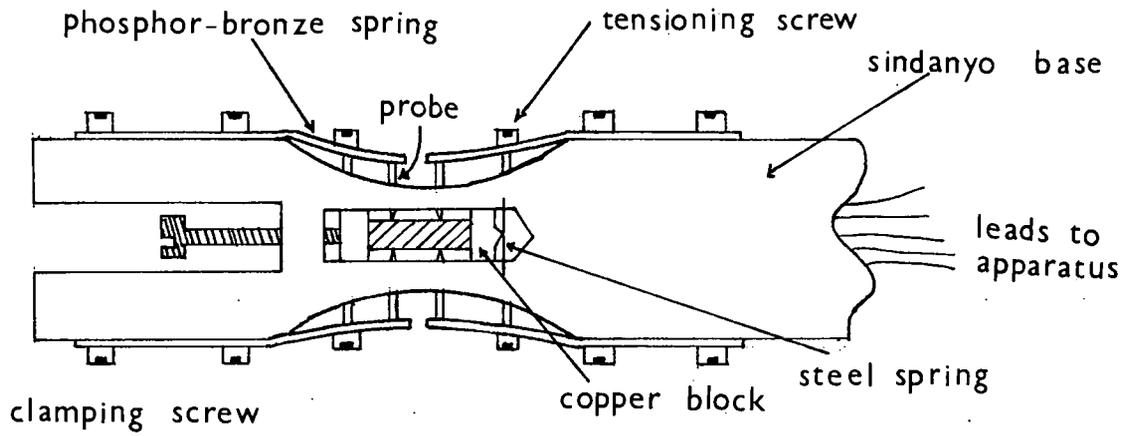
Fig. 3.10. Hall effect sample holder.
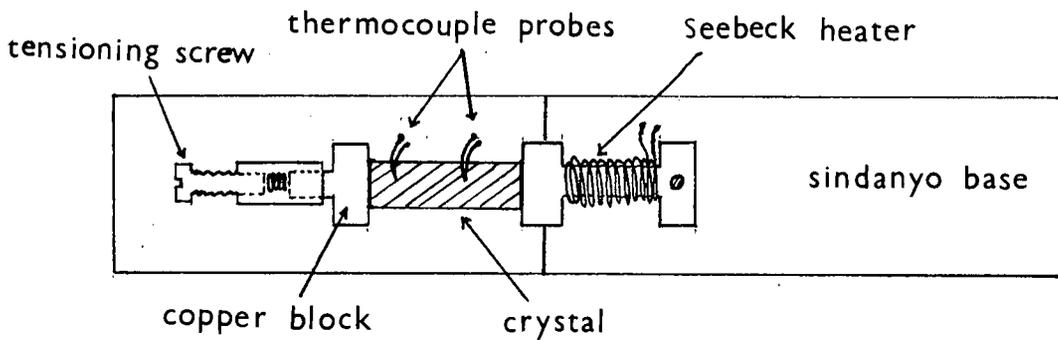
Fig. 3.11. Seebeck effect sample holder.

4b. Sample Holders

Two sample holders were used, one for measuring the Hall effect, conductivity, and magnetoresistance; the other for measuring the Seebeck and magneto-Seebeck effect. Slight variation of the first was necessary to measure the longitudinal magnetoresistance. This sample holder could be attached in turn to a brass rod which was journalled in two bearings, so that it could be rotated along a vertical axis. The crystal could thus assume any desired angle with the magnetic field, in a horizontal plane.

The holder used for Hall effect etc. is shown in fig(3.10). The base was machined from Sindanyo, an excellent thermal and electrical insulator. The probes were made from phosphor-bronze wire, ground to fine points and located opposite each other. They were held in contact by phosphor-bronze springs, tensioned by screws. The current leads were attached to two copper blocks, one of which pressed against a small steel spring, the other pressing against the sample by means of an adjustable screw. Usually colloidal silver in Dag dispersion was used to make ohmic low resistance current contacts. A non-inductive heater was provided on the back of the holder. Temperatures were measured by a copper-constantan thermocouple embedded in a thick copper block which lay between the heater and the sample. A thin mica sheet separated the sample from the thermocouple and the copper block.

The distances between the probes, and the distances of the probes from the current contacts were measured using a travelling microscope.

The holder used for measuring the Seebeck and magneto-Seebeck effects is shown in fig(3.11). The base was again made of syndanyo to which was screwed a small heater which provided the required temperature gradient. The sample was placed against the end of the heater and pressed against it by a copper block tensioned by a spring and screw. The sample was insulated from the base by a piece of mica. Two matched copper constantan thermocouples were used for measuring temperatures, and the copper lead in each served as a voltage probe. The thermocouples were sprung on the surface of the sample and good thermal and electrical contact was ensured by using small blobs of colloidal silver. Care was taken to keep these contacts small and to centralise each one on the sample.

4c. <u>Indium Contacts</u>

Silver contacts were not found very satisfactory for high resistivity samples as they were noisy. To investigate the current-voltage characteristics, contacts were necessary which would be linear, non-injecting and of low resistance. Therefore, indium contacts were tried. First a thin sample (50μ thick of a high resistivity alloy was cleaned and dried and small contact areas, opposite to each other on
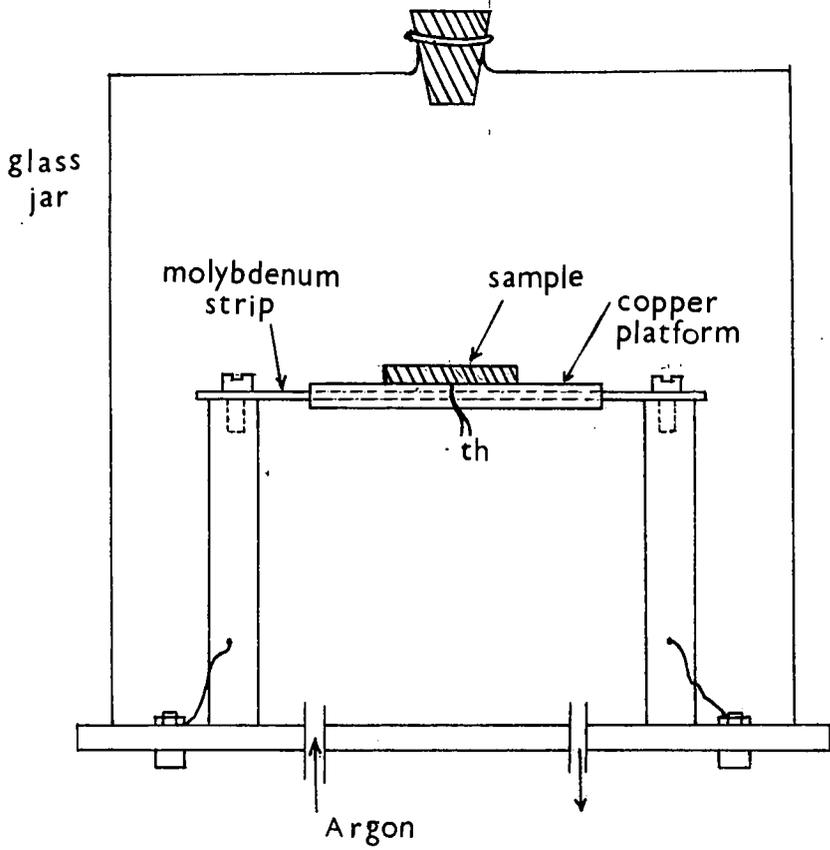
Fig. 3.12. Apparatus for making indium contacts.
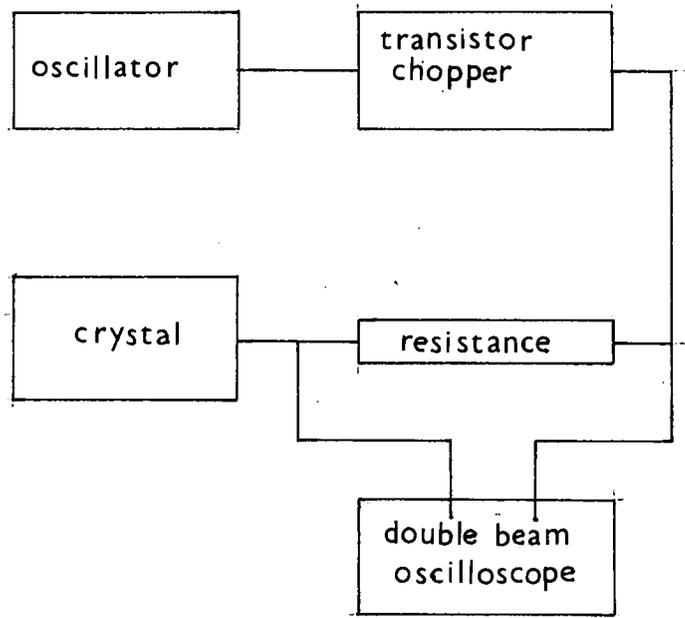
Fig. 3.13. Circuit for investigating V-I charactics using D.C. pulses.

the two surfaces, were coated with layers of indium using conventional high vacuum (10μ torr) evaporation techniques. Indium was outgassed and evaporated from a molybdenum strip. The crystal was mounted above the heater strip and in contact with a suitable aluminium mask.

After the evaporation the crystal was placed in the apparatus shown in fig(3.12) where it could be heated by radiation from a molybdenum strip in an atmosphere of Argon. On heating to about $165^{\circ}C$, just above the melting point of indium, the evaporated indium dots wetted the sample. Next the specimen was cooled, and freshly cut slices of 1 mm diameter indium wire were pressed on to the ends of two thin, tinned copper wires, which served as electrical leads. The crystal was placed on one indium dot so that the evaporated indium was in contact with it. The other dot was placed on the crystal, and was covered with a thin sheet of mica, on which was placed a small weight. The indium made good contacts on melting. A similar method was used to make contacts with crystals used for measuring photoconductivity.

4d. The Magnet

The magnet was a medium sized air-cooled electromagnet which provided an induction of 5800 Gauss at a pole gap of 5 cm, working at 10 amperes and 120 V D.C. It could be run for sufficient time to take all the measurements without any noticeable drop in induction. The pole faces were

7 cm in diameter, there was a considerable increase in induction towards the edge of the pole-pieces. In the central area of the pole faces, where the sample was located, the induction was more uniform with a variation of $\pm$ 1% over the length of the sample.

Part II Experimental Arrangement and Procedure.

Section 1. Electrical Measurements

1a. Current Voltage Characteristics, High Field Effects

The ohmic nature of contacts, at low fields, was checked by examining the linearity of its current voltage character- istic over at least two decades of the current, from 10^{-3} A to 10^{-1}A.

To investigate the current voltage characteristic at high fields ($\sim$ 1000 V/cm), it was necessary to apply this field in the form of short pulses, to avoid overheating. Square wave pulses of between 20 to 100 μ sec duration at repitition rates of between 10 - 50 c//sec were supplied by Solartron GO 1101 pulse generator. By using a transistor chopper between the generator and the crystal, a maximum of 30 volts at 5 A could be applied to the crystal. The crystal was mounted on a thick copper block to avoid over- heating. Measurements on the voltage waveforms were made using a double beam Tektronix 545A oscilloscope. By meas- uring the voltage developed across a known resistance in series with the crystal, the current through the crystal was calculated. A diagram of the circuit is shown in fig(3.13)

Readings at liquid nitrogen temperature were taken using a cryostat.

1b. Conductivity.

The leads from the Hall effect holder in its dewar were taken to a switch network, which allowed various probes to be connected in turn to a Philips D.C. micro-voltmer, GM 6020. This could measure voltages down to $10 \, \mu V$ on its low impedence range of 1 megohm, and up to $10 \, V$ on its high range of 100 megohms. The input impedences were much higher than any sample impedence measured. The current was supplied from accumulators and could be adjusted accurately by means of cascaded potentiometers and a milliammeter. The accuracy of the milliammeter could be checked by measuring the voltage deveoped across a $10 \, \Omega$ standard resistance. The temperature of the sample was measured with a potentiometer and galvanometer, with reference to the ice-point. Readings were taken with the temperature of the specimen increasing from $77^O K$ to room temperature. As this took over three hours, little error was introduced due to non-isothermal conditions. The heater was then switched on to attain higher temperatures. The magnetoresistance was measured at $77^O K$ while the crystal was immersed in liquid nitrogen, and at $300^O K$. The variation of magnetoresistance with the angle between the current and the magnetic field was also measured at

these temperatures.

The conductivity was calculated from the formula

$$\sigma = \frac{I}{V_c} \frac{1}{wd} \quad \text{ohm}^{-1} \text{cm}^{-1} \tag{3.3}$$

Where I is the current through the sample, l is the distance between the conductivity probes, w is the width, and d is the thickness of the sample. The voltage V_c is the mean of the voltages for both directions of the current, and is free from the error introduced by thermoelectric effects when the temperature of the specimen is not uniform (172).

1c. Magnetoresistance

The magnetoresistance was calculated from the change in resistance with magnetic field according to

$$\frac{\Delta\rho}{\rho_0} = \frac{\rho_H - \rho_0}{\rho_0} = \frac{V_H - V_0}{V_0} \tag{3.4}$$

where V_H and V_0 are the voltages across the probes with and without the magnetic field H respectively. Any thermoelectric voltages could again be eliminated by reversing the current and taking the mean of the two readings. The reversal of the magnetic field was also necessary to eliminate any component of the Hall voltage present due to misalignment of the probes. The shorting of the Hall field causes

a transverse current which increases the magnetoresistance.
The treatment of the effect of shorting at the end contacts
on magnetoresistance is given by Drabble and Wolfe (173).
They have shown that the geometrical effects are less
apparent if the resistivity of the sample is measured
between probe electrodes on the side of the sample. Each
probe should be at a distance greater than w from the current
electrodes. Such side contacts can however set up spurious
geometric effects unless they are made from very fine wires.
This is important when carrying out measurements on high
mobility semiconductors. The end contact shorting effects
are negligible if the length to width ratio is greater than
5 ⁚ 1 for InSb (174).

As was pointed out before, the magnetoresistance is
very sensitive to any non-uniformity or inhomogeneity in
a sample. It is possible to get large values of magneto-
resistance due to the short-circuiting of the Hall voltage
by the more highly conducting regions.

1d. Hall Coefficient

The Hall coefficient was calculated from the formula

$$R = \frac{d}{HI} \, V_H \times 10^8 \quad cm^3/coulomb \qquad (3.5)$$

If the current electrodes are of different material from
the sample a temperature difference exists. The resulting
heat flow produces a Nerst potential difference at the
Hall probes, and a transverse temperature difference due

to the Righi-Leduc effect. An additional transverse temperature gradient is due to the Ettinghausen effect. These temperature gradients produce a thermo e.m.f. at the Hall probes, which reverses with I and H in the same way as the Hall voltage. This error can be eliminated by reversing I or H rapidly because the temperature gradients require time of the order of seconds to become established. Thermoelectric voltages which do not reverse with current are eliminated by reversing I and averaging. The magnetic field is reversed to eliminate the effect of the out of balance voltage due to misalignment of the probes. This voltage is usually much smaller than the Hall voltage, but for high resistivity samples it was necessary to bias this voltage off using a potentiometer in one of the probe leads. Corrections to the measured Hall voltage due to end contact shorting (175) were applied if the sample geometry required it.

le. Seebeck Effect

The leads from the two copper-constantan thermocouples in the Seebeck holder were led to two potentiometers, which measured the temperatures using sensitive galvanometers. The two copper leads were used as voltage probes, the voltage being measured by a Philips D.C. microvoltmeter. Readings were started at 77^OK and continued to room temperature, when the heater was switched on to obtain temperatures up to 455^OK. At set temperatures, the temp-

eratures of the hot and cold end of the sample were measured, the average being taken as the temperature of the sample. The potential difference was also noted at the same time. The Seebeck coefficient was calculated from

$$\alpha = \frac{\Delta V}{\Delta T} \qquad \mu V/^O K \qquad (3.6)$$

where ΔV is the measured voltage difference and ΔT the temperature difference. The relationship between voltage and temperature could be assumed to be linear provided that ΔT max $\sim 6^O$ over a length of 8 - 10 mm. The minimum value of ΔT which could be accurately measured was $\sim 2^O K$.

1f. Magneto-Seebeck Effect

The magneto-Seebeck effect was also measured in the same manner when a transverse magnetic field was applied, giving from equation (1.95), chapter 1,

$$Q = \frac{\alpha_H - \alpha_o}{} = \frac{\Delta V_H - \Delta V_o}{\Delta T} \qquad (3.7)$$

$$(T, \Delta T \text{ constant})$$

Errors introduced in the measurement of the magneto-Seebeck effect due to various other thermomagnetic effects are negligible with the size of the magnetic field used.

Section 2. <u>Optical Measurements</u>

2a. <u>Measurement of transmission.</u>

Two sources of radiation were used. For the near infra-red, a 750 watt tungsten lamp sufficed, but beyond 2 microns wavelength it was necessary to use a Nerst filament. Transmission measurements were taken with a Barr and Stroud double monochromator type VL 2 and with a Hilger and Watts spectrometer type D 285. Throughout the range used, 1μ to 10 μ, Rocksalt prisms were used, and all the measurements were taken at room temperature. A lead sulphide cell connected to a Barr and Stroud thermocouple amplifier type 7921 was used as a detector up to 3μ. The radiation was chopped at a frequency of 800 c/s. Beyond 3μ a linear vacuum thermopile served as a detector. The thermopile was wrapped in cotton wool to protect it from strong heat currents. The chopper frequency was accordingly changed to 10 c/s. The crystal was mounted on a steel plate against a blank aperture, so that all the area of the aperture was covered. The crystal was placed between the spectrometer slit and the chopper, so that radiation was incident normally on it. First, transmission through the crystal was measured as a function of wavelength. Then the crystal was taken off the aperture without disturbing the position of the aperture, and the transmission through the blank hole was measured. The ratio of the two readings gave the absolute value of transmission through the crystal.
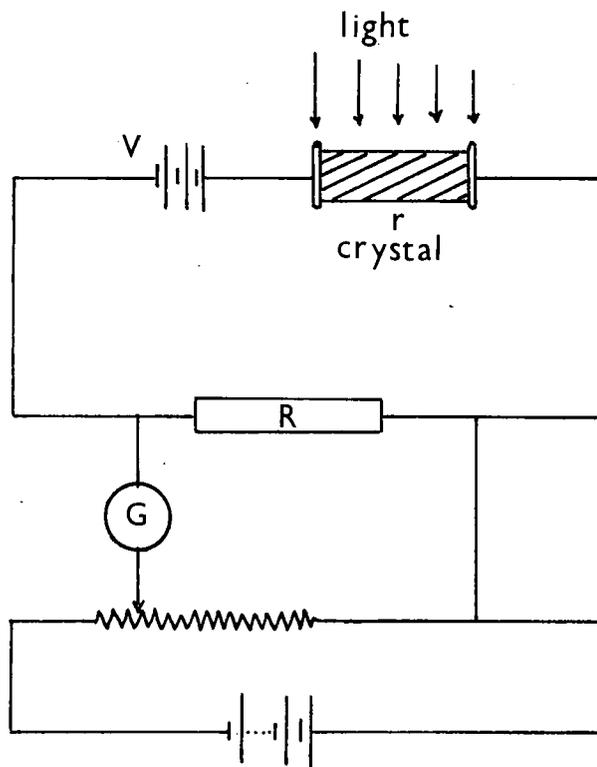
Fig . 3.14 . Standard d.c. compensation circuit using constant illumination

This procedure was necessary as there is a rapid change of transmission with wavelength due to absorption peaks in the atmosphere. To keep the intensity of radiation from the sources constant, stabilized voltage supplies were essential. The size of the spectral slits was chosen, in each case, as small as possible to keep the dispersion small. At least two crystals of each composition were thus investigated to take into account the loss due to reflection.

2b. Measurement of Photoconductivity

For photoconductivity measurements the specimen was placed in a covered box such that monochromatic light from the spectrometer was incident normally on the surface of the sample. Since $\Delta\sigma_{st}/\sigma_o$ was found to lie between 0.2 and 0.3 it was necessary to eliminate the dark current to increase the sensitivity of the apparatus. A standard D.C. compensation circuit using continuous illumination shown in fig (3.14) was, therefore used. The voltage drop across the load R in darkness was first compensated with a potentiometer P, and then the change of the voltage on illumination was measured. For optimum sensitivity R should be equal to the crystal resistance r.
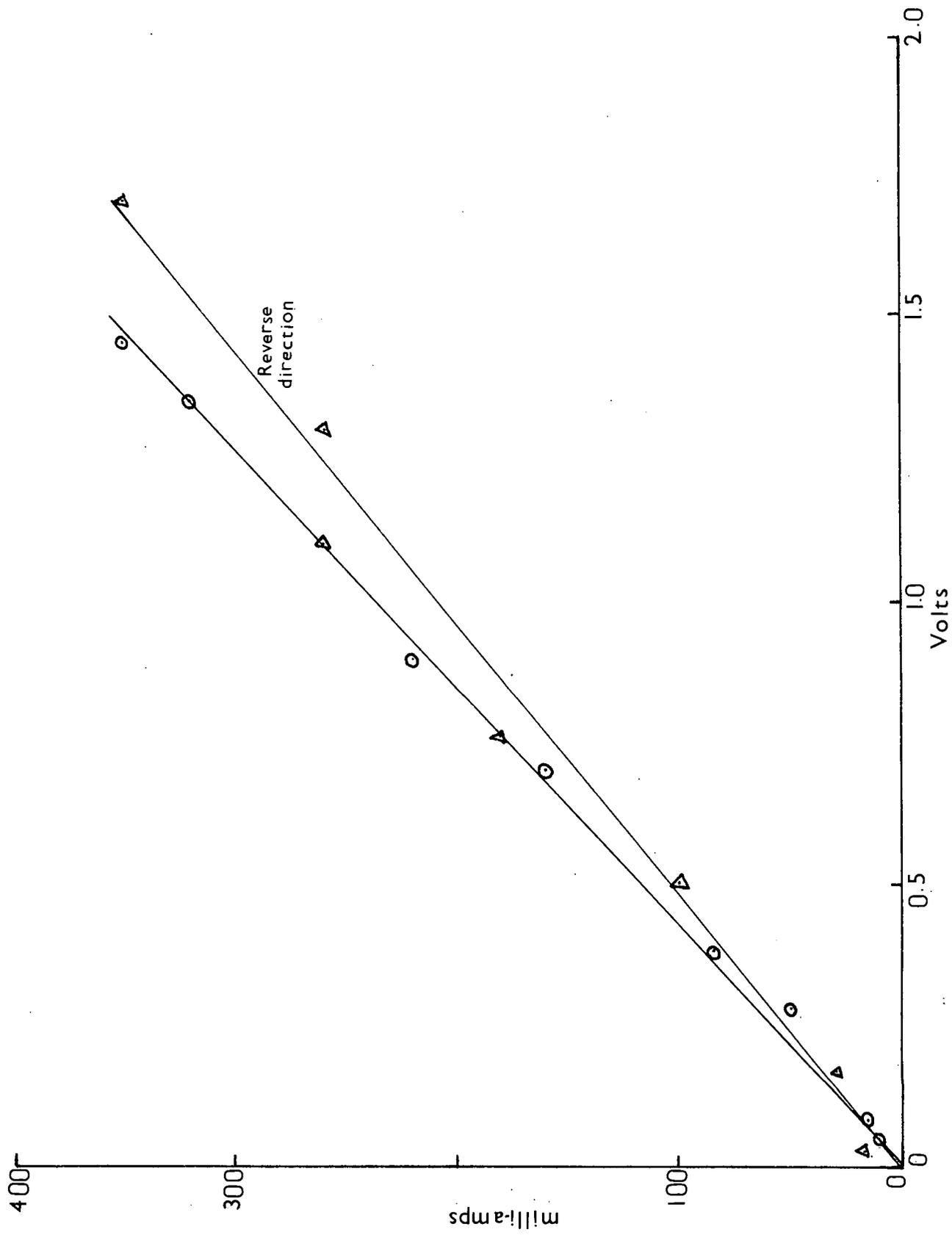
Fig. 4.1. Low field V-I characteristic for 37.5 mol % alloy.

C H A P T E R   4:

ELECTRICAL PROPERTIES OF Hg_3Te_3-In_2Te_3 ALLOYS

Introduction

The experimental results on the electrical, galvano-magnetic and thermomagnetic properties of the alloys in the range 0 - 75 mol % In_2Te_3 are presented in this chapter. The chapter begins with a brief description of the current-voltage characteristics. Then each alloy composition is dealt with separately. Discussion of the results is given simultaneously to preserve continuity and the conclusions are given at the end of the chapter.

Section 1.   Voltage-Current Characteristics and High

Field Effects.   —

1a. Low Field Characteristics

The D.C. and A.C. characteristics of some of the samples were investigated to make sure that Ohm's law was obeyed over a wide range of current. A typical V-I plot for a 37.5 mol % sample of size 12 mm x 2 mm x 2 mm with Silva-dag contacts is shown in fig.(4.1). It is seen that Ohm's law is obeyed over more than two decades of current. Similar linear V-I relationships were observed for other alloys using Silva-dag,
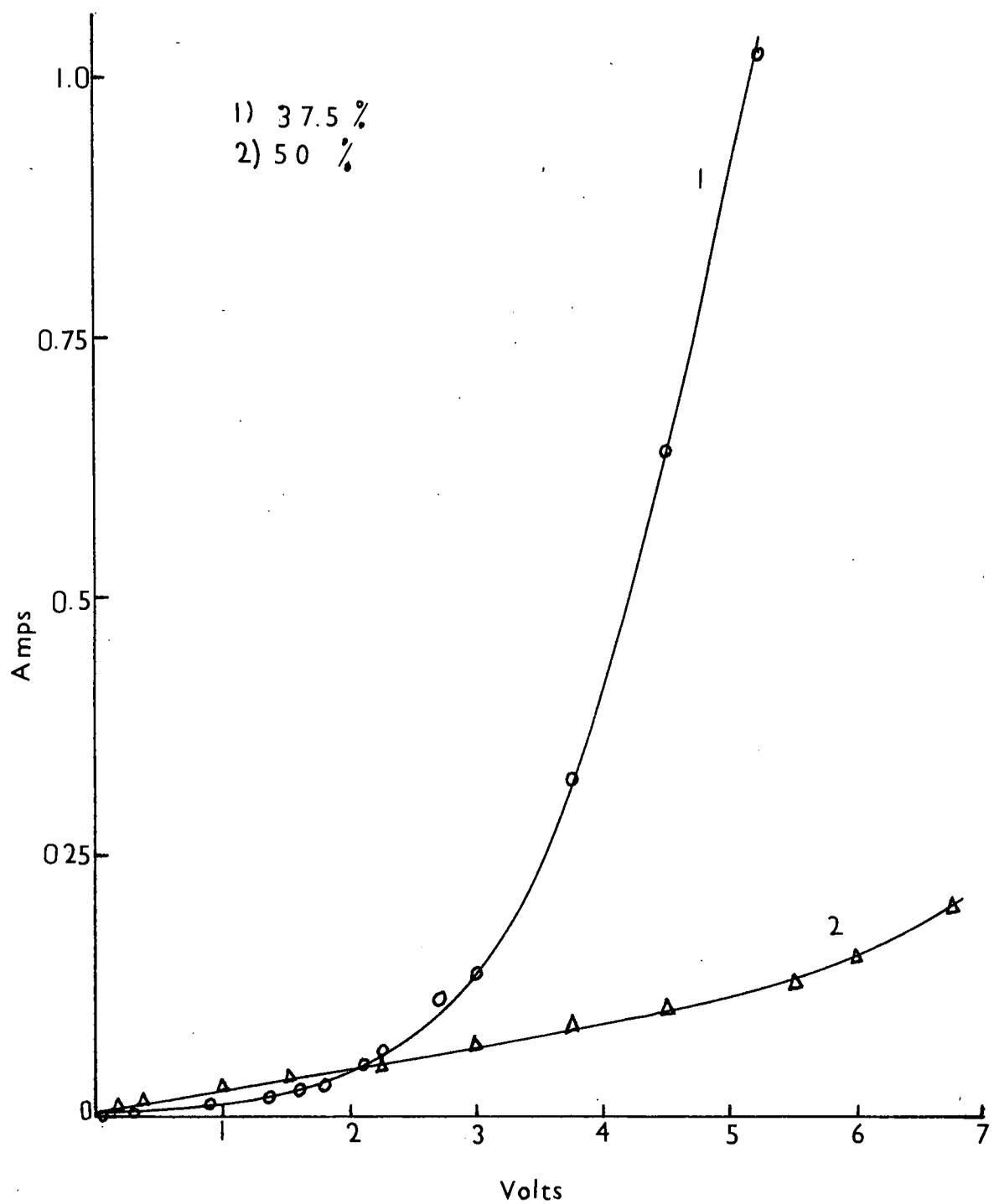
Fig. 4.2. High field V–I characteristics at room temperature using In–Ga contacts.
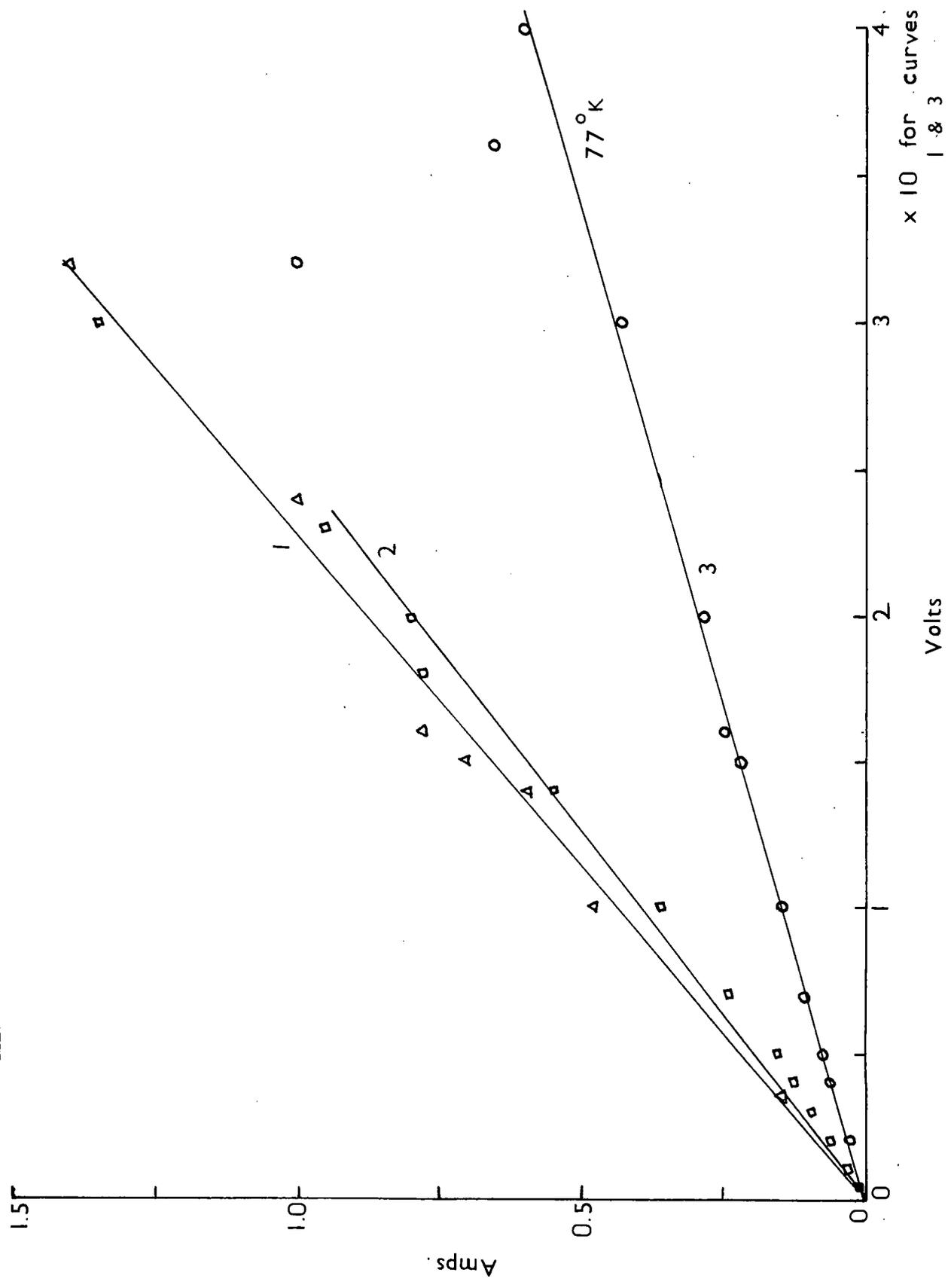
Fig. 4.3. High field V-I characteristics for 50 mol % alloy at a) 300°K 1-before breakdown 2-after breakdown b)3 - at 77°K using indium contacts.
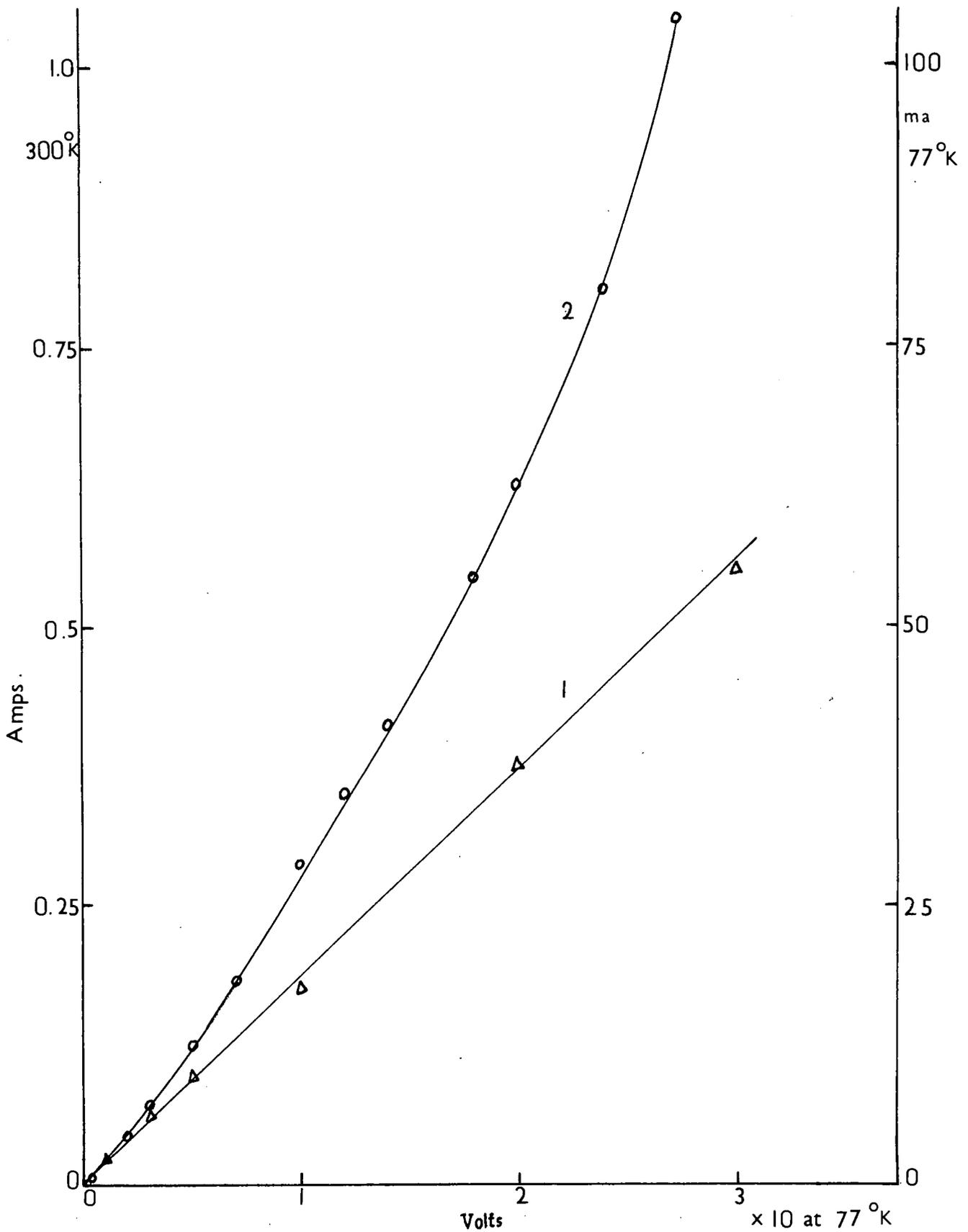
Fig. 4.4. High field V-I characteristics for 37.5 mol % alloy
1) 300°K 2) 77°K using indium contacts.

In - Ga and In contacts.

1b. High Field Characteristics

To study the high field characteristics crystals of thicknesses varying from 20 to 100 µ were used. Initially In - Ga contacts were tried as they were easier to make. The V-I characteristics at 300^OK for the 37.5 and 50 mol % alloys using 20 µsec pulses at the repetition rate of 50 c/sec are shown in fig.(4.2). It is seen from the figure that at smaller fields the current increases linearly with the applied voltage. However, at high fields the current increases rapidly as the voltage is increased showing that the In-Ga contacts are not Ohmic at high fields. To make sure that the non-linearity was not due to the overheating of the crystals, they were cooled to liquid nitrogen temperatures and the readings were repeated, but no improvement was noticed.

Indium contacts were therefore tried. Fig.(4.3)shows the results for a 50 mol % sample at 300^OK before and after breakdown. The V-I plots are good straight lines and the resistance of the sample before and after breakdown is 240 Ω and 2 Ω respectively. The same crystal was then measured at 77°K and the results are also shown in fig.(4.3). The experimental points again lie on a straight line. Fig.(4.4) shows similar results for a 37.5 mol % sample. It is seen from the figure that the V-I plot for the 37.5 mol % sample at 77°K is not linear and that the current increases rapidly as the field increases. This could happen if the mobility at
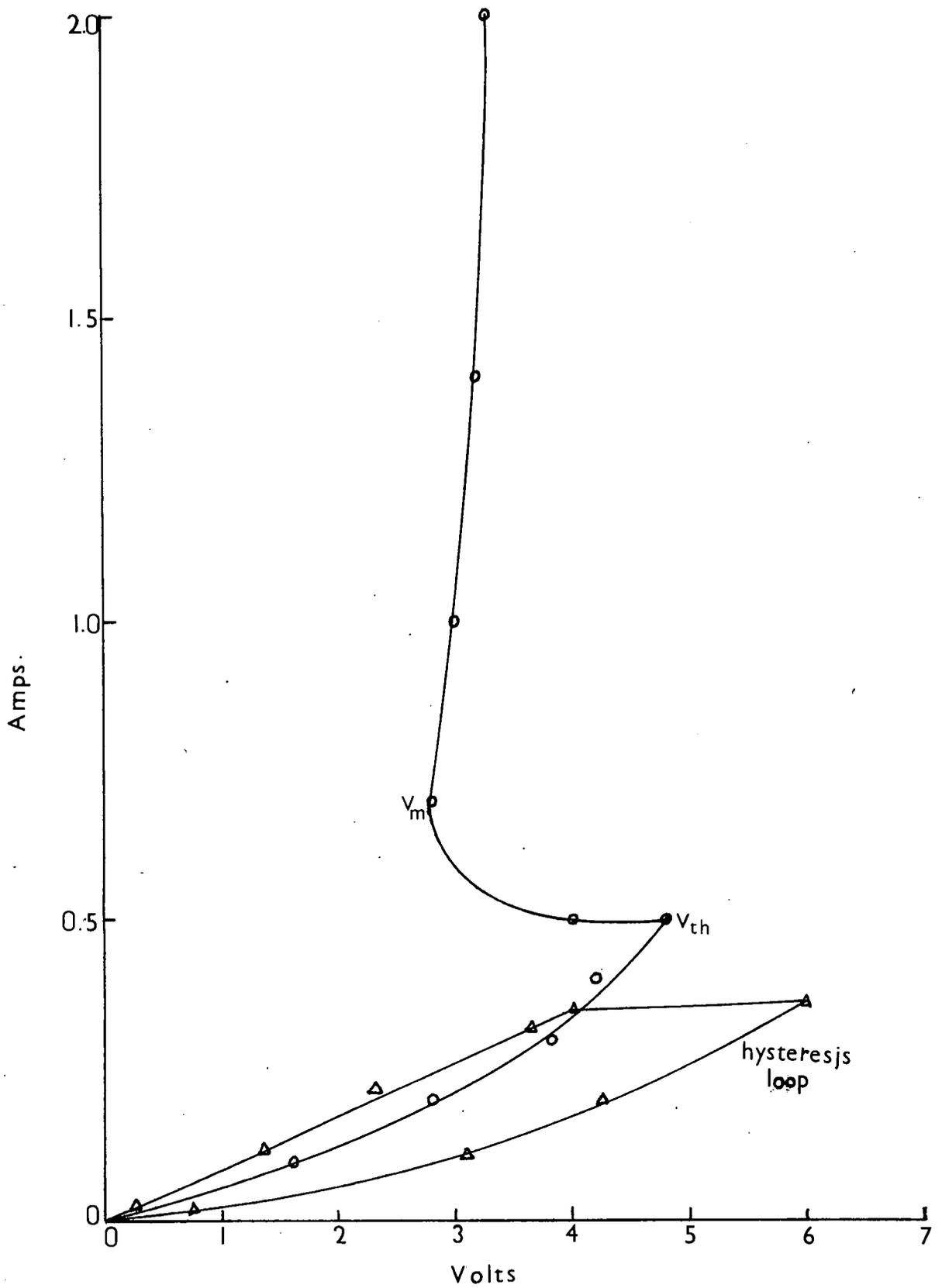
Fig. 4.5. Effect of oxidation of indium contacts on V-I characteristics.

77^OK being limited by impurity scattering increases with
the field as was observed by Oliver,(176) in GaAs. Oliver
observed that the mobility increased as $F^{1/2}$ and has given a
theoretical discussion of the results. This effect seems
unlikely in the present case as one would expect the same
kind of behaviour for the 50 mol % sample. The same result
can be expected if the number of carriers taking part in
conduction increases for example by impact ionization
of impurities or by injection from contacts, and this appears
to be the likely explanation.

The effect of oxidation of the In contacts on the V-I
characteristic can be severe as shown in fig.(4.5). The
crystal in effect behaves as a p-i-n diode, Holonyak (177).
Lampert (178) has given an analysis of the double injection
in insulators (semi-insulators) from which he predicts the
existence of a negative resistance region under certain
conditions. The current first increases up to a threshold
value as the square of the voltage as expected of single carrier
space-charge-limited emission. After the threshold voltage is
reached the current increases through a negative resistance region
because of contribution from the holes, until the voltage
drops to a value $V_m \sim (\frac{\sigma_n}{\sigma_p}) V_{th}$. Then the crystal behaves
as a semiconductor and the current increases through a positive
resistance region. Illumination was found to lower the thresh-
old voltage as observed for other materials. Curve 2 shows the
hysteresis loop.

No current oscillations could be detected even at fields as high as 10^3V/cm in either the 30, 37.5 or the 50 mol % alloys.   Various pulse lengths and repetition rates were used.   At liquid Nitrogen temperature the field strength was $\sim 10^4$V/cm.
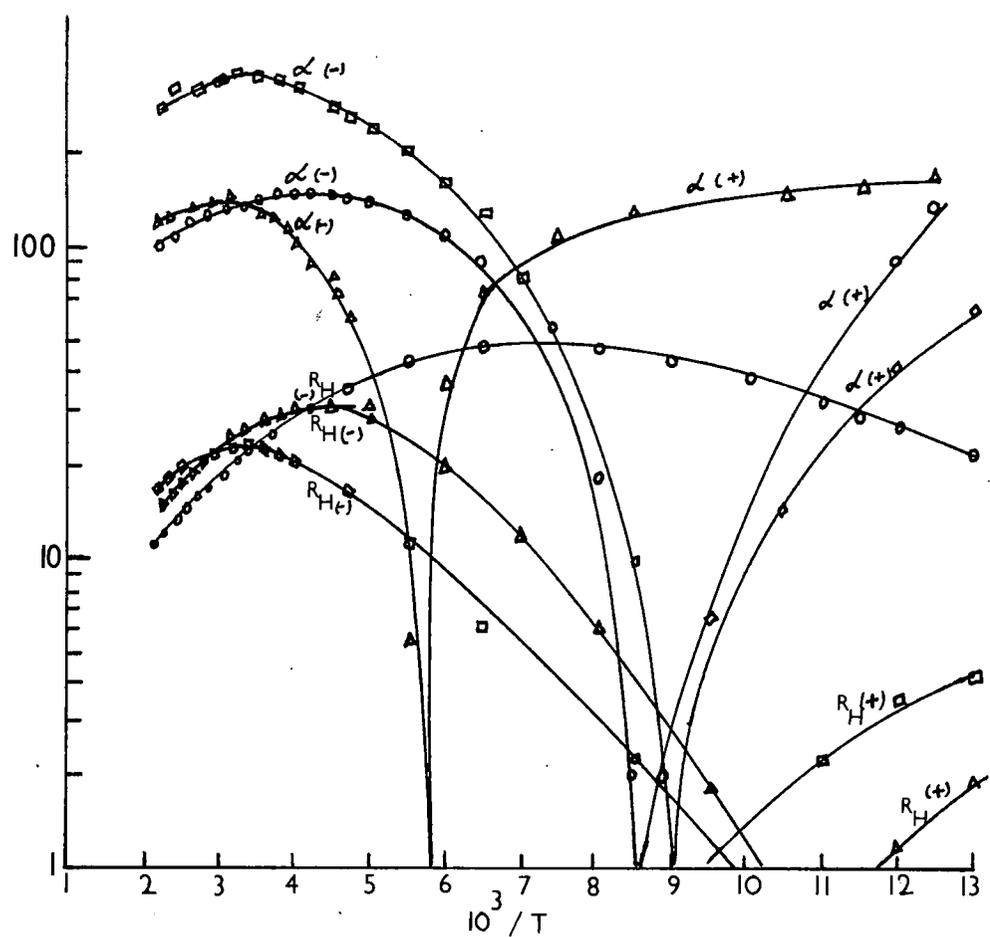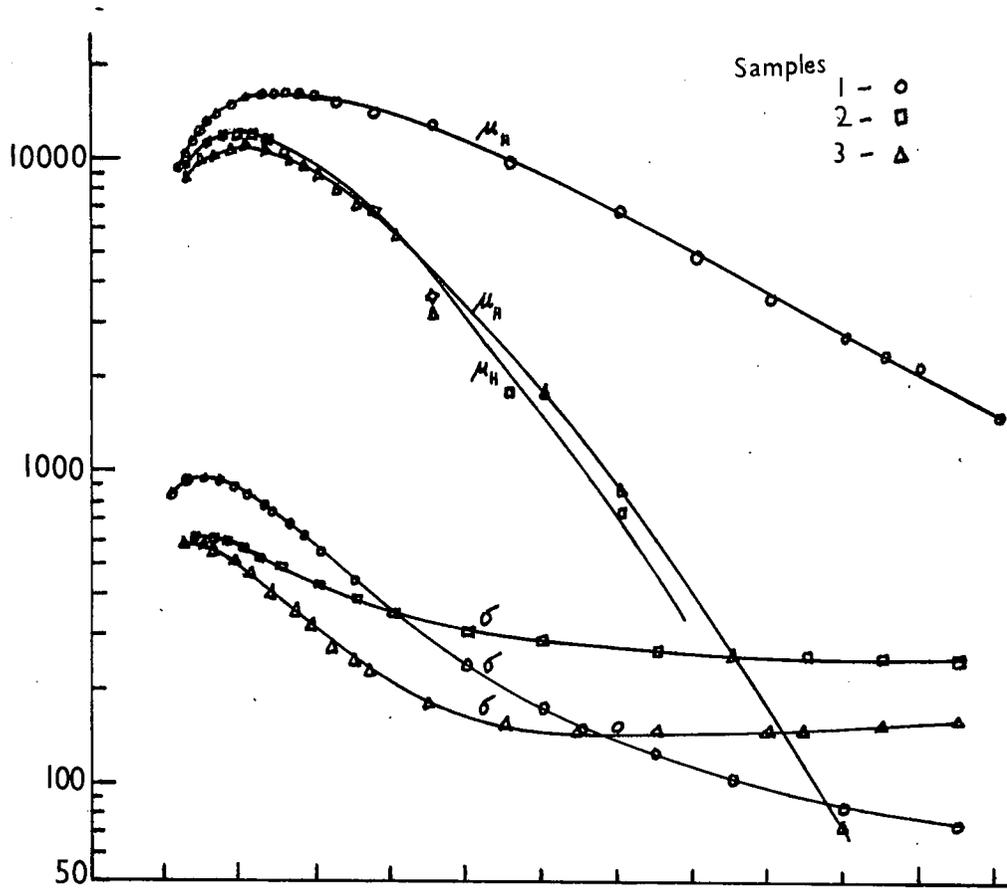
Fig. 4.6. Electrical results for HgTe samples no 1, 2 and 3.

Section 2. Properties of HgTe

As mentioned before, Lewis (107) had carried out detailed investigations of the electrical properties of HgTe and the effect of annealing on these properties. However anomalous results were obtained for some samples in the measurements of magneto-resistance and magneto-Seebeck effects. As no satisfactory explanation of these effects was available it was thought necessary to investigate samples with length to width ratio of about 10 so that the end contact shorting effects could be completely eliminated. Also the lateral contacts were made extremely thin to avoid spurious geometrical effects.

2a. Electrical Properties

A sample (no. 1) of size 22mm x 2mm x 2mm was therefore prepared and the electrical properties were investigated in the temperature range 77 to 455^OK. The electrical properties were again measured after annealing sample 1 in Hg-vapour at 300^OC for 70 hours (sample 2) and subsequently for 180 hours (sample 3). All the results are shown in fig.(4.6). It is seen from the figure that for sample 1 the Hall coefficient R_H is negative throughout the temperature range and shows a broad maximum of 50 at 143^OK. The Seebeck coefficient α changes sign and becomes positive below 115^OK. For sample 2, R_H shows a negative maximum of 22 at 285^OK and becomes positive below 110^OK. R_H increases in value over that for sample 1 above 300^OK. α is also larger above 150^OK. As a result of further annealing (sample 3) R_H still shows a negative maximum of 30 at 200^OK and changes sign below 100^OK.
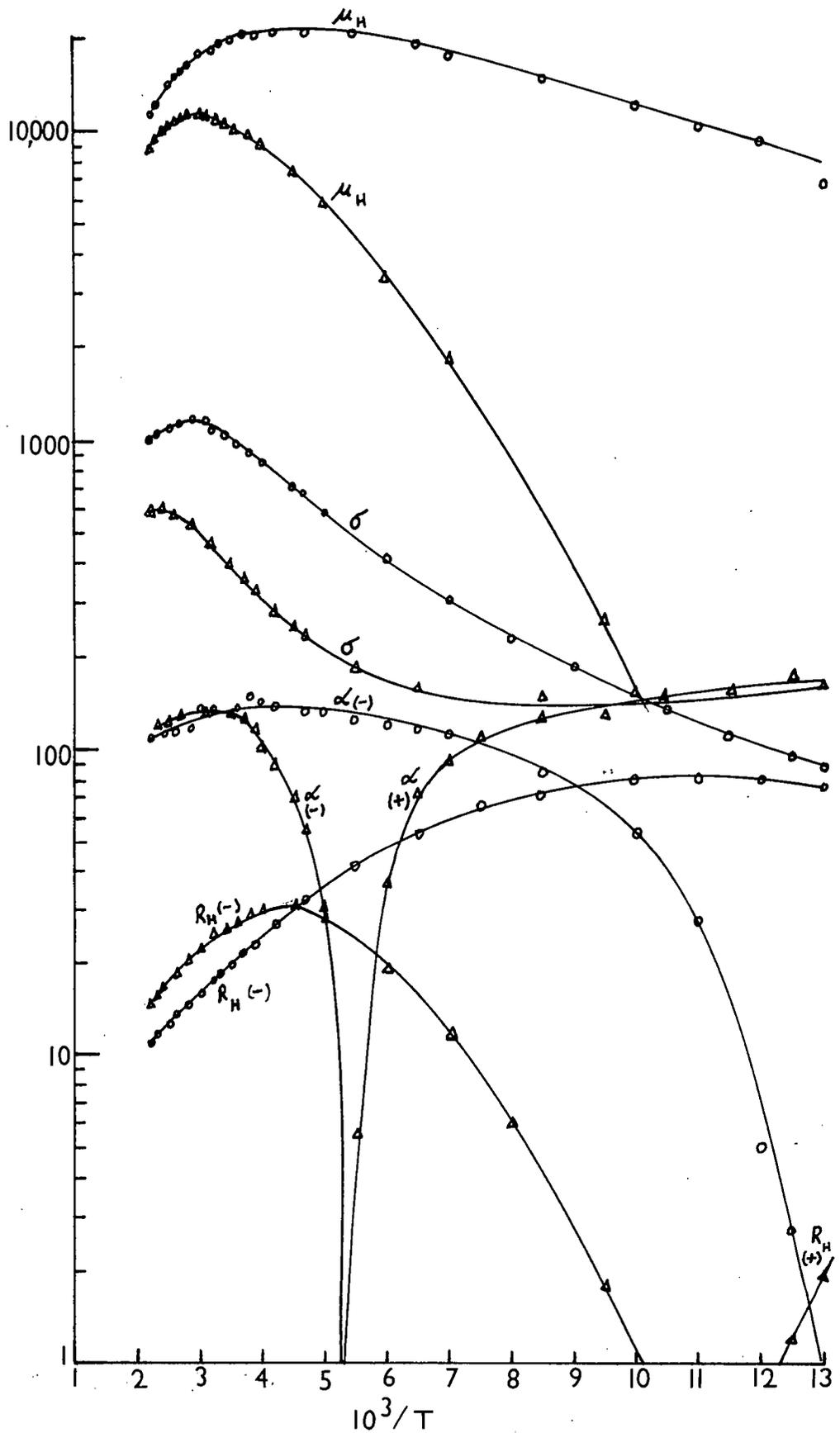
Fig. 4.7. Electrical results for Hg Te samples no 4 and 5.
o - Sample 4 , Δ - Sample 5 .

as a result of annealing in Hg-vapour. This is in contradiction to the results of Giriat (97) and Wagini and Reiss (109), but agrees with the findings of Lewis (107). As a result of annealing the conductivity σ decreases at higher temperatures but shows an increase at lower temperatures. Giriat observed a uniform increase in σ throughout the temperature range. The Hall mobility μ_H decreases after annealing as observed by Giriat for samples annealed beyond the optimum annealing time. However in the present work no optimum annealing time was observed.

As sample 1 was prepared by the Bridgman method from stoichiometric amounts of Hg and Te, it was decided to check whether the same results could be obtained for HgTe grown by Delves' (74) technique. A sample (no. 4) of HgTe grown by static freeze from the composition $Hg_1Te_{1.025}$ was obtained from Mr. Alper in this laboratory. The ingot from which sample 4 was made had been annealed in Hg-vapour at 300^OC for 100 hours. The electrical properties of sample 4 were measured in the temperature range 77-455°K. Sample 4 was then annealed in Hg-vapour at 300^OC for 150 hours (sample 5) and the electrical properties were again measured. The results for samples 4 and 5 are shown in fig.(4.7). For sample 4, R_H is negative throughout the temperature range and shows a broad maximum of 80 at 91°K. α goes through zero at about 80°K. The electron mobility has a maximum value of 21000 cm^2/vsec at 240°K. The results for sample 5 are identical with those

for sample 3 and confirm that HgTe becomes more p-type as a result of annealing in Hg-vapour. The electrical properties of the 5 samples at 300 and 77°K are given in tables (4.1) and (4.2) respectively.

Table(4.1). Electrical Properties of HgTe at 300°K

Sample	α $\mu v/^OK$	σ $ohm^{-1}cm^{-1}$	R_H cm^3/C	$\mu_H = R_H\sigma$ $cm^2/vsec$	n cm^{-3}	Remarks
1	-136	780	-21	16200	3.33×10^{17}	as grown
2	-360	520	-22	11500	3.42×10^{17}	sample 1 annealed for 70hrs. at 300°C.
3	-136	420	-25	10600	2.94×10^{17}	sample 2 annealed for 180hrs. at 300°C.
4	-140	1100	-18.5	19500	3.98×10^{17}	grown from $Hg_1Te_{1.025}$, annealed for 100hrs at 300°C
5	-136	440	-25	10800	2.94×10^{17}	sample 4 annealed for 150hrs. at 300°C.

Table (4.2) Electrical Properties of HgTe at 77°K

Sample	α $\mu v/^\circ K$	σ $ohm^{-1}cm^{-1}$	R_H cm^3/C	$\mu_H = R_H\sigma$ $cm^2/vsec$	n or p cm^{-3}
1	+160	72	-21.5	1500	3.4×10^{17}
2	+60	255	+5.5		1.34×10^{18}
3	+170	160	+2		3.68×10^{18}
4	0	86	-76	7000	9.68×10^{16}
5	+170	160	+2		1.34×10^{18}

Taking the values of the intrinsic carrier densities n_i from Giriat (97) and using a two carrier model the values of b for all the 5 samples were determined from the Hall coefficient maximum using equations (1.73), (1.74) and (1.75). Assuming that the hole density p remains constant below the temperature of the Hall maximum, the values of b, μ_e, μ_h and n at 77°K were also evaluated and are given in table (4.3).

2.b.   Mobility Ratio and Scattering Parameter

Table (4.3) Values of b,n,p,μ_e and μ_h calculated from

the Hall maximum.

Sample	b from Hall maximum	b assuming p constant below Hall maximum	Temperature °K	n/cm^3	p/cm^3	$\mu_e \frac{cm^2}{vsec.}$	$\mu_h \frac{cm^2}{vsec}$
1	9		143	3.2×10^{16}	2.6×10^{16}	17600	2000
1		13	77	$4. \times 10^{15}$	2.6×10^{17}	17500	1350
2	19		286	7.8×10^{16}	1.48×10^{18}	20000	1050
2		19	77	7.36×10^{14}	1.48×10^{18}	19360	1046
3	16		238	5.75×10^{16}	9.2×10^{17}	14780	923
3		24	77	1.18×10^{15}	9.2×10^{17}	25300	1060
4	6		91	1.84×10^{16}	1.1×10^{17}	20720	3450
4		6.6	77	9.9×10^{15}	1.1×10^{17}	20480	3406
5	same as sample 3						

The temperature dependence of the Hall mobility was determined from the formula $\mu_H = AT^a$ where A is a constant. The values of the exponent a are given in Table (4.4)

Table (4.4). Values of exponent a in $\mu_H = AT^a$.

Sample	Temperature range ^oK	a in $\mu_H = AT^a$	Remark
1	350 - 455	-1.70	
	77 - 125	+3.1	Two carrier effect
4	350 - 455	-1.64	
	77 - 125	+1.44	

Since α becomes positive at 77^oK for sample 4 the value of a between $77-125^o$ could also be influenced by two carrier effect and may not indicate ionized impurity scattering. a has a value of ~ -1.7 in the temperature range $350-450^oK$ at least for samples 1 and 4. Since the temperature dependence of the mobility is close to the $T^{-1.5}$ law characteristic of acoustic lattice scattering it is tempting to assume it a dominant scattering mechanism. However similar behaviour was observed in InSb and Ehrenreich (179) showed that a combination of polar optical and electron-hole scattering gives the $T^{-1.7}$ law. In this case the relaxation time τ is only slightly dependent on the electron energy E i.e. the

scattering parameter s in $\tau = \omega E^S$ is approximately zero. The same may hold good in the case of HgTe in the intrinsic range above 300^OK.

2c. Effective Mass

Samples 1 and 4 are intrinsic above 250^OK. Since the mobility ratio $\gg 1$, $n = \dfrac{r}{eR_H}$ (equation 1.68). From the values of R_H at these temperatures it will be seen that the carrier densities are all in excess of $10^{17}/cm^3$ and the samples are partially degenerate. Therefore from equation (1.90) the value of η can be obtained and hence the value of $\dfrac{m^*}{m_o}$ from equation (1.33). The values of $\dfrac{m^*}{m_o}$ for samples 1 and 4 were calculated for different values of s and are given in table (4.5).

Table (4.5). The Effective Mass Ratio for HgTe at 300, 400 and 455^OK.

Sample	Temperature ^{O}K	Scattering Perameter s		$\dfrac{m^*}{m_o}$	n/cm^3
1	300	-1/2	1.3	0.037	3.33×10^{17}
	400	-1/2	1.9	0.027	4.46×10^{17}
	455	-1/2	2.3	0.023	4.48×10^{17}
1	300	0	2.2	0.026	
	400	0	3.0	0.019	
	455	0	3.5	0.017	
1	300	1/2	3.2	0.020	
	400	1/2	4.2	0.014	
	455	1/2	4.8	0.013	

Table (4.5) continued.

Sample	Temperature $^{\circ}K$	Scattering Parameter s		$\dfrac{m^*}{m_o}$	n/cm^3
2	300	-1/2	1.25	0.038	3.42×10^{17}
	400	-1/2	1.85	0.030	4.96×10^{17}
	455	-1/2	2.1	0.026	5.68×10^{17}
2	300	0	2.2	0.027	
	400	0	2.9	0.0184	
	455	0	3.3	0.018	
2	300	1/2	3.2	0.020	
	400	1/2	4.1	0.0154	
	455	1/2	4.4	0.014	

The values of $\dfrac{m^*}{m_o}$ calculated from the Seebeck coefficient data are in fact the average values and not the values at the Fermi level. These values should therefore be smaller than the values for the same carrier concentration determined from reflectivity and magnetoreflection data. However since $\eta > 1$ between 300 and $455^{\circ}K$ the average values should not be very different from the values at the Fermi energy (180). The average value of m^*/m_o for $s = -1/2$ is ~ 0.03 and for $s = 0, \sim 0.024$ for a carrier concentration of $4.7 \times 10^{17}/cm^3$. The value from magnetoreflectivity is ~ 0.038 for a carrier concentration of $4.3 \times 10^{17}/cm^3$ (111). Thus it would appear
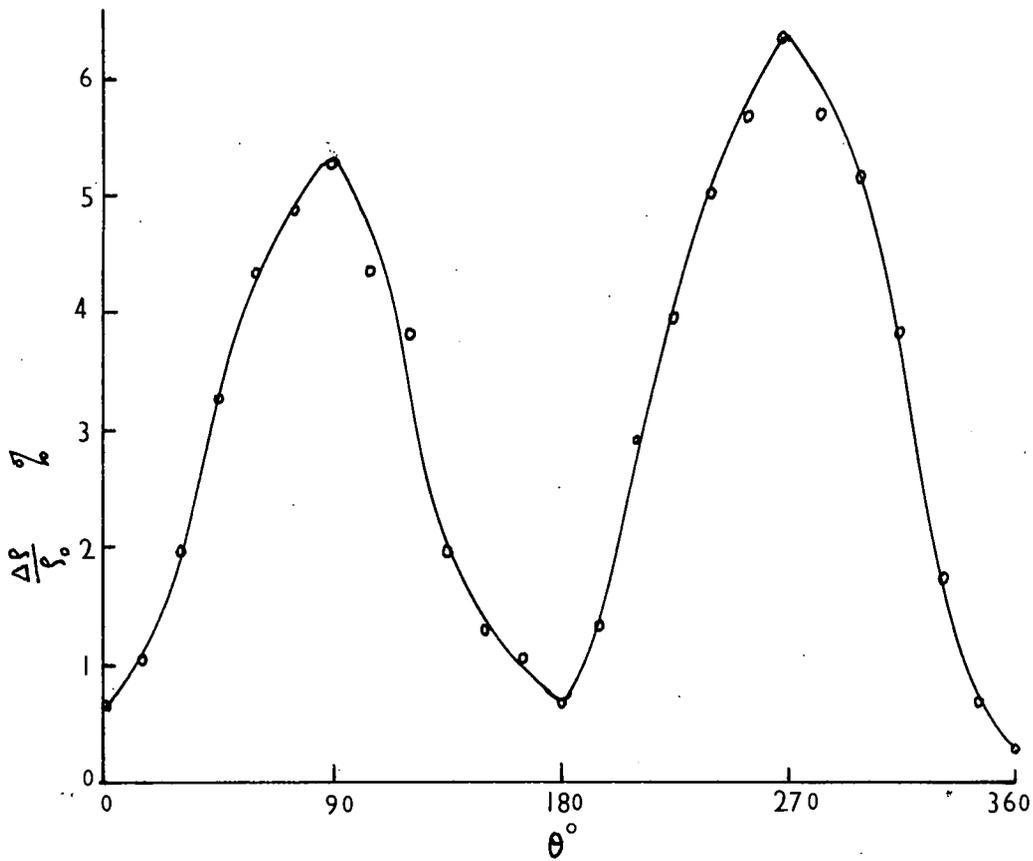
Fig. 4.8 a. $\Delta\rho/\rho_0$ vs θ for HgTe sample I.
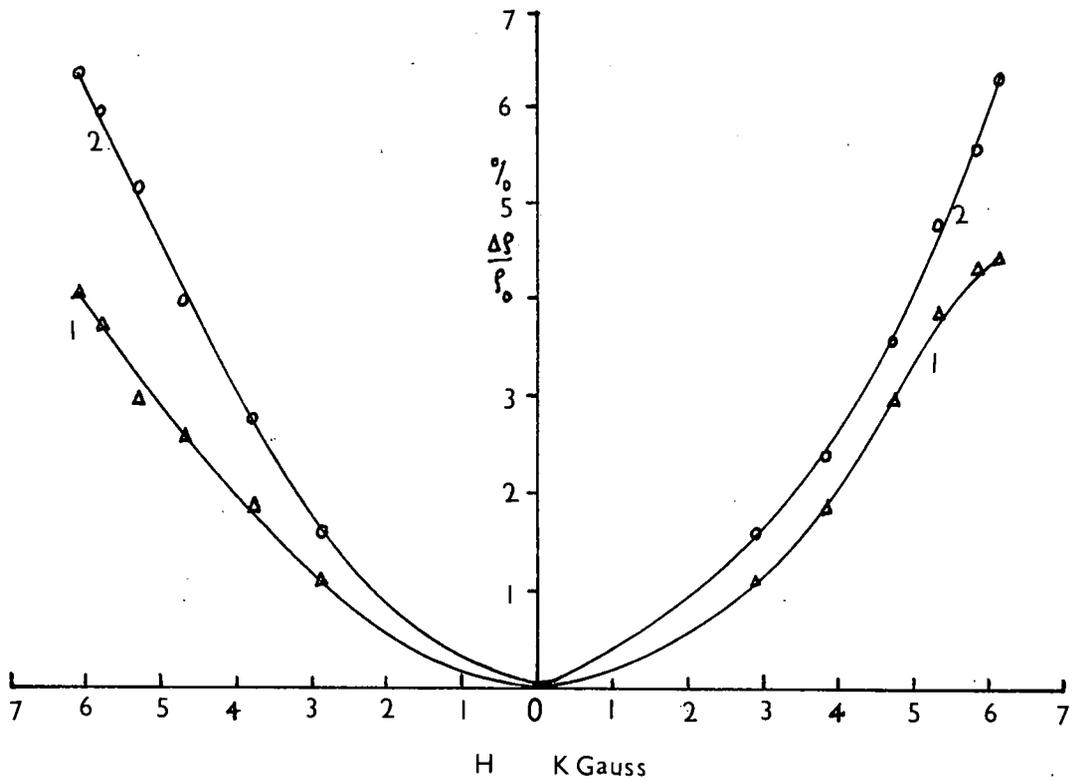
Fig. 4.8 b. $(\Delta\rho/\rho_0)_\perp$ vs H for HgTe sample I at 1) 77 and 2) 300 $^{\circ}$K

that the values of $\frac{m^*}{m_o}$ assuming s = -1/2 are in better agreement with the values determined from reflectivity and magneto-reflection. The higher values of $\frac{m^*}{m_o}$ and η at 300°K could then be explained by assuming that s $> -1/2$ at 300°K because of the change in the scattering mechanism below 300°K. Otherwise it could be possible if p $>$ n below 300°K. However table (4.3) shows that for sample 1 n $>$ p even at 143°K. The same should also be the case for sample 4.

2d.   Magnetoresistance Effect

The variation of magnetoresistance with the angle Θ between current and magnetic field for sample 1 was determined at room temperature and the result is shown in fig.(4.8). It is seen from the figure that the variation of $\frac{\Delta\rho}{\rho_o}$ with Θ is almost sinusoidal and that the longitudinal magneto-resistance is very small. This would indicate that the energy surfaces are isotropic.

The isothermal transverse magnetoresistance for sample 1 was measured at 300 and 77°K as a function of the magnetic field and the results are shown in fig.(4.8). It is seen that the variation of $\frac{\Delta\rho}{\rho_o}$ is symmetrical for both the directions of the field and that $\frac{\Delta\rho}{\rho_o} \propto H^2$ upto at least 6 KG. No anomalous results were observed at any temperature. The anomalous results observed by Lewis (107) might therefore be due to the geometrical effects. At 300°K the magneto-resistance was $\frac{\Delta\rho}{\rho_o H^2}$ = 0.08 μ_e^2/C_1^2 where H is in Oersteds,
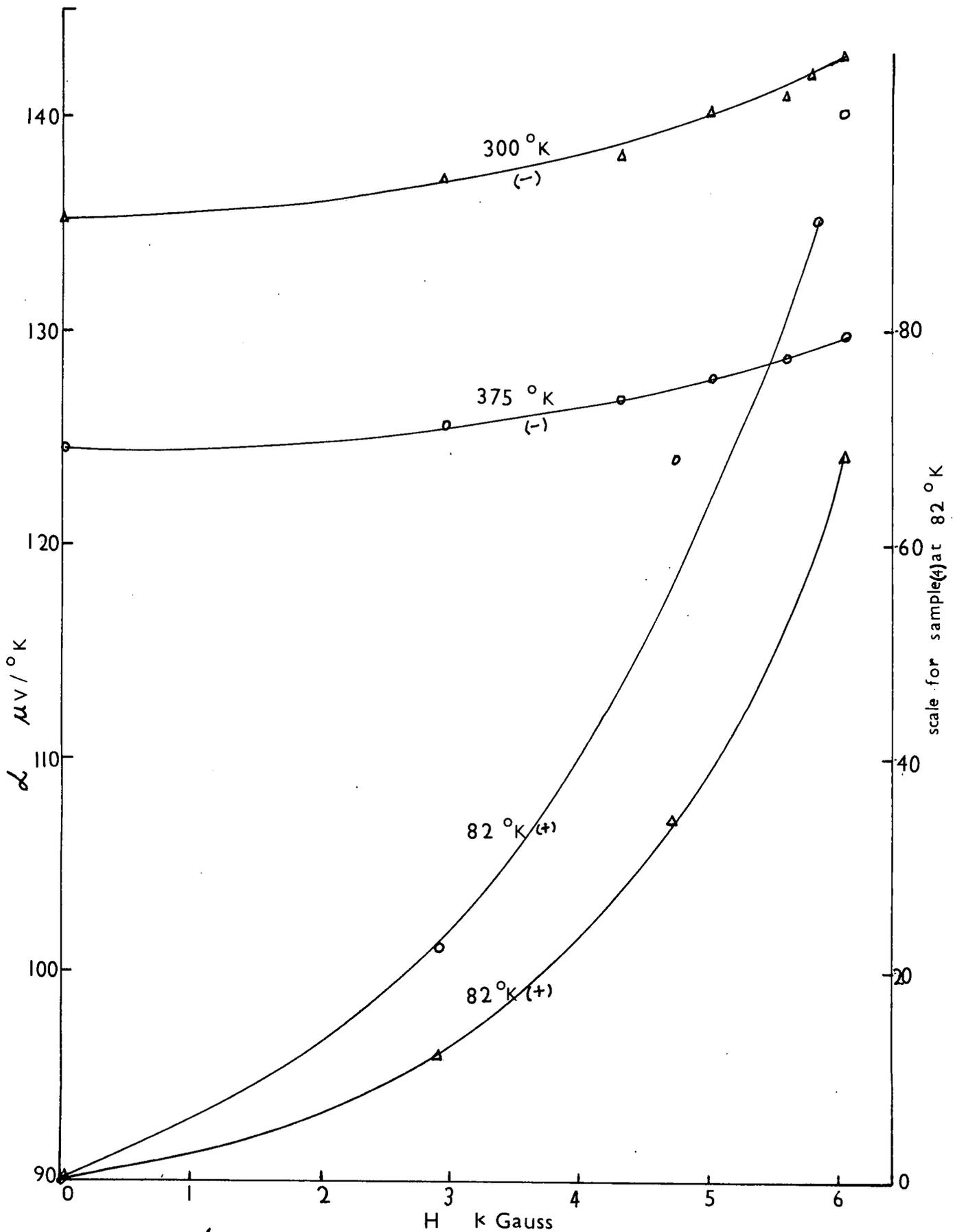
Fig. 4.9. α vs H for HgTe samples no 1)—o, and 4)—Δ.

μ_e in cm^2/vsec and C_1 is 10^8. From equation (1.88) an intrinsic material with s = O will have a magnetoresistance ratio

$$\frac{\Delta\rho}{\rho_o H^2} = \frac{\mu_e^2}{bC_1^2} \qquad (4.1)$$

giving b $\sim$ 12; b comes out to be $\sim$ 14 for s = -1/2. The values of b at 143^oK obtained from the Hall coefficient maximum is 9. The agreement between the two is therefore reasonable. At 77^oK the value of $\frac{\Delta\rho}{\rho_o H^2}$ is 0.04 μ_e^2/C_1^2 assuming μ_e = 17500cm^2/vsec.

2e. Magneto-Seebeck effect

The variation of the isothermal Seebeck coefficient with magnetic field at 375° and 77^oK was measured for sample 1 and the results are shown in fig.(4.9). The results for sample 4 at 300^oK and at 77^oK are also shown in fig(4.9) It is seen from the figure that the magneto-Seebeck coefficient Q^{ll} is positive at 375 and 300^oK for samples 1 and 4 respectively. For parabolic conduction bands this indicates that the scattering parameter s is negative. $(\alpha_H - \alpha_0)/(k/e) = -0.08 \mu_e^2 H^2/C_1^2$ for sample 4 at 300^oK. However since this is the region of intrinsic conduction and the formula for mixed conduction is complicated it is difficult to compare the experimental results with theory.

Therefore no indication of the value of s can be obtained.

Since the conduction band is known to be non-parabolic (109), (123) it is difficult to give much importance to the sign of the magneto-Seebeck effect. Similar results had been obtained by Ehrenreich (179) for p-type InSb samples in the intrinsic range. He found that the best fit with experiment could be obtained by assuming polar optical scattering and non-parabolic conduction band. Wagini (181) also observed similar behaviour in InSb. Wagini has calculated theoretically the values of $\alpha_H - \alpha_O$ for parabolic and non-parabolic conduction bands for varies scattering mechanisms. He has shown that for non-parabolic bands the magneto-Seebeck coefficient is positive for q = -1, -2 and -3.

The magneto-Seebeck results at 77°K are complicated due to two carrier effects. The Seebeck coefficient is positive and shows a rapid increase with increasing magnetic field. $(\alpha_H - \alpha_O) / (k/e) = 0.52 \; \mu_e^2 H^2/C_1^2$ for sample 1 and $0.54 \; \mu_e^2 H^2/C_1^2$ for sample 4 at 77°K. This is because the electron contribution to α is greatly reduced because of the high electron mobility, and the hole contribution remains and tends to saturate at high fields. Now according to Wagini (181), for non-parabolic bands the electron contribution reduces only for ionized impurity scattering. Therefore ionized impurity scattering should be the dominant scattering mechanism at low temperatures. However, Lewis and Wright (108) obtained very low values of m^*/m_O at 100°K assuming

ionized impurity scattering. This may indicate that the assumption s = 3/2 is not correct (a point to be discussed fully later), or it might be that two carrier effects were important in their samples at low temperatures.

2f. Variation of Hall Coefficient with Magnetic Field

The variation of R_H with H at 300° and 77^OK was measured for samples 1 and 4. R_H was found to be independent of H at 300^OK for both samples. However at 77^OK R_H increased by a factor > 3 as H was decreased from 6000 G to 0. Now R_H could increase either due to the two carrier effect or due to the change in r ($R_H = -r/ne$) because of the transition from the high field case (r = 1) to the low field case (r = 1.93 assuming ionized impurity scattering). Since the increase in R_H is much more than could be expected due to the latter effect alone it follows that two carrier effects are important at 77^OK for both the samples.

FIG. 4.10
VARIATION OF HALL COEFFICIENT WITH RECIPROCA[L]
OF ABSOLUTE TEMPERATURE
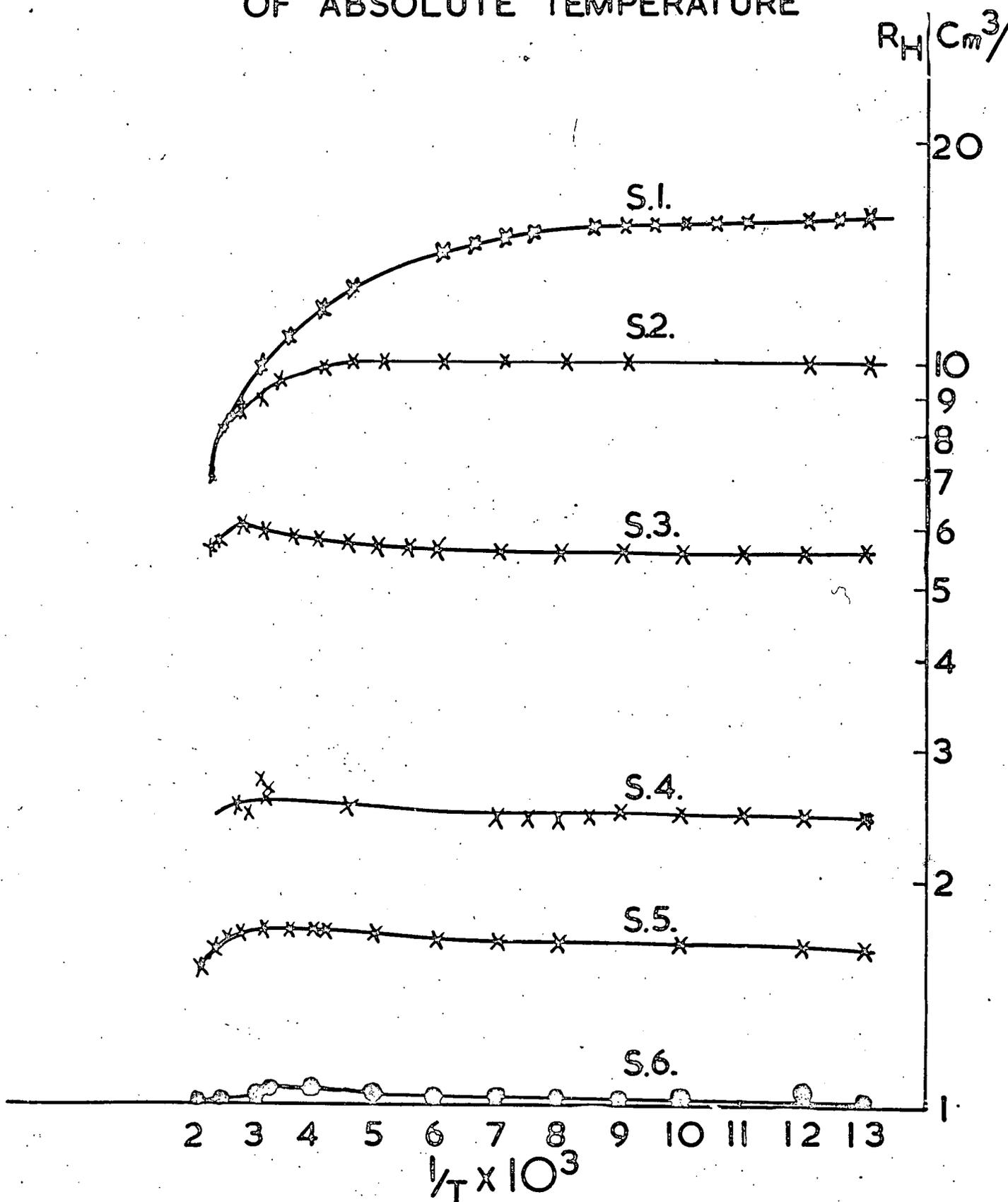
FIG.4.11

VARIATION OF CONDUCTIVITY WITH RECIPROCAL OF ABSOLUTE TEMPERATURE.
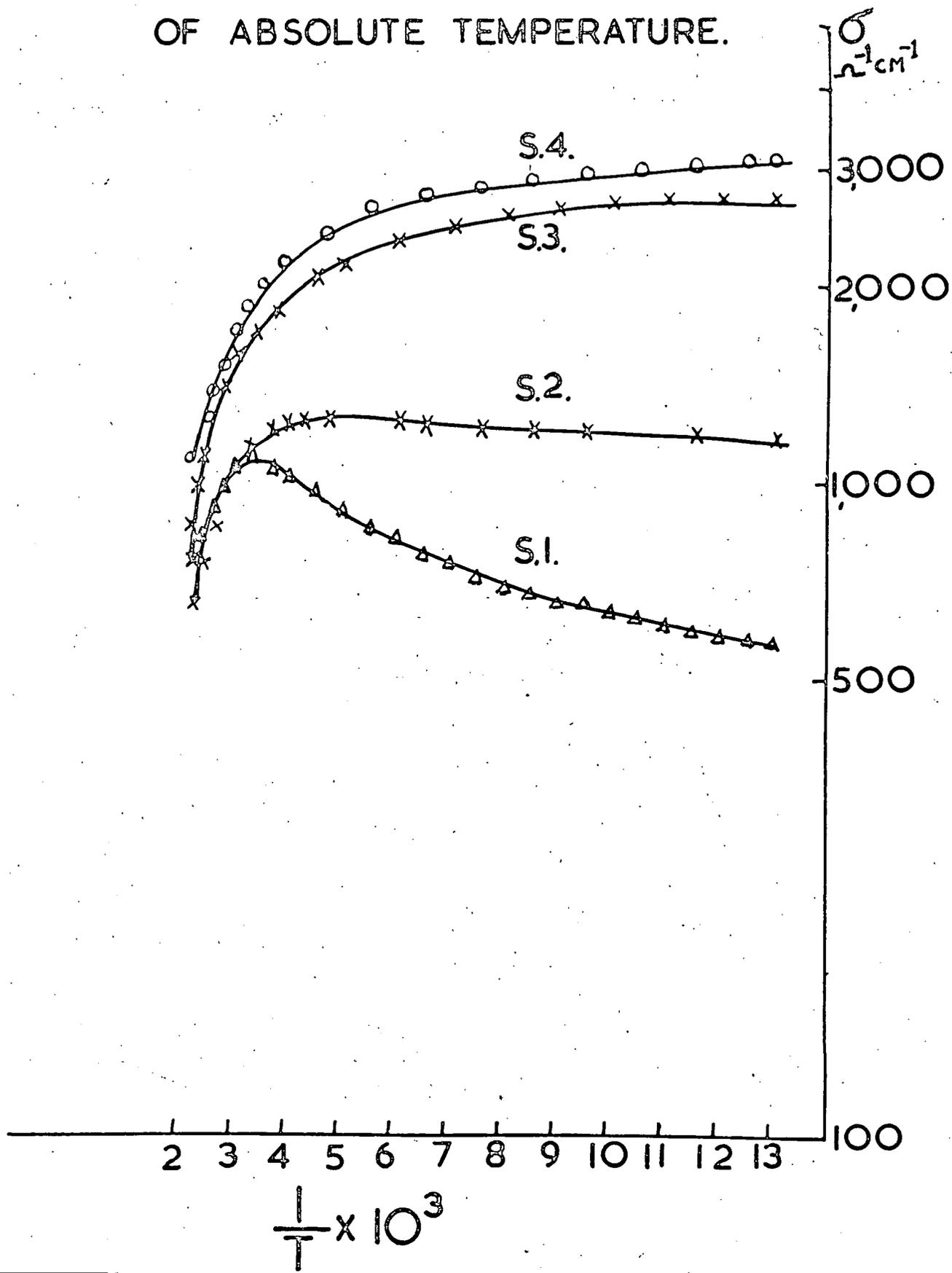
Section 3. 4 mol % Alloy

Wright (112) predicted from the optical results of Spencer (132) and Woolley and Ray (157) that a zero value of E_g corresponding to the lattice parameter of 6.446 Å should occur at the 4 mol % alloy. The composition was therefore expected to show the lowest effective electron mass for the $Hg_3Te_3-In_2Te_3$ alloy system. The purpose of studying the 4 mol % alloy was to check the above prediction.

3a. Electrical Properties and Scattering Parameter

A single crystal ingot with 4 mol % In_2Te_3 was prepared and four samples were obtained out of the same ingot. All the samples were n-type at 300^OK and 77^OK. Samples numbers 1 and 4 were cut with their lengths along [100] direction and samples numbers 2 and 3 were cut with their lengths along [110]. Samples numbers 5 and 6 were obtained by annealing samples 3 and 4 respectively in Hg-vapour at 250^OC for 50 hours to get higher carrier concentrations. It was noted that annealing in Hg-vapour made the samples more n-type. The samples are numbered in order of increasing carrier concentration.

In figure (4.10) R_H is shown as a function of reciprocal temperature from 77 to 455^OK. R_H is negative throughout the temperature range for all samples and is independent of temperature below 200^OK for samples 3, 4, 5 and 6. Figure (4.11) shows the dependence of σ on temperature. The curves

FIG.4.12

VARIATION OF SEEBECK COEFFICIENT WITH
RECIPROCAL OF ABSOLUTE TEMPERATURE.
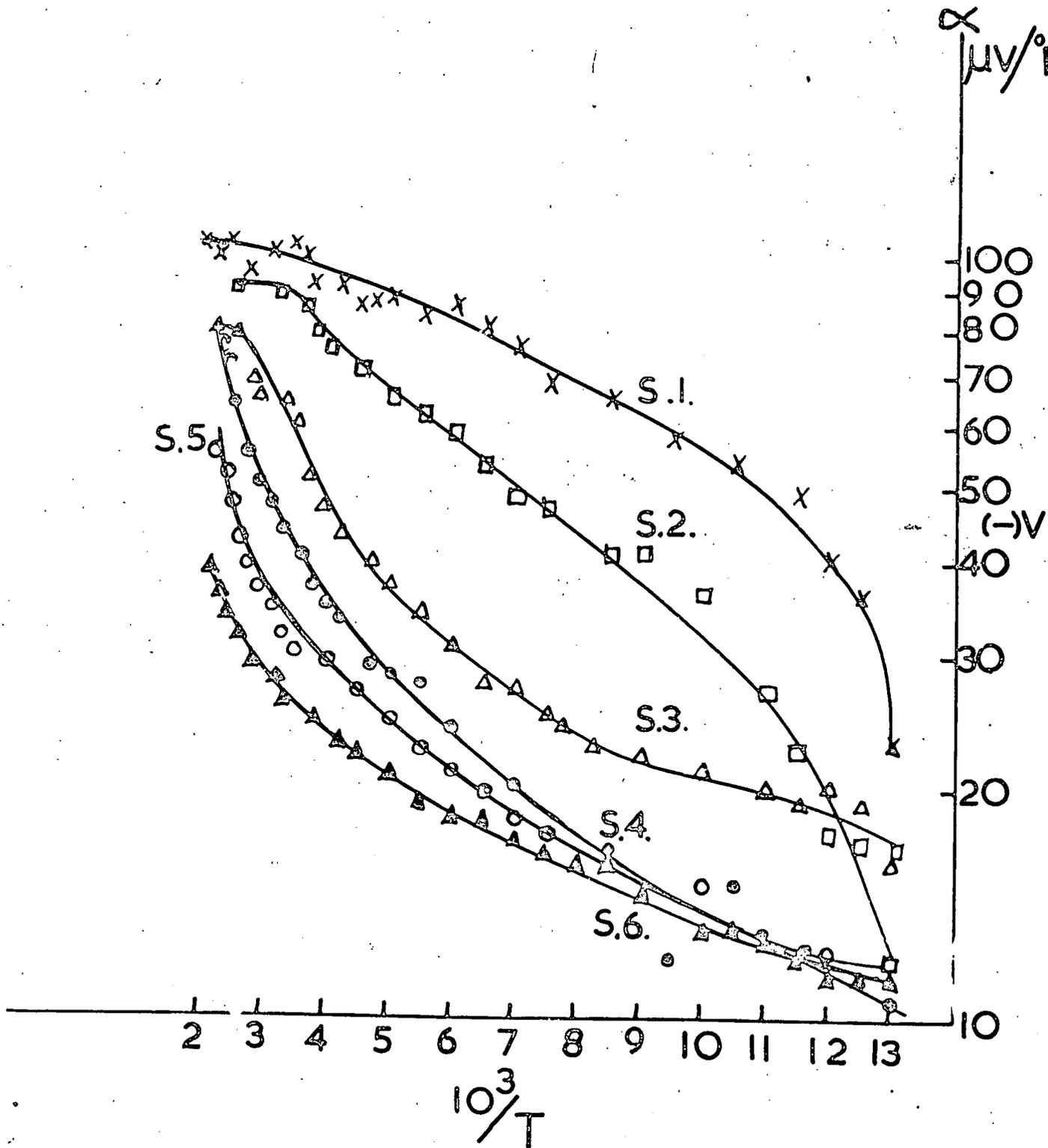
FIG. 4.13

VARIATION OF HALL MOBILITY WITH RECIPROCAL OF ABSOLUTE TEMPERATURE.
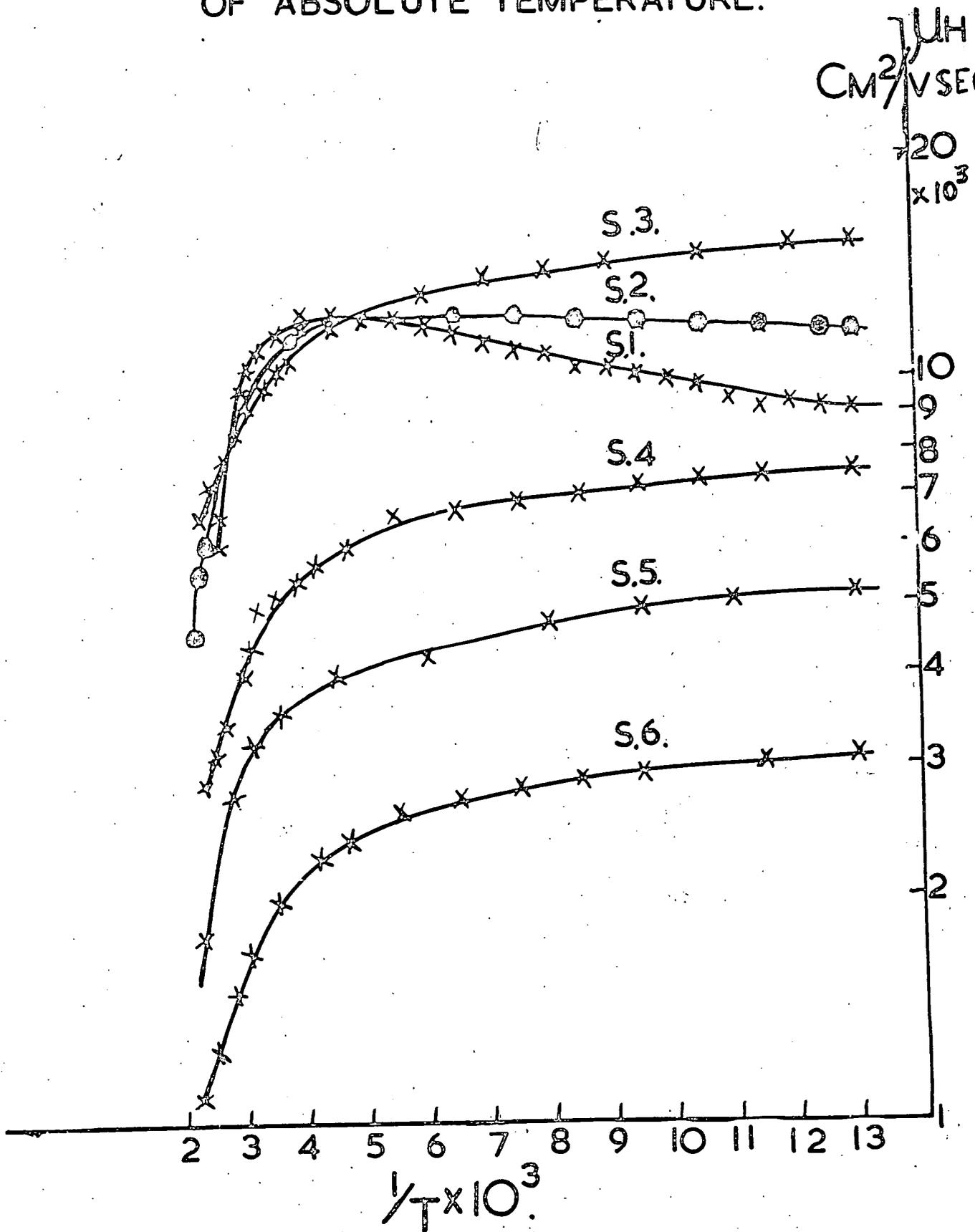
for samples 5 and 6 are the same as that for sample 4
showing that the conductivity does not increase further
with increasing carrier concentration. The Seebeck coefficient
for the samples is shown in figure (4.12). It is seen from
the figure that α is negative throughout the temperature range
for all the samples but decreases rapidly for samples 1 and 2
around 77°K. This might indicate a strong contribution from
holes for samples 1 and 2 at low temperatures. The remaining
samples are extrinsic n-type below 200°K. The variation of the
Hall mobility with the reciprocal of absolute temperature is
shown in fig.(4.13). At low temperatures the mobility increases
with carrier concentration up to about 10^{18} carriers/cm^3
(samples 1, 2 and 3). The increase in mobility suggests that
these samples are compensated and that the acceptor density
N_A decreases during annealing reaching zero in sample (3)
when the donor density N_D reaches 10^{18}/cm^3. The highest
mobilities were 13000cm^2/vsec at 250°K and 15000 cm^2/vsec
at 100°K for samples 1 and 3 respectively. Above about 2 x
10^{18} carriers/cm^3 μ_H decreases with increasing carrier density
at all temperatures and is proportional to $\frac{1}{n}$. Since the
impurity density increases as the electron concentration
increases, one would expect the scattering to be dominated
by ionized impurity in this concentration range. However the
behaviour does not fit the established theories for ionized
impurity scattering (Brooks, Conwell and Weisskoph, Mansfield).

In the concentration range n = 10^{18} to n = 6 x 10^{18} the

behaviour resembles more nearly that of PbTe in the range

10^{19} - 10^{21} as observed by Ioffe and Stilbans (183) and

Allgaier and Houston (184). Allgaier and Houston proposed a

simple geometrical scattering in the degenerate case giving

μ_e independent of temperature and proportional to $N_I^{-4/3}$.

For this type of scattering s should have a value -1/2. Although

the dielectric constant of HgTe is lower than that of PbTe

($\sim$ 15 cf $\sim$ 100) it seems likely that this simple model is

relevant. Alternatively there could be neutral defects

associated with the donor centres. This would lead to s = 0.

The values of the exponent a determining the temperature

dependence of mobility are given in table (4.6).

Table (4.6) Values of Exponent a in $\mu_H = AT^a$

Sample	1	2	3	4	5	6
a in the temperature range 300 - 455°K	-1.77	-1.89	-1.55	-1,62	-2.0	-1.44
a in the temperature range 77 - 200°K	0.34	0.11	-0.18	-0.18	-0.26	-0.19

In the temperature range 300 - 455°K the mean value of a is -1.7.

There is evidence of a fairly high mobility ratio so that

μ_H is determined primarily by μ_e, thus the behaviour resembles

that of HgTe and InSb. Therefore for mixed scattering s can
be assumed to be small and $\sim$ 0. For acoustic scattering
s = -1/2. In the temperature range 77 to 200°K the value of a
changes from +0.34 for sample 1 to -0.22 for sample 5. The
electrical properties of all the samples at 300 and 77°K are
given in tables (4.7) and (4.8) respectively.

Table (4.7). Electrical Properties of 4 mol %

In$_2$Te$_3$ at 300°K

Sample	α $\mu v/^O K$	σ $ohm^{-1}cm^{-1}$	R_H cm^3/C	$\mu_H = R_H \sigma$ $cm^2/vsec$	n cm^{-3}	Remark
1	-96	1100	-10.5	11300	6.14×10^{17}	as grown
2	-90	1180	-9.5	11200	6.58×10^{17}	as grown
3	-62	1750	-5.9	9700	1.08×10^{18}	as grown
4	-43	1900	-2.6	4800	2.51×10^{18}	as grown
5	-32.5	1900	-1.73	3400	3.61×10^{18}	sample 3 annealed in Hg at 250°C for 50 hours.
6.	-25	1900	-1.05	1750	5.95×10^{18}	sample 4 annealed in Hg at 250°C for 50 hours.

Table (4.8). Electrical properties of 4 mol %

In_2Te_3 at $77^O K$

Sample	α $\mu v/^O K$	σ $ohm^{-1} cm^{-1}$	R_H cm^3/C	$\mu_H = R_H \sigma$ $cm^2/vsec$	n cm^{-3}
1	-23	570	-16	9000	3.86×10^{17}
2	-22	1180	-16.5	11800	3.79×10^{17}
3	-17	2750	-5.6	15000	1.10×10^{18}
4	-10.5	3100	-2.4	7600	2.57×10^{18}
5	-12	2750	-1.64	5200	3.61×10^{18}
6	-11.5	3100	-1.02	3100	6.10×10^{18}

3b. Effective Mass

The values of the effective mass were calculated assuming s = -1/2 and s = 0 at 400, 300 and $150^O K$ and are given in tables (4.9), (4.10) and (4.11) respectively.

Table (4.9). Effective Mass Ratio m^*/m_o for 4 mol %

In_2Te_3 at $400^O K$

Sample	n/cm^3	η assuming s=-1/2	m^*/m_o assuming s=-1/2	η assuming s=0	m^*/m_o assuming s=0
1	7.01×10^{17}	2.2	0.032	3.4	0.023
2	7.35×10^{17}	2.9	0.028	4.3	0.020
3	1.1×10^{18}	3.2	0.034	4.9	0.022
4	2.6×10^{18}	4.7	0.041	6.55	0.03
5	3.9×10^{18}	5.9	0.043	8.7	0.032
6	6.25×10^{18}	8.6	0.041	12.7	0.028

Table (4.10) Effective Mass Ratio m^*/m_o for 4 mol % In_2Te_3 at 300^oK.

Sample	n/cm^3	η assuming s=-1/2	m^*/m_o assuming s=-1/2	η assuming s=0	m^*/m_o assuming s = 0
1	5.59×10^{17}	2.3	0.036	3.7	0.023
2	6.58×10^{17}	2.9	0.033	4.2	0.023
3	1.06×10^{18}	4.6	0.031	6.76	0.021
4	2.4×10^{18}	6.6	0.037	9.75	0.026
5	3.61×10^{18}	8.75	0.037	12.91	0.026
6	5.95×10^{18}	11.6	0.045	15.2	0.030

Table (4.11). Effective Mass Ratio m^*/m_o for 4 mol % In_2Te_3 at 150^oK.

Sample	n/cm^3	η assuming s=-1/2	m^*/m_o assuming s =-1/2	η assuming s=0	m^*/m_o assuming s=0
1	4.22×10^{17}	3.65	0.041	5.49	0.028
2	6.25×10^{17}	5.42	0.037	8.15	0.025
3	1.10×10^{18}	10.2	0.029	15.24	0.020
4	2.5×10^{18}	13.2	0.039	19.85	0.028
5	3.8×10^{18}	14.6	0.047	21.9	0.031
6	6.13×10^{18}	16	0.058	24.0	0.039
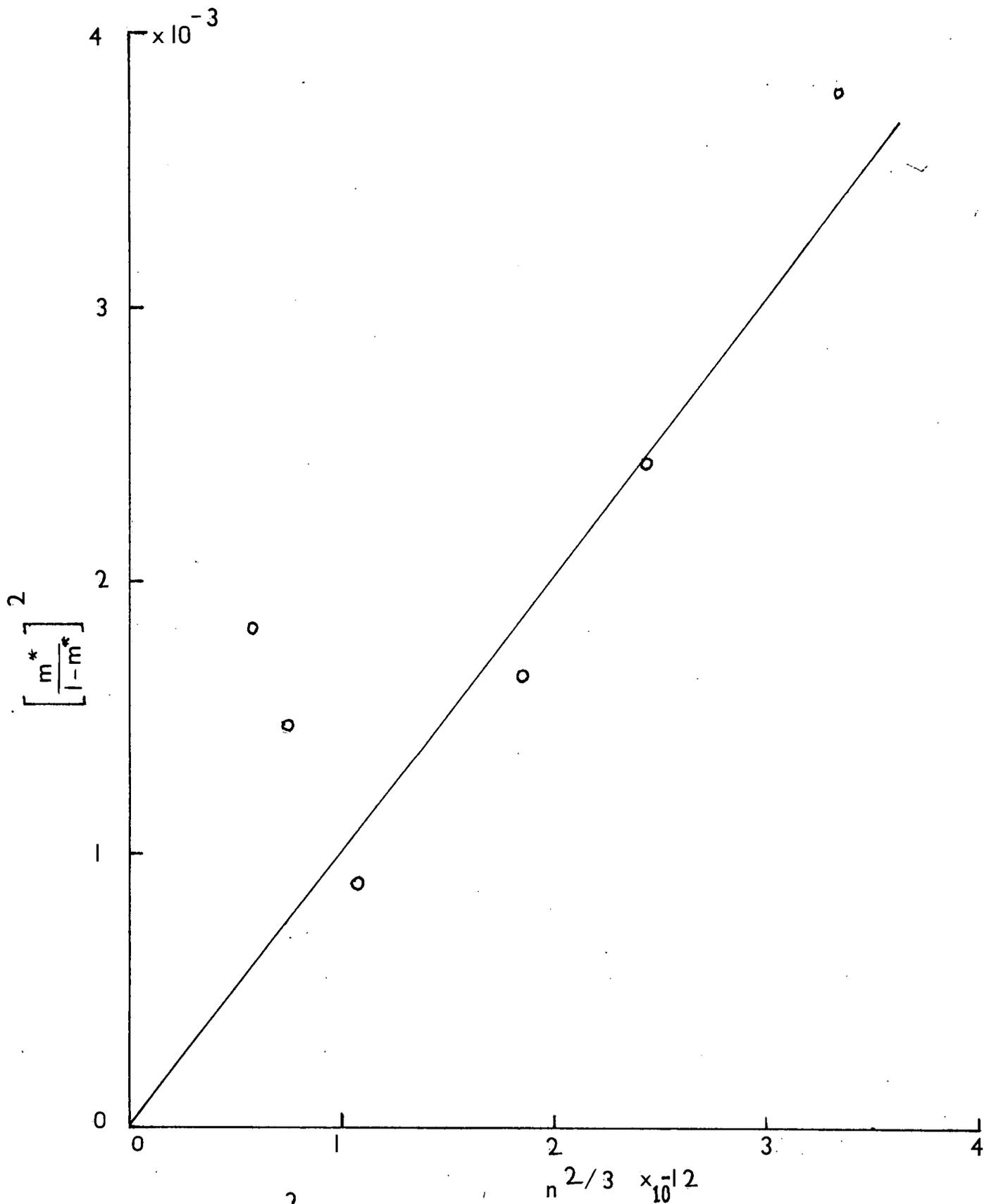
Fig. 4.14 $\left[\dfrac{m^*}{1-m^*}\right]^2$ vs $n^{2/3}$ for 4% samples at $150°K$.

Since samples 1 and 2 are not heavily doped low weightage should be given to the values of the effective mass for these samples. For the rest it is seen from the tables that the effective mass, assuming the same value of s at all temperatures, increases with carrier concentration indicating a non-parabolic conduction band. It is also seen that m^* decreases with increasing temperature and resembles the behaviour for InSb observed by Wagini (181). It can be shown from the tables that the Fermi level remains constant from 400 to $150^{\circ}K$ for samples 3, 4, 5 and 6 which are completely degenerate. Therefore the effective mass also should not change appreciably in this temperature range. Thus the scattering parameter s seems to remain constant from 77 to $400^{\circ}K$ since the variation in the value assumed for s leads to a large variation in m^* with T. The effective mass for the 4 mol % alloy is smaller than that for HgTe for the same carrier concentration. The average value of m^* assuming s = 0 is 0.028 and assuming s = -1/2, 0.04 for a carrier concentration of $2.5 \times 10^{18}/cm^3$.

Assuming s = -1/2 it is found that $\eta > 3$ for all the samples at $150^{\circ}K$. Thus it can be assumed that there is sharp degeneracy and that m^* refers to the mass at the Fermi level. An attempt may be made to fit the effective mass data with Kane's theory according to equation (1.17). The graph of $(m^*/1-m^*)^2$ vs $n^{2/3}$ at $150^{\circ}K$ is shown in figure (4.14). There is considerable scatter but a straight line can be drawn through the experimental points provided low
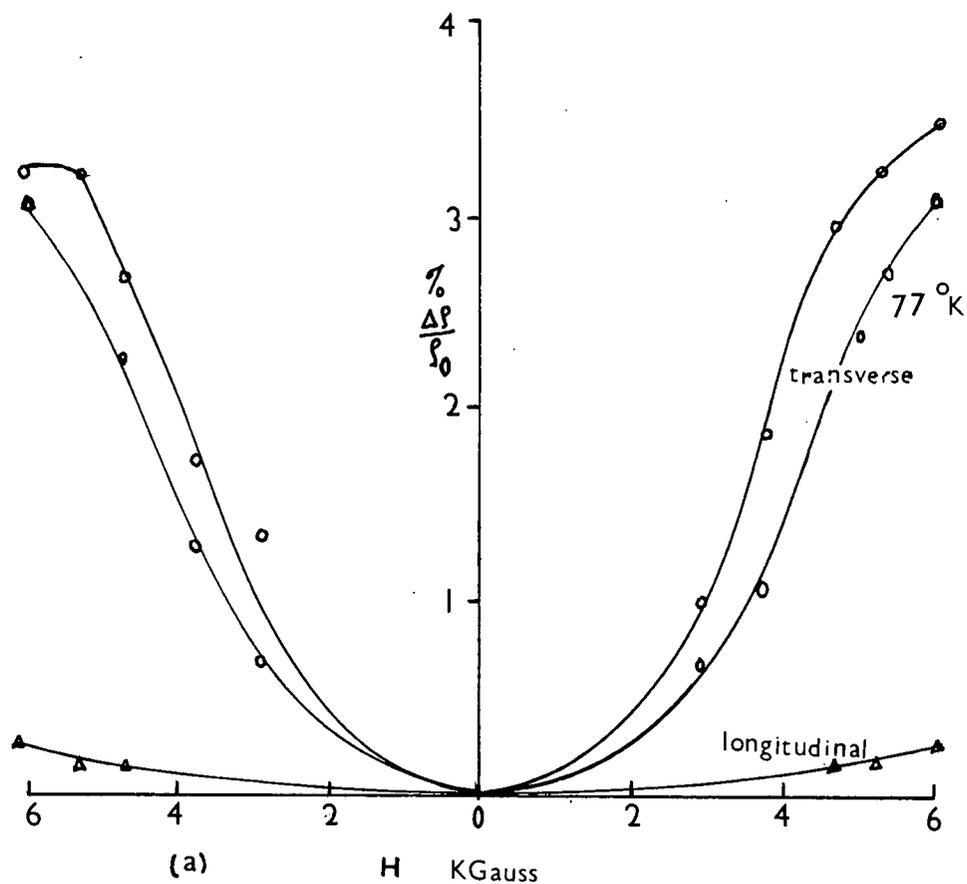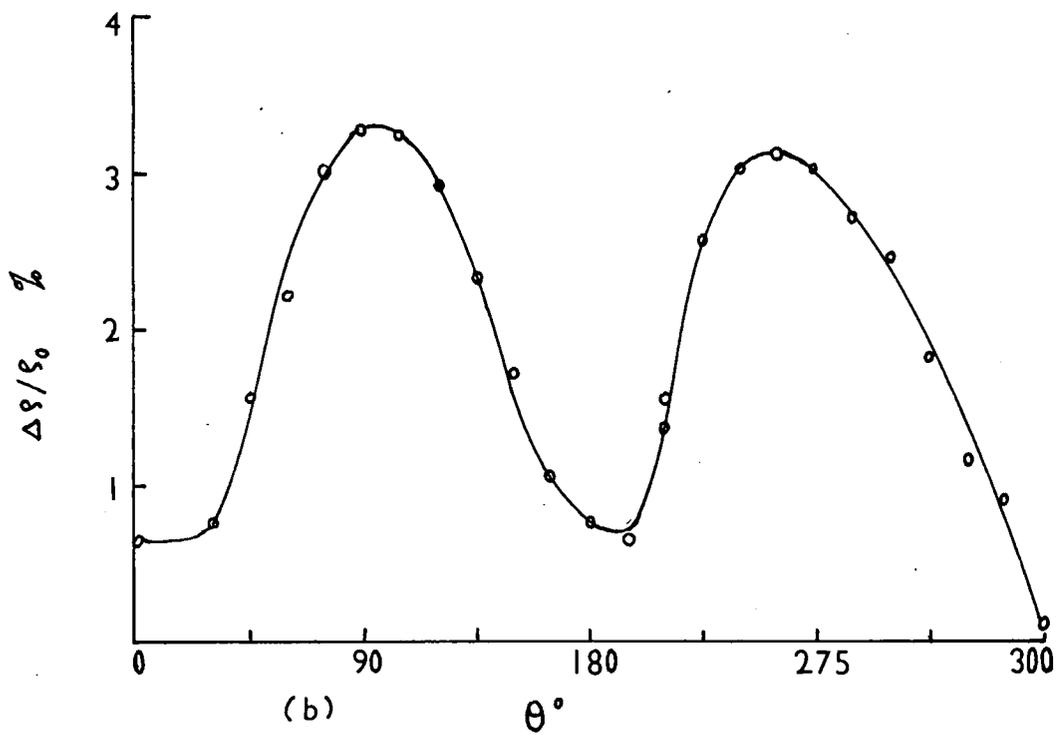
Fig. 4.15. Variation of $\frac{\Delta \rho}{\rho_0}$ vs θ and H at $300\ ^{\circ}K$ for 4% sample 1.

MAGNETO SEEBECK FOR SAMPLES NO.1.& 3.
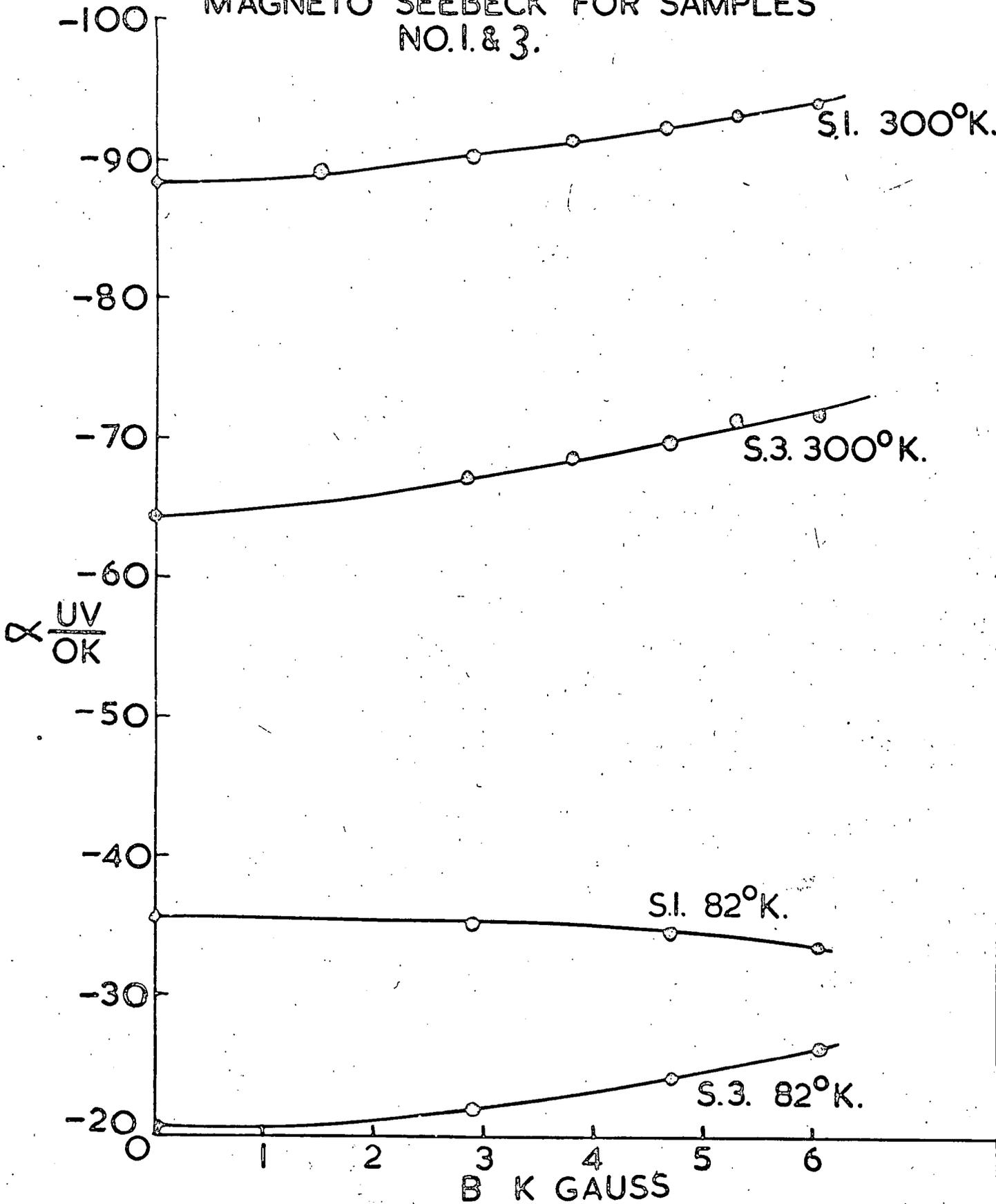
FIG.4.16

weightage is given to the values for samples 1 and 2. The value of P is $\sim 8.8 \times 10^{-8}$ ev-cm and E_g is not very far from zero though it is difficult to get reliable value for E_g.

3c. Magnetoresistance

Magnetoresistance measurements were carried out on sample No. 1 at 300 and 77°K and the results are shown in fig.(4.15). Figure (a) shows the variation of $\frac{\Delta\rho}{\rho_o}$ with H for both transverse as well as longitudinal directions. It is seen that $\frac{\Delta\rho}{\rho_o}$ varies parabolically with H for both the directions in accordance with simple theory. Above 5000 Gauss saturation was noticeable. The transverse magneto-resistance ratio at 300°K was found to be $\frac{\Delta\rho}{\rho_o H^2} = 0.08 \ \mu_e^2/C_1^2$. This is the same as for HgTe and indicates $b \sim 12$ if $s = 0$ and $n = p$. At 82°K $\frac{\Delta\rho}{\rho_o H^2} = 0.05 \ \mu_e^2/C_1^2$ which is however not very instructive as n and p cannot be deduced accurately.

The value of $\frac{\Delta\rho}{\rho_o}$ for the longitudinal direction is very small compared with the transverse indicating isotropic band structure. The variation of $\frac{\Delta\rho}{\rho_o}$ with the angle Θ between the current and the magnetic field was measured at 300°K for sample 1 and is shown in fig.(4.15b). The variation is almost sinusoidal as for HgTe confirming the isotropic band structure.

3d. Magneto-Seebeck Effect

The magneto-Seebeck effect for samples 1 and 3 was measured at 300°K and at 82°K and the results are shown in fig.(4.16). From the figure it is seen that for sample 1

the isothermal Seebeck coefficient increases with magnetic field at $300^{O}K$ but decreases at $82^{O}K$. For parabolic bands this would indicate that the scattering parameter is negative at $300^{O}K$ but positive at $82^{O}K$. However in view of the non-parabolic nature of the conduction band too much importance cannot be given to the sign of the magneto-Seebeck effect. For sample 3 with higher carrier concentration α increases with magnetic field strength at room temperature as well as at liquid nitrogen temperature. This indicates that impurity scattering is not dominant at any temperature. The value of $(\alpha_H - \alpha_o)/(k/e)$ at $300^{O}K$ is $- 0.23 \, \mu_e^2 H^2/C_1^2$ and at $82^{O}K$ $(\alpha_H - \alpha_o)/(k/e) = -0.07 \, \mu_e^2 H^2/C_1^2$. For a non-degenerate sample assuming s = -1/2 and parabolic bands $(\alpha_H - \alpha_o)/\frac{k}{e} \frac{\mu_e^2 H^2}{C_1^2}$ should be = -1.07 for the weak field case. However $\eta = 4.6$ at $300^{O}K$ assuming s=-1/2. Now according to Tsidilkovskii (185), for $\eta \sim 4.5$ the value of $Q^{||}$ should be reduced by a factor 4 from the non-degenerate value. Thus the agreement between theory and experiment seems to be quite good.

Sample 3 is highly degenerate at $82^{O}K$ with $\eta = 17$ assuming s = -1/2. Therefore $(\alpha_H - \alpha_o)/(k/e)$ can be calculated using the simple expression given by Rodot (186)

$$\frac{\alpha_H - \alpha_o}{k/e} = \frac{\mu^2 H^2/C_1^2}{1+\mu^2 H^2/C_1^2} \, \frac{2\pi^2}{\eta} \tag{4.1}$$

The value of $(\alpha_H - \alpha_o)/(k/e)$ from equation (4.1) comes out to be 0.058 assuming s = -1/2, while the experimental value

is 0.04. Therefore it would appear that s has a value $\sim$ -0.35. Wagini (181) has shown that the theoretical value of $(\alpha_H - \alpha_o)$ for s = -1/2 with parabolic bands is of the same order as that for q = -2 and non-parabolic bands, where q is defined from $\mu_q = \mu_{qo} \, k^q (\frac{dE}{dk})^2$ and q = -2 corresponds with the same scattering mechanism as that for s = 0 in the parabolic case. In either case the value of m^* should be the same as the two cases give the same theoretical value of α assuming constant Fermi level. It is worth noting that Cuff et al (187) investigated the effect of non-parabolicity on the Nerst coefficient in PbTe and found it to be quite small.

The Hall coefficient as a function of magnetic field for sample 1 was measured at 300 and 77°K but no significant variation in R_H was noted.
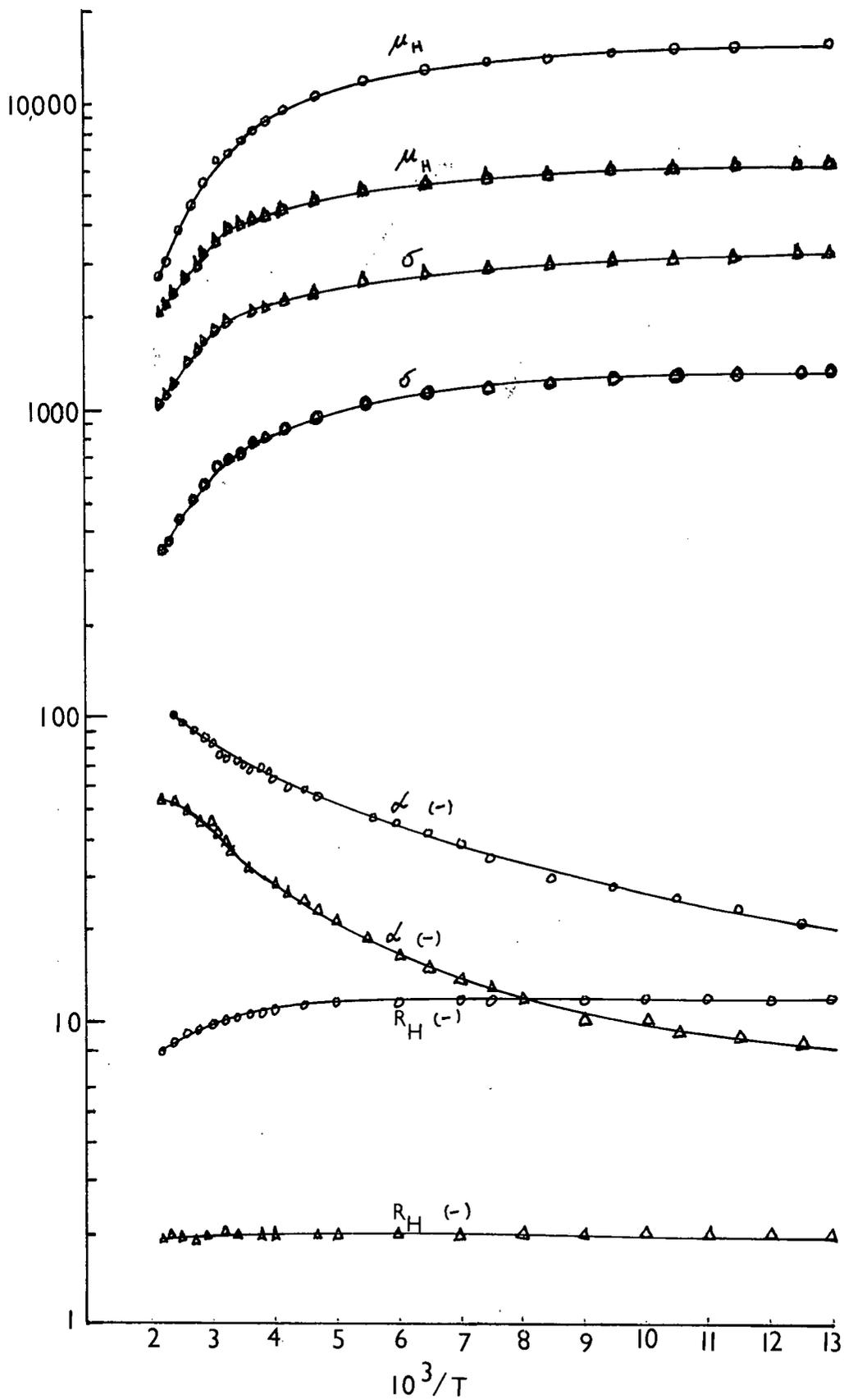
Fig. 4.17. Electrical results for 7 mol % In_2Te_3.

Sample 1 — o   Sample 2 — △

Section 4.   7 mol % In_2Te_3

4a.   Electrical Properties and Scattering Parameter

From optical absorption results it was noted that the zero energy gap occurs at 7 mol% In_2Te_3 and not at 4 mol% In_2Te_3. Therefore it was decided to study the 7 mol % alloy to check whether the lowest effective mass for the $Hg_3Te_3 - In_2Te_3$ system occured at this composition.

Sample No. 1 is as prepared   and sample 2 was obtained by annealing sample 1 in Hg-vapour at 250^OC for 70 hours.   The electrical results for the two samples are shown in fig.(4.17). It is seen from the figure that the results are similar to those for the 4 mol % alloy.   The mobility decreases with the increase of carrier concentration. α and R_H are both negative throughout the temperature range and decrease on annealing. R_H is almost constant throughout the temperature range from 450 - 77^OK for sample 2. σ has increased after annealing. The highest observed mobility is 15000 cm^2/vsec at 77^OK for sample 1 with n = 5.39×10^{17}/cm^3.   The electrical properties at 300 and 77^OK are given in Table (4.12).

Table (4.12)   Electrical Properties of 7 mol %

In_2Te_3 at 300 and 77^OK

Sample	α $\mu v/^OK$	σ $ohm^{-1}cm^{-1}$	R_H cm^3/C	$\mu_H = R_H\sigma$ cm^2/vsec	n cm^{-3}	Remark
300^OK						
1	-72	685	-10.1	6900	6.13×10^{17}	as grown

Sample	α $\mu v/{}^{o}K$	σ $ohm^{-1}cm^{-1}$	R_H cm^3/C	$\mu_H = R_H\sigma$ $cm^2/vsec$	n cm^{-3}	Remark
			$300^{o}K$			
2	-36	1900	-1.95	3600	3.21×10^{18}	sample 1 annealed in Hg for 70 hrs. at $250^{o}C$
			$77^{o}K$			
1	-20	1300	-11.6	15000	5.39×10^{17}	
2	-8	3100	-1.95	6000	3.21×10^{18}	

The value of the exponent a in $\mu_H = AT^a$ is ~ -1.9 between 300 and $450^{o}K$ indicating again that $s \sim 0$ for mixed scattering or $-1/2$ for acoustic scattering. In the temperature range 77 to $200^{o}K$ the value of a varies from -0.19 for sample 1, to -0.24 for sample 2. In this temperature range both the samples are degenerate and as before $s \sim 0$ assuming neutral impurity scattering or $s \sim -1/2$ assuming simple geometrical scattering.

4b. Effective Mass

The values of m^* calculated assuming $s = 0$ and $-1/2$ are given in table (4.13)

Table (4.13) Effective Mass Data for 7 mol % In_2Te_3.

Sample	Temperature $^\circ K$	n/cm^3	η assuming $s = -1/2$	m^*/m_0 assuming $s = -1/2$	η assuming $s = 0$	m^*/m_0 assuming $s = 0$
1	400	7.18×10^{17}	2.5	0.03	3.9	0.021
2	400	3.21×10^{18}	5.8	0.039	8.4	0.027
1	$300^\circ K$	6.13×10^{17}	3.8	0.025	5.83	0.017
2	$300^\circ K$	3.21×10^{18}	8.1	0.037	12.0	0.025
1	150	5.44×10^{17}	7.20	0.026	10.8	0.017
2	150	3.21×10^{18}	20.3	0.03	30.5	0.02

It is seen from the table that the Fermi level seems to remain constant from 400^OK to 150^OK for both the samples. Therefore one would not expect the effective mass to change appreciably with temperature. Therefore the value of s must remain constant from 150 to 400^OK. The average value of m^* assuming s = 0 is $\sim$ 0.024 m_o and that assuming s = $-1/2 \sim 0.035 m_o$ corresponding to the carrier concentration of $n \sim 3.2 \times 10^{18} / cm^3$. Thus the effective mass is lower than that for the 4 mol % alloy. This indicates that the zero energy gap occurs at the 7 mol % alloy and not at the 4 mol % alloy, in agreement with the optical results. The effective mass increases with carrier concentration as for the 4 mol % alloy.
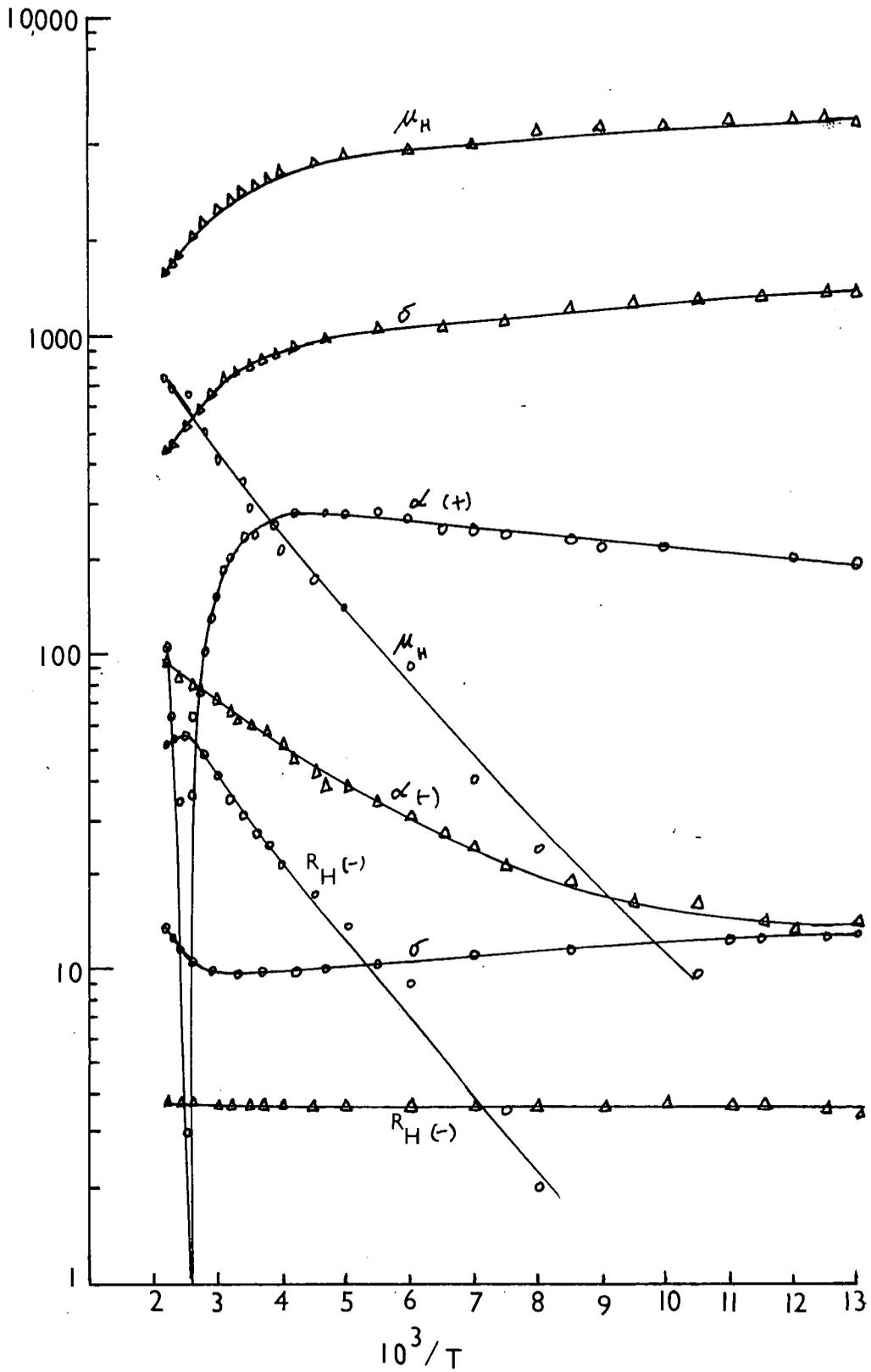
Fig .4.18 . Electrical results for 15 mol % In_2Te_3 .

o- Sample 1   Δ- Sample 2

Section 5.   15 mol % In_2Te_3

5a.   Electrical Properties and Effective Mass

The 15 mol % alloy was found to be the highest single phase composition before the two phase region between 20 - 30 mol % compositions. Therefore it was thought necessary to investigate it to see how the mobility and the effective mass change up to this composition. Fig.(4.18) shows the electrical results for sample 1 as prepared and after annealing in Hg-vapour at $300^\circ C$ for 75 hours (sample 2). In sample 1 there are two carrier effects throughout the temperature range and α changes sign at about $400^\circ K$. R_H shows a negative maximum at the same temperature. The value of the mobility ratio b obtained from the Hall maximum is$\sim$50 at $400^\circ K$. The results for the annealed sample are similar to those for the 4 and 7 mol % alloys with high carrier densities, showing guasi-metallic behaviour. The maximum value of μ is 4800 cm^2/vsec at $80^\circ K$ for a carrier density of n = 1.8 x 10^{18}/cm^3. The exponent a indicating the temperature dependence of the mobility is $\sim$ -1.45 in the temperature range 300 - $455^\circ K$ and$\sim$ -0.39 in the range 77 - $250^\circ K$. This indicates that s is constant through-out the temperature range as for the 4 and 7 mol % alloys. The electrical properties of the two samples are given in table (4.14) and the effective mass values in table (4.15).

Table (4.14)   Electrical Properties of 15 mol %

In_2Te_3 at 300 and $77^{\circ}K$

Sample	α $\mu v/^{\circ}K$	σ $ohm^{-1}cm^{-1}$	R_H cm^3/C	$\mu_H = R_H\sigma$ $cm^2/vsec$	n cm^{-3}	Remark
			$300^{\circ}K$			
1	210	9.75	-33	350	2.23×10^{17}	as grown
2	-61	760	-37	2750	1.69×10^{18}	sample 1 annealed in Hg at $300^{\circ}C$ for 75 hours
			$77^{\circ}K$			
1	190	13				
2	-14	132	-3.6	4600	1.74×10^{18}	

Table (4.15) Effective Mass Data for 15 mol % In_2Te_3

Sample	Temperature $^{\circ}K$	n/cm^3	η assuming $s=-1/2$	m^*/m_o assuming $s=-1/2$	η assuming $s = 0$	m^*/m_o assuming $s \cong 0$
2	400	1.69×10^{18}	3.2	0.043	5.2	0.028
	300	1.71×10^{18}	4.4	0.044	6.9	0.029
	150	1.76×10^{18}	11.0	0.037	16.4	0.025

The average value of m^* assuming $s = 0$ is $\sim 0.027\ m_o$ and assuming $s = -1/2$ is 0.041 corresponding to a carrier concentration of $1.72 \times 10^{18}/cm^3$. The effective mass for the 15 mol % alloy is greater than that for the 7 mol % alloy for the same carrier concentration.

5b. Magnetoresistance

The Magnetoresistance of sample 2 was measured at 77 and 300^oK. The value of $\frac{\Delta\rho}{\rho_o H^2}$ at 77^oK is $0.03\ \mu_e^2/C_1^2$ and at 300^oK $0.08\ \mu_e^2/C_1^2$. At 300^oK $\eta = 4.4$ assuming $s = -1/2$. Therefore the value of the magnetoresistance ratio $\frac{\Delta\rho}{\rho_o H^2}$ $\sim 0.05\ \mu_e^2/C_1^2$ for parabolic bands assuming $s = -1/2$. However according to Wagini (181) the magnitude of $\Delta\rho/\rho_o$ at 300^oK is nearly the same for parabolic bands assuming $s = -1/2$ or non-parabolic bands assuming $q = -2$. Therefore the agreement between theory and experiment is quite good for either of the assumptions as the error in the measurement of $\Delta\rho/\rho_o$ is $\sim 50\%$. At 77^oK the value of $\Delta\rho/\rho_o H^2$ should be $\sim 0.01\ \mu_e^2/C_1^2$ for $s = -1/2$ and parabolic bands since $\eta > 10$. Thus the experimental value seems to be higher than one would expect from theory. The magneto-Seebeck effect was too small to measure.
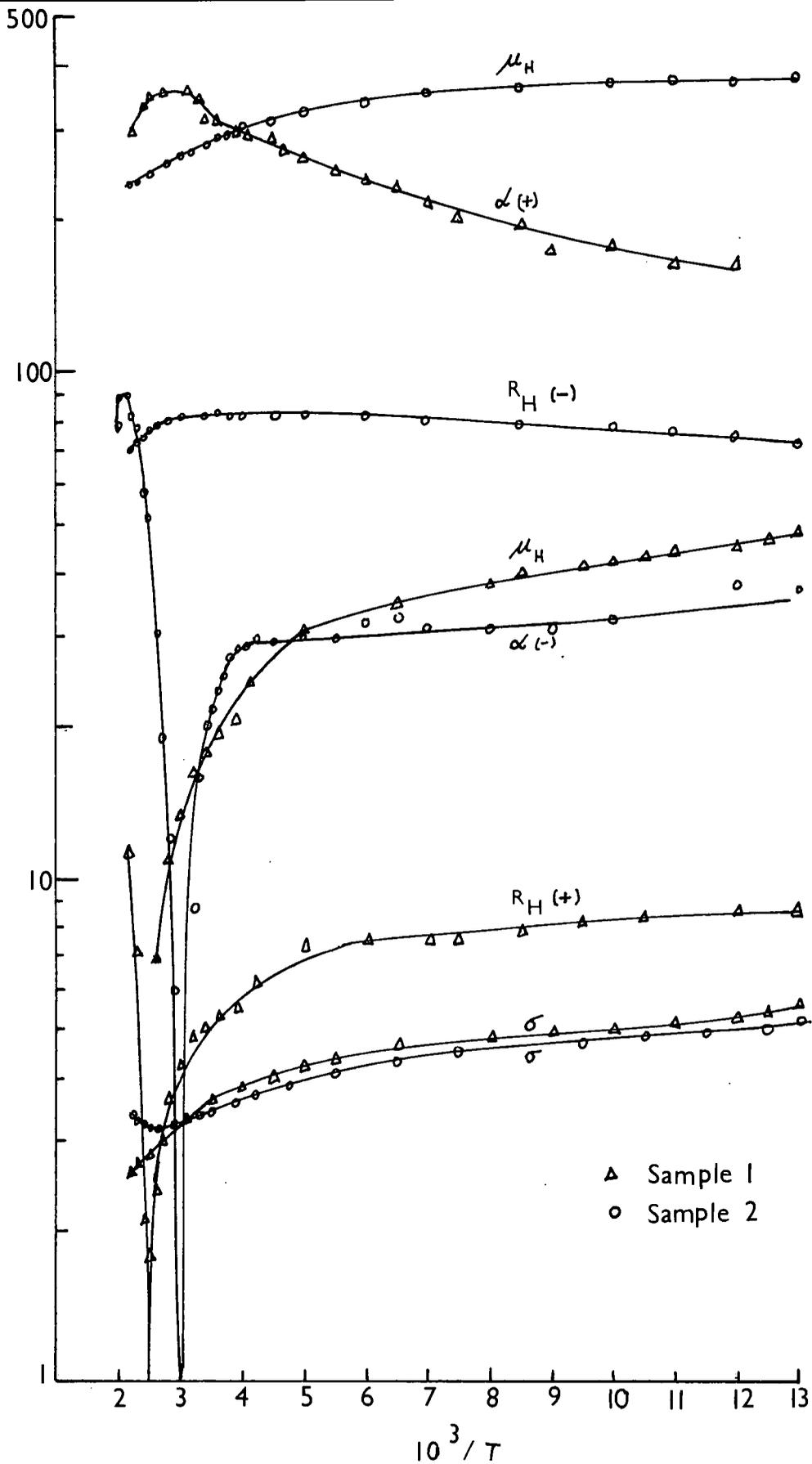
Fig. 4.19. Electrical results for 34 mol % In_2Te_3.

Section 6.   34 mol % In_2Te_3.

This was found to be the lowest single phase composition after the two phase region between 20-30 mol % In_2Te_3. It was difficult to get long ingots as they usually showed cracks. However portions sufficiently big to make samples for electrical measurements were obtained free of cracks. X-ray powder photographs showed that the composition was ordered.

Sample 1 as prepared was p-type at room temperature and sample 2 was obtained by annealing sample 1 in Hg-vapour at 200°C for 60 hours. The electrical results for the two samples are shown in fig.(4.19). Sample 1 is p-type below 450°K with a hole density of 9×10^{17} cm^{-3} at 77 - 100°K. The maximum hole mobility is 46 at 77°K. The mobility follows a $T^{-0.45}$ law below 200°K. For sample 2, R_H has become negative throughout the temperature range but α is still positive below 335°K. This indicates a large mobility ratio. R_H shows a negative maximum at 280°K and the value of b determined from it is ~ 22. The maximum values of the electron mobility are 370 cm^2/vsec at 77°K and 270 cm^2/vsec at 300°K. It was found difficult to raise the electron concentration by annealing for short periods of time. Annealing for weeks may be necessary to get high values of n. It was also noticed that annealing at higher temperatures made the samples porous probably due to decomposition at the surface.

The electrical properties at 300 and 77^OK are given in table (4.17) and the effective mass values at 150^OK assuming s = -1/2 and 0 are given in table (4.18)

Table(4.17)   Electrical Properties of 34 mol %

In$_2$Te$_3$ at 300° and 77^OK

Sample	α $\mu v/^O$K	σ ohm^{-1}cm^{-1}	R_H cm^3/C	$\mu_H = R_H\sigma$ cm^2/vsec	n or p cm^{-3}	Remark
			300^OK			
1	335	3.4	+4.9	17	1.5×10^{18}	as grown
2	15	3.4	-81.5	275	8.65×10^{17}	sample 1 annealed in Hg at 200^OC for 60 hours.
			77^OK			
1	155	5.5	8.5	47.5	8.65×10^{17}	
2	36	5.1	-71	370	1.03×10^{18}	

Table(4.18)   Effective Mass Data for 34mol% In$_2$Te$_3$

Sample	Temperature	p/cm^3	assumed s	η	m_h^*/m_o
1	150^OK	9.68×10^{17}	-1/2	-0.4	0.36
1	150^OK	9.68×10^{17}	0	+0.4	0.2

Because of low mobility it was not possible to measure either the magnetoresistance or the magneto-Seebeck effect.
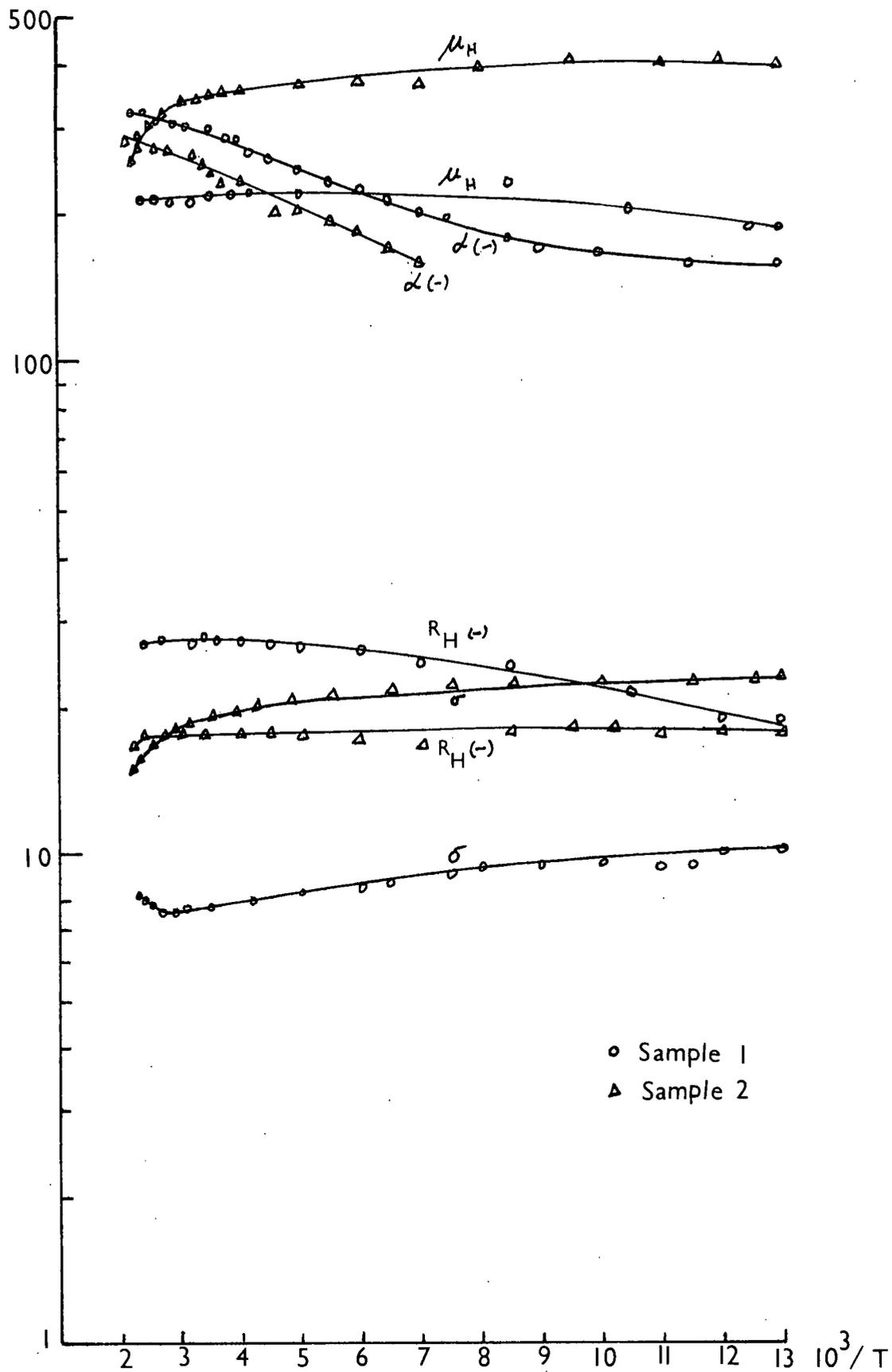
Fig. 4. 20.   Electrical   results   for   37.5   mol % In_2Te_3.

Section 7.   37.5 mol % In_2Te_3

No previous results except those of Sepncer on poly-
crystalline samples were available as the samples studied
by Lewis (107) were found to be the 7 mol % samples. The optical
results suggest that there may be a change in the band struc-
ture at the 37.5 mol % composition. Therefore it was thought
necessary to study the single crystal specimens.

Good single crystals of this single phase ordered compound
were obtained free of cracks. As prepared the samples were
wholly n-type. Fig.(4.20) shows the results for sample 1 as
prepared with $n = 3 \times 10^{17}/cm^3$ at $300^{O}K$. The maximum value
of μ_e is 310 cm^2/vsec at $200^{O}K$. Sample 1 was annealed in Hg-
vapour at $250^{O}C$ for 260 hours and the results are also shown
in fig.(4.20) . As a result of annealing R_H has become
independent of temperature from 400 to $77^{O}K$ and has reduced
in value from 27 to 18 at $300^{O}K$. σ has nearly doubled in
value. The electron mobility at $300^{O}K$ has increased from
210 to 330 cm^2/vsec and the maximum value of μ_H is 400
cm^2/vsec at $77^{O}K$.

The values of a giving the temperature dependence of the
mobility are given in table (4.19), and the electrical
properties are given in table (4.20).

Table (4.19). Values of a in $\mu_H = AT^a$

Sample	a in the range 350 - 455°K	a in the range 77 - 200°K
1	0	0.15
2	- 1.0	-0.12

Table (4.20) Electrical Properties of 37.5 mol %
In$_2$Te$_3$ at 300 and 77°K

Sample	α $\mu v/^OK$	σ $ohm^{-1}cm^{-1}$	R_H cm^3/C	$\mu_H = R_H\sigma$ $cm^2/vsec$	n cm^{-3}	Remark
			300°K			
1	−295	7.7	−27.6	215	2.68×10^{17}	as grown
2	−250	19	−17.6	340	4.18×10^{17}	sample 1 annealed in Hg for 260 hrs.at 250°C
			77°K			
1	−155	10.2	−19	185	3.87×10^{17}	
2		23	−17.7	400	4.16×10^{17}	

The values of the effective mass have been calculated
assuming s = -1/2 and 0 and are recorded in table (4.21)

Table (4.21). Effective mass data for 37.5 mol % In$_2$Te$_3$

Sample	Temper- ature ^OK	n/cm^3	η assum- ing s=−1/2	m*/m$_o$ assuming s=−1/2	η assum- ing s= 0	m*/m$_o$ assuming s=0
1	400	2.63×10^{17}	−1.5	0.103	−0.9	0.071
2	400	4.18×10^{17}	−0.95	0.10	−0.4	0.073
1	300	2.68×10^{17}	−1.3	0.122	−.0.75	0.088
2	300	4.18×10^{17}	−0.6	0.108	0	0.082
1	150	2.89×10^{17}	−0.2	0.136	+0.7	0.086
2	150	4.18×10^{17}	0.8	0.105	1.6	0.075

The average values of m* for sample 2 assuming s=0 and s=−1/2 are

0.077m$_o$ and 0.104m$_o$ respectively corresponding to the carrier
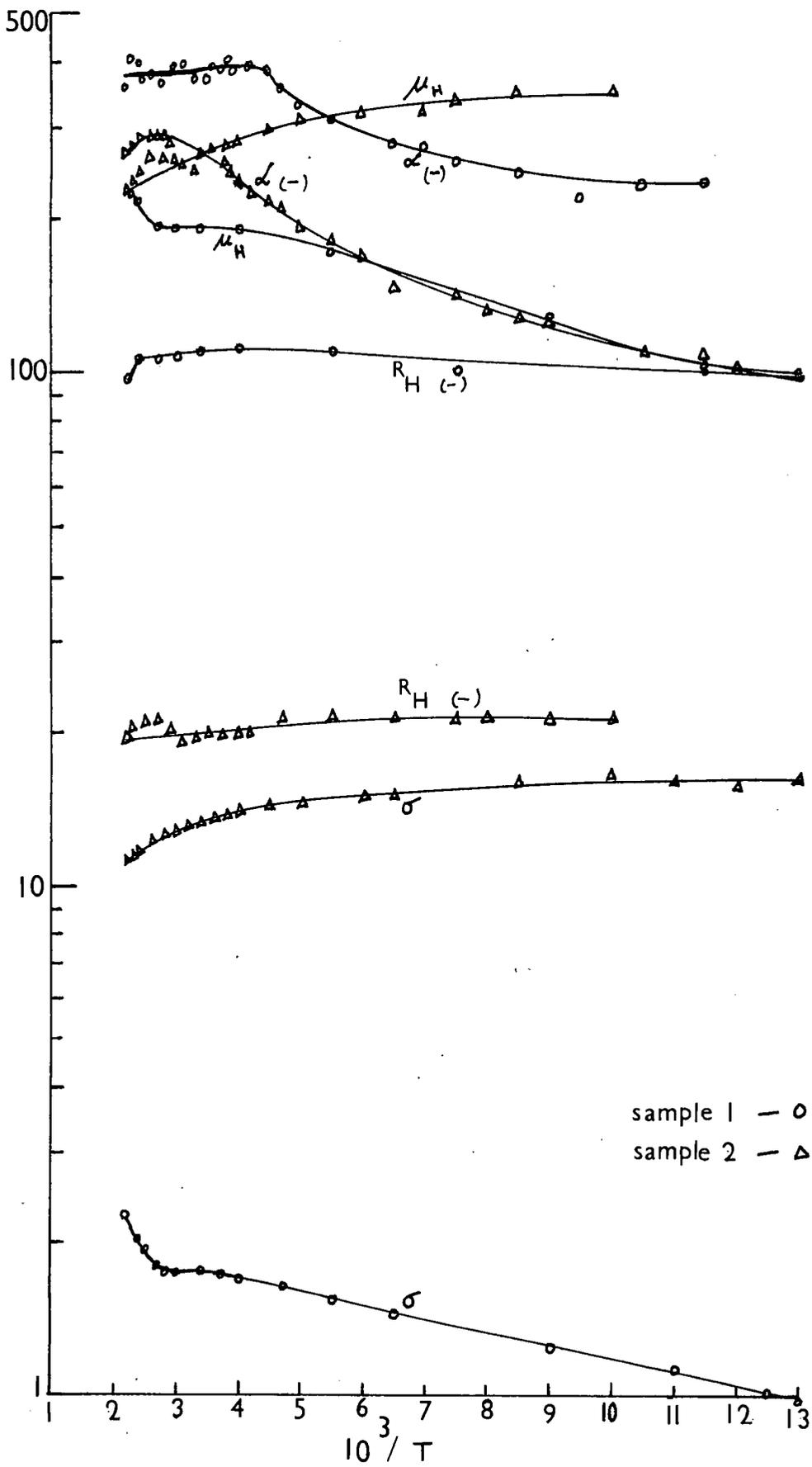
Fig. 4.21. Electrical results for 40 mol % alloy.

concentration $n \sim 4.2 \times 10^{17}$. At this composition there is no evidence to decide which of the two values is correct.

Section 8. <u>40 mol % In_2Te_3</u>

Single crystal portions big enough to produce the samples for electrical work were obtained. Sample No. 1 was wholly n-type as grown with 6.7×10^{16} carriers/cm^3. The electrical results for sample 1 are shown in fig. (4.21). The maximum mobility is 220 cm^2/vsec at 450°K. R_H does not vary much from 400 to 77°K. Sample 1 was annealed in Hg-vapour at 300°C for 500 hours (sample 2) and the results are also shown in fig.(4.21). As a result of annealing R_H has reduced by a factor of 5 and σ has increased considerably. The maximum mobility is 360 cm^2/vsec at 90°K. Both the samples are n-type extrinsic from 400 to 77°K. The exponent giving the temperature variation of the mobility is given in table (4.22) and the electrical properties are recorded in table (4.23).

Table (4.22). Values of a in $\mu_H = AT^a$ for 40 mol % In_2Te_3

Sample	a in the range 350 - 450°K	a in the range 77 - 200°K
1	$\sim$ 0	+0.68
2	-1.0	-0.23

Since the behaviour of sample 2 resembles the heavily doped
samples of the 4 and 7 mol % alloys and a is -0.23 in the
range 77 - 200°K, it may be assumed that simple geometrical
scattering is important in this temperature range and that
s ~ -1/2. However since a is + ve for sample 1, s cannot be
assumed to be -1/2 and must be > -1/2. An assumption of neutral
impurity scattering in the range 77 - 200°K would mean that
s ~ 0 for sample 2 and > 0 for sample 1.

Table (4.23) Electrical Properties of 40 mol %

In_2Te_3 at 300 and 77°K

Sample	α $\mu v/°K$	σ $ohm^{-1}cm^{-1}$	R_H cm^3/C	$\mu_H = R_H\sigma$ $cm^2/vsec$	n cm^{-3}	Remark
			300°K			
1	-390	1.75	110	190	6.69×10^{16}	as grown
2	-275	13.5	-19.8	265	3.72×10^{17}	sample 1 annealed in Hg at 300°C for 500 hrs.
			77°K			
1	-225	1...	-98	98	7.51×10^{16}	
2	-96	16	-21	336	3.5×10^{17}	

The values of the effective mass have been claculated
assuming s = -1/2 and 0 and are given in table (4.24)

Fig. 4.22. R_H & σ vs $10^3/T$ for 50 mol% alloy.

Table (4.24) Effective mass Data for 40 mol % In_2Te_3

Sample	Temperature $^{\circ}K$	n/cm^3	M assuming s = -1/2	m^*/m_o assuming s=-1/2	η assuming s= 0	m^*/m_o assuming s=0
1	400	6.88×10^{16}	-2.5	0.079	-1.95	0.056
2	400	3.77×10^{17}	-1.2	0.108	-0.6	0.076
1	300	6.69×10^{16}	-2.35	0.094	-1.9	0.075
2	300	3.72×10^{17}	-1.0	0.127	-0.45	0.092
1	150	7.0×10^{16}	-1.0	0.084	-0.4	0.053
2	150	3.45×10^{17}	1.0	0.085	1.9	0.06

The average values of m* assuming s = 0 and s = -1/2 are 0.076 m_o and 0.107 m_o respectively corresponding to a carrier density of $3.6 \times 10^{17}/cm^3$.

Section 9.   50 mol % In_2Te_3

9a.   Electrical Properties and Scattering Parameter.

The 50 mol % ordered composition studied by Lewis (107) in fact contained 1 part Hg_3, 0.94 parts In_2 and 2 parts Te_3. Moreover due to the uncertainties in the measurement of the Seebeck coefficient no values of the effective mass were reported.   Therefore this composition is thoroughly investigated.

Single crystal samples of this disordered compound were obtained.   As prepared the samples were p-type at low temperatures as shown by curve 1 fig.(4.22). R_H shows a negative maximum
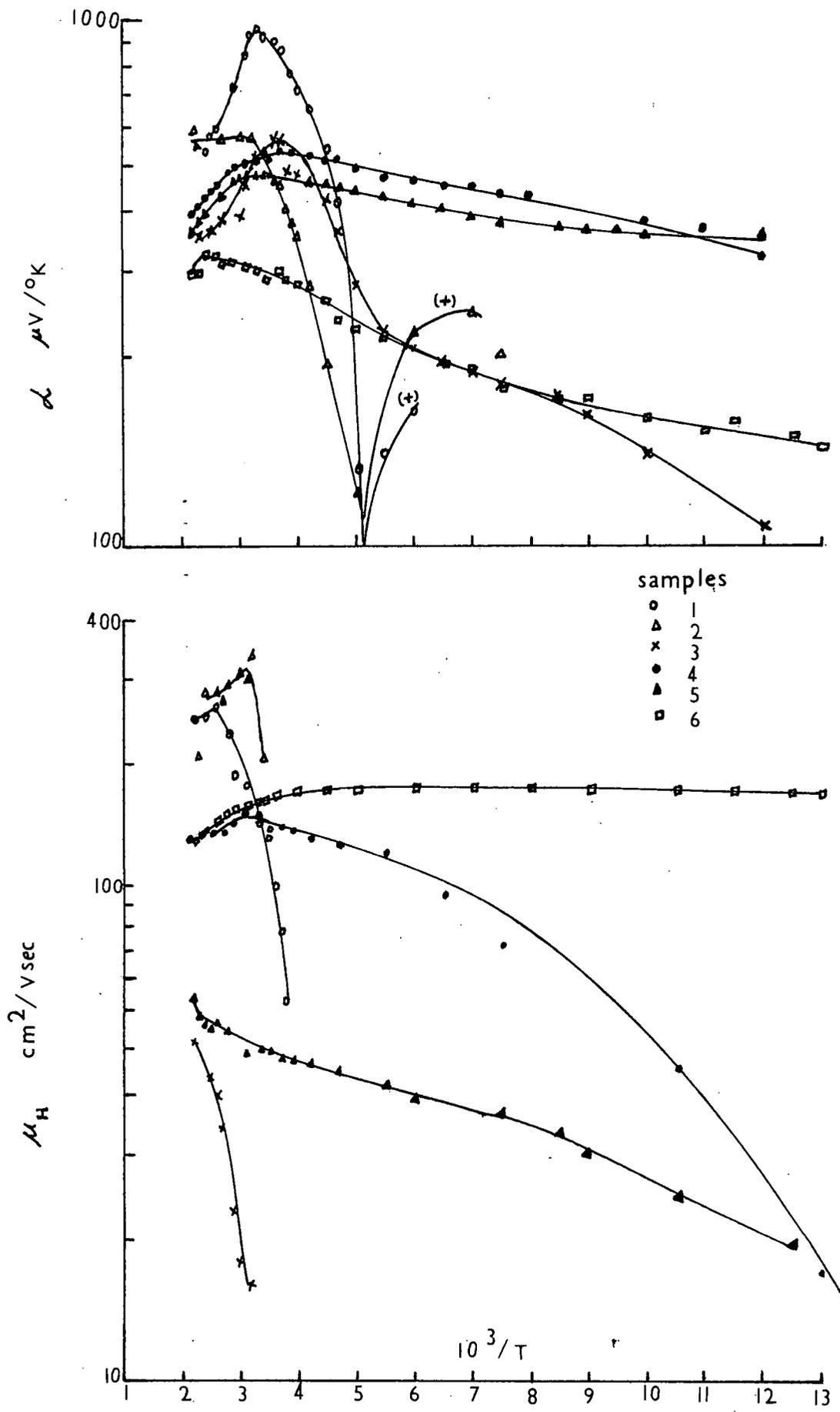
Fig. 4.23. α & μ_H vs 1/T for 50 mol % alloy.

at about 300^OK. The value of b deduced from the Hall maximum is ~ 10. The electrical conductivity σ is 10^{-3} ohm^{-1}cm^{-1} at 260^OK and rises steeply with increasing temperature due to intrinsic behavour. The high impedence of the crystals created some difficulties in the measurements but these were overcome by using indium contacts. Annealing in Hg raised the electron density at lower temperatures as shown by curves 2 - 6 in fig.(4.22). Sample 2 was obtained by annealing sample 1 in vacuum for 75 hours at 300^OC. Sample 3 was also obtained by annealing another sample in vacuum. Sample 4 was annealed in Hg-vapour at 250^OC for 50 hours. Sample 5 was obtained from sample 4 by a further anneal of 50 hours at 250^OC. Sample 6 was annealed in Hg-vapour at 300^OC for 360 hours. The variation of μ_H and α with 1/T for the six samples is shown in fig.(4.23). The values of μ_H for all samples at 300^OK are ~ 200 cm^2/vsec. The mobility increased with increasing temperature from 77^OK to room temperature for all samples except for sample 6. For sample 6 the mobility is almost constant near 200 cm^2/vsec from 77 to 200^OK. The values of mobility are higher than those reported by Spencer (132) for polycrystalline samples. The mobility ratio b for sample 1 is ~ 10 at room temperature. The electrical properties at 300 and 77^OK are given in tables (4.25) and (4.26) respectively. The values of the exponent a giving the temperature dependence of the mobility for samples 4, 5 and 6 are given in table (4.27).

Table (4.25).   Electrical Properties of 50 mol %

In$_2$Te$_3$ at 300°K

Sample	α μv/°K	σ ohm^{-1}cm^{-1}	R_H cm^3/C	$\mu_{H_2} = R_H\sigma$ cm^2/vsec	n cm^{-3}	Remarks
1	-950	2×10^{-3}	-85000	150	8.7×10^{13}	as grown
2	-540	10^{-2}	-23000	230	3.2×10^{14}	annealed in vacuum for 75 hrs. at 250°C
3	-530	4.3×10^{-3}	-3800	16	1.94×10^{15}	annealed in vacuum for 50 hrs.at 250°C
4	-510	2.05×10^{-1}	-730	152	1.0×10^{16}	annealed in Hg for 50hrs. at 250°C.
5	-475	9.4×10^{-2}	-525	50	1.40×10^{16}	sample 4 annealed in Hg for 50hrs. at250°C
6	-300	3.38	-49.2	167	1.5×10^{17}	annealed in Hg for 360hrs. at 300°C

Table (4.26).   Electrical Properties of 50 mol %

In$_2$Te$_3$at 77°K

Sample	α μv/°K	σ ohm^{-1}cm^{-1}	R_H cm^3/C	$\mu_{H_2} = R_H\sigma$ cm^2/vsec	n cm^{-3}	
1	-	-	-	-	-	
2	-170	-	-	-	-	
3	-60	2.3×10^{-4}	-	-	-	
4	-300	3.1×10^{-2}	-490	17	1.50×10^{16}	
5	-360	2.8×10^{-2}	-610	17	1.21×10^{16}	
6	-130	3.5	-49	175	1.50×10^{17}	

Table (4.27)   Values of exponent a in $\mu_H = AT^a$

for 50 mol % In_2Te_3

Sample	a in the range 300 - 455°K	a in the range 77 - 200°K
4	~ 0	1.52
Sample 5	a between 150-450°K 0.38	a between 77 - 125°K 1.52
Sample 6	a between 300 - 455°K -0.45	a between 77 - 170°K 0.06

It is seen from the table that in the temperature range 77 - 200°K a is + ve for samples 4 and 5 and ~ 0 for sample 6. This would indicate that there is a strong contribution from ionized impurity scattering for samples 4 and 5 or that there are two carrier effects present. The values of the effective mass m* calculated assuming s = 3/2 for samples 4 and 5 at 150°K are ~ 0.02 m_o which are very low considering the low mobility in this alloy. This indicates that s < 3/2. However, since a is + ve s should be > -1/2. Sample 6 resembles in behaviour the heavily doped samples of the 4 and 7 mol % alloys and since a ~ 0 in the range 77 - 200°K s should be nearer -1/2

assuming simple geometrical scattering and ~ 0 assuming neutral

impurity scattering. The values of the effective mass for

samples 4, 5 and 6 are given in table (4.28).

9b. Effective Mass and Energy Gap

Table (4.28). Effective Mass data for 50 mol % In_2Te_3

Sample	Temperature ^{o}K	n/cm^3	η assuming s=-1/2	$m*/m_o$ assuming s=-1/2	η assuming s=0	$m*/m_o$ assuming s = 0
4	400	2.68×10^{16}	-3.0	0.059	-2.5	0.042
5	400	3.34×10^{16}	-2.65	0.054	-2	0.035
6	400	1.57×10^{17}	-1.6	0.077	-1.05	0.056
4	300	1.01×10^{16}	-3.9	0.074	-3.4	0.053
5	300	1.39×10^{16}	-3.4	0.066	-2.9	0.047
6	300	1.50×10^{17}	-1.35	0.086	-0.8	0.062
4	150	9.08×10^{15}	-3.2	0.087	-2.7	0.062
5	150	1.23×10^{16}	-2.5	0.067	-2.0	0.049
6	150	1.49×10^{17}	0.2	0.071	1.1	0.046

From the table it is seen that the average values of m*

assuming s = 0 and -1/2 for sample 6 are ~ 0.055 m_o and 0.078 m_o

respectively for a carrier concentration $n \sim 1.5 \times 10^{17}/cm^3$.

The value of m* with s = 0 appears to be too low considering

the fact that the mobility ~ 200 and that m* for In_2Te_3 is

~ 0.7 m_o (140). Therefore $s \sim -1/2$ seems to be more reasonable

for sample 6. This agrees with the deduction from the
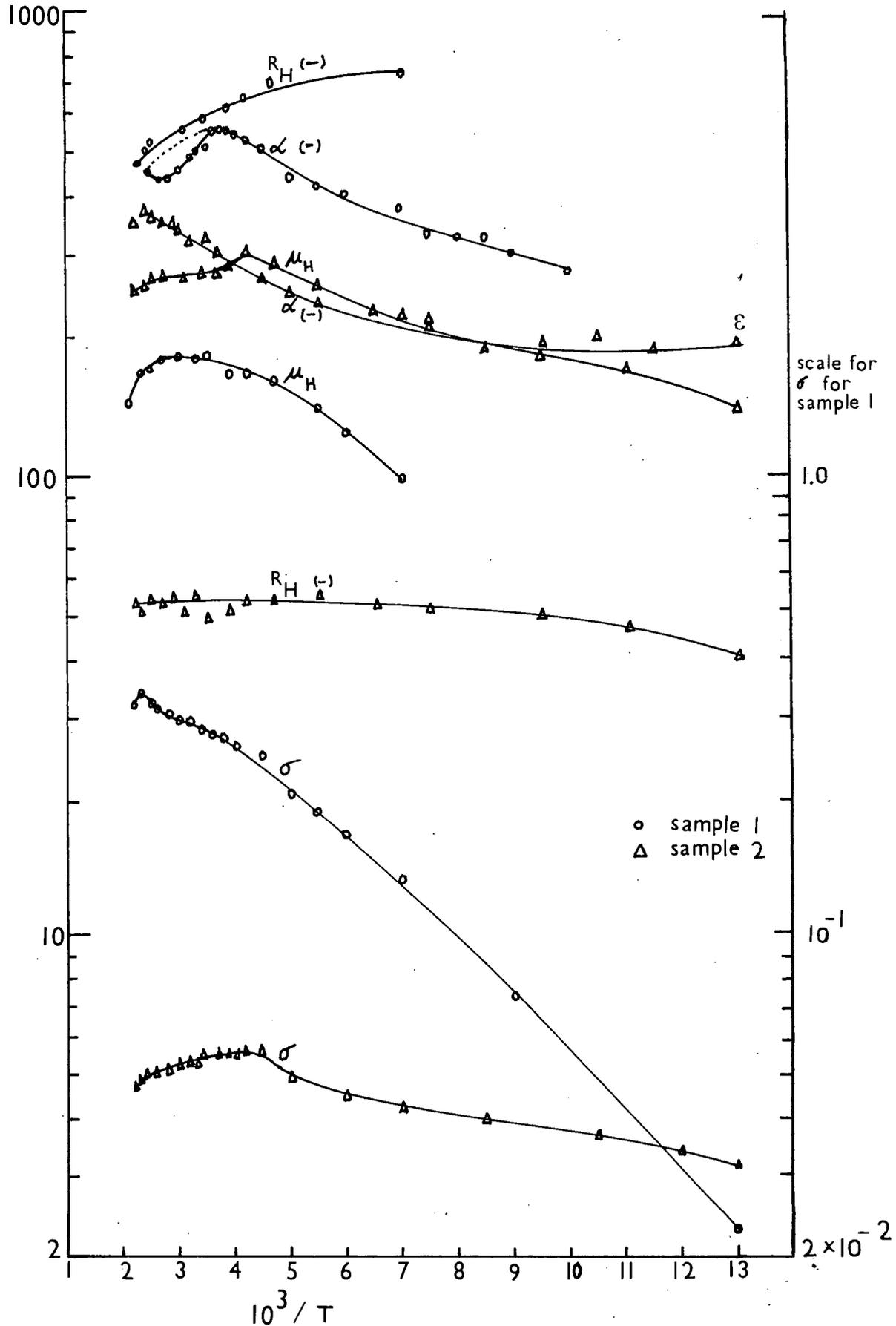
temperature variation of the mobility.

Fig. 4.24. Electrical results for 75 mol % In₂Te₃.

Samples 1, 2 and 3 are intrinsic above $300^{\circ}K$ and $\ln RT^{3/2}$ is proportional to $1/T$. The average slope corresponds with $E_g = 0.6$ ev. However the range of measurements was too samll to give accurate values. The values of R correspond with m_e^* = 0.07 m_o and $m_h^* = 0.3$ m_o. For samples 4 and 5 which have been annealed in Hg-vapour the value of E_g from $\ln RT^{3/2}$ vs $1/T$ plots is of the order of 0.22 ev. This could indicate that a deep donor level is introduced as a result of annealing in Hg-vapour.

Section 10.   75 Mol % In_2Te_3.

Only Busch et al (163) have measured the electrical properties of this ordered alloy. It was extremely difficult to prepare good single crystals as the ingot showed numerous cracks. However, two single crystal samples were obtained for electrical measurements. As grown both the samples were p-type at room temperature and had resistivity of the order of 20 Ωcm. It was difficult to measure the Hall coefficient accurately. Sample 1 was annealed in Hg-vapour for 70 hours at $300^{\circ}C$ and the electrical properties were measured. The results are shown in figure (4.24). It was difficult to measure R_H below $150^{\circ}K$. The electrical results for sample 2 which is annealed in Hg-vapour at $300^{\circ}C$ for 170 hours are also shown in fig.(4.24). It is seen that R_H is negative and almost constant in the temperature range 450 to $100^{\circ}K$. The mobility passes through a maximum at about $240^{\circ}K$ and has the value $290cm^2$/vsec, decreasing to $100cm^2$/vsec at $77^{\circ}K$. The values of a in

$\mu_H = AT^a$ are given in table (4.29) and the electrical properties at 300 and 77^OK are given in table (4.30).

Table (4.29). Value of a in $\mu_H = AT^a$ for

75 mol % In_2Te_3

Sample	a between 400 – 455°K	a between 77 – 200°K	Remark
1	–1.35	1.15	Two carrier effects at low temperatures

Sample	a between 300 – 455°K		a between 77 – 200°K
2	–0.22		0.6

From table (4.29) it appears that the value of s is ~ –1/2 for sample 1 at high temperatures. Since a is 0.6 for sample 2 in the range 77 – 200°K the assumption of simple geometrical scattering in this temperature range would indicate that s>–1/2 and the assumption of neutral impurity scattering would indicate that s > 0. The values of m* calculated assuming different values of s are given in table (4.31)

Table (4.30). Electrical properties of 75 mol %

In$_2$Te$_3$ at 300 and 77°k

Sample	α $\mu v/^OK$	σ ohm^{-1}cm^{-1}	R_H cm^3/C	$\mu H = R_H\sigma$ cm^2/vsec	n cm^{-3}	Remark
			300°K			
1	−500	0.29	−575	180	1.27x10^{16}	annealed in Hg for 70 hrs. at 300°C
2	−280	5.3	−53	330	1.39x10^{17}	annealed in Hg for 170 hrs. at 300°C.
			77°K			
1		2.3x10^{-2}				
2	−180	3.2	−41	140	1.79x10^{17}	

Table (4.31) Effective Mass Data for 75 mol % In$_2$Te$_3$.

Sample	Temperature^{O}K	n/cm^3	η assuming s=−1/2	m*/m$_o$ assuming s=−1/2	η assuming s=0	m*/m$_o$ assuming s=0
1	400	1.46x10^{16}	−3.8	0.06	−3.25	0.046
2	400	1.40x10^{17}	−2.1	0.098	−1.6	0.072
1	300	1.27x10^{16}	−3.8	0.085	−3.3	0.058
2	300	1.39x10^{17}	−1.75	0.104	−1.2	0.074
2	150	1.41x10^{17}	−0.4	0.091	+0.3	0.065

The average values of m* assuming s = 0 and s = −1/2 for sample 2 are 0.07m$_o$ and 0.098 respectively for a carrier concentration of 1.4x10^{17}/cm^3. It is not possible to get an accurate estimate of the value of s.

Section 11. Conclusions

11a. O - 15 mol % In$_2$Te$_3$ alloys

Annealing in Hg-vapour at 250 - 300°C appears to make HgTe more p-type. This agrees with the findings of Lewis (107) but is contrary to the results of Giriat and other workers. It is difficult to give any definite explanation for this result.

The effect of annealing in Hg-vapour on the alloys is to increase the electron concentration and make them more n-type. Annealing times of the order of a few days are sufficient to raise the carrier density by an order of magnitude. This indicates that mercury diffuses fairly rapidly into these low percentage alloys.

The room temperature mobiliy reduces from about 20000 cm^2/vsec for HgTe to $\sim$ 3000 cm^2/vsec for the 15 mol % alloy. For heavily doped samples the mobility decreases as 1/n and is almost independent of temperature in the temperature range 77 - 200°K. This indicates that the simple theory of geometrical scattering proposed by Allgaier and Houston (184) is applicable and that s$\sim$-1/2. To be consistent with this s should also have the value -1/2 in the temperature range 300 - 455°K for HgTe and all the low percentage alloys. The magnetoresistance and magneto-Seebeck results for the 4 and 15 mol % alloys also indicate that s$\sim$-1/2 provided it is assumed that the non-parabolicity does not have an appreciable effect. Thus it seems that acoustic lattice scattering is dominant in the temperature range 300 - 455°K.

The average values of the effective mass for HgTe, 4, 7 and 15 mol % alloys assuming s = -1/2 are as follows:

	m^*/m_o	n/cm^3
HgTe	0.03	4.7×10^{17}
4%	0.04	2.5×10^{18}
7%	0.035	3.2×10^{18}
15%	0.041	1.7×10^{18}

Though the effective mass obtained in this thesis is the density of states mass it should not be very different from the effective mass at the Fermi energy as in most cases $\eta > 1$. However, the HgTe samples were partially degenerate and the average value of m^*/m_o given above should be smaller than the actual value as that obtained from magneto-reflection and reflectivity measurements. Considering this it can be concluded that the lowest effective mass for the same carrier concentration occurs at the 7 mol % composition and not at the 4 mol % composition as suggested by Wright (112).

The effective mass for the 4 and 7 mol % alloys increases with carrier concentration indicating that the conduction band is non-parabolic. Rough indication that Kane's theory may be applicable is obtained.

Since there is no drastic change in any property from HgTe to the 15 mol % alloy it can be safely concluded that the HgTe band structure continues up to at least the 15 mol % alloy.

11b. 34 - 75 mol % In_2Te_3 alloys.

As prepared the 37.5 and 40 mol % alloys were n-type and
the 34, 50 and 75 mol % alloys were p-type. Annealing in Hg-
vapour at 250 - 300°C makes these alloys more n-type. However
it is found that the rate of diffusion of mercury in these alloys
is very slow and that annealing times of the order of weeks are
necessary to obtain high carrier densities. The electron mobility
in these alloys is of the order of 200 - 300 cm^2/vsec and does
not seem to reduce rapidly with the addition of more In_2Te_3.
Ordering in the 34, 37.5 and 40 mol % alloys does not appear
to increase the mobility above the general trend. This
contradicts Spencer's findings. The maximum hole mobility in
the 34 mol % composition is ∼ 50 cm^2/vsec and the mobility ratio
is ∼ 20. In general the values of mobility obtained in this
thesis for single crystal samples are higher than those obtained
by Spencer (132) for polycrystalline material.

The simple theory of geometrical scattering seems to hold
good for the heavily doped samples in the temperature range
77 - 200°K. However it was not possible to obtain very high
carrier concentrations by annealing in Hg-vapour. Therefore s may
be > -1/2 in many cases. The value of s in the temperature
range 300 - 455°K also appears to be ∼ -1/2. Assumption of a
different value gives strong variation of m^* with T. The
average values of the effective mass assuming s = -1/2 are
given below

% alloy	m^*/m_o	p or n/cm^3
34	0.36 (hole)	$9 \times 68 \times 10^{17}$
37.5	0.104	4.2×10^{17}
40	0.107	3.7×10^{17}
50	0.078	1.5×10^{17}
75	0.098	1.4×10^{17}

The values of m^*/m_o are not the values at the Fermi energy as $\eta < 0$ in most of the cases. Therefore these values represent the average values of the effective mass and should be smaller than the values at the Fermi level. The effective mass for In_2Te_3 obtained by Zhuze et al from electrical data is $\sim 0.7\ m_o$.

The low mobility and high effective mass of these alloys as compared to the 0 - 15 mol % alloys might indicate that there is a change in the band structure at the 34 - 37.5 mol % composition and that a heavy mass band has moved below Γ_6 at this composition as suggested by Wright (112).

It was found that indium fused contacts were ohmic and non-injecting. However it was not possible to observe any negative resistance effect in the 37.5, 40 or 50 mol % alloys at room or liquid nitrogen temperature with fields ~ 1000 V/cm.

CHAPTER   5:

OPTICAL PROPERTIES OF $Hg_3Te_3-In_2Te_3$

ALLOY SYSTEM

Introduction

All the work reported earlier on optical absorption in the $Hg_3Te_3-In_2Te_3$ alloys had been carried out on polycrystalline samples. Therefore it was thought necessary to investigate the energy gap of single crystal alloys. No photoconductivity measurements on these alloys have been reported so far, so it was decided to study the spectral response of photoconductivity and to get an idea of the energy gap.

Section 1.

1a. Optical Absorption

Transmission measurements were carried out on single crystal samples of 10, 15, 20, 30, 34, 37.5, 40,50 and 75 mol % In_2Te_3 alloys. At least two samples of different thickness were used for compositions more than 15 mol % In_2Te_3 in order to correct for reflection. From equation (1.125), the transmission coefficients T_1 and T_2 for the two samples are

$$T_1 = (1 - R^2) \exp(-Kd_1) \left.\begin{array}{c} \\ \\ \\ \end{array}\right\}$$

$$T_2 = (1 - R^2) \exp(-Kd_2) \quad (5.1)$$

assuming that reflectivity R is the same for both the samples,
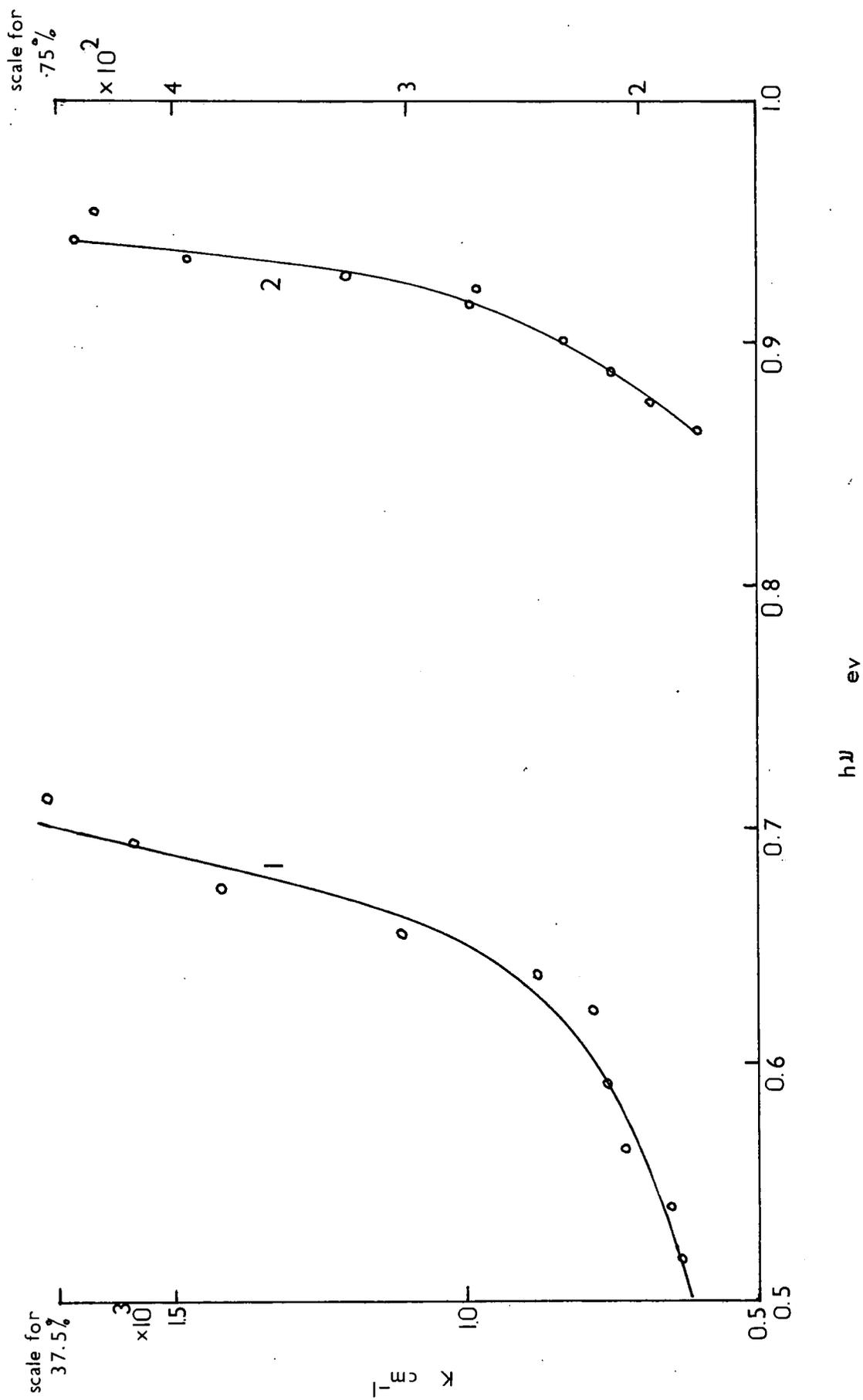
Fig. 5.1. k vs hν for 1) 37.5 and 2) 75 mol% In_2Te_3
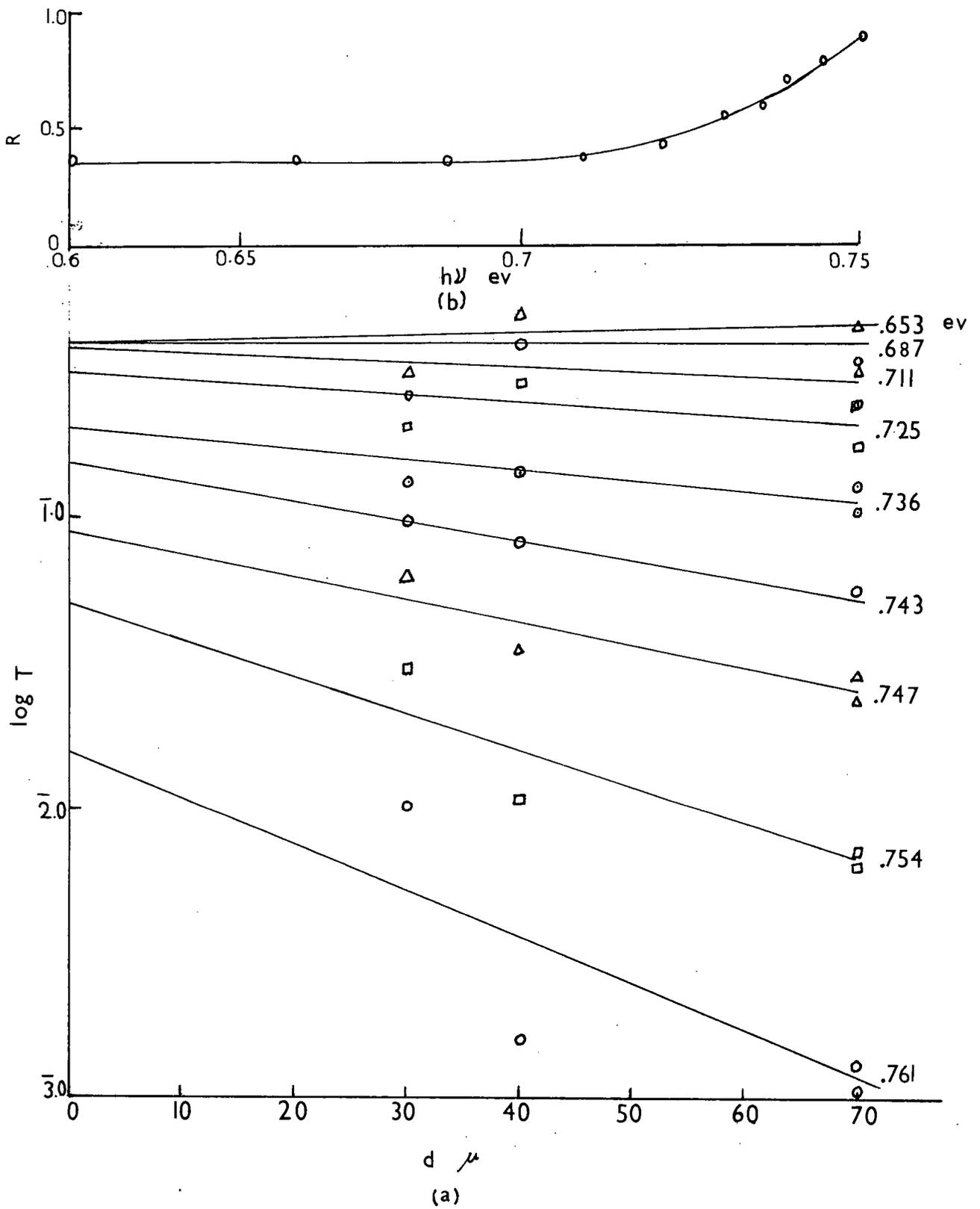
Fig. 5.2. a) Variation of transmission with thickness for 50 % samples.
b) Variation of reflectivity for 50 mol % alloy.

Fig. 5.3. K^2 vs $h\nu$ for 1) 10 & 2) 15 mol % In_2Te_3.

Fig. 5.4. K^2 vs hν for 1) 20 & 2)30 mol % In_2Te_3.

Fig. 5.5. K^2 vs $h\nu$ for 1) 34, 2) 37.5, & 3) 40 mol % In_2Te_3.
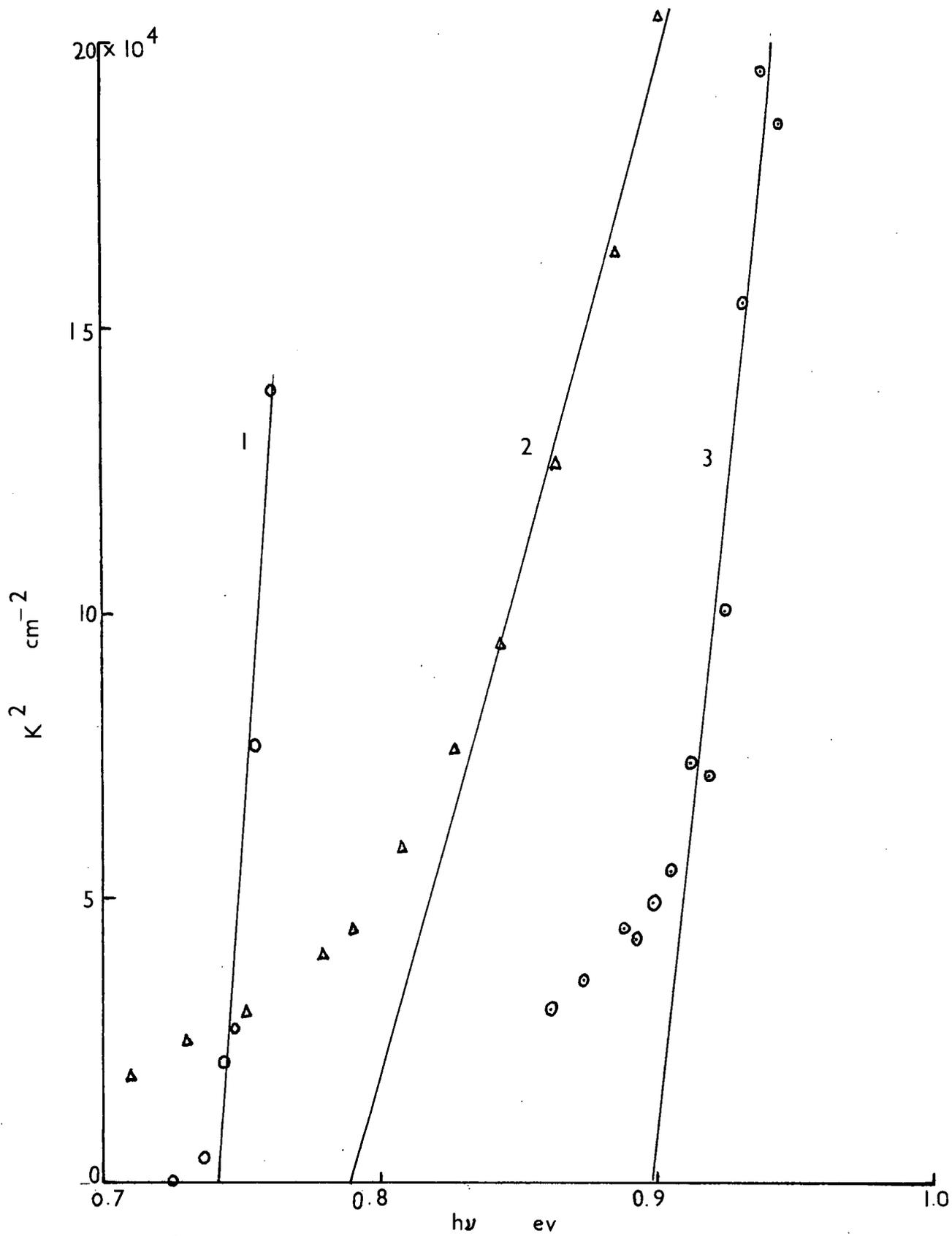
Fig. 5.6. K^2 vs $h\nu$ for 1) 50 % disordered , 2) 50 % ordered , & 3) 75 % alloys.

which is a reasonable supposition. The reflectivity R can thus be eliminated giving

$$K = \frac{\ln T_2 - \ln T_1}{(d_1 - d_2)} \qquad (5.2)$$

Typical plots of k vs hν for the 37.5 and 75 mol % alloys are shown in fig.(5.1).

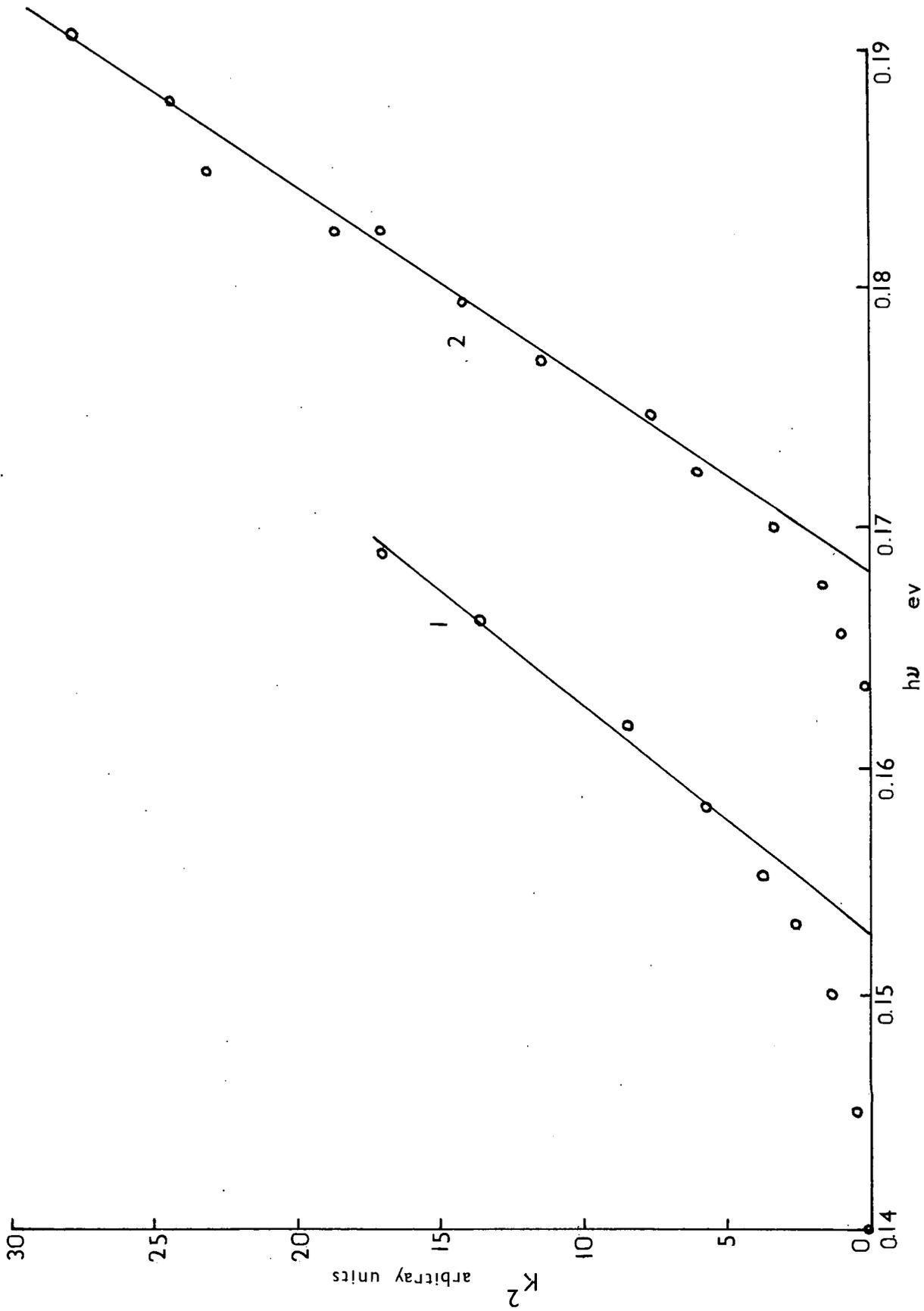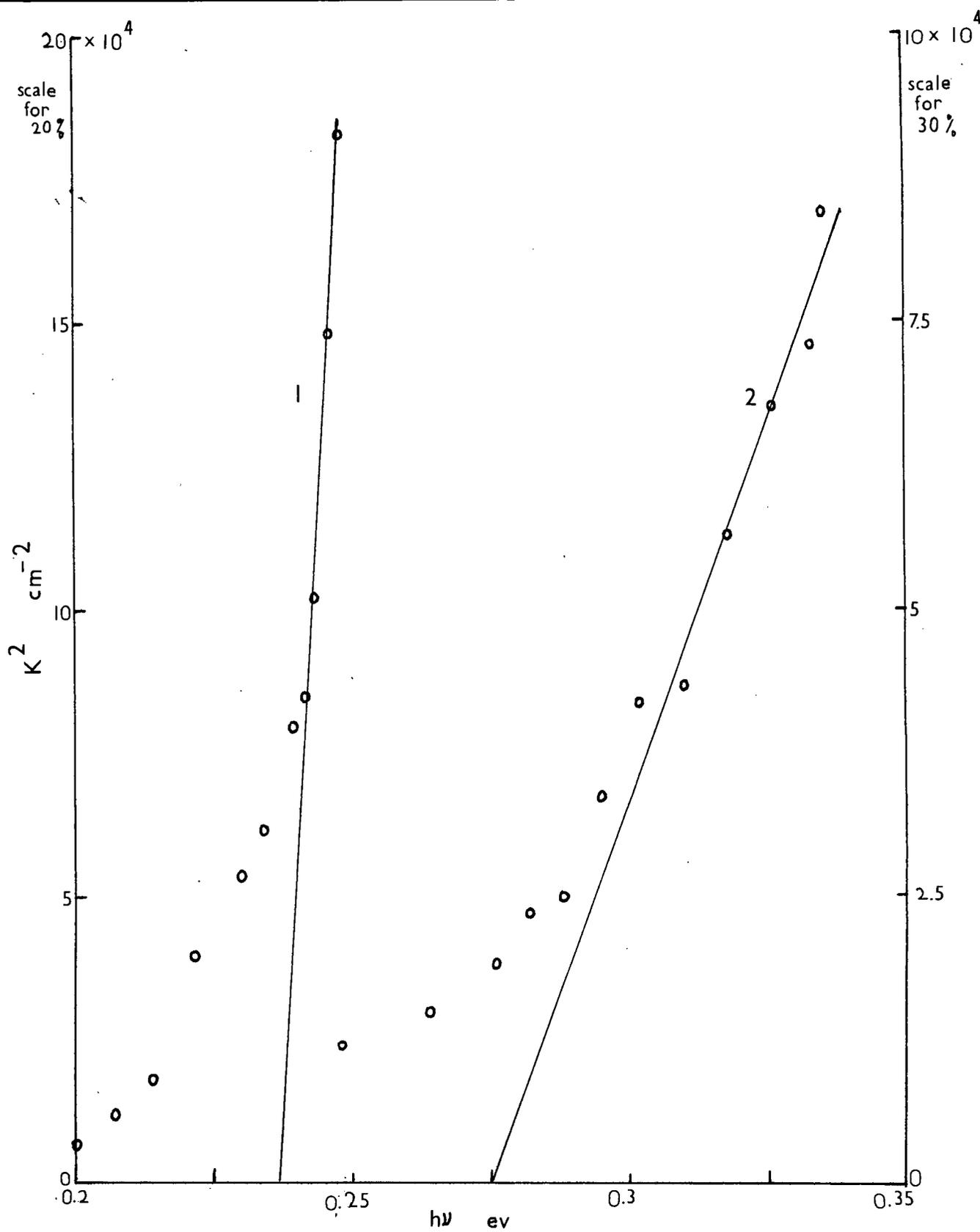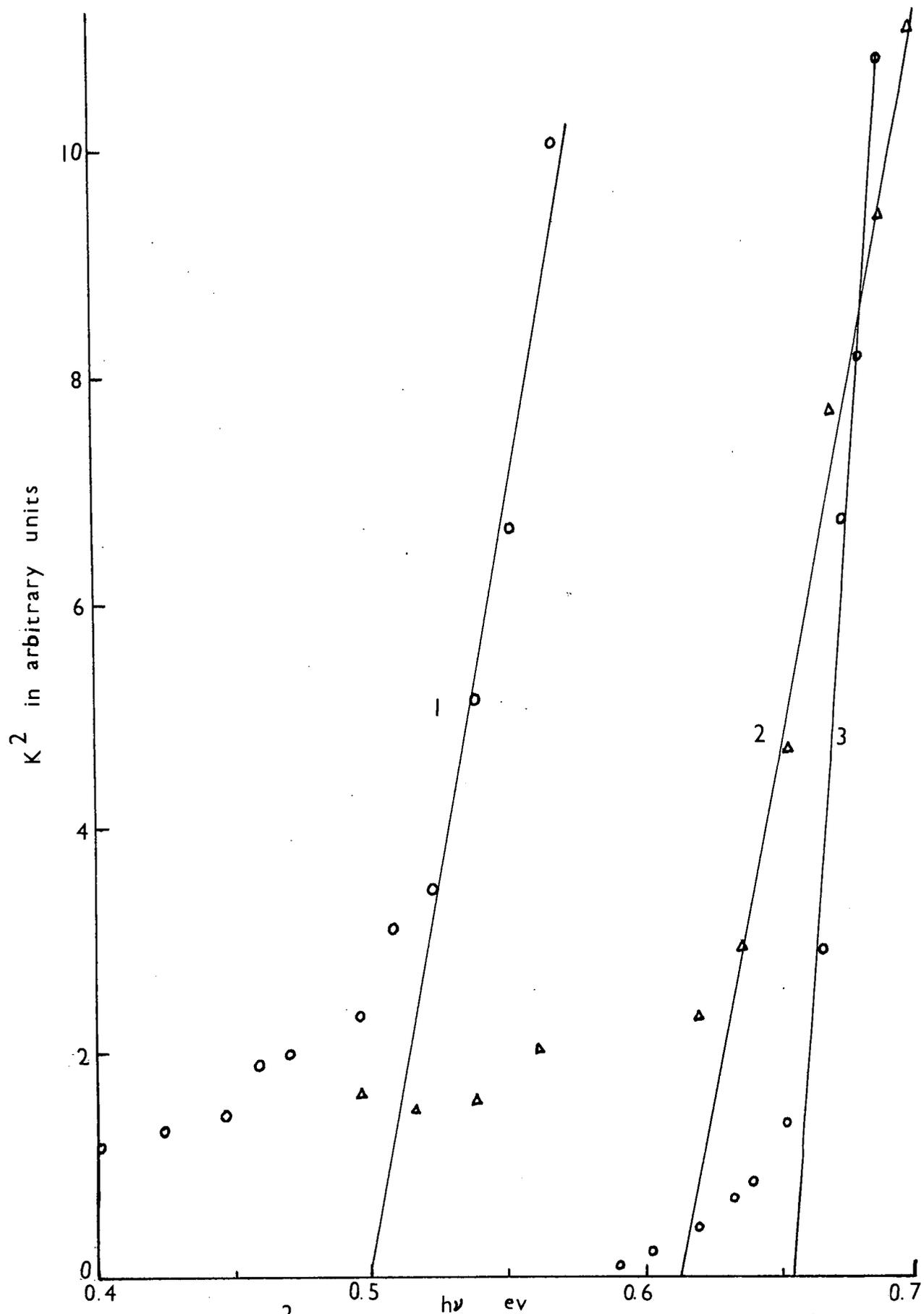The reflectivity can also be determined, and more accurately, if transmission measurements have been carried out on more samples of the same alloy. Plots of ln T vs d at different wavelengths would then give straight lines with intercepts $2\ln(1-R)$ on the ln T axis. This is shown in fig.(5.2) for four samples of the 50 mol % alloy. Fig.(5.2) also shows the reflectivity thus obtained. As expected the reflectivity increases as the absorption coefficient increases near the absorption edge.

The plots of K^2 vs hν for the 10, 15 and 20, 30 mol % alloys are shown in fig.(5.3) and (5.4) respectively. The 20 and 30 mol % alloys, which are two phase, show noticeable tails on the long wavelength side of the absorption edge. It is seen from the figure that good straight lines can be drawn through the experimental points at higher energies indicating direct (allowed) transitions according to equation (1.135) chapter 1.

The K^2 vs hν plots for the 34, 37.5 and 40 mol % alloys are shown in fig.(5.5) and for the 50 and 75 mol % alloys are shown in fig.(5.6). Fig. (5.6) also shows the plot for the ordered 50 mol % sample (Lewis and Wright). Good straight

lines can again be drawn through the experimental points at high energies. The ordered 37.5, 50 and 75 mol % samples all show noticeable tails on the long wave-length side whereas absorption seems to rise sharply near the edge for the disordered 50 mol % alloy as for the single phase alloys 10, and 15 mol % In_2Te_3. An attempt was made to check whether indirect transitions were responsible for the tails in the 20, 37.5 and the ordered 50 mol % alloys by plotting $\left[h\nu K_T(\Delta E - h\nu)^2 \right]^{1/x}$ (x = 2 or 3) against $h\nu$ as discussed in chapter 1, part II, section 1e. However, straight line portions indicating indirect energy gap could not be obtained in any case. Spencer (1,32) had noticed the presence of an indirect gap at 0.58 eV in the 37.5 mol % alloy.

The values of the direct energy gaps determined from the intercepts of the straight line portions on the energy axis are given in table (5.1), together with the values of the lattice parameters determined from X-ray powder photographs.

Table (5.1)   Energy Gap and Lattice Parameter of

Hg_3Te_3-In_2Te_3 Alloys.

Composition % In_2Te_3	Lattice Parameter a_o in Å	Energy Gap eV
0	6.461	-0.08 by extrapolation
4	6.458	---
7	6.441	---
10	6.428	0.15
15	6.423	0.17
20	6.408 6.356	0.24
30	6.354	0.26
34	6.343	0.5
37.5	6.339	0.61
40	6.330	0.65
50	6.305	0.74
50 ordered	6.30	0.78
75	6.226	0.87

It is seen from the table that ordered 50 mol % sample shows

a much bigger energy gap than the disordered alloy.

The effect of annealing in vacuum and in Hg-vapour on the

absorption edge was investigated in the 50% alloy. It was

found that there is no detectable change in the energy gap due

to annealing either in vacuum or in mercury. This is in con-

formity with the observation that there is no noticeable change

in the lattice parameter as a result of annealing.

1b.   Variation of Energy Gap with Lattice Parameter

and Composition.

The variation of the direct energy gap with lattice param-
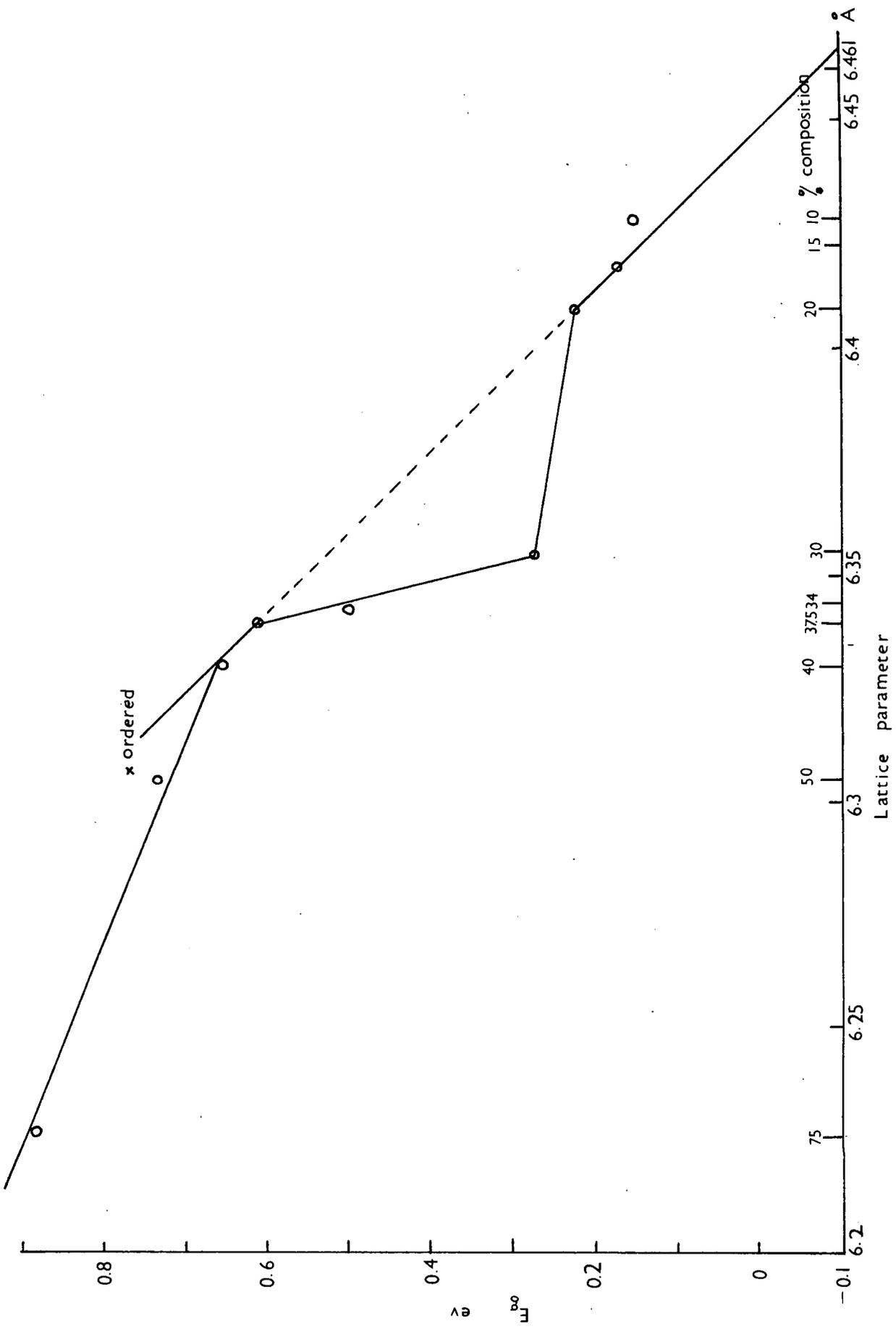
Fig.5.7. Variation of E_g with lattice parameter and composition.

eter and composition is shown in fig.(5.7). It is seen
from the figure that there is a plateau between 20 and 30
mol % In_2Te_3 at about 0.25 eV. This corresponds to the
two phase region and agrees with the findings of Spencer (132).
However the values of energy gap obtained in this thesis are
slightly lower than those reported by Spencer. This might
be due either to a difference between single crystal and
polycrystalline samples or to the different method of analysing
the results. A straight line can be drawn through the points
for single phase alloys from 0 to the 37.5 mol % composition.
The points corresponding to the two-phase alloys in the range
20 to 30 mol % In_2Te_3 are off the line. This indicates that
the direct energy gap varies linearly from 0 to 15 mol % In_2Te_3
and from 30 to 37.5 mol % composition extending in fact to
40 mol % In_2Te_3, confirming Wright's conclusions (112). For
higher percentages of In_2Te_3 the energy gap increases less
steeply with lattice parameter, which could indicate a change
in the band-structure at about 40 mol % In_2Te_3. The value of
E_g for HgTe obtained by extrapolation is - 0.08 eV, correspond-
ing to the lattice parameter of 6.461 Å.

Section 2.   <u>Spectral Response of Photoconductivity</u>

It was possible to measure the photoconductivity of high
resistivity samples only. Therefore measurements were carried
out on 37.5, 40, 50 and 75 mol % alloys. The spectral response
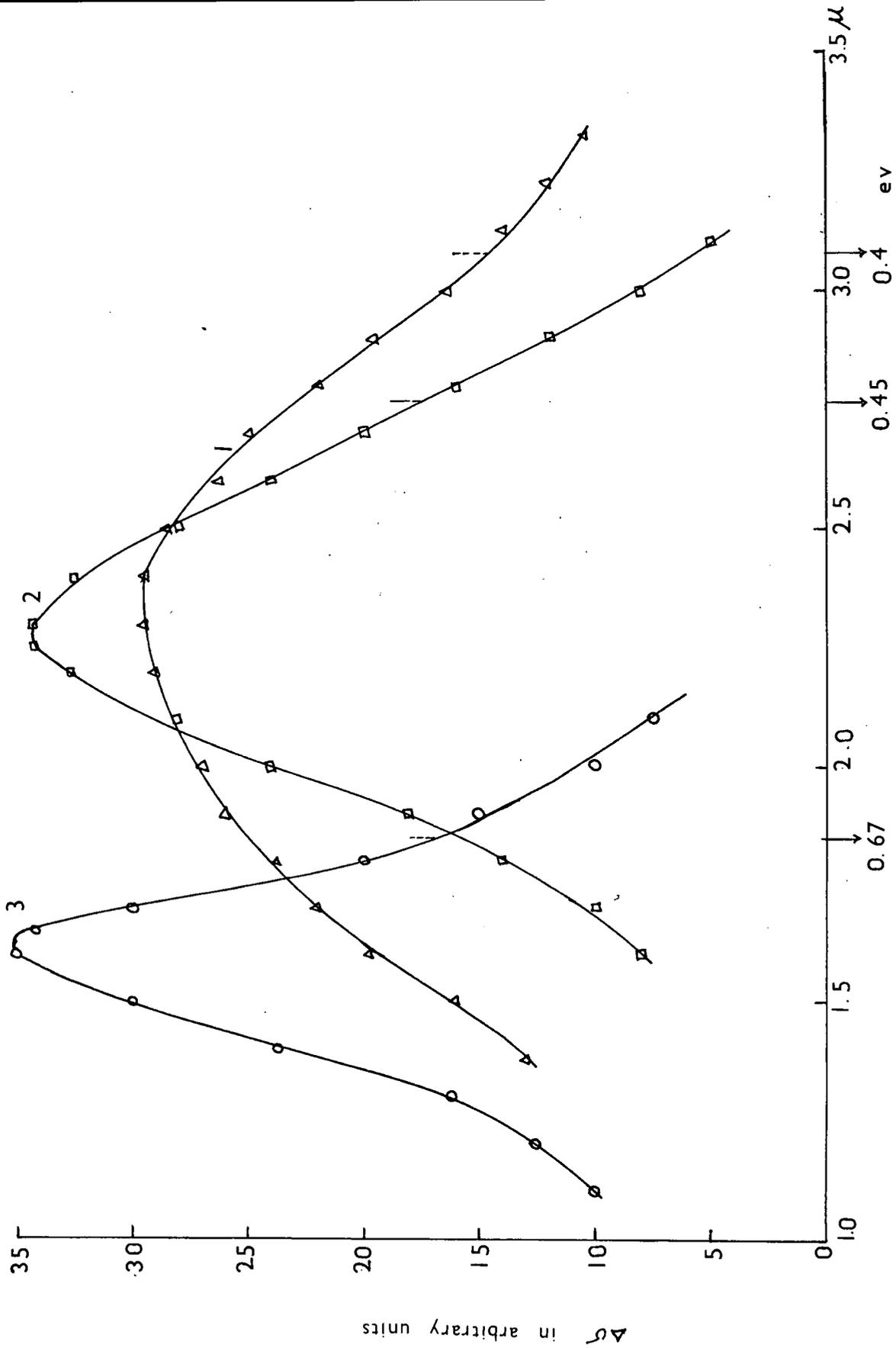curves for the 37.5, 40 and 75 mol % compositions are shown in

Fig. 5.8. Spectral response of photoconductivity for 1) 37.5 , 2) 40, &3)75 mol % In₂Te₃.

Fig.5.9. Spectral response of photoconductivity for 50 mol % In_2Te_3
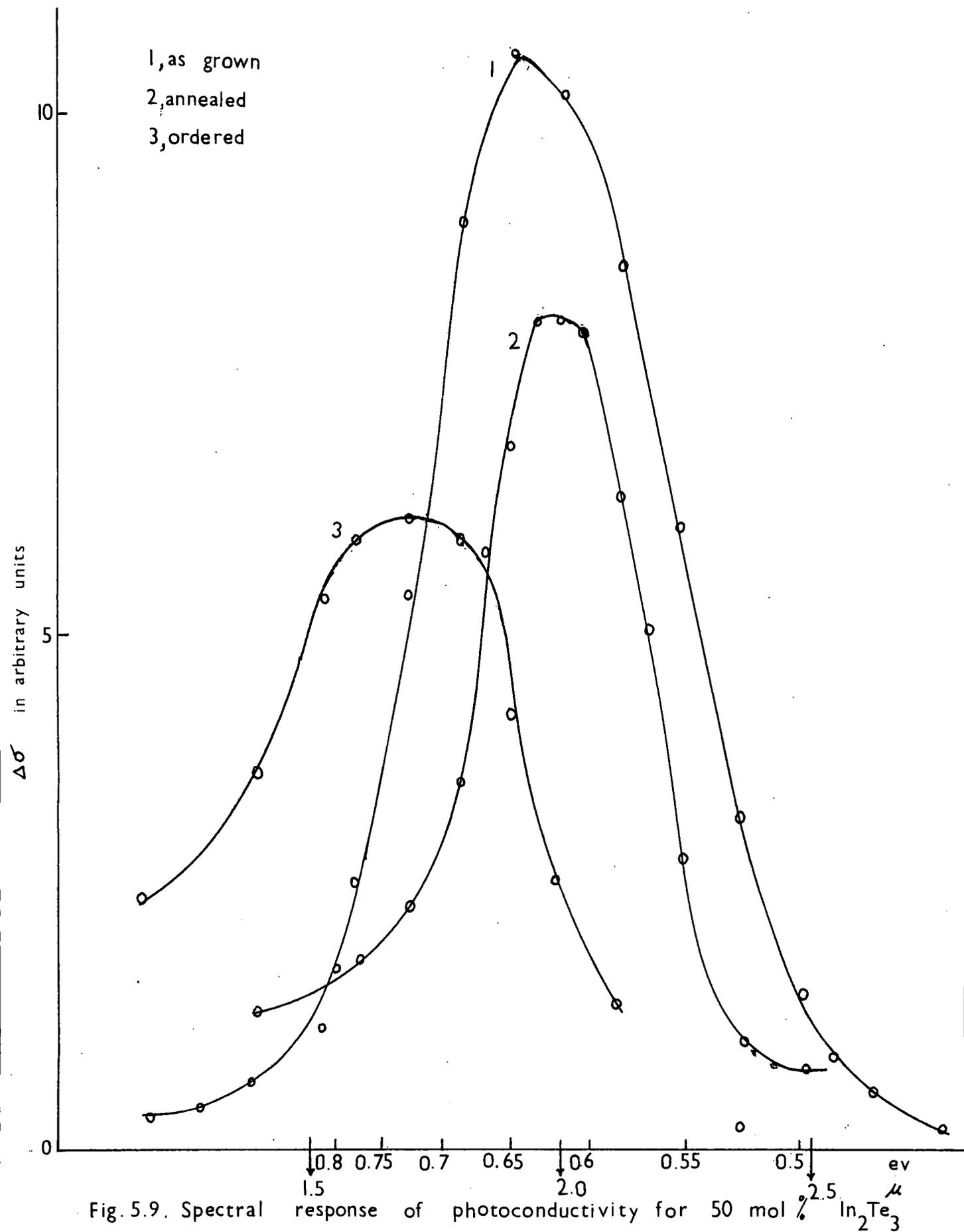
fig.(5.8). The positions of maxima occur at 0.52, 0.55 and 0.78 eV respectively and the $\lambda 1/2$ points are at 0.4, 0.45 and 0.67 eV respectively.

The spectral response curves for the 50 mol % disordered and ordered (Lewis and Wright) samples are shown in fig.(5.9). The effect of annealing in vacuum or in Hg-vapour at 300°C for 75 hours was also determined and the curve for the annealed sample is also shown in fig(5.9). It is seen from the figure that annealing in either vacuum or mercury has little effect on the position of the peak. The unannealed sample shows a maximum at 0.65 eV with a $\lambda 1/2$ point on the long wavelength side at 0.55 eV. The ordered sample (curve 3) shows a maximum near 0.73 eV and the $\lambda 1/2$ point at 0.65 eV. Thus the ordered 50 mol % alloy shows a larger energy gap in conformity with the results obtained from absorption measurements.

In each case the photoconductivity threshold occurs at appreciably lower energy than the main absorption edge. This type of behaviour has been observed in In_2Te_3 and Mg_2Sn as mentioned before.

Section 3. Conclusions

There is a linear variation of the optical energy gap with lattice parameter for the single phase alloys up to at least the 37.5 mol % composition. The optical gap for the two phase region between 20 - 30 mol % In_2Te_3 shows a plateau at ~ 0.25 eV confirming Spencer's work (132). However the values of the energy gap

obtained in this thesis are slightly lower than those obtained by Spencer for polycrystalline material. The second plateau between 40 and 50 mol % In_2Te_3 observed by Spencer was not noticed.

The linear variation of the energy gap indicates that the HgTe band structure continues at least up to 37.5 mol % composition thus supporting the evidence from electrical work. The break in the curve at about 40 mol % In_2Te_3 may indicate a change in the band structure as indicated by the electrical properties.

The energy gap for the ordered 50 mol % alloy is greater than that for the disordered alloy, which could mean that ordering increases the energy gap above the general trend. However it was not possible to verify it in the case of the 34, 37.5 and 40 mol % alloys because these compositions could not be obtained in the disordered form.

The value of E_g for HgTe obtained by extrapolation of the results for the single phase alloys from 40 to 10 mol % In_2Te_3 is -0.08 eV. corresponding to the lattice parameter of 6.461 Å.

The values of E_g obtained from photoconductivity measurements are lower than those obtained from absorption measurements. Since the plots of K^2 vs $h\nu$ for the alloys investigated for photoconductivity show a prominent tail on the long wavelength side with the exception of the disordered 50 mol % alloy, according to de Vore(70) one would expect the photoconductivity threshold to shift towards the long-wavelength side due to aborp-

tion in the tail. The shift in the case of the disordered 50

mol % alloy could be due to the scattering of light as indicated

by the reflectivity plot.

R E F E R E N C E S

1. Ioffe A.F., Physics of Semiconductors, p.139 (1957).

2. Smith R.A., Semiconductors p.59 (1961).

3. Kroger F.A., and Vink H.J., Solid State Physics Vol 3, p.321 (1956).

4. Blakemore J., Semiconductor Statistics, p.17 (1962).

5. Ziman J.M., Principles of the Theory of Solids, p.20 (1964).

6. Olsen J.L., Electron Transport in Metals, p.12 (1962).

7. Smith R.A., Semiconductors, p.31 (1961).

8. Kutasov V.A., Thermoelectric Properties of Semiconductors, p.10 (1964).

9. Sosnowski L., Proc. Int. Conf. Physics of Semiconductors, Paris, p.34 (1964).

10. Ziman J.M. Principles of the Theory of Solids, p.99 (1964).

11. Kane E.O., J.Phys. Chem.Solids, 24, 249 (1957).

12. Wright G.B., Strauss A.J., and Harman T.C., Phys. Rev., 125, 1534 (1962).

13. Varie C. and De Camps, Phys. Stat. Sol., 9, 797 (1965).

14. Kolodziejczak J., Sosnowski L., and Zawadzki W.,Proc. Int. Conf. Semiconductor Physics, Exeter, p.94 (1962).

15. Kolodziejczak J. and Sosnowski L., Acta. Phys. Polon, 21, 339 (1962).

16. Spenke E., Electronic Semiconductors,p.60 (1958).

17 Smith R.A., Semiconductors, p.99 (1961)

18. Ziman J.M., Principles of the Theory of Solids, p.159 (1964).

19. Blakemore J., Semiconductor Statistics, p.76 (1962).

20. Blakemore J., Semiconductor Statistics, p.79 (1962).

21. Blakemore J., Semiconductor Statistics, p.104 (1962).

22. Blatt F.J., Solid State Physics vol 4, p.213 (1957).

23. Blakemore J., Semiconductor Statistics, p,119 (1962).

24. Blakemore J., Semiconductor Statistics, p.125 (1962).

25. Blakemore J., Semiconductor Statistics, p. 133, (1962).

26. Blatt F.J., Solid State Physics vol 4, p.214 (1957).

27. Smith R.A., Semiconductors, p.91, 92 (1961).

28. Ziman J.M., Principles of the Theory of Solids, p.179 (1964).

29. Tsidil'kovskii I.M., Thermomagnetic Effects in Semiconductors, p.31 (1962).

30. Putley E.H., The Hall Effect and Related phenomena p.77(1960).

31. Blatt F.J. Solid State Physics vol 4, p.321(1957).

32. Putley E.H., The Hall Effect and Related phenomena p.79-80(1960).

33. Tsidil'kovskii I.M., Thermomagnetic Effects in Semiconductors, p.35 (1962).

34. Putley E.H., The Hall Effect and Related phenomena, p.72(1960).

35. Putley E.H., The Hall Effect and Related phenomena, p.81(1960).

36. Putley E.H., The Hall Effect and Related phenomena, p.118(1960).

37. Putley E.H., The Hall Effect and Related phenomena, p.96(1960).

38. Putley E.H., The Hall Effect and Related phenomena, p.97(1960).

39. Smith R.A., Semiconductors p.126 (1961).

40. Smith R.A., Semiconductors p.172, 174. (1961).

41. Tsidil'kovskii I.M., Thermomagnetic Effects in Semiconductors, p.4. (1962).

42. Tsidil'kovskii I.M., Thermomagnetic Effects in Semiconductors, p.83, 84 (1962).

43. Tsidil'kovskii I.M., Thermomagnetic Effects in Semi-conductors, p.92 (1962).

44. Ziman J.M., Electrons and Phonons, p.44, (1963).

45. Bardeen J. and Schockley W., Phys. Rev., 77, 407 (1950).

46. Gibson A.F., Course 22 Semiconductors, p.204 (1963).

47. Smith R.A., Semiconductors p.146 (1961).

48. Gibson A.F. Course 22 Semiconductors, p. 206 (1963).

49. Enz. C, Physica, 20, 983 (1954).

50. Blatt F.J., Solid State Physics vol.4, p.336 (1957).

51. Harrison W.A., Phys. Rev. 104, 1281 (1956).

52. Conwell E.M. and Weisskopf V.F., Phys Rev., 77, 388 (1950).

53. Brooks H. Phys. Rev., 83, 879 (1951).

    Herring C. (unpublished).

54. Mansfield R., Proc. Phys. Soc., B69, 76 (1956).

55. Pearson G.L. and Bardeen J., Phys. Rev., 75, 865 (1949).

56. Erginsoy C., Phys. Rev., 79, 1013 (1950).

57. Smith R.A., Semiconductors p.152 (1961).

58. Dexter D.L. and Seitz F., Phys. Rev., 86, 964 (1952).

59. Beer A.C., Galvanomagnetic Effects in Semiconductors, p.312 (1963).

60. Beer A.C., Galvanomagnetic Effects in Semiconductors, p.315 (1963).

61. Moss T.S., Optcial Properties of Semiconductors, p.1,(1961)

62. Moss. T.S, Optical Properties of Semiconductors,p.13(1961).

63. Bardeen J., Blatt F.J. and Hall L.H., Photoconductivity Conference Wiley N.Y., p.36-37 (1954/1956).

64. Fan H. Y. Shepherd M.L. and Spitzer W., Photoconductivity Conference, Wiley N.Y. (1954/56).

65. Weiher R.L. and Ley R.P., Jour. App. Phys. 37,299 (1966).

66. Moss. T.S., Optical Properties of Semiconductors,p.46(1961)

67. Moss. T.S, Optical Properties of Semiconductors,p.45(1961)

68. Fredrikse H.P.R. and Blunt R.F., Photoconductivity Conference, p.442, (1954/56).

69. Ryvkin S.M., Photoelectric Effects in Semiconductors, p.1 (1964).

70. De Vore mentioned by Bube R.H., Photoconductivity of Solids, p.392 (1960).

71. Fredrikse H.P.R., and Blunt R.F. Photoconductivity Conference p.418 (1954/56).

72. Moss T.S., Optical Properties of Semiconductors,p.41(1961).

73. Hansen M. and Adenko K.,Constitution of Binary Alloys p.840 (1958).

74. Delves R.T. and Lewis B.J., J.Phys.Chem.Solids, 24,549(1963).

75. Suchet J.P., Chemical Physics of Semiconductors p.3 (1965).

76. Lawson W.D., Nielsen S., Putley E.H. and Young A.S., J. Phys. Chem. Solids. 9, 325 (1959).

77. Brebrick R.F. and Strauss A.J., J.Phys.Chem. Solids 26, 989 (1965).

78. Delves R.T., Brit. J. Appl Phys., 16 , 343 (1965).

79. Blum A.I. and Regel A.R., Zhur. Tekh. Fiz., 21, 316 (1951).

80. Nikol'skaya E.I. and Regel A.R., J.Tech.Phys. U.S.S.R., 25, 1347, 1352 (1955).

81 Elpat'evskoya O.D. and Regel A.R., J.Tech.Phys. U.S.S.R., 27, 45 (1957). (Trans: Sov.Phys. (Tech.Phys.)) 2, 35 (1957).

82. Tsidil'kovskii I.M., Sov.Phys. (Tech.Phys.), 2,1622(1957).

83. Carlson R.O., Phys. Rev., 111, 476 (1958).

84. Black J. et al, Bull. Am. Phys. Soc. Ser. II,3,15(1958).

85. Harman et al, J.Phys. Chem.Solids, 7, 228 (1958).

86. Quillet A. et al, Proc.Int.Conf. Semiconductors, Exeter,
p.711 (1962).

87. Rodot H. and Triboulet R., Comptes Rendus, Paris,
254, 852 (1962).

88. Dziuba Z., Acta. Phys. Polon., 26, no.5, 897 (1964).

89. Krucheanu Ye et al, Kristallografiia, 9, no.4,537(1964).

90. Rarenko I.M. and Gavaleshko N.P., Rost. Kristollov,
6, 267 (1965).

91 Crucceanu E. et al., Fizika Tverdogo Tela, 7,no.6,1808(1965).

92. Moronchuk Yu E. et al. Sistemy, Novsibirsk, Sb. 15,67-75(1965)

93. Kobus A. and Ignatowicz S.Jr. Solid State Electronics,
9, no. 5, 595 (1966).

94. Rodot H. and Rodot M., Comptes Rendus, Paris, 248,937(1959);
Comptes Rendus, Paris, 250, 1447 (1960).

95. Strauss A.J. et al. Proc. Int. Conf. Semiconductors, Exeter,
p.703 (1962).

96. Rodot H., J. Phys. Chem. Solids, 25, 85 (1964).

97. Giriat W. Brit. J. Appl. Phys. 15, 151 (1964).

98. Sharavskiy P.V. and Khabarova V.A., Sb. Fizika Dokl.,
no.22, Nauchn Conferentsii Leningr., Inzh. - Stroit. int.
L. p.5 (1964).

99. Giriat W. et al Proc Int. Conf. Phys. Semiconductors,
Paris, p.1251 (1964).

100. Dziuba Z., Acta. Phys. Polon. 25, no. 5, 757 (1964).

101. Dziuba Z. and Zakrzewski T., Phys. Stat. Sol. 7,1019(1964).

102. Tovstyuk K.D. et al. Izv. Akad. Nauk. S.S.S.R. Ser. Fiz,
28, no. 6,1057 (1964).

103. Ivanov-Omskii V.I. et al. Doklady, 162,no.6,1269(1965).

104. Hlasnik I. Phys. Stat. Sol., 13, no.2,K61 (1966).

105. Chubova L.K. et al, Ukrains'kyi Fizichnyi zhurnal, 10, No. 6, 630 (1965).

106. Kolosov E.E. and Sharavskii P.V., Fizika Tverdogo Tela, 7, no. 12. 3679 (1965).

107. Lewis J.E., Ph.D. Thesis, Durham University (1965).

108. Lewis J.E. and Wright D.A., Brit. Jour. Appl. Phys. 17, 783 (1966).

109. Wagini H. and Reiss B., Phys.Stat.Sol., 15, 457 (1966).

110. Groves S. and Paul W., Phys.Rev.Letters, 11, 194 (1963).

111. Harman T.C. et al, Solid St. Commun., 2, 305, (1964).

112. Wright D.A., Brit.J.App. Phys. 16, 939 (1965).

113. Kolodziejczak J., Int.Conf. Physics Semiconductors, Paris p.1147 (1964).

114. Piotrzkowski R. et al., Phys.Stat.Sol., 8, K135 (1965).

115. Cardona M., J.Phys. Chem. Solids, 25, 1543 (1963).

116. Delves R.T., Proc. Phys. Soc., 87, 809 (1966).

117. Olimpu I. et al. Comptes Rendus Hebdomadaires des Seances de la l'Academie des Sciences, 260, no.6, 3591-94 (1965).

118. Yamamoto M. and Fukuroi T., J.Phys.Soc. Japan, 21, 2428(1966).

119. Quillet A., J.Phys.Radium, 23, 93 (1962).

120. Blue M.D., Phys.Rev. 134, A226 (1964). Proc.Int.Conf. Phys. Semiconductors, Paris, p.233 (1964).

121. Cardona M. and Greenaway D.L., Phys. Rev.,131,98(1963).

122. Scouler W.J. and Wright G.B., Phys.Rev. 133, A736(1964).

123. Varie C. and Decamps E., Phys.Stat.Sol., 9, 797 (1965).

124. Sniadower L. et al., Phys. Stat.Sol., 8, K43 (1965).

125. Sorokin D.M., Sov.Phys.Sol.State, **2**, 2091 (1961).

126. Ivanov-Omskii V.I. et al, Izv.Akad.Nauk. U.S.S.R. Ser. Fiz. **28**, no.6,1057 (1964).

127. Wojas J., Phys.Stat.Sol., **12**, no.1, 407 (1965).

128. Braithwaite J., Proc.Phys.Soc., **B64**, 274 (1951).

129. Kruse P.W. et al, Infra-Red Physics, **2**, 53 (1962).

130. Ioffe A.V. and Ioffe A.F.,Sov.Phys.Sol.State, **2**,719(1960).

131. Rodot M. et al,J.Appl.Phys., **32**, 2254 (1961).

132. Spencer P.M., Thesis, University of Durham (1963): Brit. J.Appl.Phys., **15**, 625 (1964).

133. Kelemen F. et al., Phys.Stat.Sol., **11** no.2, 865(1965).

134. Stradling R.A., Proc.Phys. Soc. (G.B.) **90**,pt.1, 175 (1967)

135. Mavroides J.G. and Kolesar D.F., Sol.State Comm., **2**, no.12 363-64 (1964).

136. Hansen M. and Adenko K., Constitution of Binary Alloys, p. 863 (1958).

137. Holmes P.J. et al., J.Phys.Chem.Solids, **23**, 1 (1962).

138. Zaslavskii R.I. and Sergeeva V.H.,Sov.Phys.Sol.State, **2**, no.11, 2556 (1961).

139. Woolley J.C., Pamplin B.R., and Holmes P.J., J.Less.Comm. Metals, **1**, 362 (1959).

140. Zhuze V.P. et al, Sov. Phys.Sol.State, **2**, no. 11, 2545(1961).

141. Sclar C.B.,Carrison L.C., and Schwartz C.M., Science, **143**, 352 (1964).

142. Atroshchenko L.V. et al, Izvestiia Neorganicheskie Materialy, **1**, no.12, 2140 (1965).

143. Palatnik L.S. et al. Doklady, 165, no.4, 809 (1965).

144. Hahn H. and Klinger W., Zeit.Anog.Chem. 260, 97 (1949).

145. Gasson D.B. et al, Proc.Int.Conf.Semiconductor Physics, Prague, p.1032 (1960).

146. Inuzuka H. and Sugaike S., Proc.Acad.Japan. 30,383(1954).

147. Woolley J.C. and Pamplin B.R., J.Elect.Chem.Soc. , $\underline{101}$, 874 (1961).

148. Ioffe A.F., Doklady Akad. Nauk. S.S.S.R, $\underline{16}$,no.10(1952); Sov.Phys.Tech.Phys., $\underline{2}$,1049(1957); Sov.Phys.Sol.State, $\underline{1}$, 139, 141 (1960).

149 Chizhevskaya S.N. and Glazov V.M., Doklady Akad. Nauk. S.S.S.R., $\underline{145}$, no.1 115 (1962).

150. Sergeeva V.M. and Shelyleh A.I., Fiz.Tuer.Tela. $\underline{2}$, no.2, 347 (1960).

151. Petrusevitch V.A. and Sergeeva V.M., Sov.Phys.Sol.State, $\underline{2}$, 2652 (1961).

152. Woolley J.C. et al, J.Phys.Chem.Solids., $\underline{19}$, 147 (1961).

153. Zaslavskii A.I. et al Sov.Phys.Sol.State, $\underline{2}$, no. 11 2565 (1961).

154. Zmirnov et al, Sov.Phys.Sol.State, $\underline{1}$, 555 (1960); and Sov.Phys.Sol.State, $\underline{2}$, 527 (1961).

155. Petrusevitch V.A. et al., Sov.Phys.Sol.State, $\underline{2}$, no. 11, 2573 (1961).

156. Hahn H. et al., Z.anorg.Chem., $\underline{279}$, 241 (1955).

157. Woolley J.C. and Ray B., J.Phys.Chem.Solids. $\underline{15}$,27(1960).

158. Pamplin B.R., Thesis, Nottingham University (1960).

159. Spencer P.M., Pamplin.B.R. and Wright D.A., Proc.Int. Conf. Physics of Semiconductors, Exeter,p.244 (1962).

160. Mason D.R. and Cook J.S. J.Appl.Phys., $\underline{32}$, 475 (1961).

161. Ray B. and Spencer P.M., Sol.State.Commun. $\underline{3}$, 389 (1965).

162. Ray B. and Spencer P.M., Private Communication (1967).

163. Busch G. et al. Halbleiter und Phosphore (Brunswick Vieweg), 470 (1958).

164. Gilman J.J., The Art and Science of Growing Crystals, p. 372 (1963).

165. Putley E.H., The Hall Effect and Related phenomea,p.45(1960).

166. Spencer P.M., Thesis, University of Durham (1963); Brit.
     J.Appl.Phys., 15, 76 (1964).

167. Lewis J.E., Ph.D. Thesis, Durham University p.94 (1965).

168. Spencer P.M., Thesis, University of Durham (1963): Brit.
     J.Appl.Phys., 15, 104 (1964).

169. Lewis J.E., Ph.D. Thesis, Durham University p.95 (1965).

170. Henry N.F.M. et al, Interpretation of X-ray Diffraction
     Photographs, p.77 (1961).

171. Henry N.F.M. et al, Interpretation of X-ray Diffraction
     Photographs, p.190 (1961); see also ch.11, p.168 for
     the method of taking powder photographs and ch.6,
     p.71 for Laue Photographs.

172. Putley E.H. The Hall Effect and Related phenomena.p.42(1960).

173. Drabble J.R. and Wolfe R., J.Electronics Control, 3,
     259 (1957).

174. Hilsum C. and Rose-Innes A.C., Semiconducting III-V
     Compounds, p.151 (1961).

175. Beer A.C., Galvanomagnetic Effects in Semiconductors,
     p.57 (1963).

176. Oliver D.J., Proc. Int. Conf.Phys.Semiconductors, Exeter,
     (1962), p.133.

177. Holonyak N.Jr. et al, Phys.Rev.Letters 8, 426,(1962).

178. Lampert M.A., Phys.Rev. 125, 126 (1962).

179. Ehrenreich H., J.Phys.Chem.Solids, 9, 129 (1959).

180. Smith R.A., Semiconductors p.112. (1961).

181. Wagini H. Zeit. Naturforsch., 19a, 1541 (1964).

182. Ioffe A.F. and Stilbans L.S., Reports on Progr. Phys.,
     22, 167 (1959).

183. Allgaier R.S. and Houston B.B.Jr., Proc.Int.Conf.Phys.
     Semiconductors, Exeter (1962) p.172.

184. Tsidil'kovskii I.M., Thermomagnetic Effects in Semiconduct-
      ors, p. 171 (1962).

185. Rodot M.,Compt.rend., <u>243</u>, 129 (1956).

186. Cuff K.F. et al.,Proc.Int.Conf.Phys.Semiconductors,
      Exeter, (1962) p.316.